Stable and Ultra-Stable Laser Systems for a Mobile Strontium Optical Clock

by

Dariusz Tadeusz Świerad

A thesis submitted to
The University of Birmingham
for the degree of
DOCTOR OF PHILOSOPHY

Ultracold Atoms Group
School of Physics and Astronomy
College of Engineering and Physical Sciences
The University of Birmingham

December 2017

Abstract

This thesis presents a realisation of the most demanding laser systems for a mobile strontium optical clock. First, stable 689 nm cooling lasers are presented: an amplified semiconductor diode laser and a prototype of the semiconductor disc laser (SDL/VECSEL). The first was stabilised to a novel miniaturised multi-laser frequency stabilisation system that allows to stabilise all the six lasers used in the strontium optical clock. The latter was used for the first time in the second-stage cooling of strontium to obtain a cold cloud of trapped atoms.

An atomic optical clock requires a laser oscillator for interrogating the clock transition. This thesis presents the construction and discusses the performance of the cutting-edge ultra-stable interrogation lasers at 698 nm. One of the systems is a stationary system based at the University of Birmingham, with the instability of 5×10^{-15}. A mobile version of the interrogation laser is also presented and characterised in this work. The laser reaches instability of 8×10^{-16}, which is one of the best results for a mobile system. The mobile laser is a part of the space optical clock project (SOC2), in which a record-low instability for the bosonic strontium was observed of $< 4 \times 10^{-16}/\sqrt{\tau}$.

Dla Klaudii

Dla moich rodziców

ACKNOWLEDGEMENTS

This thesis has benefited from a vast number of people who are my friends, mentors, advisers and supervisors. At the beginning I would like to thank Prof. Kai Bongs for giving me the opportunity to join the Cold Atoms group at the University of Birmingham, for useful discussions, support and trust. Special thanks to Dr. Christian Lisdat and Dr. Uwe Sterr for their great supervision during my secondment at the Physikalisch-Technische Bundesanstalt (PTB). I will always remember your immense hospitality and help that you gave me. Thank you for extremely useful and instructive discussions and for always speaking English in my company. It was an honour working with you. I also want to thank Dr. Rodolphe Le Targat and Dr. Jérôme Lodewyck from the Paris Observatory for their help and advice.

I would like to thank everyone working with me in the clock experiment at the University of Birmingham. Thanks to Dr. Yeshpal Singh for his understanding, kindness and keeping our experimental group running. I should especially thank Dr. Ole Kock and Dr. Joshua Hughes for guiding me through the spider web of cables in the laboratory and for being keen on sharing their knowledge and experience with me. Particularly, I thank Dr. Lyndsie Smith for being a great lab companion, for many comforting discussions and advice. It was you Lyndsie, who sacrificed your entire lab snack box so that I could have my first one. Also, I want to thank Stefano Origlia for being a good colleague, being helpful and for sharing his Parmigiano-Reggiano with me. Many thanks to Dr. Wei He for his support, kindness, for telling interesting stories, bringing the gummy bears and good mood to our lab. Special thanks to Sruthi Viswam for her help with the experiment, support and smile. I also thank Dr. Huadong Cheng for introducing me to the experiment and performing the first measurements with me. A big thank you to all the summer and 4^{th} year students: Patrick, Dan, Matt, Huang and Alex for their help and contribution to development of the experiment.

During my secondment at PTB I have met many friendly people who I must to thank. First of all, I would like to thank Dr. Sebastian Häffner for sharing his knowledge and experience on the ultra-stable lasers and providing help for the entire time during my visit. Also, thanks to Dr. Stefan Vogt for his precious time while writing his thesis and Dr. Christian Grebing for his help with the frequency counters. Many thanks to

Jacopo, Ali, Sören, Andreas and Silvio for being friendly and helpful. Special thanks to Dr. Thomas Legero for teaching me the "dark art" of optical contact bonding. I also thank Dr. Harald Schnatz for his kindness and making me feel welcome in his group.

Thank you to the whole Cold Atoms group. You are growing so fast that I am not able to list all your members any more. I should begin with thanking Dr. Anna Kowalczyk for her help and good advise in every topic from the science to booking flights. Special thanks to Clemens, George, Marisa, Alex, Ole, Nadine, Ania and Artur for many good moments together. I also want to thank my peers Harry for his extreme kindness, Andreas for his friendliness and Daniel for his calmness. Many thanks to Dr. Vincent Boyer and Dr. Jon Goldwin for very useful discussions. I would also like to thank Dr. Plamen Petrov for his advise and explanations. Also, thanks to Dr. Jochen Kronjäger for his help with electronics. I must to thank Chris, Plamen, Andy, Harry and Ania for help in exercising brain when playing bridge at the lunch breaks. Huge thank you to the entire team in the mechanical workshop and Stephen Brookes in particular for their fantastic realisation of my mechanical designs. Thank you to Chow and Ian from the stores for always finding the necessary bits and pieces. I also want to thank John Bryant for access to the clean room facilities.

I would like to thank all my friends from the Maria Skłodowska-Curie Initial Training Network: Clemens, George, Saurabh, Thomas, Noaman, Sindhu, Amruta, Marco, Mattia, Nazanin, Niko, Muhammad and Ivan. I am very glad to know you and you made every of our network meetings worthwhile. Thank you to my second supervisor within the network Dr. Christoph Becker for discussions and friendliness. Big thank you to the management and supervisory board of the network and in particular Dr. Thomas Fernholz for very good coordination. Thanks to Romina Davoudi for continuous report reminders and devotion to the network.

I need to thank Matthew Gray from ARUP for his help with vibrational measurements in the lab and Mr. Phil Atkins for a discussion on the acoustic isolation. I would also like to thank Dr. David Pabœuf for his help with the VECSEL. I also want to thank Curtis Hentschel and a dear friend, Dr. Chau Meng Huat, for editorial help and proofreading my thesis. I want to thank the entire SOC2 consortium and especially Prof. Stephan Schiller for the coordination and his friendliness.

I acknowledge the support from the FP7 Maria Skłodowska-Curie Actions of the European Commission, via the Initial Training Network QTea (contract-No. MCITN-317485). Part of the research leading to these results has also received funding from the European Union Seventh Framework Programme (FP7/2007-2013) under grant agreement No. 263500.

Finally, I thank all my friends, family, former supervisors and teachers. Foremost, I want to thank my wife Klaudia for her patience, help, support, love and understanding.

CONTENTS

LIST OF FIGURES

LIST OF TABLES

CHAPTER 1

INTRODUCTION

Timekeeping has always been very important to humanity from the early beginnings. As the fourth dimension, somebody could say that time is just as important as the other three spatial dimensions. Although it is possible to imagine living in a world without one spatial dimension, like Edwin A. Abbott in his book entitled "Flatland: A romance of many dimensions" [1], nobody can imagine living without the temporal dimension, time.

Scientific testimony to the importance of time measurement is given by the fact that nowadays it is the most accurately measured fundamental physical quantity, reaching uncertainty of 2×10^{-18} expressed in fractional units for the most stable ytterbium ion clock described by Nicholson et al. in [2]. In comparison, the most accurate measurement of mass can be done with an order of $< 5 \times 10^{-9}$ relative uncertainty [3, 4]; and the most accurate measurement of temperature is in the order of 10^{-7} [5, 6, 7].

As the speed of light constant is by definition equal to 299 792 458 m/s exactly, it is possible to link the definition of length to time, and that is exactly how the meter unit is defined in the SI unit system [8]:

> "The meter is the length of the path travelled by light in vacuum during a time interval of 1/299 792 458 of a second."

The ability to accurately measure time is therefore necessary to precisely determine the length of an object. Modern length measurement methods involve using lasers [9] and the most precise is based on laser interferometry. The wavelength of that laser must be very well defined, which is achieved by stabilising it to a reference (e.g. molecular), similar to how it is stabilised in an optical atomic clock.

1.1 Short history of clocks

The road towards modern atomic clocks was very long and originated from the very beginning of everything that we know. The Earth's spin around its own axis is the most evident example of how time can be observed. It is the reason for the occurrence of day and night which can be counted to measure the time. The moon orbiting the Earth is another example of an astrophysical oscillator that can be used to measure time. Our ancestors used full moons to count synodic months that last on average $\sim$ 29.5 days long [10]. Changing seasons, caused by the Earth orbiting the Sun, were another source of information, allowing them to count the years.

To be able to more precisely determine the time of day, our ancestors learnt how to measure the day's phase. They used a wall or stick that cast different shadows depending on the position of the Sun in the sky. By assigning different positions of the shadow to different parts of a day (hours), the first sundials were created [11]. Sundials were good enough to determine the time of day and to measure hours. However, they had many cons as they could not be used indoors, during the night or on a cloudy day, on a ship and finally, they were not precise enough to measure short periods of time. To overcome these obstacles, other chronometers were also invented.

One of them was a water clock that used the steady flow of water to measure time intervals. It was already known in ancient Egypt that the most advanced designs had a passive feedback mechanism for regulating the water flow rate. Using water in the clock could be troublesome as it could not be moved during operation, and it would not work in temperatures below the freezing point of water. The latter problem was eliminated by replacing the water with liquid mercury. However, a very neat solution was to use very fine sand instead of liquid. This idea gave birth to a sand glass. Although the accuracy of a liquid clock could be better under controlled conditions, the sand glass was easy to produce, more compact and it turned out to be very useful on the ships, where they were used for navigation [12].

Another way of measuring time intervals was based on the steady rate of a chemical reaction. This reaction was mainly the burning of different fuels like wax or coal oil [13].

In the 16^{th} century, Italian scientist Galileo Galilei was the first to study the properties of the pendulum, and its ability to measure time intervals. The first to implement the pendulum in a clock, however, was Dutch mathematician Christiaan Huygens in the 17^{th} century. Huygens also developed a spring balance clock that had the great advantage of being operational in every position, independent of the gravitational field. Both the pendulum and spring balance clocks were the first steps towards constructing the marine chronometer that revolutionised the navigation around the seas [14].

Early 20^{th} century was the time of the first electronic clocks. The most significant was the quartz clock that uses a quartz crystal as an oscillator. When an alternating voltage is applied to the crystal, it vibrates, thanks to the piezoelectric effect [15]. Each crystal has a different resonant frequency, which depends on the shape of the crystal and its physical properties. Most commonly, crystals are calibrated to resonate at $\sim$ 32768 Hz, which corresponds to 2^{15} Hz. This number is convenient since the signal at this frequency can be simply divided down to 1 Hz by using binary frequency dividers. The magnitude of the frequency is chosen to be a trade off between optimising the size of the crystal, and the power consumption of the resonant electronic circuit [15].

Early atomic clocks

The beginning of the 20^{th} century was also the time of the first developments towards atomic clocks; although the idea of using electromagnetic waves to realise time standards can be traced back to 1873 when James Clerk Maxwell proposed it in his book "A treatise on electricity and magnetism" [16]. It all started with the revolution in quantum physics, and advances in experimental methods and apparatus. Stern and Gerlach contributed towards developing the molecular beam techniques with their famous series of experiments around the year 1922, where they first demonstrated separation of molecules occupying different magnetic states by using an inhomogeneous magnetic field [17]. The inhomogeneous magnetic field was later used in beam caesium clocks for the initial state preparation of atoms and the final state detection. In 1937, Isidor Isaac Rabi came up with a method of exciting the magnetic resonance in molecular beams [18] and a year after, together with his team, was the first to observe a magnetic resonance in molecular beams [19]. Positive results motivated Rabi to use his method to construct the first atomic clock. Their project was unfortunately interrupted by the second World War, but even if it had been continued they would have obtained accuracies of the order of 10^{-8}. This was achievable with existing clocks at the time and would not have brought any advantage [20].

In 1949 Norman Foster Ramsey, a former PhD student of Rabi, invented a new method of addressing the molecular beams by using two separated oscillatory fields [21]. He subsequently showed the method to work experimentally in the following years. The new scheme of interrogating the atoms increased the resolution significantly making the way for the first atomic clocks.

In 1955 Louis Essen and Jack Parry developed the first caesium atomic clock at the National Physical Laboratory (NPL) in Teddington, UK. They were also the first to measure the frequency of the hyperfine clock transition in caesium, which became the base for other atomic clock experiments, and eventually led

to the redefinition of the second in 1967 [20]. The International Committee on Weights and Measures agreed on the definition of a second as follows [8, 22]:

> "The second is the duration of 9 192 631 770 periods of the radiation corresponding to the transition between the two hyperfine levels of the ground state of the caesium 133 atom."

Atom fountain clocks

The Ramsey method of interrogating the atoms involves two, preferably identical, oscillatory fields that atoms pass through. The molecular beam travelled horizontally in early experiments, which needed two identical Ramsey resonators. In the 1950s Jerrold Zacharias tried to realise a new idea of using only one Ramsey resonator by transforming the horizontal orientation of the experiment into vertical, with the atom source aiming upwards [23]. The main point of the idea was that the atoms pass through the resonator once in their way up and turn back due to gravitational acceleration, passing through the same resonator in their way back down. This method was supposed to select only slow atoms from the whole thermal distribution, increasing the resolution of the measurement and removing some systematic errors. This type of atomic clock was named after fountains because of the stream of atoms going up and then reversing back down. Unfortunately, Zacharias' experiment with hot molecular beam did not bring any positive results and it was soon abandoned [24].

The idea of the fountain clock was resurrected after the invention and development of laser cooling and trapping methods [25]. Cooled and trapped cloud of atoms have much smaller temperatures than a beam of thermal atoms in the order of a few μK [24]. Additionally, such a cloud can consist of hundreds of millions of atoms giving a good signal to noise ratio. Velocity of the cloud is distributed around zero, which helps to prevent the expansion of the cloud. It can therefore be ejected up so that it passes through the Ramsey cavity on the way up, and on the way down. In modern fountain clocks, lasers are not only used for cooling and trapping atoms, but also for state preparation and state detection.

In 1989 John Hall led the theoretical consideration of the fountains [26] with ultra-cold atoms, and in the same year, Mark Kasevich realised the first experiment with sodium, in which he obtained a 2 Hz wide Ramsey fringe [27]. Although he did not build an optical clock out of it, the first fountain clocks appeared soon after, with the development of the first caesium fountain for metrological use in France [28]. This design became the basis for future fountain clock designs

Clocks in space

When the Soviet Union launched the first man-made satellite Sputnik [29] into space, it opened a new era for space exploration and inspired scientists and governments to create a navigation system with the help of satellites.

The very first satellites were equipped with very stable quartz clocks. Thanks to the high stability and robustness of the clock it was possible to generate a stable radio frequency signal. A signal sent from such a satellite and received by a stationary point on Earth would be shifted in frequency due to a Doppler shift. This shift is significant as the velocity of the orbiting satellite can reach very high values on the order of 10^4 km/h. If the orbit and speed of the satellite are well known, based on the shape of the recorded Doppler curve, it is possible to determine the location of a receiver on the ground. This technology was known as the Navy Navigation Satellite System (NNSS, NAVSAT or TRANSIT) [30] and was developed mainly for navigation around the seas. One of the requirements for the NNSS was that it should not take longer than the 2 minutes emergence time of a submarine to determine the position. Location calculations required high computational power to adequately fit the Doppler curve, which was not easy in the 1960s. The 2 minute requirement was eventually achieved, but this was still relatively long and its applications were mainly limited to vessels and stationary objects. For long measurement times lasting days, it was possible to determine the position down to a metre accuracy [31].

The first atomic reference standards to be sent into space were launched on the Navigation Technology Satellite (NTS-1) in 1974 [32, 33]. NTS-1 carried a pair of rubidium vapour frequency standards and their goal was to test the concept of the atomic standards in space. Soon after in 1977, a pair of the first space caesium clocks were launched into space on the Navigation Technology Satellite 2 (NTS-2) [34, 33, 32]. Thanks to the lower instability of the new atomic clocks of 5×10^{-13} and 2×10^{-13} for satellite NTS-1 and NTS-2 respectively [32], it was finally possible to try out new things that could not be tested with quartz clocks. For example, NTS-2 was used to test the gravitational time shift associated with Einstein's theory of general relativity. The NTS-2 mission also proved the potential of the atom frequency reference, which led to further development of the modernised Global Positioning System (GPS).

1.2 Clock operation

Despite different mechanisms being used in different types of clocks, the basic idea of their operation remains the same. In figure 1.1 a schematic diagram of a clock operation is presented.

Every clock needs to consist of an oscillator and a reference. The oscillator generates a periodic signal that can be compared with the eigenfrequency of the reference. The difference between the frequencies of the oscillator and reference is observed by a detector and the detuning information is processed and fed back to the oscillator mechanism which then corrects its frequency to reach the reference eigenfrequency. In this way, the stability of the reference is transferred into the oscillator. The time is obtained by counting the ticks of the oscillator, which can by done by a person or mechanism for slow oscillations. For fast oscillations, it might be necessary to divide the frequency to be able to read the result.

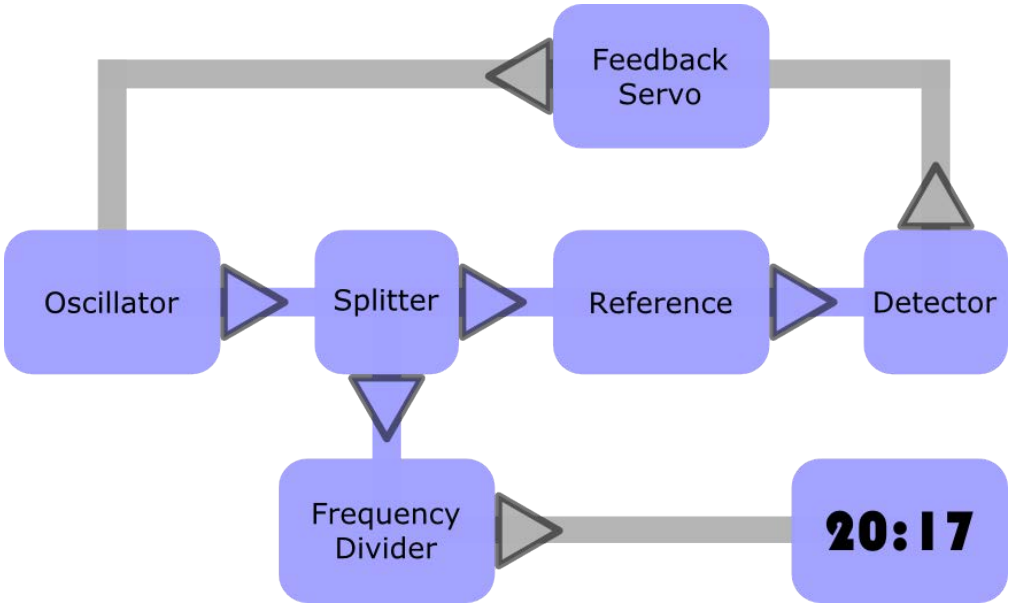

Figure 1.1: Schematics of a clock. The frequency signal ν_{osc} from an oscillator is split into two parts. One part is compared with a reference frequency ν_{ref} with the help of a detector. The signal from the detector is processed by a feedback servo to generate an error signal, which is used to correct the frequency of the oscillator. The frequency of the second part of the signal is divided and delivered to an output e.g. digital time display.

The pendulum is a good example of the reference in a mechanical clock. The length of the pendulum and gravitational field dictate its oscillation eigenfrequency. The clock is powered by the potential energy stored in the clockspring, which is the clock's oscillator. The frequency of the pendulum is transferred to the clockspring by an escapement mechanism. If it was not for the escapement, the clock spring would unwind with an unknown angular frequency. Escapement acts as a feedback servo, stopping and releasing the unwinding spring with every swing of the pendulum. Additionally, the escapement uses the potential energy of the clockspring to excite the pendulum, preventing its oscillations from dying out. The eigenfrequency of a 25 cm long pendulum in Earth's gravitational field is approximately equal to 1 Hz, which is much higher

than the Earth's rotation frequency equal to ~ 12 μHz. To make the comparison between the two clocks, it is useful to divide the frequency of the pendulum clock by using gearing, commonly known as clockwork, which powers the minute and hour hand on the clock dial.

The same analogies also work for an optical atomic clock. The clock laser is the oscillator that is shone over the reference atoms. Part of the laser light energy is transferred to the atoms causing excitation if the frequency of the laser is equal to the frequency of the reference clock transition. Detuning of the laser from the oscillator can be observed with a detection scheme, and an appropriate error signal can be generated by an electronic feedback servo that adjusts the optical frequency of the laser. Although this setup is enough to become a stable frequency standard, the optical frequency is too high to be directly compared with any other electronic or mechanical clock, and thus it needs to be divided into lower frequencies. This is done by an optical frequency comb, which is the counterpart of the mechanical gearing.

The aforementioned error signal is a function of the detuning from the reference resonance, and it carries essential information on how to reach it. It can be any function that crosses zero for a detuning value equal to zero and preferably linear in that section. Now consider an oscillator having frequency ν_{osc}, and reference at frequency ν_{ref}. The best error function would be a function that is not only linear around the resonance, but in the entire domain. It can be written as $f_{err}(\nu_{osc}) = A \cdot (\nu_{osc} - \nu_{ref})$, where A is a sensitivity coefficient. For each argument of this function there is only one unique value. Therefore, it is possible to precisely know how much to correct the laser's frequency to tune it back to resonance, no matter how far it is detuned. In practice, such an error signal is very difficult or even impossible to obtain. One reason is that both the reference and the oscillator consist of a spectrum of different frequencies rather than a single frequency only. In an optical atomic clock, this is usually a Lorentz, or Gaussian distribution, both for the laser oscillator and atomic reference. An example of the frequency spectrum for a Lorentzian shape oscillator and reference is presented in the top part of figure 1.2. The reference, drawn with a black curve, acts as a bandpass filter that absorbs every frequency except for the Lorentzian-shaped band around its eigenfrequency ν_{ref}. For an oscillator with detuning $\Delta\nu$, drawn as a green curve, only the frequencies within the band pass will be transmitted through the reference. In the figure, this is marked as the intersection of green and black profiles. Blue and red shadowed intersection areas correspond to frequencies lower and higher than the resonance frequency of the reference, respectively. An example error signal can be generated by subtracting the blue part of the intersection from the red part, and it is plotted for different values of detuning $\Delta\nu$ in the bottom part of figure 1.2. An error signal with a similar shape, but opposite sign could be obtained by differentiating the reference bandpass function.

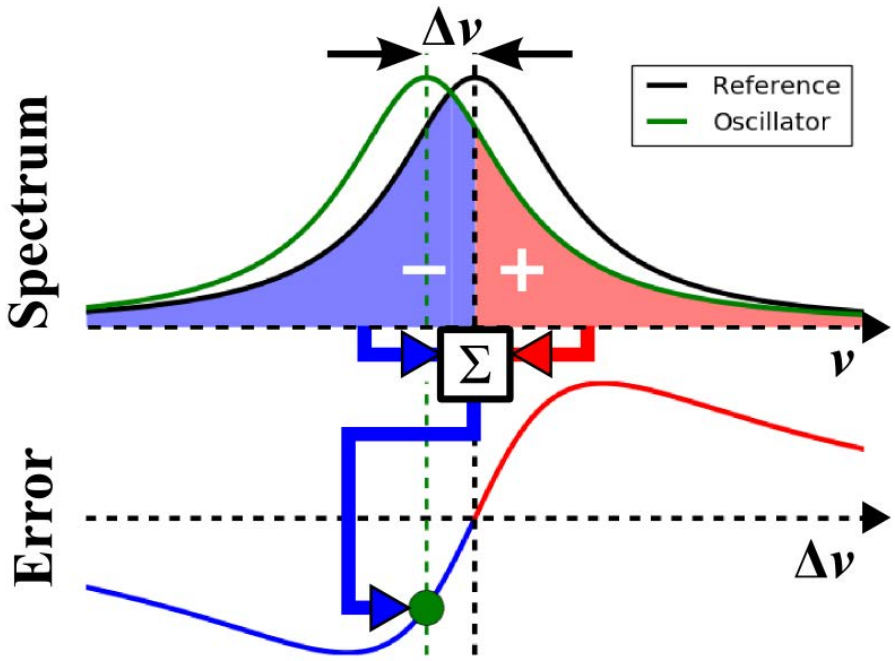

Figure 1.2: Schematics of error signal generation. **(top)** Lorentzian shaped frequency spectrum of an oscillator and reference, plotted with green and black solid lines, respectively. The central frequency of the oscillator ν_{osc} and reference ν_{ref} are marked with green and black dashed lines, respectively. The detuning of the oscillator from the reference frequency is $\Delta\nu = \nu_{osc} - \nu_{ref}$. Spectra intersection of reference and oscillator signals is marked with blue and red area. Blue and red colours show part of the intersection for frequencies lower and higher than the reference frequency ν_{ref}, respectively. **(bottom)** An example error signal is obtained by subtracting the blue area from the red area, and is generated for different detuning values $\Delta\nu$. The green point shows an error value generated for detuning visible in the top part of the figure.

1.3 Optical atomic clocks

It is a natural question to ask, why develop more complicated optical clocks if there are already well established atomic microwave clocks available. One of the reasons is the quantum projection noise, which is the fundamental limitation for all the atomic clocks. Obtaining an accurate measurement with an atomic clock depends on measuring atom population in the excited and ground state. Quantum projection noise is caused by random population fluctuations, which affect the reading accuracy. Optical transitions can have a lower value of the quantum projection noise, which can be estimated for a specific atomic transition with the following equation [35]

$$\sigma(\tau) \simeq \frac{\Delta\nu}{\nu_0}\frac{\sqrt{T}}{\sqrt{N\tau}} \tag{1.1}$$

where ν_0 and $\Delta\nu$ is the frequency and linewidth of the transition, respectively, N is the number of particles measured, T is the period of the coherent measurement, and τ is the total averaging time. As presented by the formula, the noise value will be smaller for a transition with narrower linewidth $\delta\nu$, or higher frequency ν_0. The latter motivates the use of the optical transition over the microwave hyperfine transitions. The limit can also be lowered by increasing the number of atoms or by a longer interrogation time.

1.3.1 Operation

In figure 1.3 a simplified scheme of how an optical atomic clock works is presented. First, an ultra-stable laser is required to probe the atomic clock transition. The laser beam is shone onto the cooled and trapped sample of atoms. An absorption signal is observed with a detector, while a servo system generates an error signal to provide feedback to the laser. As the laser stabilises to the atomic transition, its frequency strictly follows the frequency of the atomic reference transition. The time can be obtained by counting the frequency; however, for a laser, the frequency is equal to hundreds of THz and existing electronics is not fast enough to count the oscillations. One way of transferring the stability into lower frequencies is by using an optical frequency chain, which is described in more detail in [36]. A less complicated solution came with the invention of an optical frequency comb by T. W. Hänsch [37], who was honoured with a Nobel prize in 2005. The optical frequency comb is a phase-locked femtosecond laser that consists of a very broad spectrum of light, resembling a comb when plotted in frequency space. The teeth spacing of the comb is equal to the repetition rate of the laser, while the carrier envelope offset is equal to the phase difference between the pulses. The latter is eliminated in the difference frequency combs thanks to frequency difference generation [38]. The frequency comb can be stabilised to the clock laser with a signal generated by taking a beat note between the laser and one tooth of the frequency comb. This will transfer the stability of the clock laser to every tooth of the frequency comb creating a link to microwave frequencies that can be counted with electronics or compared with microwave atomic clocks.

1.4 Importance of atomic clocks

One of the possible applications of the atomic clocks is chronometric geodesy [39, 40], sometimes referred to as relativistic geodesy. According to the theory of general relativity, time flows differently in different gravitational potentials due to time dilation [41]. Optical clocks are sensitive enough to measure very small changes in time due to this effect, and therefore, can be used to measure gravitational potential. The difference

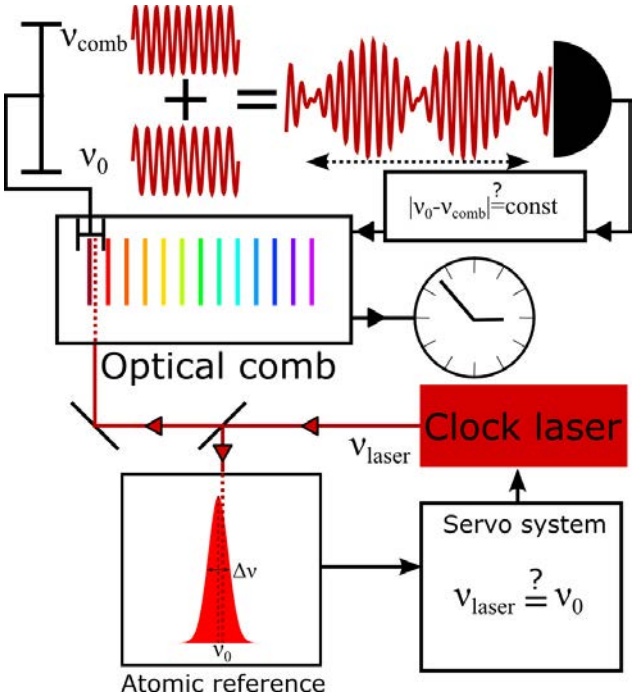

Figure 1.3: Schematic of an optical atomic clock. The clock laser is locked to the atomic reference with the help of a servo system. Part of the laser beam is sent to the optical frequency comb where a beat note between the laser and frequency comb tooth is generated. The beat note is used to stabilise the frequency comb, which transfers the stability of the clock laser into lower frequencies that can be counted by fast electronics.

in time flow can be observed by comparing two optical clocks operating at different gravitational potentials e.g. at different altitudes.

Thanks to the high stability and accuracy of optical clocks, it is also possible to put the fundamental physics to test. One example is in measuring the stability of fundamental constants. Some experiments suggest that fundamental constants such as the electron to proton mass ratio, the fine structure constant, and the light quark mass might be susceptible to drift [42, 43]. It is also possible to test the gravitational red-shift of Einstein's equivalence principle, by sending optical clocks into space, such as with the STE-QUEST project [44].

The global economy may also be influenced by atomic clocks. All national and international trades depend strongly on the time of released information and changing prices for example due to change of the exchange rates. Although insignificant to the average person, for large banks and financial institutions, it is crucial to be able to tell precisely the time of a transaction. It happened that unsynchronised clocks by as low as 15 ms were used for early release of trading information that when picked up by special algorithm it led to an early trade worth $25 millions in shares [45]. Thanks to atomic clocks it is possible to precisely synchronise clocks

between trading institutions, not only within a single country, but worldwide. Another example of the impact on the economy, as well as the ecology, is the use of the atomic clock for the synchronisation of power stations. A national electricity grid is connected to many power stations across the country, which inject alternating current into the grid. Phase and frequency of the current injected by the power station should match the phase and frequency of the power grid to achieve the best efficiency. The better the synchronisation of the power stations, the more accurate the phase and frequency of the injected current will be, resulting in the reduction of energy losses.

Improvement in atomic clocks can also improve the accuracy of the global positioning system (GPS). Every GPS satellite has an atomic clock on-board that is synchronised with other GPS satellites and metrological institutions on Earth. GPS satellites produce and distribute a radio frequency signal with information on their position and time when the signal was sent. The signal needs time to travel the distance between the satellite and receiver. That time can be computed by comparing the time of sending and receiving the signal and is used to calculate the distance between the satellite and receiver. By having access to signals from at least four GPS satellites, it is possible to determine latitude, longitude and altitude of the receiver. Sophisticated receivers can determine the position to an accuracy of a centimetre [46]. Making GPS even more precise will further improve navigation, as well as other fields of research such as geology and meteorology. The GPS signal is already being used in the remote sensing of water vapour in the atmosphere to improve the weather forecasts [47, 48].

1.5 State-of-the-art

1.5.1 Optical clocks

The atomic optical clocks keep beating new stability and accuracy records year by year. The best strontium lattice clocks achieve uncertainty levels as low as 10^{-18} [2, 49, 50], with the lowest uncertainty level of 2×10^{-18} obtained by Nicholson et al. [2] at JILA, USA. The most recent stability record of 3.1×10^{-17} at one second was obtained by Campbell et al. at JILA, USA [51], beating 1.8×10^{-16} obtained by Ushijima et al. [49] at RIKEN, Japan.

Single ion optical clocks can reach similar level of performance with uncertainty on 10^{-18} level, with Huntemann et al. obtaining the lowest value for the single ion clock of 3×10^{-18}, with ytterbium ion at PTB, Germany.

The transportable systems are more difficult to construct and they feature larger uncertainties on 10^{-17}

level. The most accurate transportable strontium lattice clock, presented very recently by Koller et al. [52], has uncertainty of 7.4×10^{-17} and instability of 1.3×10^{-15} at one second.

1.5.2 Ultra-stable lasers

Ultra-stable, narrow-linewidth lasers are not only an indispensable part of the optical clocks [53, 54], but also are used in the field of fundamental physics [55, 56, 57], such as test of Lorentzian invariance [58, 59, 60, 61], metrology [62], gravitational wave detection [63, 64], search for dark matter [65, 66], and Einstein's theory of general relativity [67, 39]. The ultra-stable lasers can also find application in creation of a new generation of radar systems [68], ultra-stable microwaves generation [69] and communication [70].

An ultra-stable laser is obtained by stabilising a laser to an optical resonator made of an ultra-low expansion material, such as ULE glass or Zerodur. State-of-the-art lasers can reach instabilities on a very low level of 10^{-17}. One of the best instability was obtained by a laser with a 48 cm long cavity at the room temperature, reaching value as low as 8×10^{-17} as presented by Häfner et. al [71] at PTB, Germany. Even lower instability was achieved very recently with a cryogenic single-crystal silicon cavity, reaching value of 5×10^{-17}, as presented by Matei et al. [72] at PTB, Germany in collaboration with JILA, USA. The paper also reports of obtaining ultra-narrow linewidth of 5 mHz and it features very low drift of 100 μHz/s. For comparison, drift of the room temperature ULE cavity presented by Häfner et. al [71] was 15 mHz/s, which is two orders of magnitude higher.

Traditionally, the optical resonator uses dielectric mirrors that limit the performance of the ultra-stable laser due to the Brownian noise. Recent developments in crystalline mirror coatings lead to reduction of the Brownian noise by ten times [73, 74] and are likely to contribute to beating new stability and linewidth records of the ultra-stable lasers in the near future [72].

The mobile ultra-stable laser is more difficult to construct. The optical cavity in such a system needs to be rigidly mounted and it should be small in size. Also, the laser requires more attention as when it comes to making it less sensitive to changing acceleration, which is unavoidable in the mobile environment. Different geometries have been tested by various groups around the world. An ultra-stable laser with spherical cavity design was demonstrated by Leibrandt et al. [75], with acceleration sensitivity between 1×10^{-10}/g and 4×10^{-11}/g for different axes, where g is the standard gravitational acceleration. A vertically mounted mobile cavity was presented by Argence et al. [76], with acceleration sensitivity between 4×10^{-11}/g and 1×10^{-11}/g. A horizontal cavity was presented by Nazarova et al. [77], with acceleration sensitivity between 3.0×10^{-10}/g and 3.2×10^{-11}/g. Another horizontal transportable cavity, with special ridges used for

mounting, was presented by Chen et al. [78] and it features acceleration sensitivity between 3.9×10^{-10}/g and 1.7×10^{-11}/g. An alternative force-insensitive cube cavity design was presented by Webster et al. [79], with acceleration sensitivity between 2.5×10^{-11}/g and 1×10^{-13}/g. The cube cavity seems to be the best solution for the mobile experiment when it comes to vibration insensitivity. Downside of the cavity is its volume that grows cubically with the length.

The longer the cavity is, the narrower its spectral linewidth. Due to the volume constraints, the mobile cavities not always can be as long as their stationary versions. Also, the rigid mounting of the mobile cavity requires larger contact surface area with the cavity's housing. In a result, the performance of the mobile ultra-stable lasers is lower and usually of the order of 10^{-15}. One of the best instability results of a mobile system was reached by Argence et al. [76] with $\sim 5 \times 10^{-16}$ and in a transportable optical clock system developed at PTB, with $\sim 4 \times 10^{-16}$ as presented in [52, 80].

1.6 This work

My thesis reports on progress in the development of the mobile laser systems, necessary for the realisation of the mobile strontium lattice optical clocks. This thesis together with theses written by B. O. Kock [81], W. He [82] and L. L. Smith [83] create a whole picture of the miniaturisation process of the lattice strontium clocks at the University of Birmingham. While the other theses focus mostly on the development of the atomic package, this work shows the realisation of the most demanding laser used for the interrogation of atoms, which commonly limits the performance of an optical clock. Along the development of the interrogation laser, this thesis also presents construction of the laser used for the second-stage cooling of strontium, which is the second most demanding laser in the experiment. The work also presents a frequency stabilisation system (FSS), designed to stabilise all the lasers in the strontium lattice clock experiment, with a single optical cavity.

At the beginning of chapter 2, I discuss the basic concepts of a frequency reference. In this chapter, I also introduce the Allan deviation as a tool of inspecting the frequency stability. I give examples of different types of noise and analyse the behaviour of the Allan deviation. At the end of the chapter, I discuss the use of a Fabry-Pérot interferometer and atoms as a reference frequency standard, and briefly indicate the most important sources of inaccuracy and instability.

In chapter 3, I talk about the use of strontium as a frequency standard. I present a typical strontium lattice clock cycle sequence and give a short introduction to how the strontium energy structure is used to cool and trap the atoms.

In chapter 4, I show a design of the modular, amplified diode laser system that I have built for the second-stage cooling of strontium. Also in the chapter, I report on using a prototype of the semiconductor disk laser for second-stage cooling of strontium, for the first time. At the end of the chapter, I present a design and construction of the compact optical cavity that I have built for the frequency stabilisation system (FSS).

In chapter 5, I present construction of the ultra-stable stationary laser that I have built to use for the interrogation of strontium atoms. The laser system can also serve as an ultra-stable frequency reference to stabilise the optical frequency comb and it can be used to characterise other laser systems. In the chapter, I also analyse the vibrational and acoustical isolations that can improve performance of the interrogation laser. Also, I discuss the influence of the RF frequency modulators stability on the stability of the lasers. In section 5.4, I show the construction of the mobile interrogation laser, which was built within the space optical clock 2 (SOC2) project. As part of the collaboration between different institutions across Europe, I have assembled the interrogation laser system, using the components provided by different partners. I have characterised the mobile interrogation laser and prepared it to be integrated with the atomic package. At the end of the chapter, I compare the instability of the interrogation lasers and the RF frequency sources.

CHAPTER 2

FREQUENCY STANDARDS

Timekeeping relies on a source of frequency that defines equally spaced intervals of time, which can be counted to keep track of the time passed. Years, full moons (months), and days were the first observed phenomena used to measure time. The ancient civilisations observed 12 full moons every year, which inspired them to establish the duodecimal system [10]. With 12 as a base, they decided on dividing daylight into 12 parts when constructing a sundial clock. Back then, night was considered to be completely separate from day, and it also was divided into 12 equal parts. Egyptians used 12 stars to determine time during the night. Dividing both day and night into 12 parts was probably the origin of the 24 hour day [84]. As people were able to measure even shorter periods of time using sand clocks and water clocks, they invented minutes and seconds. These originated from Greek astronomers, who used a sexagesimal system derived from Babylonians, and were even used before, by the Sumerians. The number 60 was considered to be a convenient number as it could be easily divided by 1, 2, 3, 4, 5, 6, 10, 12, 15, 20, 30, and 60; where 2, 3, and 5, are the prime numbers. Dividing an hour into 60 minutes, brought ease into calculating the time for events occurring 1 to 6 times in an hour. Since the number 60 is also divisible by 12, it could easily fit into the 12 hour clock's dial.

2.1 Frequencies of the clocks

Let us consider two rulers with different ticks, as presented in figure 2.1. The red ruler has ticks every centimetre, whereas for the green ruler, every millimetre. Both rulers can be used to measure the length of a blue rod, also shown in the figure, which gives the result of 3 cm when measured with the red ruler, and 3.4 cm when measured with the green ruler. As the green ruler's ticks are more frequent, it is possible to measure objects with higher precision. Although it would be useful for measuring short objects, it would be

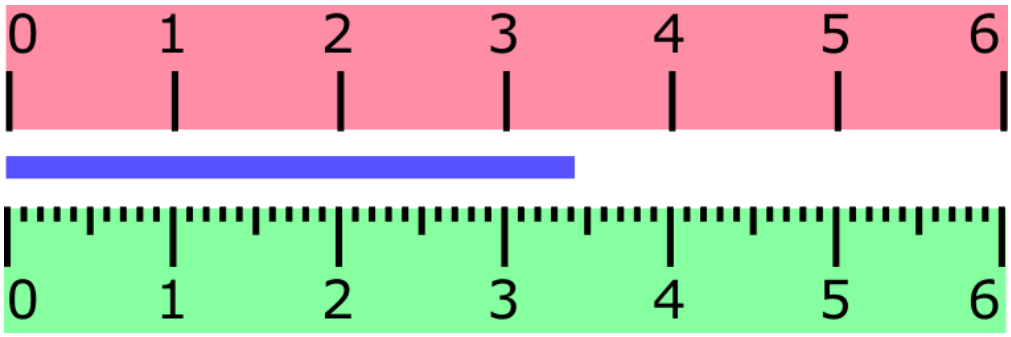

Figure 2.1: An example with two rulers used to measure the length of an object.

overkill for measuring a 100 m long football pitch.

By analogy with the rulers, time can be measured with high or low precision clocks. The more frequent the ticks of the clock, the more precisely we can measure time. In table 2.1, different ranges of frequencies, and their corresponding periods, are presented together with the clock type. The Earth's year, and day, have relatively low frequencies of 32 nHz, and 11 μHz, respectively. By constructing a sundial, people were able to measure the phase of the day's oscillation, and determine time more precisely, however, not precisely enough to count minutes and seconds.

Frequency	Period	Oscillator
1 nHz – 1 μHz	10^{9} s – 10^{6} s	Earth (1 year), Moon (1 Month)
1 μHz – 1 mHz	10^{6} s – 10^{3} s	Earth (1 day)
1 mHz – 1 Hz	10^{3} s – 10^{0} s	Pendulum
1 Hz – 1 kHz	10^{0} s – 10^{-3} s	Pendulum, Balance spring, Pulsar
1 kHz – 1 MHz	10^{-3} s – 10^{-6} s	Quartz, Electronic
1 MHz – 1 GHz	10^{-6} s – 10^{-9} s	Quartz, Electronic
1 GHz – 1 THz	10^{-9} s – 10^{-12} s	Microwave source, H maser, Cs atomic clock
1 THz – 1 PHz	10^{-12} s – 10^{-15} s	Laser source, Optical atomic clock
1 PHz – 1 EHz	10^{-15} s – 10^{-18} s	
1 EHz – 1 ZHz	10^{-18} s – 10^{-21} s	X-ray source

Table 2.1: Example of oscillators for different frequency ranges and corresponding periods. Data taken from [15].

With the invention of the pendulum clock, the frequency of oscillation was increased to levels of 1 Hz. Subsequent improvements to the pendulum clock revolutionised navigation, thanks to Huygens' marine chronometer which allowed determination of the position at sea.

Pulsar is a celestial body discovered recently in 1967. It is a very stable oscillator emitting electromagnetic radiation with the frequency spread from Hz level up to gamma radiation [85, 86, 87]. Low frequency pulsars with frequencies Hz - kHz range were first to be discovered and it was shown that they feature very high stabilities, similar to atomic clocks [88] and could be used in the construction of pulsar clocks [89].

A quartz crystal is the most popular oscillator operating in the range from kHz to GHz with electrically induced oscillations. Its popularity is mostly a result of a good trade off between relatively high stability, compactness and low cost.

The atomic clocks and hydrogen masers feature frequencies in the level of few GHz. In particular, caesium atomic clock used in the definition of second operates at the frequency of 9,192,631,770 Hz [8, 22]. Optical atomic clocks operate at optical frequencies of couple hundreds of THz, for example $\sim$ 429.2 THz in the case of strontium, $\sim$ 518.3 THz for ytterbium and $\sim$ 411.2 THz for calcium ion. Atomic clock based on mercury atoms uses transition from the outside of visible range with even higher frequency $\sim$ 1.129 PHz [55].

Tendency shows that higher clock performance can be obtained by moving to higher frequencies and it can be expected that future developments will result in creating clocks based on x-ray or even gamma radiation.

2.2 Precision and accuracy

It is important to know the difference between precision and accuracy. Precision is the ability to get the same result over many measurements. In practice, by increasing the precision of a measured value, it is possible to increase the number of digits, in the number representing the measured value. The dominant type of error in a precise measurement is systematic error.

Different from precision is accuracy, which describes the ability to get the true result. Sometimes, an accurate value can be obtained by performing many measurements and looking at the distribution of the results to learn about statistics of the measurement. This knowledge allows to find the expectation value for example from the parameters of a fitted statistical distribution function.

The difference between precision and accuracy is shown in figure 2.2. The red dots on each axis show the true value of a measurement. Blue ticks represent the measured values. The first set of measurements **(a)** is not accurate and not precise. Measurement **(b)** is precise but not accurate. Measurement **(c)** is accurate but not precise. Finally, measurement **(d)** is both accurate and precise.

For example, the pulsar clocks, shown in table 2.1, are not the most precise clocks. However, they can give a very accurate measurement of time, when averaged over a long period.

In the case of the atomic clocks, transitions between the energy levels are used as a reference frequency.

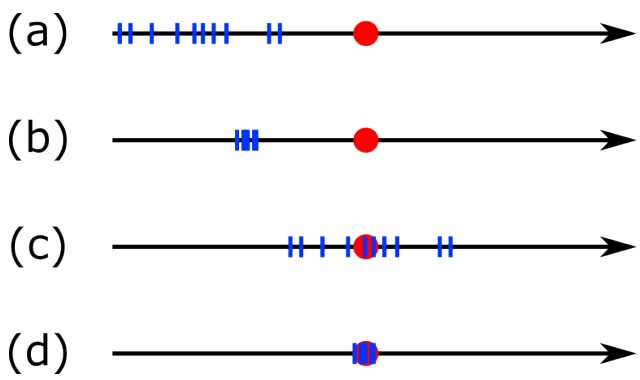

Figure 2.2: Chart showing the difference between precision and accuracy. The red dots represent the true value, while the blue ticks show the results of measurement. **(a)** Measurement which is not precise and not accurate. Measured values comprise of large systematic error and large random error. **(b)** Measurement precise but not accurate. Measured values comprise of low random error and large systematic error. **(c)** Accurate but not precise measurement. Measured values comprise of low systematic error and large random error. When averaged, measured values get close to the true value. **(d)** Measurement accurate and precise. Measured values comprise of both low systematic error and low random error.

In analogy to the ruler from the previous subsection, the higher frequency of an atomic transition, the better precision of the clock. This is different from accuracy, which depends mostly on how well defined the transition is and whether it is sensitive to external factors.

2.3 Stability

2.3.1 Allan deviation

The standard variance is a very good tool to assess the amplitude of an error in measurements where its mean is equal to zero. In the case of an oscillator, the systematic error can be largely significant and its value can change in time. Allan variance is often used to describe the stability of an oscillator. It was introduced to replace standard variance which is unable to give any information about types of error.

Allan variance is defined as [90]

$$\sigma_y^2(\tau) = \frac{1}{2}\left\langle(\overline{y}_{i+1} - \overline{y}_i)\right\rangle = \frac{1}{2(M-1)}\sum_{i=1}^{M-1}(\overline{y}_{i+1} - \overline{y}_i)^2 \tag{2.1}$$

where M is the number of intervals, $\overline{y}_i$ is the average fractional frequency of the interval i and brackets $\langle a\rangle$ stand for expectation value of a. The average fractional frequency can be defined as the derivative of phase x

$$\overline{y}_i = \frac{1}{\tau}(x_{i+1} - x_i). \tag{2.2}$$

It is common to use Allan deviation as well, which is simply the square root of Allan variance

$$\sigma_y(\tau) = \sqrt{\sigma_y^2(\tau)} \tag{2.3}$$

Allan deviation allows to distinguish between different types of noise when plotted. More details about Allan variance and interpreting data can be found in [91].

2.3.2 Types of noise

Allan deviation is a very useful tool that can be used in the characterisation of noise in frequency measurements. By analysing the shape of the Allan deviation, it is possible to distinguish different types of noise in the measured frequency. The power law is a tool that describes the relation between the slope of the Allan deviation, and the dominant type of noise [15].

Random frequency walk (Brownian noise)

Random walk of frequency, also called Brownian frequency noise or red frequency noise, is a type of noise that accumulates as it is being averaged, and causes a frequency standard to drift away from the set frequency. If Brownian noise is dominant in the measured frequency data, the corresponding Allan deviation calculated for the frequency follows the curve given by

$$\sigma_y = A \cdot \sqrt{\tau}, \tag{2.4}$$

where σ_y is the value of the Allan deviation, A is the proportion coefficient and τ is the interrogation time.

An example of simulated Brownian frequency noise is presented in figure 2.3a. For the simulated frequency, the Allan deviation was calculated and is shown in figure 2.3b. As expected, the Allan deviation follows the $A \cdot \sqrt{\tau}$ slope.

Flicker frequency noise

Flicker frequency noise is also called pink frequency noise. The name "pink" refers to a spectral feature of this noise, which is higher for frequencies towards red (low). The noise features power spectral density proportional to $1/f$ where f is the frequency. It is a type of noise that although does not cause the long term drift of the frequency standard, is not possible to reduce by averaging over an increased interrogation time. In a frequency measurement where the flicker frequency noise is dominant, the calculated Allan deviation

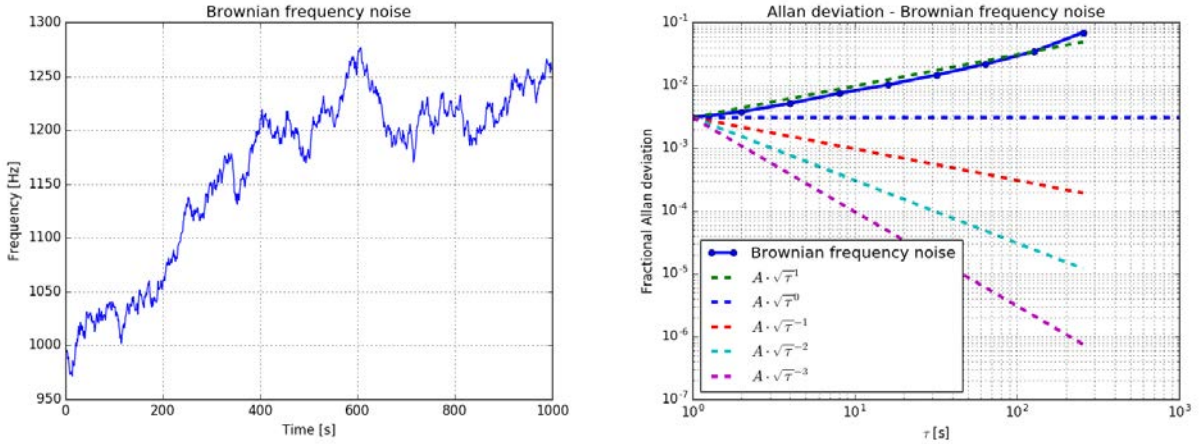

(a) (b)

Figure 2.3: Brownian frequency noise. **(a)** Generated frequency with the Brownian frequency noise only. **(b)** Allan deviation of the generated frequency with the Brownian frequency noise. The Allan deviation follows $\sigma_y = A \cdot \sqrt{\tau}$ slope.

follows the curve given by

$$\sigma_y = A \cdot \sqrt{\tau}^{0} = A. \tag{2.5}$$

A generated frequency with flicker frequency noise dominant is presented in figure 2.4a. The Allan deviation of the generated frequency is presented in figure 2.4b with blue points. As expected, it follows the blue horizontal dashed line, which suggests that the frequency is stable despite the interrogation time.

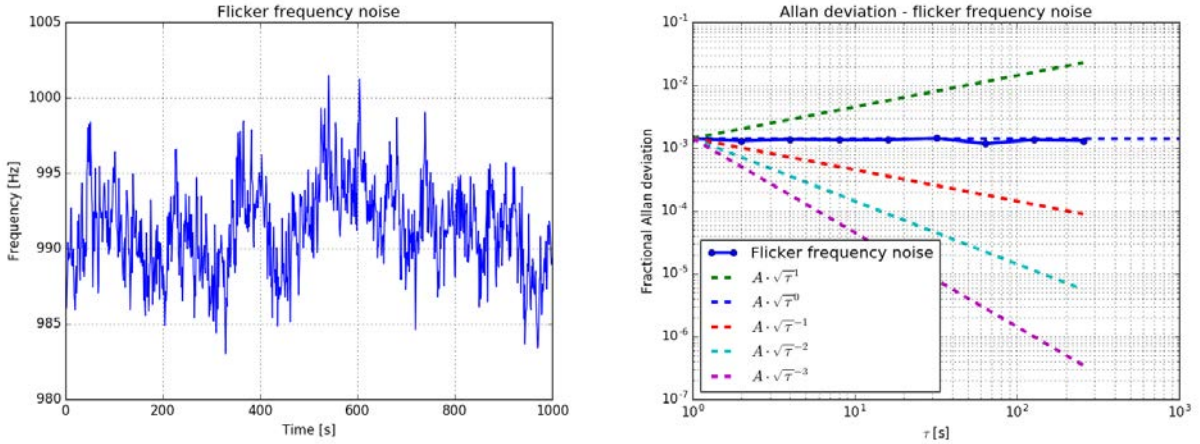

(a) (b)

Figure 2.4: Flicker frequency noise. **(a)** Generated frequency with the flicker frequency noise only. **(b)** Allan deviation of the generated frequency with the flicker frequency noise. The Allan deviation follows $\sigma_y = A \cdot \sqrt{\tau}^{0} = A$ slope.

White frequency noise

White frequency noise is a type of noise that is not systematic and its mean value averages down to zero. The noise is the same across all frequencies, meaning a flat power spectral density plot. The name "white" derives exactly from that feature in analogy to light, which appears white when consisting of all wavelengths equally. As the noise results from a Gaussian process, it can be averaged down over several measurements and longer interrogation times. When the Allan deviation is plotted for a frequency with dominant white frequency noise, it will follow the curve given by

$$\sigma_y = A \cdot \sqrt{\tau}^{-1}. \tag{2.6}$$

An example of generated white frequency noise is presented in figure 2.5a. The fractional Allan deviation of the frequency was also calculated and is presented in figure 2.5b with blue points. As expected, the longer the frequency is interrogated, the more precisely it can be measured, and the Allan deviation goes down with the interrogation time. This follows the red dashed line, corresponding to the $A \cdot \sqrt{\tau}^{-1}$ slope.

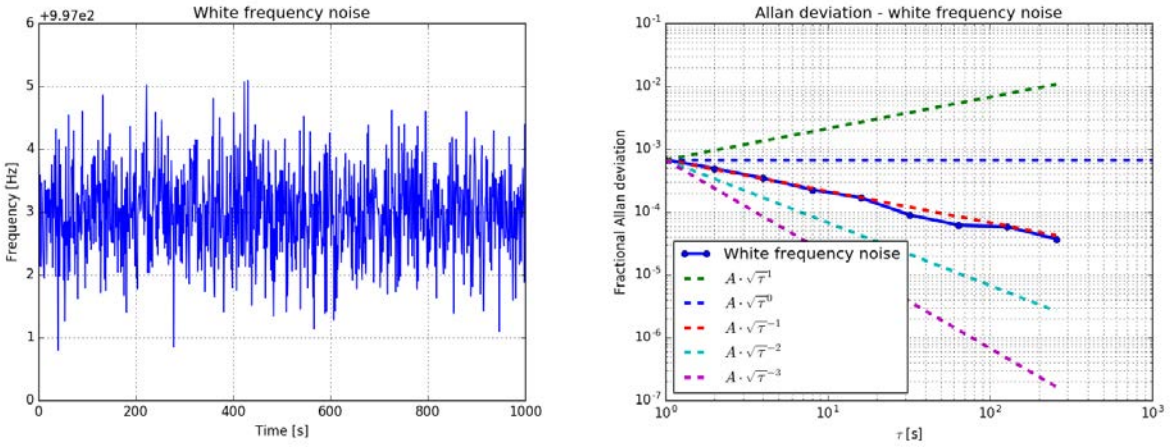

(a) (b)

Figure 2.5: White frequency noise. **(a)** Generated frequency with the white frequency noise only. **(b)** Allan deviation of the generated frequency with the white frequency noise. The Allan deviation follows $\sigma_y = A \cdot \sqrt{\tau}^{-1}$ slope.

Brownian phase noise (Random phase walk)

Every wave consists of a frequency and phase, and both the frequency and phase can be affected by different types of noise. The random frequency walk was already presented as it affects the frequency, causing its

long-term drift. Phase can also be affected by Brownian noise; however, it does not have the same resultant effect on the frequency.

To simulate the frequency with Brownian phase noise being dominant, the frequency was calculated as an instantaneous derivative of the phase noise. This result is presented in figure 2.6a. The Allan deviation of the frequency was also calculated and is presented in figure 2.3b with blue points. Clearly, it follows the red dashed line denoting the $A \cdot \sqrt{\tau}^{-1}$ slope. Comparing the figures 2.6, with figures 2.5 showing white frequency noise, it is possible to see the identity of the two types of noise. Although they can have a different origin, they cannot be differentiated from each other, and thus, are treated as the same type of noise.

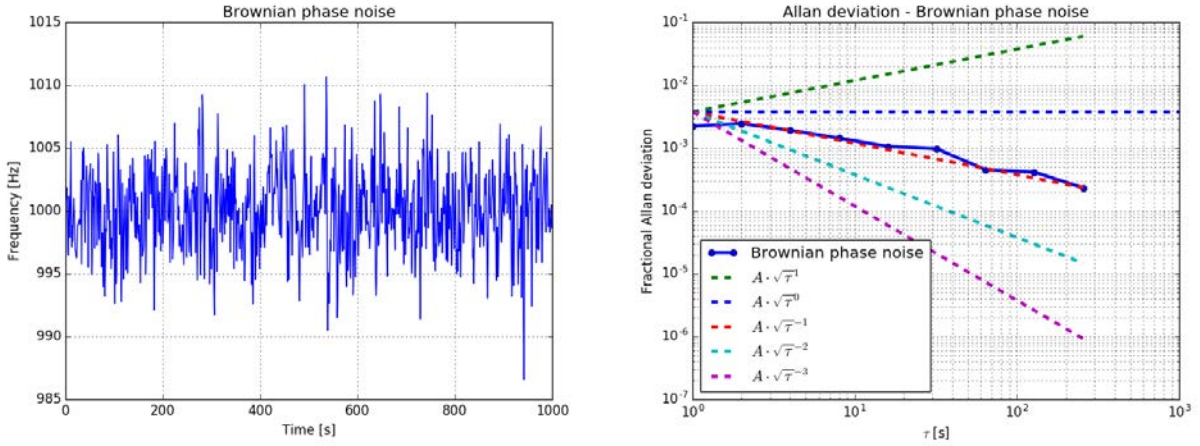

(a) (b)

Figure 2.6: Brownian phase noise. **(a)** Generated frequency with the Brownian phase noise only. **(b)** Allan deviation of the generated frequency with the Brownian phase noise. The Allan deviation follows $\sigma_y = A \cdot \sqrt{\tau}^{-1}$ slope. Note that it is the same slope as for the white frequency noise, therefore, both of them are treated as the same type of noise.

Flicker phase noise

Flicker noise can also be present on the phase of the measured waveform. An example of a frequency with flicker phase noise dominant is presented in figure 2.7a. In the case of phase noise, both the flicker and white phase noise follow the same $A \cdot \sqrt{\tau}^{-2}$ slope when Allan deviation is plotted. To increase the sensitivity of the Allan deviation, a modified Allan deviation is used to distinguish between these two types of noise. The modified Allan deviation of the generated frequency is plotted with blue points in figure 2.7b. It reduces with increased averaging time faster than the white frequency noise, following the

$$\sigma_y = A \cdot \sqrt{\tau}^{-2} \tag{2.7}$$

slope drawn in the figure with a cyan dashed line.

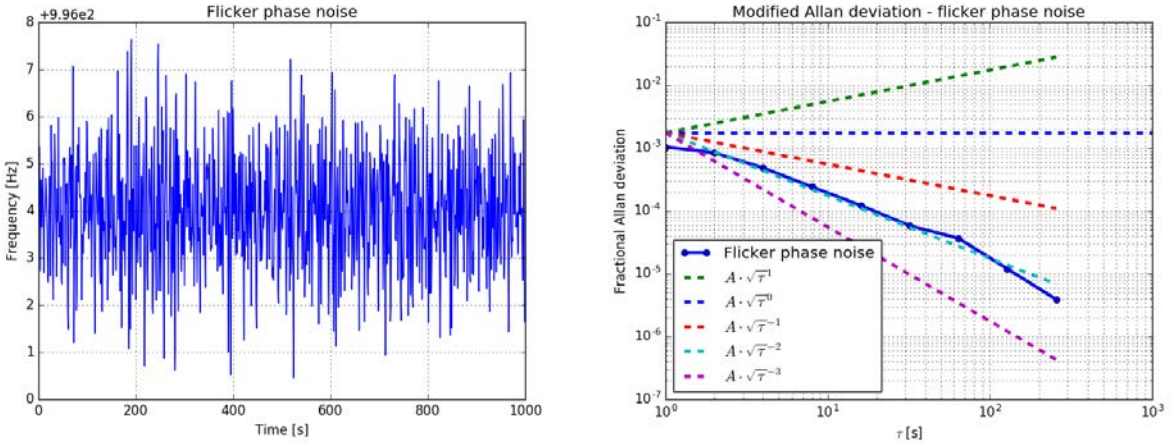

(a) (b)

Figure 2.7: Flicker phase noise. **(a)** Generated frequency with the flicker phase noise only. **(b)** Modified Allan deviation of the generated frequency with the flicker phase noise. The modified Allan deviation follows $\sigma_y = A \cdot \sqrt{\tau}^{-2}$ slope. The modified Allan deviation was used in order to increase sensitivity to distinguish flicker phase noise from white phase noise.

White phase noise

A frequency with white phase noise being dominant is presented in figure 2.8a. The frequency plot looks very similar to the frequency plot with the previously discussed flicker phase noise, and it is hard to tell the difference by only looking at the frequency plot. The modified Allan deviation is plotted in figure 2.8b with blue points. The points follow the purple dashed line denoting

$$\sigma_y = A \cdot \sqrt{\tau}^{-3}, \tag{2.8}$$

proving the usefulness of modified Allan deviation, as it allows distinction between flicker phase and white phase noise.

The frequency of an oscillator features different types of noise that can be identified by analysing different slopes present in the Allan deviation plot.

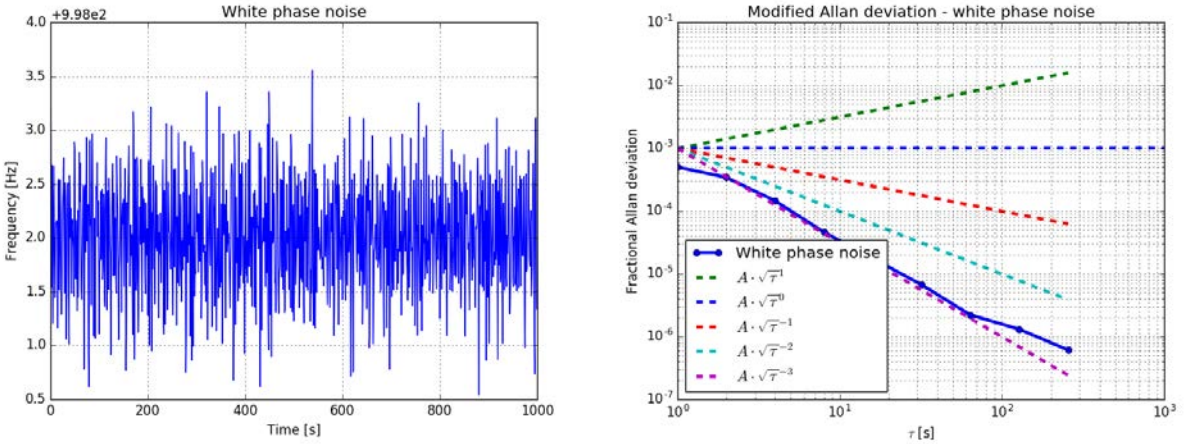

(a) (b)

Figure 2.8: White phase noise. **(a)** Generated frequency with the white phase noise only. **(b)** Modified Allan deviation of the generated frequency with the white phase noise. The modified Allan deviation follows $\sigma_y = A \cdot \sqrt{\tau}^{-3}$ slope. The modified Allan deviation was used in order to increase sensitivity to distinguish flicker phase noise from white phase noise.

2.4 Fabry-Pérot interferometer

A Fabry-Pérot interferometer (FPI) can be used for various applications. One common application is in the spectral analysis of the laser light with a scanning FPI. The focus of this thesis however, will be shifted towards another application: the stabilisation of lasers.

Stabilising a laser to the FPI simply means, transferring the FPI's length stability, to the laser's stability of its wavelength. In this context, the FPI is also called an optical reference. If the mirrors are separated by air or a vacuum, the FPI can also be referred to as an optical cavity.

An FPI consists of two reflective parallel surfaces. In the case of an optical cavity, these might be two dielectric mirrors separated by a spacer. Light injected to the cavity will circulate between the mirrors, interfering with itself during every pass [92].

In figure 2.9, the reflection of an electromagnetic wave by a dielectric mirror is depicted. The dielectric reflective coating consists of alternating layers of high and low refractive index materials [93], such as Tantalum Pentoxide Ta_2O_5 (n=2.1), and silica SiO_2 (n=1.5). The electromagnetic wave reflects at every boundary between the two materials, changing phase by 180° every time it reflects from a medium with a higher refraction coefficient than the medium it propagated from. On the other hand, there is no phase shift for a wave reflected from a lower refractive index medium. The thickness of each layer is chosen, so that the optical path length corresponds to a quarter of a wavelength of the light being reflected. This way, all the

reflected beams are in-phase, constructively interfering with each other (green waves in figure 2.9).

Light circulating between two mirrors of an optical cavity can interfere constructively during every pass, as shown on the left part of figure 2.9. In this case, the incident wave drawn in red, is in phase with the reflected wave, drawn in green. The waves form a standing wave with nodes located on the surface of each mirror.

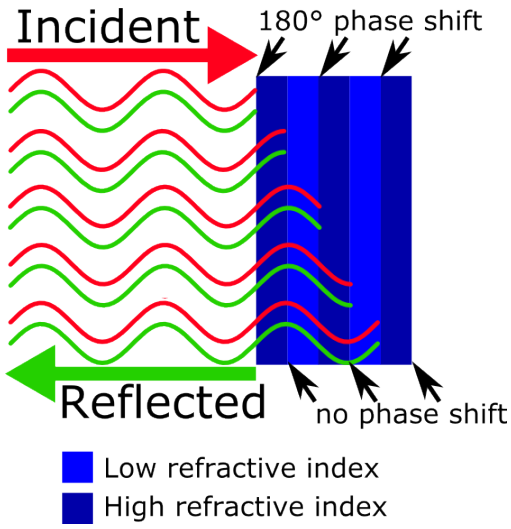

Figure 2.9: Reflection by a dielectric mirror. The dielectric coating is constructed from the alternated high and low refractive index layers, with the optical thickness designed to be equal to the quarter of wavelength of the incident light. The figure shows incident and reflected electric field of an electromagnetic wave drawn with red and green respectively. The reflected beam experiences a 180° and 0° phase shift when reflected from a higher and lower refractive index medium correspondingly.

The condition for a standing wave to form inside the optical resonator means that the nodes will form at the surface of the mirrors [92]. This can only be true for waves for which integer multiple of their wavelength equals to double the distance between the mirrors

$$\lambda = \frac{2L}{N}, \tag{2.9}$$

where L is distance between the mirrors, N is an integer number, and λ is the wavelength in optical medium. In optical frequency ν units this can be written as

$$\nu = \frac{Nc}{2L}, \tag{2.10}$$

where c is the phase velocity of light in medium. The spacing between the adjacent longitudinal modes of

the resonator is called the free spectral range (FSR) of the resonator. It can be defined as

$$\mathrm{FSR} = \frac{c}{2L}. \tag{2.11}$$

The spectral resolution of the resonator depends strictly on the free spectral range and finesse $\mathcal{F} = \mathrm{FSR}/\delta\nu$. The latter can be linked to reflectivity coefficient of the mirrors R and for high reflectivity values it can be written in the following relation [92]

$$\mathcal{F} = \pi\frac{\sqrt{R}}{1-R}. \tag{2.12}$$

The resonance width $\delta\nu$ is represented by a ratio of the mode's optical frequency and finesse of the resonator

$$\delta\nu = \frac{\mathrm{FSR}}{\mathcal{F}} = \frac{c}{2L}\frac{\pi\sqrt{R}}{1-R}. \tag{2.13}$$

The above shows that in order to have a high spectral resolution (low resonance width), the optical resonator needs to be either very long or have very high reflectivity of the mirrors.

The FPI can provide a stable frequency reference, assuming that its resonance frequency does not change. When the spacer of an optical resonator is made of an ultra-low expansion material, and placed in a stable environment, its length can become a very stable reference. Unfortunately, the length of such a resonator cannot be well defined, and it can change due to temperature or internal stresses. Therefore, the optical resonator cannot be an accurate frequency standard. Even if it was very stable in the short term, after long interrogation times, it will drift away due to material ageing that cannot be controlled. On the other hand, with very high finesse and low spectral resolution, the resonator can be very precise.

2.4.1 Sperical resonators

Spherical resonator is a special kind of an optical resonator, with mirrors being of spherical shape. Each mirror of the resonator can be described with so the g parameter

$$g_i = 1 + \frac{L}{R_i}, \tag{2.14}$$

where L is length of the resonator and R_i is the radius of curvature of the i^{th} mirror. The radius is a positive number for a convex mirror and a negative number for concave mirror. The resonator is said to be stable if the following confinement condition is met

$$0 \leq g_1 g_2 \leq 1. \tag{2.15}$$

A longitudinal mode of the spherical resonator is the Gaussian beam. For a standing wave formed inside the resonator, the curvature of the wavefront at each mirror matches the mirror's radius of curvature. Following the basic Gaussian optics, it is possible to calculate Rayleigh length z_0 of the beam formed inside the resonator by using the relation [92]

$$z_0 = \frac{\sqrt{-L(R_1+L)(R_2+L)(R_1+R_2+L)}}{(R_1+R_2+2L)}. \tag{2.16}$$

Similarly, positions of the mirrors z_1 and z_2 in respect to the waist position can be calculated using relations

$$z_1 = \frac{-L(R_2+L)}{(R_1+R_2+2L)}, \tag{2.17}$$

$$z_2 = z_1 + L. \tag{2.18}$$

Waist radius w_0 of the Gaussian beam inside the resonator is equal to

$$w_0 = \sqrt{\frac{\lambda z_0}{\pi}}. \tag{2.19}$$

Finally, it is very useful to know the beam radius w_i at the i^{th} mirror when constructing a resonator. This can be calculated using the following relation

$$w_i = w_0\sqrt{1+\left(\frac{z_i}{z_0}\right)^2}. \tag{2.20}$$

Knowing values of the above parameters also simplifies the process of mode matching the injected laser beam.

Resonant mode frequencies of the spherical resonator

As mentioned before, Gaussian beam forms the longitudinal modes of the spherical resonator. The condition for the resonant frequencies in the Fabry-Pérot interferometer, described by the equation 2.10 is still valid for the Gaussian beam inside a spherical resonator, but only if the resonator is symmetrical. This means that both the mirrors have the same radius of curvature $R_1 = R_2$. If that is not the case, it is necessary to use a more general equation for resonance frequencies of the Gaussian modes inside a spherical resonator

$$\nu = \frac{Nc}{2L} + \frac{\Delta\zeta}{\pi}\frac{c}{2L}, \tag{2.21}$$

where $\Delta\zeta = \arctan(z_2/z_0) - \arctan(z_1/z_0)$ [92]. The free spectral range still stays the same and is independent of the curvature of the mirrors.

Transverse modes of the spherical resonator

We have learnt that the Gaussian modes can be formed inside the resonator and that they correspond to the longitudinal modes. However, those are not the only solution of the Helmholtz equation inside the spherical resonator. Another valid solution of the equation are Hermite-Gaussian modes. Those are commonly called transverse electric modes (TEM) and their intensity distribution profiles are presented in figure 2.10. For more information about the nature of Hermite-Gaussian modes, please refer to [92].

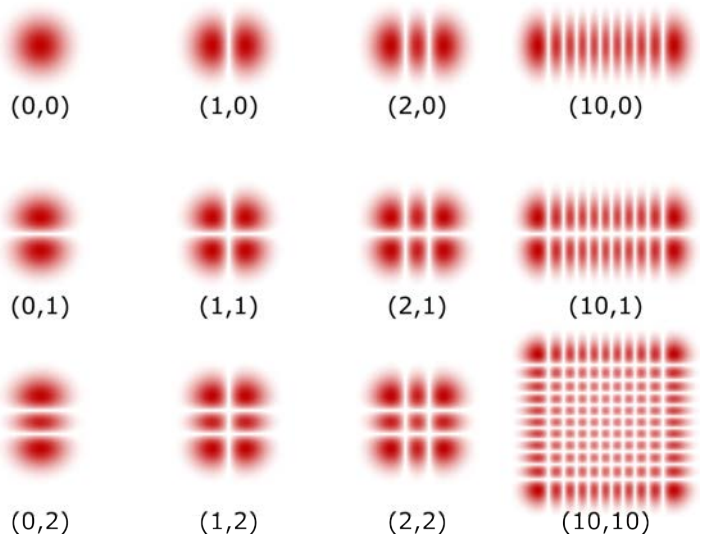

Figure 2.10: Intensity distribution for various Hermite-Gaussian modes. The numbers (l, m) indicate the mode's order.

It might be useful to write equation 2.21 in a more general form that also describes frequencies of the Hermite-Gaussian modes. This can be written as

$$\nu_{l,m} = \frac{Nc}{2L} + (l + m + 1)\frac{\Delta\zeta}{\pi}\frac{c}{2L}, \tag{2.22}$$

where l and m are the integer numbers representing the order of the mode [92]. From this equation, we can see that the same frequency corresponds to modes (l, m) and (m, l). However, it is worth highlighting that the equation is valid for a perfect resonator and in practice (l, m) and (m, l) modes are at slightly different frequencies.

2.4.2 Thermal noise in the optical resonators

In a controlled environment, the instabilities coming from a changing air pressure and vibrations can be eliminated. However, the thermal effects have a big influence on the stability of the resonator, even in a highly stabilised temperature environment. The spacer and mirror substrate of an optical resonator can be made of the ultra-low expansion material to limit the thermal behaviour. However, the mirror coating must be made of a special selection of dielectric materials, which also feature much higher coefficient of thermal expansion. The thermal noise in such mirror coatings was studied in detail by Gorodetsky [94]. The most dominant and therefore limiting type of noise is Brownian thermal noise.

Following the paper by Kessler et al. [95] the thermal noise in an optical resonators can be split into three contributions of the spacer, mirror substrate and mirror coating. Let x be the mean distance between two mirrors of the resonator. To analyse the behaviour, it is necessary to calculate power spectral density of the thermal fluctuation of x, here denoted as $S_x(f)$, where f is the fluctuation frequency of the force F_0 acting on the mirror surface. We can write

$$S_x(f) = \frac{2k_B T}{\pi^2 f^2} \frac{W_{diss}}{F_0^2}, \tag{2.23}$$

where k_B is the Boltzmann constant, T is the temperature and W_{diss} is the power dissipated in the system, averaged in time, for amplitude F_0 and frequency f of the oscillatory force [95]. The dissipated power can be defined with the use of maximum elastic strain energy U and loss angle of the system ϕ, by the following relation

$$W_{diss} = 2\pi f U \phi. \tag{2.24}$$

Here, the loss angle is an angle for which its tangent equals to the ratio of the imaginary and real part of the effective permittivity [96].

Assuming that the force acting on the mirror of an optical resonator comes from a Gaussian shape beam, it will lead to pressure distribution along the radius r, which can be written as

$$p(r) = \pm \frac{2F_0}{\pi w^2} \exp\left(-2r^2/w^2\right), \tag{2.25}$$

where w is the Gaussian $1/e^2$ radius [95].

The first to consider is the contribution coming from the coating, which directly interacts with the Gaussian beam. Assuming similar elasticity of the coating and substrate, and a homogeneous loss angle of

the coating ϕ_{ct}, the thermal fluctuations of the coating can be written as

$$S_x^{(ct)} = S_x^{(sb)}(f)\frac{2}{\sqrt{\pi}}\frac{1-2\sigma}{1-\sigma}\frac{\phi_{ct}}{\phi_{sb}}\frac{d_{ct}}{w}, \tag{2.26}$$

where σ is the Poisson ratio of the coating material, d_{ct} is the coating's thickness [95]. As the coating is a thin layer on a substrate, its thermal fluctuation is greatly influenced by the thermal fluctuation of the substrate, $S_x^{(sb)}$. This can be written as the following relation

$$S_x^{(sb)} = \frac{4k_BT}{\pi f}\frac{1-\sigma^2}{2\sqrt{\pi}Ew}\phi_{sb}, \tag{2.27}$$

where E is the Young's modulus [95].

The third part of the contribution comes from the spacer. Assuming that it is of cylindrical shape with a drilled hole inside, the averaged thermal fluctuation of the spacer over its cross-section can be written as

$$S_L(f) = \frac{4k_BT}{\pi f}\frac{L}{2\pi E\left(R_{sp}^2 - r_{sp}^2\right)}\phi_{sp}, \tag{2.28}$$

where L, R_{sp} and r_{sp} are the length, outer diameter and inner diameter of the spacer, correspondingly [95].

Finally, we can write an equation for the thermal fluctuations of the entire spacer, which consists of two coatings, two substrates and a spacer, as

$$S_x(f) = S_x^{(sp)}(f) + 2S_x^{(sb)}(f) + 2S_x^{(ct)}(f) = \frac{4k_BT}{\pi f F_0^2}\left(U_{sp}\phi_{sp} + 2U_{sb}\phi_{sb} + 2U_{ct}\phi_{ct}\right), \tag{2.29}$$

where U_{sp}, U_{sb} and U_{ct} are elastic strain energies of the spacer, substrate and coating respectively [95]. It is very useful to express the thermal fluctuations as the fractional length fluctuation of the entire resonator

$$S_y(f) = S_x(f)/L^2. \tag{2.30}$$

Both equations 2.29 and 2.30 show $1/f$ dependence. Following the noise power law [15], the $1/f$ dependence can be recognised as the flicker frequency noise, Allan deviation of which is a constant value [95]

$$\sigma_y = \sqrt{2\ln(2)S_y(f)f} = \sqrt{2\ln(2)\frac{4k_BT}{\pi F_0^2 L^2}\left(U_{sp}\phi_{sp} + 2U_{sb}\phi_{sb} + 2U_{ct}\phi_{ct}\right)} = \text{const}. \tag{2.31}$$

This shows that every resonator has its own thermal noise limit, that depends on the shape, size and material

of its components. The Allan deviation of a laser stabilised to the resonator very often averages down with the white frequency noise ($\sqrt{\tau^{-1}}$), until it reaches the thermal noise floor. The Allan deviation will then start following a positive slope, due to slow drifts of temperature of the system. Nowadays, it is relatively easy to find the thermal noise limit by means of the finite element modelling.

2.5 Atomic reference

Atoms can be very good frequency standards thanks to the internal electron energy structure that can be very well defined. This way the energy structure is always the same for an atomic species and it is independent of its location in the entire universe. More importantly, it does not change with time, for example due to the ageing process. The energy difference between two levels corresponds to the photon energy, absorbed or emitted by the electron. Every electromagnetic wave is defined by its wavelength and oscillation frequency. The frequency of a transition can be used as a reference standard and it can be very well defined and stable because of the stable nature of the atom's energy structure.

2.5.1 Microwave atomic reference

Unlike bosonic atoms that have total spin equal to an integer, fermionic atoms have total spin equal to a half of an integer, leading to additional interaction between the nuclear and electron spins. This causes the energy levels to split into a hyperfine structure.

The energy difference between hyperfine states corresponds to microwave frequencies of 300 MHz – 300 GHz, which is very convenient due to the existence of RF electronics operating in the same frequency range. This enabled a direct link between hyperfine atomic transitions, and existing electronic clocks, such as the quartz clock.

The most well known microwave atomic reference is Caesium, whose hyperfine structure is still used to define a second. The frequency of the hyperfine splitting of the ground state corresponds to 9.192631770 GHz [8].

Rabi interrogation scheme

The traditional way of interrogating atoms is to let them interact with a microwave field, inside a microwave cavity. First, atoms need to be prepared so that all occupy the same ground state. Next, they are transferred through a microwave cavity, where they interrogate with a microwave field. If the microwaves are in resonance with the atomic transition, the population of the ground and excited state will oscillate with the so called

Rabi frequency. After exiting the interrogation cavity, atoms are sorted by state to measure the phase of the Rabi oscillation. This is then used to correct the frequency of the microwaves in the interrogation cavity, to set it closer to the resonant frequency of atoms. The resolution of the measurement in this scheme, is limited by the interrogation time of the microwave field with atoms, and it can be improved by increasing the length of the interrogation cavity. Constructing large resonators to obtain better resolution brings technical difficulties, and thus, the Ramsey interrogation scheme is commonly used [97, 19, 18, 21, 20].

Ramsey interrogation scheme

The Ramsey interrogation scheme requires two resonant cavities instead of one. The interrogation time of each cavity is chosen to be a quarter of the full Rabi oscillation. Between the cavities, the atoms are left alone without any interactions, allowing them to evolve freely. Quarter of the full oscillation corresponds to a $\frac{\pi}{2}$ change in phase, thus a jargon expression is commonly used that each cavity applies a $\frac{\pi}{2}$ pulse to the atoms. For a resonant beam of light, $\frac{\pi}{2}$ pulse corresponds to the half population of the ground state being transferred to the excited state.

In figure 2.11, a schematic of each interrogation method is presented. Figure 2.11a shows an example of a simple Rabi interrogation scheme. In the figure, atoms move from left to right. As the atoms pass through the microwave cavity (green), they interact with a microwave field for an interrogation time equal to t. After passing through the interrogation cavity, the phase is measured with a detector. Figure 2.11b shows the Ramsey scheme which is very similar. However, in this case, there are two interrogation cavities separated by the free evolution time equal to T.

The Ramsey scheme is used to obtain a better resolution by using shorter pulses that interact with the atoms. The resolution is proportional to the free evolution time T [97, 21, 20].

2.5.2 Optical atomic reference

Despite the increasing accuracy and stability of microwave optical clocks, their performance is fundamentally limited by the frequency and linewidth of the atomic transition. The selection of an atomic transition is very important, and moving from microwave into higher optical frequency transitions allows an increase in the performance of the atomic clocks.

In optical atomic clocks, laser light is used to interact with the atoms, instead of microwaves. However the most common interrogation schemes still follow the Rabi and Ramsey sequence that was described in the previous subsection.

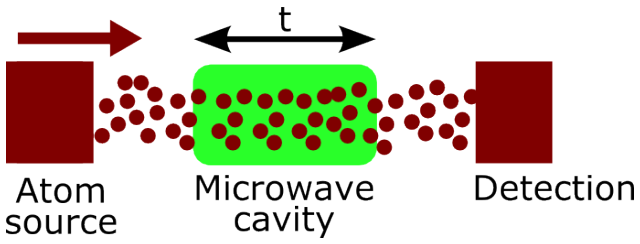

(a) Rabi interrogation scheme.

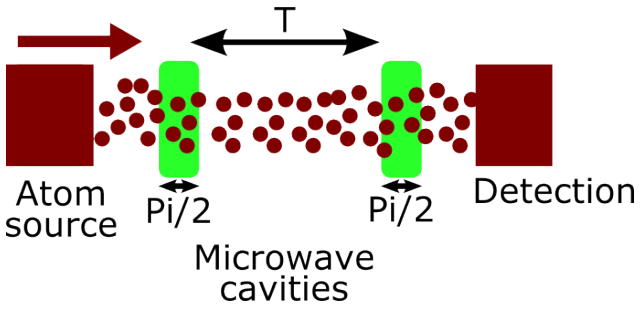

(b) Ramsey interrogation scheme.

Figure 2.11: Difference between Rabi and Ramsey interrogation schemes.

2.5.3 Linewidth broadening

In an atomic reference, the source of imprecision and instability is directly linked to the behaviour of the atomic transition, which can be susceptible to broadening or shifting.

Doppler broadening

Particles in a cloud of atoms move with velocities described by the Maxwell-Boltzmann distribution [98]. The velocity distribution $f(v)$ depends strongly on the temperature of the cloud T, and can be written as

$$f(v) = \sqrt{\left(\frac{m}{2\pi kT}\right)^3} 4\pi v^2 \exp\left(-\frac{mv^2}{2kT}\right) \tag{2.32}$$

where m is mass of particles, k is Boltzmann constant, and v is velocity.

The relative movement of an object, that is also a frequency reference, with respect to an observer, leads to a shift in the frequency recorded by the observer. This is known as the Doppler effect

$$\nu = \nu_0 \frac{\sqrt{1 - v^2/c^2}}{1 \mp (v/c)\cos\theta} \tag{2.33}$$

where ν is the frequency recorded by an observer, ν_0 is the original reference frequency of the object, v is velocity, c is the speed of light, and θ is the angle between the observation direction and direction of the movement [99, 15]. In atomic physics, the effect can introduce a distortion of the measured atomic transition frequency by shifting it, in the case of a stream of moving atoms; or by broadening the narrow, natural linewidth of the transition. In this context, any movement by the atoms during the interrogation time is undesired, as it can decrease the precision of the measurement in the case of a cloud of thermal atoms, or the accuracy in the case of the movement of the entire atom cloud. Taking the optical clock transition $^1S_0 \rightarrow {}^3P_0$ in strontium-87 as an example, the natural linewidth of the transition is in the sub-Hertz range, whereas atoms at room temperature have their linewidth broadened by up to > 500 MHz due to the Doppler effect.

It is because of this effect that the atoms need to be cooled down to the μK level with laser cooling techniques, in order to obtain the full precision of the atoms in the optical atomic clock.

Power broadening

Let us consider a resonant laser light beam being shone over an atom. The probability of the atom experiencing the absorption or stimulated emission of a photon increases with the increase of the laser light intensity. The higher the intensity, the more frequently atom will absorb and emit a photon, meaning a lower lifetime of the excited state. The Heisenberg principle links the natural lifetime τ to the natural linewidth of a transition τ in the following relation

$$\gamma = \frac{1}{2\pi\tau}, \tag{2.34}$$

which shows that shortening the lifetime increases the linewidth of the transition [99, 100].

Each transition is characterised by its saturation intensity

$$I_{sat} = \frac{2\pi^2 hc\gamma}{3\lambda^3}, \tag{2.35}$$

where h is the Planck constant, c is the speed of light and λ is the transition's wavelength [99, 15]. The saturation intensity is expressed in units of [W/m^2] and it is necessary to define the saturation parameter S_0 for the resonant laser light beam

$$S_0 \equiv \frac{I}{I_{sat}} \tag{2.36}$$

where I is the intensity of the laser light. In a two level system, a saturation parameter equal to 1 indicates that the population difference is $\frac{N_g - N_e}{N_g + N_e} = 0.5$, where N_g and N_e are the number of atoms in the ground state and excited state, respectively. The difference approaches zero for $S_0 >> 1$.

The linewidth of the transition is broadened due to the power of the on-resonant laser and it can be written as

$$\gamma' = \gamma\sqrt{1 + S_0} \tag{2.37}$$

where γ' is the broadened linewidth. It is because of the power broadening that the intensity of the clock laser probing the reference transition should not be too high. For example, the 698 nm clock transition of ^{87}Sr with a natural linewidth equal to 1.2 mHz [101] has a saturation intensity as low as ~ 4.6 nW/m^2. In practice, however, the interrogation laser does not stay perfectly on the resonance the entire time and bigger beam intensities are used to probe the transition.

Collisional broadening

When a light emitting atom experiences a collision with another body, its electronic structure is perturbed, which leads to a phase shift of the emitted electromagnetic wave. The mean free path of the atoms in the atmospheric pressure is of the order of 100 nm [102], which at room temperature, gives atoms a few hundred picoseconds between collisions on average. The mean time between the collisions τ_c can be used to calculate the Lorentzian linewidth broadening

$$\Delta\gamma = \frac{1}{\pi\tau_c} \tag{2.38}$$

Using kinetic gas theory, it is possible to write a substitute for the mean time between the collisions to obtain a more convenient formula

$$\Delta\gamma = \sqrt{\frac{3}{4mk_BT}}d^2p \tag{2.39}$$

where m is the mass of the light emitting atom, k_B is the Boltzmann constant, T is the gas temperature, d is the diameter of the atom, and p is pressure of the gas [99, 15]. The value of the linewidth broadening for a strontium atom in room temperature ($\sim$ 300 K), and atmospheric pressure ($\sim$ 100 kPa) would be $\sim$ 560 MHz. This kind of broadening is avoided by putting the experiment in a vacuum chamber to eliminate the background gas pressure.

2.5.4 Other uncertainty sources

State-of-the-art atomic clocks require a very detailed analysis of all the possible uncertainties affecting the accuracy of the measurement. For optical clocks, the largest sources of uncertainty are due to the black body radiation shift [103], the Stark shift induced by the lattice laser, and the quadratic Zeeman shift [50].

Black body radiation and Stark shift

The energy levels of the electronic structure of an atom can be influenced by an electric field, which is commonly known as the Stark shift. This shift can be caused by a laser (e.g. cooling laser, probing laser, or in the case of the optical lattice clock, the lattice laser). A special case of the Stark shift is the black body radiation shift [99, 15].

Black body radiation shift comes from the surrounding environment of the reference cloud. The most significant shift is from the vacuum chamber as it is the closest object, and usually it is shielding the radiation coming from the outside. The atoms being probed in the optical clocks have very low temperatures in the order of μK, which is about 8 orders of magnitude lower than the vacuum chamber at room temperature.

Common practice to address that source of uncertainty is to precisely control the temperature of the vacuum chamber. As the shift is adding a systematic error, it is possible to compensate for it once we know its nature. When the temperature of the vacuum chamber is very well defined, it is possible to calculate the correction to the reference frequency reading.

Another practice that helps in reducing the black body radiation shift is to place the atomic cloud inside a cryogenic chamber [49]. This method both reduces, and stabilises the surrounding temperature around the boiling point of the refrigerant, which is ~ 77 K for liquid nitrogen. On the other hand, this method is more difficult to implement, and more expensive to run.

Zeeman shift

As well as being sensitive to electric fields, the energy levels can also be sensitive to magnetic fields. This effect is known as the Zeeman effect, and its linear part can usually be easily eliminated by using magnetic shields or magnetic compensation coils. However, the quadratic part of this effect might still be significant in the case of the most accurate clocks. This effect introduces a systematic error, which can be estimated and removed from the measurement.

CHAPTER 3

NEUTRAL STRONTIUM AS A FREQUENCY STANDARD

There are many different elements available when it comes to choosing one for an optical atomic clock. Some are believed to be more or less accurate, but it is not all about accuracy that matters. A perfect element for an optical clock should be abundant and stable. More importantly, its energy levels should be accessible with existing lasers, meaning that there should be lasers available for cooling, trapping, and probing the clock transition of the atom. The atomic structure should be very well known, with suitable transitions to cool the atoms down to low temperatures, and a narrow linewidth clock transition. Ideally, clocks should be cheap to produce, easy to construct, and reliable. These qualities make the clock a good time reference, and may decide whether the atom is good enough to redefine the second in the future.

At the moment, the neutral strontium atom is one of the most probable candidates to be used in the new definition of the second [104, 105, 106]. This is not only due to the aforementioned qualities of the atom, but also due to the number of strontium clocks already built around the world. Before the redefinition, however, strontium clocks must be well tested and compared with each other, in order to ensure they all give the same results [107]. Some comparisons between different labs have already been carried out by using bidirectional satellites [108, 109] or fibre links [110, 111, 112]. In the near future, direct comparisons will be possible thanks to the development of the transportable clocks, like the one presented by Koller et al. in [52].

3.1 Energy structure of strontium

A part of the strontium energy structure, that is most important in understanding the operation of a strontium lattice clock, is presented in figure 3.1. Although every transition drawn in this figure could be used as a frequency reference, not every one is equally good. It is possible to define the resonance quality factor Q of

a transition as

$$Q = \frac{\nu}{\Delta\nu} \tag{3.1}$$

where ν and $\Delta\nu$, are the optical frequency and linewidth of the transition, respectively. The larger the quality factor, the better the transition is, to become a reference standard. Transitions with a MHz linewidth such as ${}^1\mathbf{S}_0 \rightarrow {}^1\mathbf{P}_1$ drawn with blue, and ${}^3\mathbf{P}_{0,1,2} \rightarrow {}^3\mathbf{S}_1$ transitions drawn with orange and dashed grey, have quality factors $\sim 2-30\times10^7$. The red transition ${}^1\mathbf{S}_0 \rightarrow {}^3\mathbf{P}_1$ has a narrower linewidth and therefore a higher quality factor of $\sim 6\times10^{10}$. Finally, the transition ${}^1\mathbf{S}_0 \rightarrow {}^3\mathbf{P}_0$ has an extremely narrow linewidth in the order of a millihertz for ^{87}Sr, which gives a large quality factor of $\sim 4\times10^{17}$. This is 10 orders of magnitude higher than the blue ${}^1\mathbf{S}_0 \rightarrow {}^1\mathbf{P}_1$ transition, and much higher than any other described transition. Additionally, the state can be easily addressed with diode lasers that are available at that wavelength, and thus, it is the best transition in neutral strontium to be used as a clock reference.

Nevertheless, other transitions are also important for the strontium lattice clock, as they are used for atom preparation. Atoms need to be cooled down in order to fully benefit from the ultra-narrow linewidth of the clock transition; otherwise, the linewidth will be broadened up to hundreds of megahertz due to the Doppler effect mentioned before in subsection 2.5.3. The blue transition ${}^1\mathbf{S}_0 \rightarrow {}^1\mathbf{P}_1$ with a 32 MHz linewidth is a perfect transition to be used for atom cooling. The narrower red transition ${}^1\mathbf{S}_0 \rightarrow {}^3\mathbf{P}_1$ helps in obtaining lower temperatures and is used in second-stage cooling. The ${}^3\mathbf{P}_0 \rightarrow {}^3\mathbf{S}_1$ and ${}^3\mathbf{P}_2 \rightarrow {}^3\mathbf{S}_1$ transitions help in transferring the population from the long decaying ${}^3\mathbf{P}_0$ and ${}^3\mathbf{P}_2$ states back into the ground state.

3.2 Clock cycle

A strontium lattice clock operates in sub-second cycles of preparing atoms and interrogating the clock transition. Each cycle finishes with a destructive detection of atoms that removes atoms from the trap. With no atoms in the trap it is necessary to start from the beginning, by cooling atoms and loading them into the trap. In figure 3.2, an example of a clock cycle sequence is presented. Each step of the sequence is described in detail, in the following sections. In a nutshell, strontium atoms are first cooled and trapped with a blue 461 nm laser. Simultaneously, repump lasers are being used to increase the number of atoms trapped. When the blue cooling temperature limit is reached, a red 689 nm laser is used to lower temperature of the trapped atoms. Initially, the linewidth of the laser is artificially broadened to avoid abrupt changes that would lead to more atoms being lost. Next, linewidth broadening is removed to allow single frequency cooling. Finally, atoms are transferred into an optical lattice and the red laser is turned off. Atoms confined in the optical

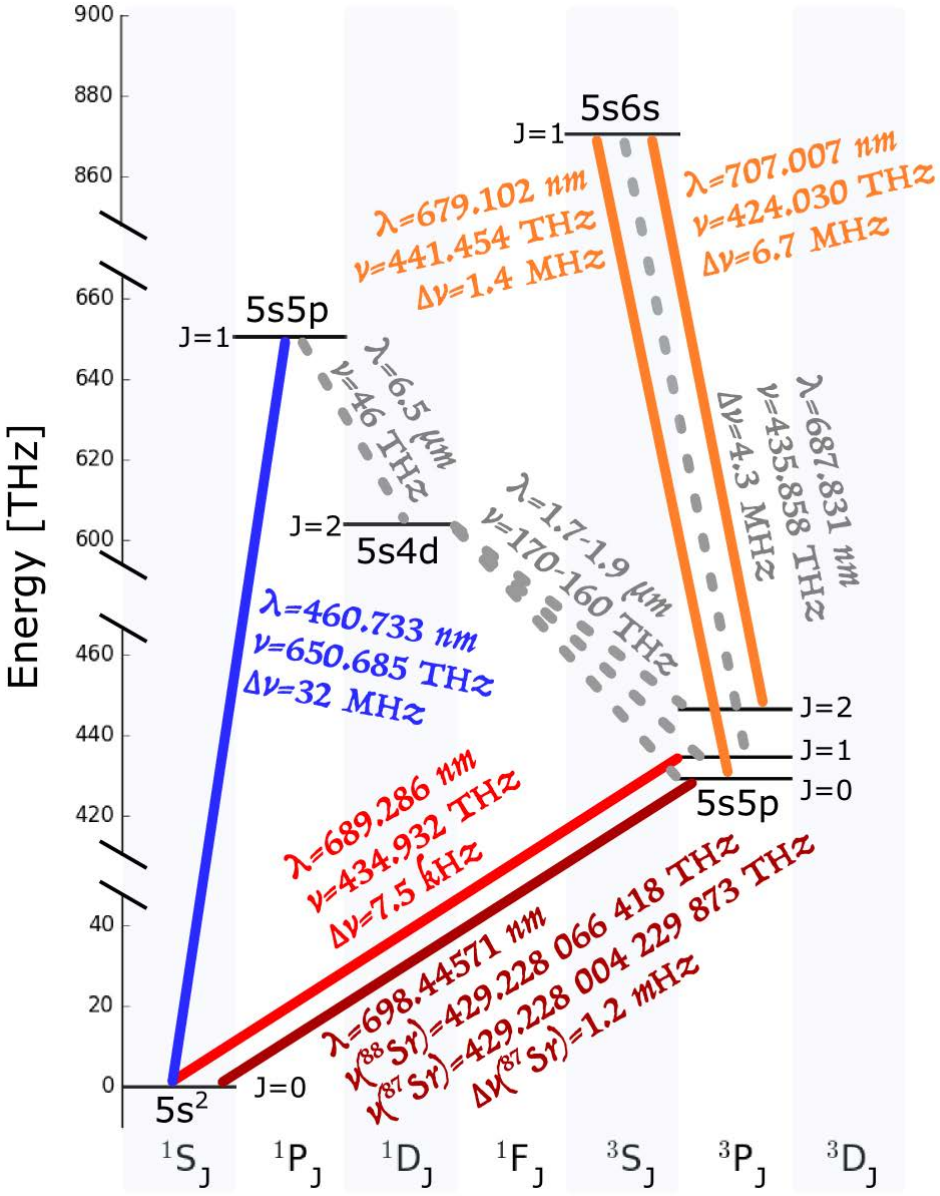

Figure 3.1: The most important energy levels and transitions in neutral strontium. λ, ν, and $\Delta\nu$ are the wavelength in vacuum, optical frequency, and natural linewidth of the transition, respectively. Data values taken from [113].

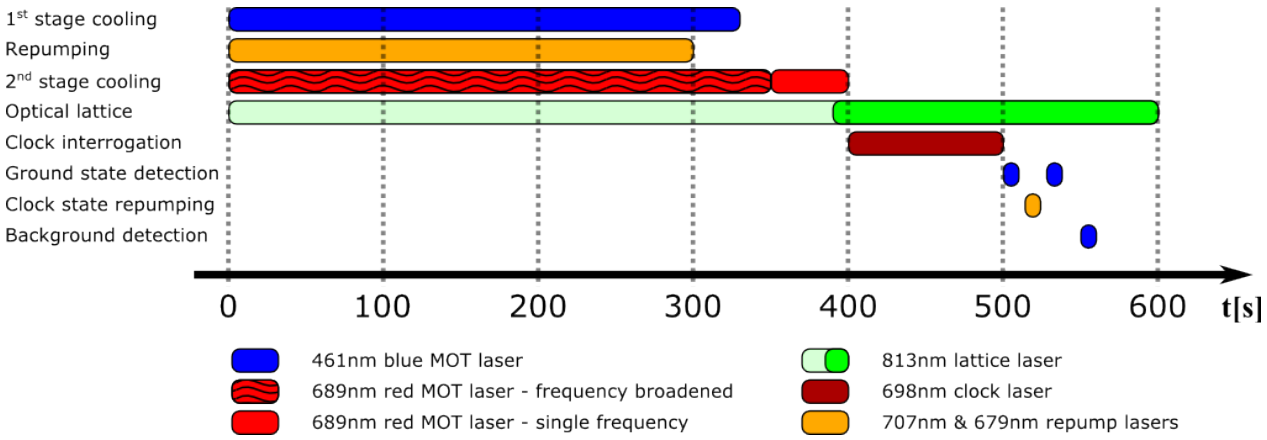

Figure 3.2: Clock cycle sequence in a strontium lattice clock. The 813 nm lattice laser, marked with green, is turned on for the entire time as it does not affect the other steps of the cycle. The time where it is not significant is marked with faded green. Times based on [114].

lattice are interrogated with a 698 nm laser. After interrogation, the blue 461 nm laser is used to destructively detect the number of atoms that stay in the ground state. Afterwards, repump lasers are used to transfer the population from the $^3\mathbf{P}_0$ clock state, down to the ground state, where they can be destructively detected by another pulse of 461 nm laser light. The sequence usually finishes by taking a background picture with the 461 nm laser turned on.

3.3 First stage cooling

In figure 3.1, the energy levels and the most important transitions in Strontium are shown. First to be described is the blue 461 nm transition $^1\mathbf{S}_0 \rightarrow {}^1\mathbf{P}_1$. This is an allowed transition between two singlet states, and therefore the spectral line for this transition is broad and has a value of about $\Delta\nu \approx 32$ MHz. The upper energy level $^1\mathbf{P}_1$ splits linearly in a magnetic field, while the ground state is insensitive to magnetic fields. This quality makes the transition good for laser cooling, and the trapping of strontium atoms. The relatively large linewidth of the transition provides a good basis to initially cool the atoms and obtain a good capture rate with the trap. On the other hand, the broad transition results in limiting the minimum temperature to which the atoms can be cooled down to. This temperature is equal to ~ 700 μK, and is mainly limited by the Doppler cooling limit [115].

3.3.1 Pre-cooling

The capture velocity of a trap describes the maximum velocity of an atom that can be captured in the trap. For a magneto-optical trap, it depends strongly on the used atomic transition, specifically on the optical frequency ν and natural linewidth $\Delta\nu$ of the transition. It can be estimated with a simple formula [116]

$$v_c = \frac{c}{Q} \tag{3.2}$$

where Q is the transition quality factor described by equation 3.1, and c is the speed of light. Using this relation, capture velocities for the blue 461 nm and red 689 nm cooling transitions can be estimated to be 15 m/s and 5 mm/s, respectively.

Every experiment in atomic physics starts from a source of atoms. Atom dispensers and ovens are the most commonly used atom sources in neutral strontium clock experiment. Both sources heat up in order to release atoms that are launched towards the main part of the experimental setup. Thermal emission of atoms leads to a velocity distribution that can be approximated by the Maxwell-Boltzmann distribution [98]. Because of the low vapour pressure of strontium, the oven needs to be heated up to high temperatures in the order of ~ 500 °C (~ 773 K) [117] to obtain a sufficient flux of atoms. The velocity probability distribution for this temperature is presented with a red curve in figure 3.3. The capture velocity of a blue magneto-optical

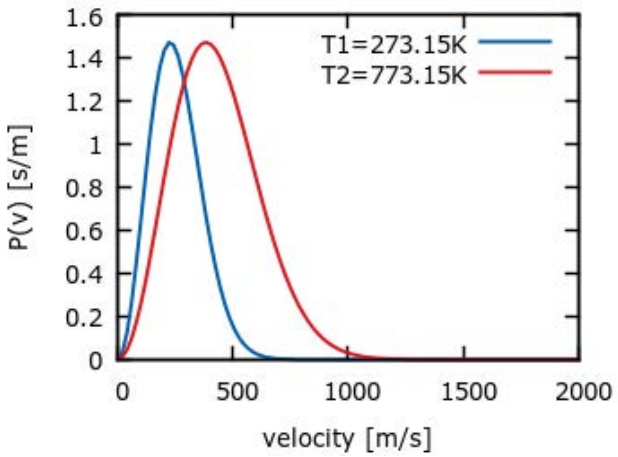

Figure 3.3: Maxwell-Boltzmann velocity distribution for 500°C ($\sim$ 773 K) and 0°C ($\sim$ 273 K) strontium atoms.

trap (MOT) is equal to 15 m/s [115], and is relatively low compared with the mean velocity of atoms exiting the atom source. This means that the blue MOT can only capture a very small fraction of atoms from the thermal distribution presented by the red curve in the figure 3.3. Replacing the oven with an atom dispenser

can slightly reduce the temperature down to $\sim 350^\circ$ C ($\sim$ 620 K) [81], which is still relatively hot. This temperature can be further reduced by using a newly developed laser controlled atom source [118] that emits atoms with thermal distribution close to room temperature, around $\sim 50\ ^\circ$ C ($\sim$ 320 K).

Atom sources are usually integrated into an experimental setup, in a way that produces a collimated beam of atoms. The beam will have a Maxwell-Boltzmann distribution of velocities, corresponding to the temperature of the atom source, only in the direction of beam propagation. Pre-cooling techniques may be used in order to increase the capture rate of the magneto optical trap. This relies on slowing atoms from the fast part of velocity distribution, down below the MOT's capture velocity. A Zeeman slower is used as a popular method of pre-cooling atoms, and will be described in the following subsection.

Zeeman slower

Let us consider a beam of atoms moving from left to right. An individual atom can be slowed down by absorbing a photon coming from the opposite direction. During the absorption, the photon's momentum $\hbar\vec{k}$ is transferred to the atom and thus reduces its speed; where $\vec{k}$ is a wave number, and $\hbar$ is the reduced Planck constant. An excited atom will spontaneously re-emit the photon in a random direction, and after many spontaneously emitted photons, the momentum coming from this effect will average down to zero. Therefore, only the absorbed photons change the atom's momentum when averaged over a long time. Assuming that a beam of atoms consists of particles moving in the same direction, it can be slowed down by taking a beam of resonant laser light and shining it from the opposite direction, as shown in the top part of figure 3.4.

An atom absorbing a photon experiences a force, that in a two level model, can be written as [119, 120]

$$\vec{F} = \hbar\vec{k}\gamma_p, \tag{3.3}$$

where γ_p is the excitation rate that depends on the saturation intensity I_s and natural linewidth $\gamma/2\pi$ of the transition, intensity I and detuning δ of the laser beam from the atomic resonance, and the Doppler shift seen by the atoms $\omega_D = -\vec{k}\cdot\vec{v}$, in the following relation

$$\gamma_p = \frac{s_0\gamma\pi}{1 + s_0 + \left(\frac{\delta+\omega_D}{\gamma\pi}\right)^2} \tag{3.4}$$

The relative movement of atoms with respect to the laser beam leads to the Doppler shift in the observed laser frequency. For a counter-propagating beam of atoms and laser light, the frequency seen by the atoms is shifted towards higher frequencies. The shift changes as the atoms are being slowed down, which causes

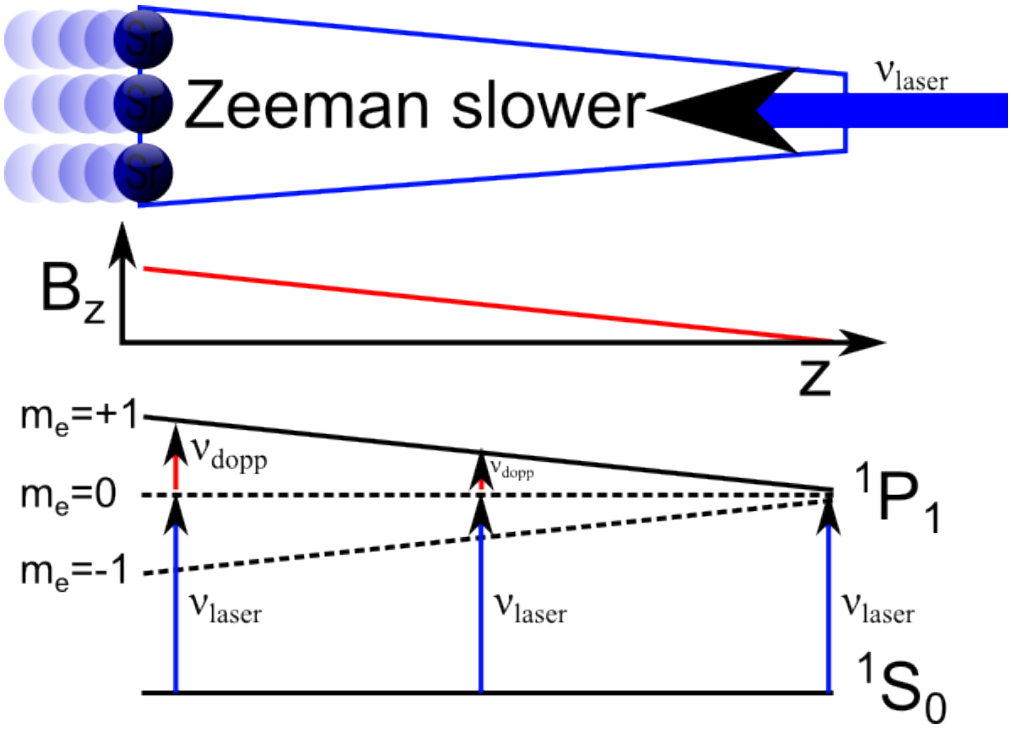

Figure 3.4: Zeeman slower operation principle. Atoms are being slowed down by a counter-propagating beam of laser light at optical frequency ν_{laser} that can be absorbed when in resonance with the atomic transition. A Zeeman slower produces a magnetic field gradient that modifies the energy of the $\{^1\mathbf{P}_1, m_e = +1\}$ energy level to compensate for the decreasing Doppler frequency shift ν_{dopp} as the atoms are being slowed down along the slower.

the monochromatic laser beam to be no longer resonant with the atomic transition. Thus, only atoms within a small range of velocities, determined by the laser detuning, can be slowed down. A narrow linewidth laser can be replaced with a broader one that produces a resonant frequency for every class of speeds. This would, however, require a more powerful laser, in order to keep the same spectral power density level. A common approach that utilises a narrow linewidth laser is modifying the energy of the upper atomic level to compensate for the decreasing Doppler shift of the slowed atoms. The Zeeman effect is used to do this as it splits the upper $^1\mathbf{P}_1$ level into three, where the magnitude of the splitting is approximately proportional to the applied magnetic field.

A Zeeman slower consists of an electromagnetic coil or a set of permanent magnets that produce a magnetic field, with a gradient along the beam of atoms. The magnetic field gradient is engineered to optimise the slowing process for a given element, which depends on the atomic source type and the output velocity target. Usually, it starts with a high magnetic field next to the atomic source and it drops down to zero at the science chamber, as presented in the middle part of figure 3.4. The bottom part of the same figure shows how the

energy levels in strontium are modified due to the magnetic field along the Zeeman slower.

In order to obtain a sufficiently slow beam of atoms, often the Zeeman slower needs to be relatively long (0.3–1 m). The longer the distance the atomic beam travels, the more it diverges, and less atoms reach the centre of the science chamber. Diverged atoms must eventually hit a wall of the vacuum chamber, where they condense, and can no longer be used in the cooling process. An alternative to the Zeeman slower is the 2-Dimensional Magneto-Optical Trap (2D MOT), which also uses laser light, but from two directions perpendicular to the direction of the flux of atoms, improving the collimation of the molecular beam. More information about the 2D MOT can be found in [121, 81].

3.3.2 Dark state repumping

Here is an example of how a good knowledge of the energy structure of strontium can further improve laser cooling efficiency. An atom excited to the $^1\mathbf{P}_1$ state can either decay to the ground state $^1\mathbf{S}_0$, which is the most probable, or through the $^1\mathbf{D}_2$ state to the metastable states $^3\mathbf{P}_0$ and $^3\mathbf{P}_2$. The lifetime of these states are equal to a couple hundred seconds [122, 123], which is relatively long compared with the sub-second long cooling cycle. Atoms occupying these states cannot absorb the light of the cooling laser. As a result, the atoms can no longer take part in the cooling process [116]. Knowing this, it is possible to find another energy level that is accessible by lasers, and can be used as an intermediate transition, to pump the atoms back to the ground state. The $^3\mathbf{S}_1$ state is perfect for this purpose as it can be reached from both the $^3\mathbf{P}_0$ and $^3\mathbf{P}_2$ state with 679 nm and 707 nm laser light, respectively. Atoms from the $^3\mathbf{S}_1$ state can decay to all three $^3\mathbf{P}_{0,1,2}$ states, and those that reach the $^3\mathbf{P}_1$ state decay further to the ground state $^1\mathbf{S}_0$. Such a process is called optical repumping, and the lasers used in the process are referred to as repump lasers, repumping lasers, or repumpers.

3.3.3 Blue magneto-optical trap

Blue magneto-optical trap (blue MOT) is a part of the first stage cooling. It consists of 3 pairs of counter-propagating beams of 461 nm light and a magnetic field produced by two coils in anti-Helmholtz configuration. Three pairs of cooling beams are needed to cool the atoms down in each of three dimensions. Instead splitting power of the laser into 6 beams, the light used for cooling atoms in one direction can be reflected back to be used for cooling the opposite direction as well. In this manner it is only necessary to split the laser beam into three, having twice as much power per beam available.

The Zeeman effect is as much important in the case of a 3D MOT as it was in the Zeeman slower. Anti-

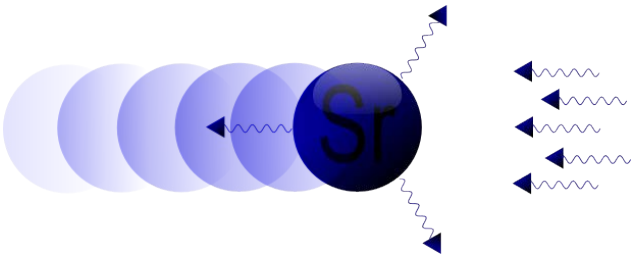

Figure 3.5: In the first stage cooling atom is being slowed down by absorbing counter-propagating photons of 461 nm light. Momentum from the photon is therefore transferred to the atom which is slowed down as an effect. Atom spontaneously decays from excited state emitting a photon in random direction. The total recoil momentum that comes from emitting photons sums up to zero after several acts of absorption.

Helmholtz magnetic coils create gradient of magnetic field with zero value in the centre. When analysing magnetic field along one dimension only, it has positive magnetic field induction value on one side of the trap while negative value on the other side as presented in top part of figure 3.6. The magnetic field splits the energy levels of ${}^1\mathbf{P}_1$ state into three as presented on the bottom part of the figure.

The role of the MOT is not only to slow the atoms but also pull hem towards the centre of the trap. Atoms that are too much to the left from the centre should experience a force acting towards the centre. This means that this atoms should only interact with the laser light coming from the left and be insensitive to the light coming from the opposite direction. Cooling laser beam pairs have orthogonal circular polarisations σ_+ and σ_- to let the atoms distinguish between the two beams. The laser frequency is red-detuned from the resonant frequency of the cooling transition. As it is depicted in figure 3.6 state with $m_e = +1$ can be only excited with σ_+ beam while state $m_e = -1$ with σ_- beam. Thus, atoms that are on the left will be excited by the left beam and pushed towards the centre while those on the right will be pushed by the right beam towards the centre. Note that detuning δ from the $m_e = 0$ state is necessary in order to avoid over-oscillation of atoms around the trap centre [115] [120]. Detuning also increases probability of absorbing cooling light for atoms being further away from the centre, increasing value of the mean force acting on the atoms. Detuning value for strontium blue MOT is usually of the order of 40–70 MHz, compared with the transition's linewidth equal to 32 MHz [83, 116].

3.4 Second stage cooling

It is possible to overcome the cooling limit of the blue cooling transition by using transition with narrower linewidth. Red 689 nm transition ${}^1\mathbf{S}_0 \rightarrow {}^3\mathbf{P}_1$ is between the ground singlet state and a triplet state that makes it thousand times less probable for a photon to be absorbed and its spectral linewidth is equal to

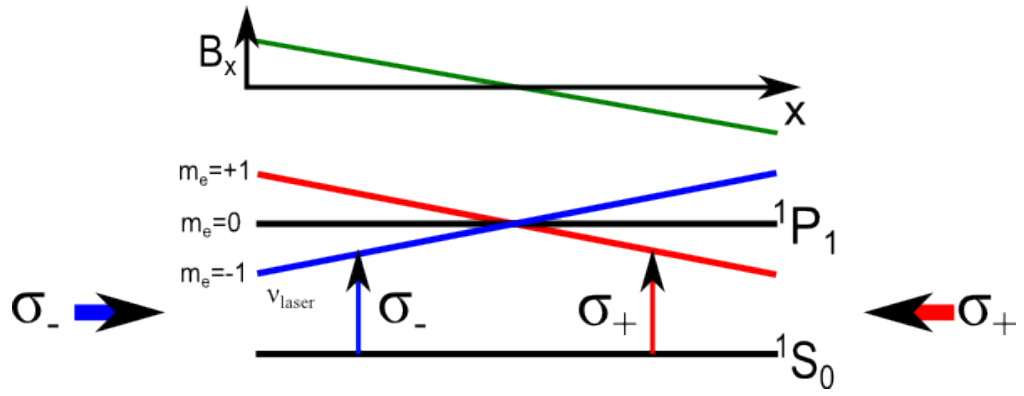

Figure 3.6: Schematics of 1-dimensional magneto-optical trap. Colours denote different polarizations: red for σ_- and blue for σ_+. State with $m_e = +1$ can be only excited with σ_+ beam while state $m_e = -1$ with σ_- beam. Thanks to that effect, atoms on the left are excited with the left beam and pushed towards the centre, while those on the right are pushed by the right beam towards the centre. Note that detuning δ from the $m_e = 0$ state is necessary.

$\Delta\nu \approx 7.5$ kHz. Narrower linewidth helps in lowering the value of the Doppler limit down to $\sim$ 200 nK. However, that temperature cannot be reached because of the recoil temperature limit equal to $\sim$ 500 nK [115].

In practice, the first phase of cooling atoms with the blue light lowers their temperature down to mK level. This temperature is not low enough for the atoms to be transferred into an optical lattice where temperature should be lower than 20 μK [124]. Therefore, usually a red 689 nm laser is used to cool atoms down by a factor of 10^3 to order of μK [125]. Reported number of atoms from the paper in a red MOT is 10^6.

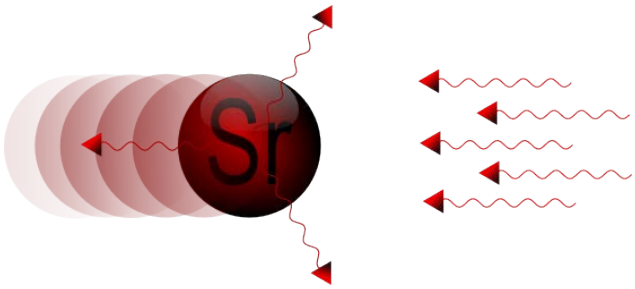

Figure 3.7: In the second-stage cooling atom absorbs counter-propagating photons of 689 nm light.

The concept of the magneto-optical trap is the same as it was in blue MOT. Using different transition requires adjusting values of the magnetic field values, beam intensities and detuning from resonance. The same anti-Helmholtz coils are used to ensure overlap of blue and red trap centres.

After atoms are cooled down in a blue MOT, the beams are turned off and magnetic field is ramped down from $\sim$ 100 G/cm to $\sim$ 3 G/cm [126]. Because of much smaller values of the magnetic field, the stray

magnetic field is no longer negligible as it was in the blue MOT. The stray magnetic field can be easily eliminated with a pair of additional compensation coils.

In the blue MOT the saturation intensity of the cooling transition is about 40 mW/cm^2 while saturation intensity of the red cooling transition is only 3 μW/cm^2 [115]. For this reason one has to be careful to not have too much power in the cooling beams and not let the atoms be heated up by the excessive power. Usually, few hundreds of μW/cm^2 of power are necessary for red cooling beam [126, 127].

3.4.1 Broadband cooling

Narrow linewidth of the red cooling transition leads to decreased capture velocity of the trap down to 5 mm/s, as it was estimated in subsection 3.3.1. Velocity of the blue MOT cooled atoms is equal to 370 mm/s, assuming they reach the Doppler cooling temperature limit of $\sim$ 700 μK. This is much higher than the capture velocity of the red MOT, which results in low transfer efficiency of atoms from blue to red MOT.

Broadband cooling is a method of increasing the capture rate of the red MOT by artificially broadening the laser linewidth. This allows atoms in every class of velocities to absorb the narrow-linewidth laser light in order to be cooled. The broadening is usually done with an acousto-optical modulator (AOM) or electro-optical modulator (EOM) by changing very fast frequency of the modulators in discrete steps in order to generate sidebands around the central laser frequency. In the experiment of Katori et al. [116], 30 sidebands separated by 50 kHz were enough to obtain 90% transfer efficiency.

Intensity hyper-saturation broadband cooling

Instead of adding sidebands to the cooling laser, it is possible to increase intensity of the cooling laser. This effect was observed in Space Optical Clock 2 (SOC2) project [114] and detailed description can be found in L. L. Smith's thesis [83]. The method involves using a powerful laser to trigger power broadening of the red 689 nm cooling transition in strontium atoms. Saturation intensity of the red cooling transition in strontium is equal to $\sim$ 3 μW/cm^2. This is a relatively low value and it is easy to have 3 orders of magnitude higher intensity of the cooing beam $\sim$ 3 mW/cm^2 that broadens the narrow transition linewidth to the order of megahertz.

Supplementing explanation can be given with the use of figure 3.8. In the figure the black solid line is the natural spectral line of the $^1\mathbf{S}_0 \rightarrow {}^3\mathbf{P}_1$ transition. The line has Lorentzian shape and linewidth equal to 7.5 kHz. Dashed lines show frequency spectrum of a resonant laser light at different intensities. All of them have Lorentzian shape and linewidth equal to 7.5 kHz. Intensity is described with saturation parameter S_0

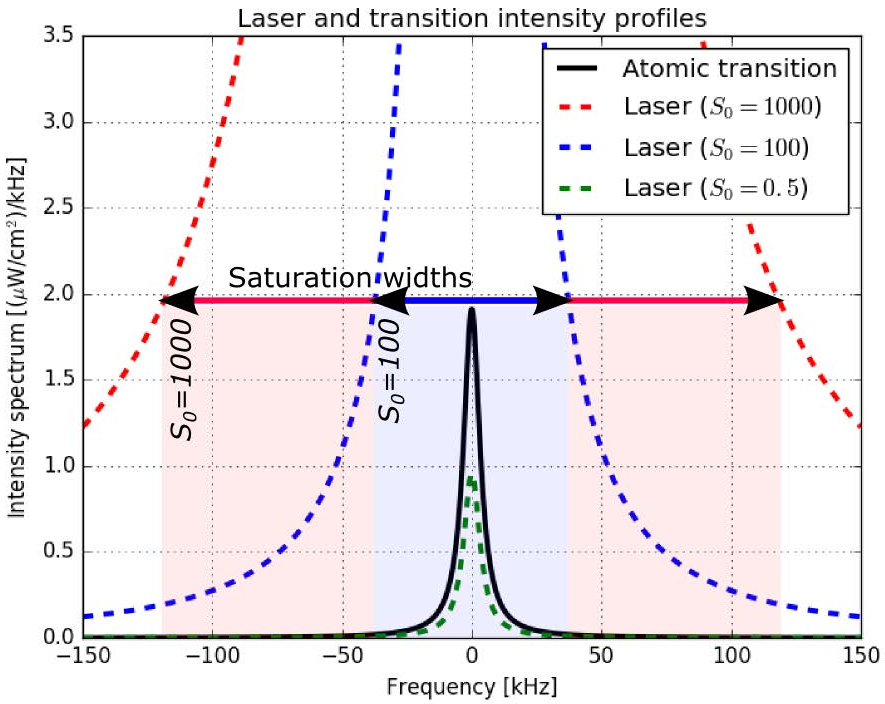

Figure 3.8: Intensity hyper-saturation effect in broadband cooling of strontium. Black solid line shows Lorentzian-shape natural line of ${}^1\mathbf{S}_0 \rightarrow {}^3\mathbf{P}_1$ transition with linewidth equal to 7.5 kHz. Different intensities of resonant laser are drawn with green blue and red dashed lines, all having Lorentzian shape and the same linewidth of 7.5 kHz. Intensities are described by saturation parameter S_0 that was defined by equation 2.36. Blue and red arrows show spectral areas where the laser intensity profiles fully saturate the atomic transition. Width of that area is defined here as saturation width. Saturation width for blue and red profiles are $\sim$ 70 kHz and $\sim$ 240 kHz respectively. Please note that different laser intensities broaden the natural linewidth of the transition, which is not presented in the figure for simplicity.

that was defined earlier with equation 2.36. Saturation widths marked with blue and red arrows show a range of frequencies, where atomic transition is fully saturated despite the laser detuning from the resonance. The higher laser intensity and saturation parameter, the wider span of laser detuning frequencies where the transition will be saturated. As a result, a laser with much higher intensity than the saturation intensity of the transition would be perceived by the atom in the same way as a laser with similar intensity but broader linewidth.

3.4.2 Single frequency cooling

The broadband red MOT is an intermediate pre-cooling step of transferring atoms from the blue MOT into the single-frequency red MOT. With atoms trapped in the broadband red MOT, it is possible to gradually reduce broadening of the red cooling laser until only the original narrow linewidth of cooling laser is left.

The laser linewidth is much narrower when compared with the original broadening and therefore the MOT obtained with the laser is referred to as a single frequency red MOT.

3.5 Optical lattice

Although the cold strontium atoms trapped in a magneto-optical trap are already very cold and confined, they are not suitable to be used as a reference. Atoms in the MOT keep being excited with the resonant laser light, which is transferring the population between the ground and excited state. Operation of strontium clock requires the clock transition $^1\mathbf{S}_0 \rightarrow {}^3\mathbf{P}_0$ to be probed with a clock laser, which cannot be done when atom is in the upper $^3\mathbf{P}_1$ state. Moreover, the presence of the red cooling light and trap's magnetic field alter the energy structure of the strontium atom, bringing more systematic errors into the final uncertainty budget of the optical clock.

An optical lattice is used to confine the cooled strontium atoms. It is created by overlapping at least two beams of laser light, having the same amplitude and wavelength, to form a standing wave. Such a standing wave creates a periodic optical energy potential that similarly to a quantum well has discrete energy levels that atoms can occupy [128].

The electric field coming from the lattice lasers shifts the atomic energy levels due to the Stark effect. The magnitude of the Stark shift depends on the wavelength and it might be different for different energy levels. A wavelength that shifts ground $^1\mathbf{S}_0$ and clock $^3\mathbf{P}_0$ states by the same factor is called magic wavelength. As the shift for both states is the same, the energy difference remains the same. The most popular magic wavelength in strontium is 813 nm. However, other magic wavelength may be found around 915 nm [115].

Figure 3.9: After two stages of cooling, atoms are confined in an optical lattice. An optical lattice is a optical potential that is created when counter-propagating beams of light create a standing wave.

3.6 Clock interrogation

When the ultra-cold strontium atoms are already confined in the optical potential, it is finally possible to use them in the main part of the experiment, which is interrogation with a clock laser. Interrogation is based

on comparing the optical frequency of the clock laser with the $^1\mathbf{S}_0 \rightarrow {}^3\mathbf{P}_1$ clock transition in order to obtain information on the detuning, which can be used to adjust the clock laser frequency. In the result, the clock laser obtains the frequency of the atomic transition, which is stable and very well defined (accurate). With the whole cooling and trapping cycle being relatively slow (0.5–1 s), it is very important that the clock laser is stable enough, not to drift too far away from the atomic resonance, between the interrogation stages. For this reason, the clock laser is stabilised to an ultra-stable Fabry-Pérot cavity, with the state-of-the-art cavities reaching instability level as low as 5×10^{-17} in fractional frequency units [129].

The interrogation of the atoms can be performed by using different methods. Anyway, it relies on applying a pulse of light to transfer the atom population from the ground to clock state. The closer the laser frequency is to the resonance, the higher probability for the atom to be excited by the light. Thus, after each pulse it is necessary to count how many atoms were excited state and how many atoms stayed in the ground state, in order to calculate what was the excitation probability.

3.6.1 First ground state detection and clean up

After the first interrogation pulse, fraction of atoms are transferred from the ground into clock state. The lifetime of the clock transition is very long when compared with the cooling cycle time and the atoms stay in the clock transition for the entire cycle time.

A resonant blue 461 nm light pulse is used to remove the atoms being in the ground state from the optical lattice. The repelling force comes from atoms absorbing the light and it is possible to record an absorption image that can be used to estimate the number of atoms in the ground state. Alternatively, the number of atoms can be inferred from measuring the fluorescence intensity e.g. with a photo-multiplying tube. Atoms in the clock state cannot interact with the blue cooling laser. Therefore, they stay confined within the lattice potential.

3.6.2 Clock to ground state repumping

Once the number of atoms in the ground state is known it is necessary to calculate how many atoms is in the clock state. Very useful for a detection would be a broad transition starting from the clock state, similar to $^1\mathbf{S}_0 \rightarrow {}^1\mathbf{P}_1$ transition used for detection of atoms in the ground state. On the other hand, this would require another laser and instead of looking for such a transition, it is possible to transfer the population of the clock state back to the ground state and use the 461 nm pulse again.

Atoms can be transferred very fast from the clock state to ground state by using the repump lasers. the

repump lasers will pump the population to the $^3\mathbf{S}_1$ state, where it decays through the $^3\mathbf{P}_1$ state down to the ground state.

3.6.3 Second ground state detection

With the atoms transferred from the clock state to the ground state, it is possible to repeat the detection scheme that was already used before. This way, the same laser with the same parameters is used for detecting populations of both states. This also makes it simpler to calculate the population ratio.

3.6.4 Background detection

During the detection of the ground state, an absorption or fluorescence image can comprise a constant systematic error, which may come from the scattered or reflected blue 461 nm detection light. To measure the value of that constant, an extra 461 nm blue pulse is produced when there are no atoms left in the optical lattice. This is commonly known as the background measurement.

CHAPTER 4

COOLING LASER SYSTEMS

This chapter presents the construction of the second-stage red cooling laser at 689 nm. First, I present a mobile amplified system in master oscillator power amplifier (MOPA) configuration that was constructed to be a part of the strontium mini clock project. The system is built in a modular box having dimensions $35 \times 25 \times 8$ cm^3 and it uses components design, such as mirror mounts, well tested in drop tower experiments. In this chapter, I also present an alternative laser technology that was tested for second-stage cooling of strontium. The laser under test was the semiconductor disc laser (SDL) also known as the vertical-external-cavity surface-emitting-laser (VECSEL). At the end of the chapter, I present construction of a compact optical cavity as a part of frequency stabilisation system (FSS), designed for the stabilisation of all the lasers used in strontium optical clock experiment. Most importantly, the cavity is designed to lock the second-stage red cooling laser, as well as, to narrow down the linewidth of the laser.

4.1 Modular amplified tunable diode laser for second-stage cooling

One of the tasks in the experiment was to design and construct a red MOT 689 nm laser. The laser does not have to be powerful, because only a couple of mW of power per trapping beam is necessary. Nevertheless, having to choose between either, two lasers in a master-slave configuration, or one master oscillator power amplifier (MOPA) laser, the latter seemed to be a better choice, due to a significantly higher power output reaching up to 500 mW, while the complexity and cost is on a similar level for either of the solutions.

The MOPA system consists of a master laser, which is the source of the desired optical frequency, amplified by an optical amplifier. The master laser in my design is an external cavity diode laser (ECDL) [130]. In a typical Fabry-Pérot (FP) laser diode, the diode's output facet partially reflects light back into the semiconductor area, triggering stimulated emission and causing it to lase. In an ECDL, the laser diode is

anti-reflection coated in order to extend the resonator beyond the laser diode, where a grating or partially reflecting mirror could be used. An ECDL can be built in free space, or by using an optical fibre as the resonator. The external cavity of an ECDL forms a resonator that allows the easy tuning of the wavelength, by filtering the spectrum of the back-reflected light. Extending the length of a resonator also results in a narrower linewidth for the laser.

An ECDL can be constructed using two popular configurations: Littrow or Littman-Metcalf [131, 132]. Schematics for each of them can be seen in figure 4.1. In the Littrow configuration, a grating diffracts the first order beam back to the laser diode, and the zero-order beam straight to the output of the laser. The wavelength of the output can be tuned by rotating the grating. In the Littman-Metcalf configuration, the laser beam hits the grating at a higher angle and the first order diffracted beam is reflected back by a mirror. The reflected beam diffracts for a second time, and part of it returns to the laser diode and stimulates emission. The grating in this configuration can be fixed, and the wavelength is tuned with the mirror instead. This has the advantage of the output beam always being at the same position. The double diffraction of the laser beam has the benefit of a narrower linewidth on the output. However, it also results in a reduced power level when compared with the Littrow configuration [133, 134].

The MOPA system needs an optical amplifier, and for a free space system, a tapered amplifier (TA) is a good solution. The TA works in a similar way to a laser diode, where both facets are accessible and anti-reflection coated. The semiconductor in the tapered amplifier chip has a special tapered shape resembling a funnel. The seed laser is being amplified more and more as it travels through the amplifier. The shape prevents the chip from being damaged by distributing the power over a larger area and lowering the power density inside the semiconductor. Laser light injected from the narrower part of the funnel triggers stimulated emission in the gain region of the amplifier, creating a new beam of laser light which has the same frequency and direction as the seed laser.

A downside of the tapered amplifier is its deformed beam shape on the output, which needs to be collimated with a cylindrical lenses in order to achieve a symmetrical collimated beam. Even the collimated beam does not have a perfectly Gaussian profile, which causes the fibre coupling efficiency to be about 50%.

The tapered amplifier chip, used in the 689 nm laser, needs to be seeded with a relatively high power (> 10 mW). For this reason, it was decided that the master laser of our MOPA system should be in the Littrow configuration, in order to maximise the power.

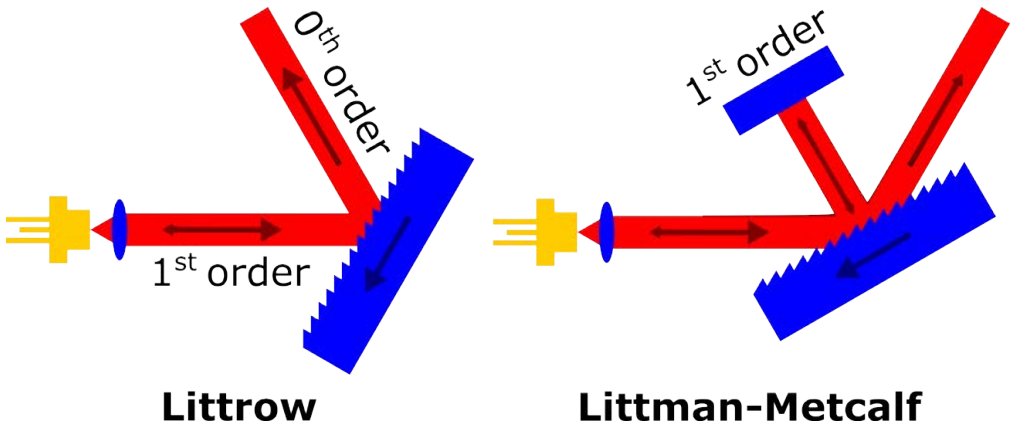

Figure 4.1: Littrow configuration versus Littman-Metcalf configuration in the External Cavity Diode Laser. Light from the laser diode is collimated and falls on a blazed grating. In the Littrow configuration (left) the first order diffracted beam goes back to the laser diode to cause stimulated emission. Wavelength can be tuned by changing the angle of the grating. In the Littman-Metcalf configuration (right) the first order diffracted beam is reflected back with a mirror. Wavelength can be tuned by changing the angle of the mirror.

4.1.1 Laser design

The ECDL cavity consists of a laser diode, grating, and a collimation lens, and it is drawn as a red rectangle in figure 4.2a. The laser's wavelength depends strongly on the diode's temperature. Thus the temperature must be kept constant to avoid wavelength fluctuations. The entire cavity is temperature stabilised with a thermoelectric cooler (TEC). A 10 Ω thermistor is used to sense the temperature of the cavity next to the laser diode socket. The laser diode was manufactured by Eagleyards Photonics, and was designed to be used in an external cavity. It is specified to output up to 35 mW of power in an ECDL. Both the laser diode and collimating lens are anti-reflection (AR) coated to avoid any interference by the back reflected light with the mode of the resonator. Without the AR coating, the front facet of the laser diode would reflect part of the light back into the semiconductor forming an optical resonator and causing stimulated emission. The modes of that internal resonator would then compete with the modes of the extended cavity, effectively reducing the mode-hop free tuning range of the laser. The grating is glued to a mirror mount with very fine adjusters, and a piezoelectric transducer is placed between the adjuster and grating's platform, to allow a precise control of the tilt.

The 0^{th} order beam exits the ECDL cavity at an angle. This is compensated for with a mirror, which sends the beam through a compact, very low power (VLP) Faraday optical isolator (FOI) with $\sim$ 40 dB isolation. The laser beam profile is elliptical, therefore, it needs to be shaped with an anamorphic prism pair (APP) in order to fit through the small aperture, of the isolator, of $\sim$ 2.7 mm. The isolator protects the ECDL from the back-reflected light coming from the other optical components. The back-reflected light can

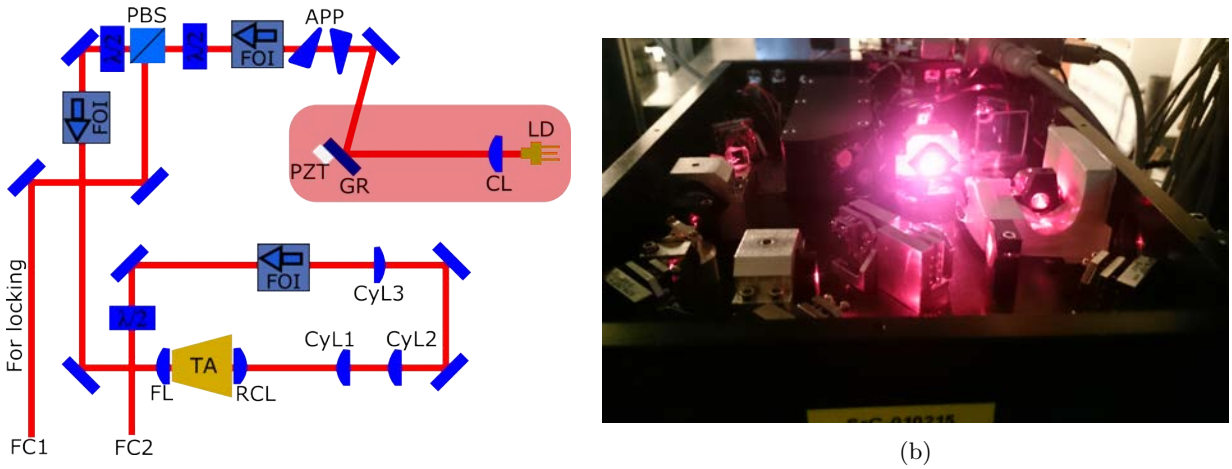

(a) (b)

Figure 4.2: **(a)** Master oscillator power amplifier (MOPA) design for the second-stage cooling of strontium. LD – laser diode; CL – collimation lens; GRT – grating; PZT – piezoelectric transducer; APP – anamorphic prism pair ;FOI – Faraday optical isolator; $\lambda/2$ – half-wave plate; PBS – polarisation beam splitter; FC – fibre coupler; FL – focusing lens; TA – tapered amplifier; RCL – re-collimating lens; CyL – cylindrical lens **(b)** Picture of the working MOPA.

not only affect the stability of the laser, but also damage the laser diode.

After the isolator the beam is split into two by using a polarising beam splitter (PBS) and a half-wave plate retarder, which allows the continuous adjustment of the power ratio between the beams. The weaker beam, with ~ 250 μW of power, is coupled into a fibre-integrated electro-optical modulator and can be used for the stabilisation of the laser. The stronger beam passes through an additional 40 dB isolator, and is used to seed the tapered amplifier chip with ~ 15 mW of power. The second isolator is needed to isolate the stray light emitted by the TA, which is a small fraction of the output power, but for high amplification values it becomes more significant. To match the mode of the seeding beam with the mode of the TA, a focusing lens is used.

The tapered amplifier chip is integrated within a bone package and it was provided from Toptica Photonics. I designed a special holder to mount the chip inside the laser, which enables a trouble-free replacement of the bone mount. The holder is made of copper, which acts as a very good heatsink, and is temperature stabilised with a Peltier element. The amplified beam after the TA is deformed because of the tapered shape of the amplifier, and needs to be reshaped. First, the beam is re-collimated with a spherical lens. However, the beam is more divergent in one direction than in the other (astigmatism), which needs to be compensated with a cylindrical lens (lens CyL2 in figure 4.2a). Two additional cylindrical lenses form a telescope to shape the oval shape of the beam (CyL1 and CyL3 in the figure). The beam passes through an optical isolator

again, which protects the TA chip from being damaged, and is fibre coupled.

The MOPA system is compact and modular, having dimension $35 \times 25 \times 8$ cm^3. The maximum obtained powers are 300 mW, 216 mW and 71 mW, measured after the TA, isolator, and fibre, respectively.

4.1.2 Narrowing the 689nm laser

Let us consider the Lorentzian-shaped spectral lines of an atomic transition, and of laser light. Each of them is defined by its full width at half maximum (FWHM) linewidth. Laser spectroscopy is based on scanning the laser spectral line across the atomic line, to measure the absorption spectrum. Line shape of the measured spectrum will be a convolution of two Lorentzian functions, which is also a Lorentzian function with the FWHM linewidth equal to the linear sum of FWHM linewidths of the atomic transition and the laser [135]. The smaller the laser linewidth is, compared with the atomic transition, the more negligible the effect it has on the shape of the observed absorption spectrum. In laser cooling, the laser linewidth should also be much narrower than the linewidth of the atomic transition, so that the final temperature is limited by the width of the transition only, and not by the laser.

The natural linewidth of the red MOT cooling transition $^1\mathbf{S}_0 \rightarrow {}^3\mathbf{P}_1$ is as low as 7.5 kHz. The red cooling laser with a ~ 1 kHz linewidth should be low enough to obtain the best cooling results.

Free-running linewidth of the MOPA laser is estimated to be in 30–100 kHz range. This value is much higher than the target 1 kHz, which brings the need of narrowing down the linewidth. It can be done by very fast locking the laser to a high finesse optical resonator. The MOPA laser was initially locked to a triangular Fabry-Pérot interferometer made of invar, which has a low coefficient of thermal expansion in comparison to other metals.

The invar triangular cavity was not stable enough to meet the second-stage cooling requirements, which was the motivation to construct a more stable and more compact optical resonator, described later in section 4.3.

4.1.3 Laser current source

Size and miniaturisation play an important role in constructing a mobile experiment. Compactness saves space and energy consumption, as well as it helps get closer to the commercialisation of the device. Not only do we focus on reducing the size of the optical components and vacuum chambers in our experiment, but also on building more compact electronics. In many mobile experiments, electronics consume the most amount of space, and it is common to see experiments where electronics occupy ten times more space than the main

part of the experiment.

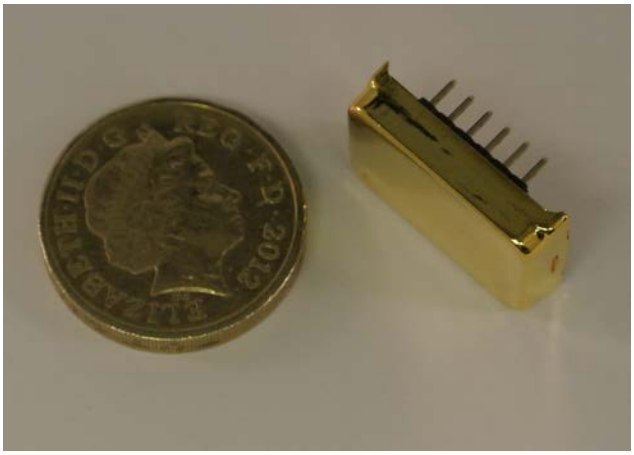

Figure 4.3: Current source chip next to a pound sterling coin.

In the red cooling laser design, a new compact current source was used. It was manufactured by Analog Technologies Inc. and is specified to have a very low noise below 2 μA (0.1 Hz to 0.5 MHz RMS) with a stability below 100 ppm/°C. In the red cooling laser, two such chips were used. One giving up to 200 mA of current, powering the diode; and the second giving up to 1 A of current, driving the tapered amplifier chip. A picture of the chip next to the pound coin is presented in figure 4.3.

4.2 Semiconductor disk laser for atom cooling

In the process of miniaturisation it is important to be open for newly emerging technologies that can simplify the experiment. An example of such technology is the semiconductor disk laser (SDL), which can be constructed to operate at the wavelength of the second-stage cooling transition in strontium [136]. The advantage of the laser is its relatively high power of $>$ 100 mW without using an additional amplifier, clean beam profile and its tunability.

This section reports on testing the semiconductor disk laser for laser cooling of strontium. The laser uses AlGaInP semiconductor and it is described in detail in [136].

4.2.1 Laser chip

Semiconductor disk lasers, or vertical external-cavity surface-emitting lasers (VECSEL), are a newly emerging kind of semiconductor laser, that delivers a high optical power output with a spectrally narrow linewidth. The VECSEL chip, as presented in figure 4.4a, consists of a semiconductor active layer that is deposited on

top of a Bragg reflector, on a substrate. In figure 4.4b, a photograph of a VECSEL chip is shown, where the chip is visible as a black square wafer. On top of the chip, a circular diamond heat spreader plate is mounted, for better heat removal from the chip. In contrast to a semiconductor laser diode, the VECSEL chip is not pumped with current but with a high-power laser light. A green Verdi laser is used to produce the pump beam in our case, with a power level of around 3 W at 532 nm.

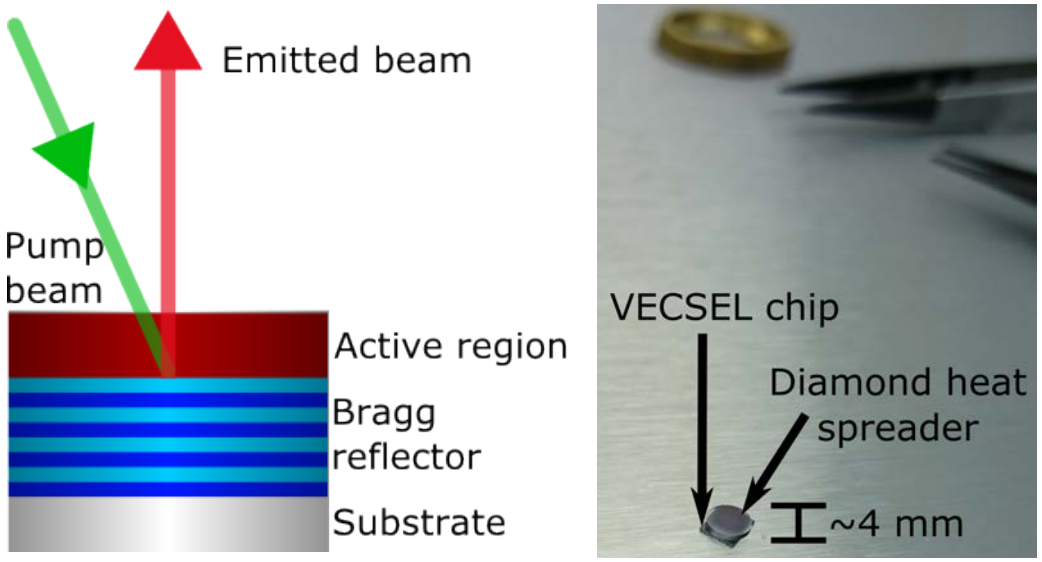

(a) (b)

Figure 4.4: **(a)** Diagram of a VECSEL chip. **(b)** Photograph of a VECSEL chip with a diamond heat spreader contacted on top.

4.2.2 VECSEL construction

The VECSEL chip needs an external resonator in order to form a laser. In figure 4.5 a complete laser design is presented. The VECSEL chip is mounted in a mirror mount, on top of a thermoelectric cooler (TEC) that stabilises its temperature. On the hot side of the TEC, a water block is mounted for water cooling which is used to sink the heat coming from the pump laser. Although the pump light is fully absorbed by the gain medium, a small amount of light is reflected from a diamond heat spreader, which is contacted on top of the VECSEL chip with a capillary bonding method. The VECSEL chip emits a beam perpendicular to its surface, which is collimated by a concave mirror M1 mounted on a piezoelectric transducer (PZT). The collimated beam passes through a birefringent filter (BRF) and hits the output mirror M2. The laser can be coarsely tuned over a range of ten nanometres, by changing the angle of the birefringent filter and the temperature of the VECSEL chip with the TEC. The PZT provides fine tuning of the laser by changing the

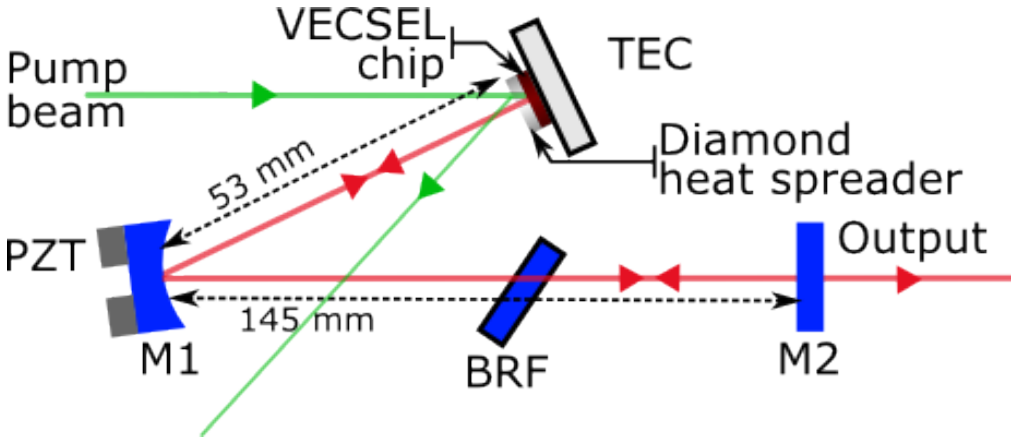

Figure 4.5: Diagram of the VECSEL (vertical external-cavity surface-emitting laser). TEC – thermoelectric cooler, PZT – piezoelectric transducer, BRF – birefringent filter, M1 – concave mirror with 100 mm ROC, M2 – flat output mirror.

length of the laser's cavity, which spreads between the M2 mirror and the Bragg reflector on the VECSEL chip.

The laser outputs up to 120 mW of red laser light at 689 nm through its main output. Additionally, two weak beams, with the power level close to a mW, leak through the concave mirror M1, and can be used for stabilising the laser, or for inspection. The laser outputs a relatively high power laser beam compared with an ECDL (external-cavity diode laser) operating at the same wavelength, which gives powers up to 30 mW. Even higher power levels can be obtained by using a MOPA (master-oscillator power amplifier) system, which outputs up to 500 mW thanks to the use of a tapered amplifier. However, the beam profile, after the tapered amplifier, is degraded significantly. In contrast to that, the VECSEL naturally has a good Gaussian beam profile, shaped by the laser's cavity. The beam profile of the VECSEL, measured at the laser output, is presented in figure 4.6. Both the vertical and horizontal beam profile has a $1/e^2$ Gaussian beam diameter equal to 2.0 mm. Another disadvantage of the tapered amplifier is that it can introduce extra noise to the laser's spectrum, broadening the spectral linewidth of the laser, which does not occur in the VECSEL.

To obtain a stable and narrow linewidth laser, it is required that the pump beam is at a stable power level. Fluctuating power would change the temperature of the gain medium, leading to instability in the laser. On the other hand, frequency fluctuations in the pump laser does not affect the frequency stability of the VECSEL. Another source of instability in the VECSEL is caused by the change in length of the laser's cavity. This includes slow temperature drifts as well as vibrations. The latter is mainly induced by the water cooling system on the VECSEL chip, and was identified to be the most significant. To compensate for the vibrations, the laser was stabilised with a PZT mounted on the M1 mirror to an external Fabry-Pérot

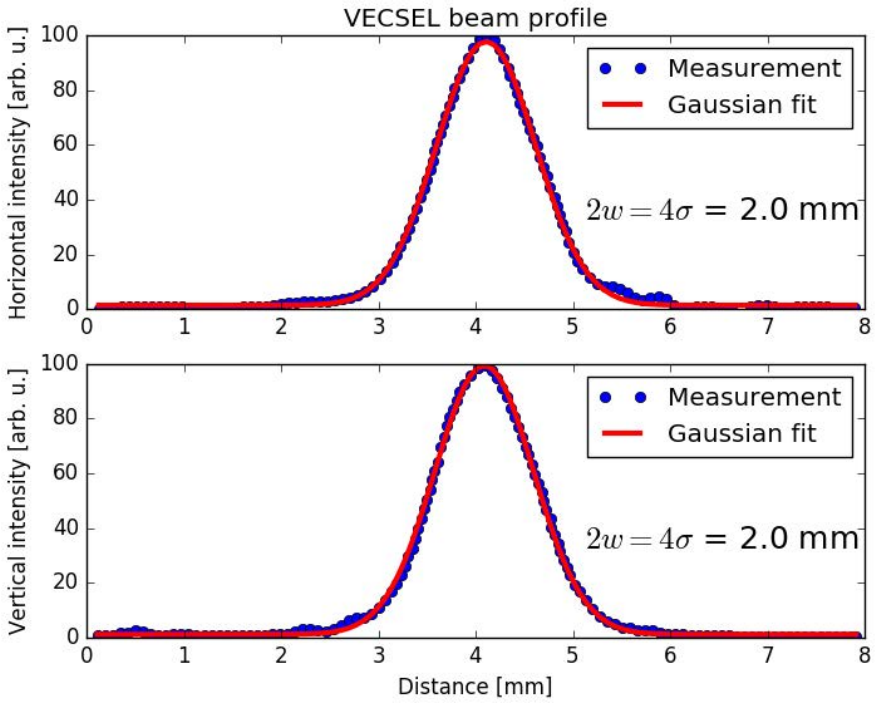

Figure 4.6: Beam profile of the VECSEL measured directly at the main output.

interferometer (FPI), using a side-of-fringe locking technique on the transmitted signal.

The goal of the campaign the University of Birmingham took part in, was to test whether it is possible to use a VECSEL to cool the atoms, especially the second-stage cooling of strontium using the $^1\mathbf{S}_0 \rightarrow {}^3\mathbf{P}_1$ transition. Requirements for the second-stage cooling laser are particularly high, due to the narrow natural linewidth of the $^1\mathbf{S}_0 \rightarrow {}^3\mathbf{P}_1$ transition being equal to ~ 7.5 kHz. Therefore, the VECSEL should not only have an intrinsic narrow linewidth, but should also be stable to stay on the transition.

To test the laser, a SOC2 (space optical clock 2) atomic package was used, which is described in [83]. The VECSEL was set up in a neighbouring laboratory, since the only available pump laser was already there, thus it was necessary to guide its light with a 10 m long fibre to reach the atomic package. As presented in figure 4.7, before coupling into the fibre, the light first passes through a Faraday optical isolator (FOI), and an AOM which provides additional isolation and can be used for fine-tuning the frequency of the laser beam. The laser beam after the AOM is split into two beams and coupled into two 10 m long fibres. One fibre was used to deliver the light to the FPI for stabilisation. The second fibre was coupled with a fibre beam splitter (FBS), to separate part of the light for inspection. The remaining part was split again into three beams, that covered the three directions in the laser cooling of atoms, to obtain a magneto-optical trap (MOT).

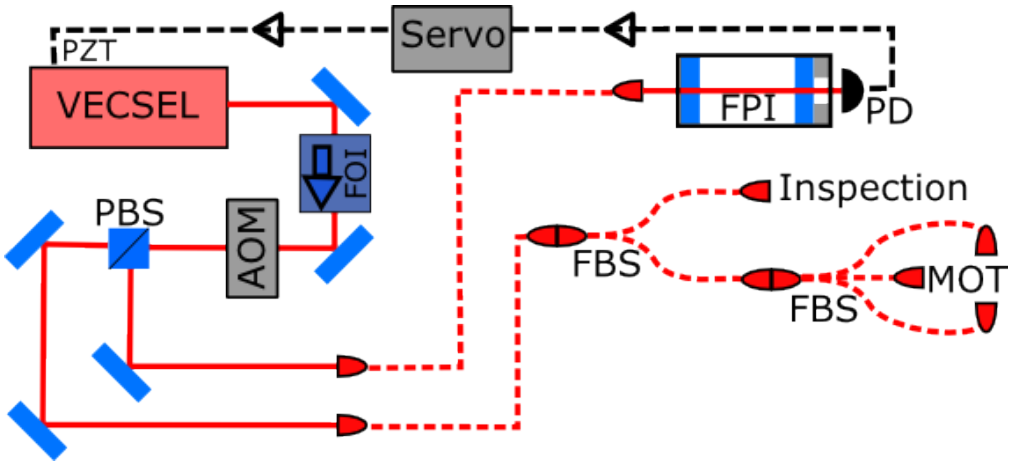

Figure 4.7: Diagram of a setup used for laser cooling with a VECSEL. FOI – Faraday optical isolator, AOM – acousto-optical modulator, FPI – Fabry-Pérot interferometer, PD – photodiode, MOT – magneto-optical trap, PBS – polarising beam splitter, FBS – fibre beam splitter, PZT – piezoelectric transducer. VECSEL is stabilised to a piezo tunable Fabry-Pérot interferometer with a servo electronics, using the side of the fringe locking method.

4.2.3 VECSEL linewidth

The linewidth of the VECSEL was measured by superimposing its beam with a reference laser beam, to obtain a beat note which was analysed with a spectrum analyser. A commercial ECDL diode laser was used as a reference laser. This was stabilised to a 10 cm long optical cavity, under vacuum, with a finesse of around 10000, and was described in detail in a paper by Nevsky et al. [59]. As described in the paper, the laser's linewidth is below 1 kHz, with a small linear drift of approximately 0.5 Hz/s, which makes the laser a good, stable reference. The frequency spectrum of the beat note is presented in figure 4.8a, with a triple Lorentzian function (red line) fitted to the measured data points (blue points). The full width at half maximum (FWHM) of the Lorentzian function fitted to the carrier is equal to 54 kHz. The spectrum also features two Lorentzian-shape sidebands, 500 kHz away from the carrier. The sidebands come from the locking bandwidth of the reference laser's electronics, which usually is around 500 kHz. It is believed that the linewidth of the VECSEL is limited by the locking method. The laser is stabilised to an external cavity with a finesse above 1000, which is placed in atmospheric pressure. In figure 4.8b, a recorded beat note frequency is presented (top), as well as the corresponding fractional Allan deviation (bottom). The peaks in the frequency plot correspond to the opening and closing of the doors in the laboratory where the FPI was located. Even with the doors kept closed, local pressure fluctuations, caused for instance by air currents, limited the value of the fractional Allan deviation to be higher than 2×10^{-10} (value calculated for the first 30 s from the top figure 4.8b), which corresponds to 87 kHz for the absolute Allan deviation. This value is

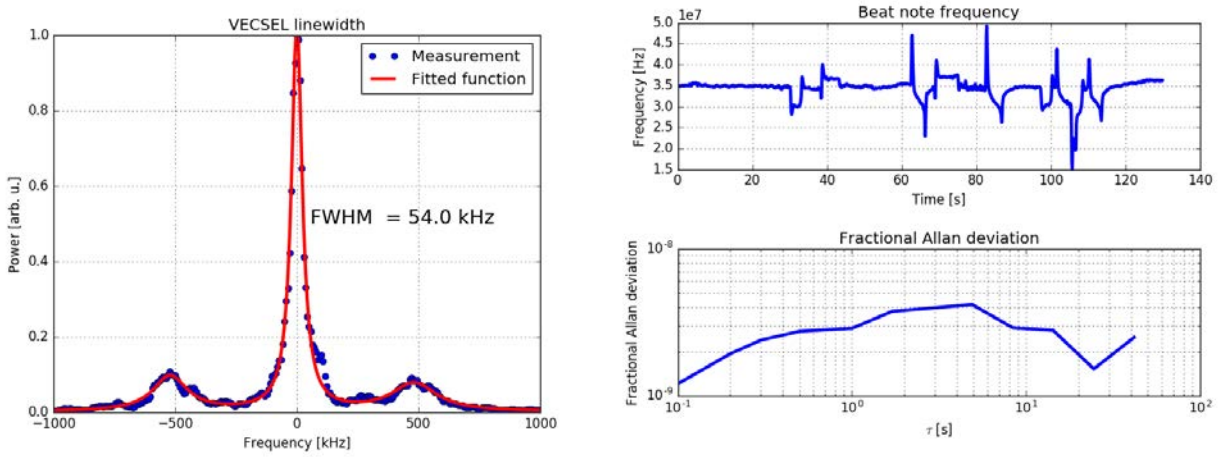

(a) (b)

Figure 4.8: **(a)** Frequency spectrum of a beat note measurement between the VECSEL and a commercial narrow-linewidth diode laser system. The residual bandwidth of the spectrum analyser was 30 kHz, and the sweep time was 2.274 ms across a 5 MHz span. The red line shows a triple Lorentzian function fitted to the blue data points. **(b)** Measured frequency of a beat note between the VECSEL and highly-stabilised commercial ECDL laser (top) and fractional Allan deviation of the frequency (bottom). Peaks in the frequency measurement correspond to the opening and closing of the door in the laboratory.

close to the value of the linewidth from figure 4.8a.

4.2.4 VECSEL for second-stage cooling

Although the measured linewidth is not good enough to obtain the lowest possible temperature of the MOT, it is sufficient for the initial second-stage broadband cooling. As shown previously in figure 4.7, light from the VECSEL is coupled into the fibre and guided to the atomic package. When switching the lasers between a commercial ECDL laser and the VECSEL, a fibre to fibre connector is used, to ensure the alignment of the beams inside the science chamber remains the same. The laser beam is evenly split into three MOT beams, and each beam is used to provide cooling in one of the three directions.

To make a second-stage red MOT with the VECSEL, initially, atoms needed to be trapped in a first-stage blue MOT. To do this, a 922 nm commercial diode laser, with a second harmonic generation at 461 nm, was used. After optimising the blue MOT, the sequence for the red MOT was optimised using a commercial diode laser operating at 689 nm. Once everything was optimised, the red cooling light was replaced with light from the VECSEL by just reconnecting the fibre.

A picture of a MOT obtained with the VECSEL is presented in figure 4.9a. To take this picture, a pulse of resonant 461 nm blue cooling light was used to fluoresce the cloud, as the red fluorescence is not strong

enough to be clearly visible on the camera. The Gaussian fit to the atomic cloud is shown in figure 4.10a and it gives the dimensions to be $4\sigma_h = 0.42$ mm and $4\sigma_v = 0.34$ mm. For comparison, pictures of magneto-optical traps obtained with the commercial ECDL laser are presented in figures 4.9b, 4.9c, and 4.9d. Fitted Gaussian functions to the pictures are presented in figures 4.10b, 4.10c, and 4.10d, respectively. Figures 4.9b and 4.10b show a cloud of strontium atoms in the optimised broadband frequency MOT, where the diameters of the cloud are approximately three times smaller, and equal to $4\sigma_h = 0.13$ mm and $4\sigma_v = 0.09$ mm. Figures 4.9c and 4.10c show a reduced broadband frequency MOT, where the cloud has diameters of $4\sigma_h = 0.06$ mm and $4\sigma_v = 0.05$ mm. Finally, figures 4.9d and 4.10d show the single frequency MOT, with cloud diameters of $4\sigma_h = 0.07$ mm and $4\sigma_v = 0.05$ mm. The number of atoms in the VECSEL MOT could be estimated from the fluorescence intensity of the cloud, and was found to be $\sim 1 \times 10^6$. For comparison, the estimated atom number obtained in a broadband second stage MOT with the commercial laser is $\sim 6 \times 10^6$.

The reason for the VECSEL MOT cloud being bigger than the commercial ECDL MOT clouds is the higher temperature of the strontium atoms. Due to the poor stabilisation of the VECSEL, it was unable to stay on atomic resonance for long enough, however, this can easily be improved in the next iterations of the VECSEL.

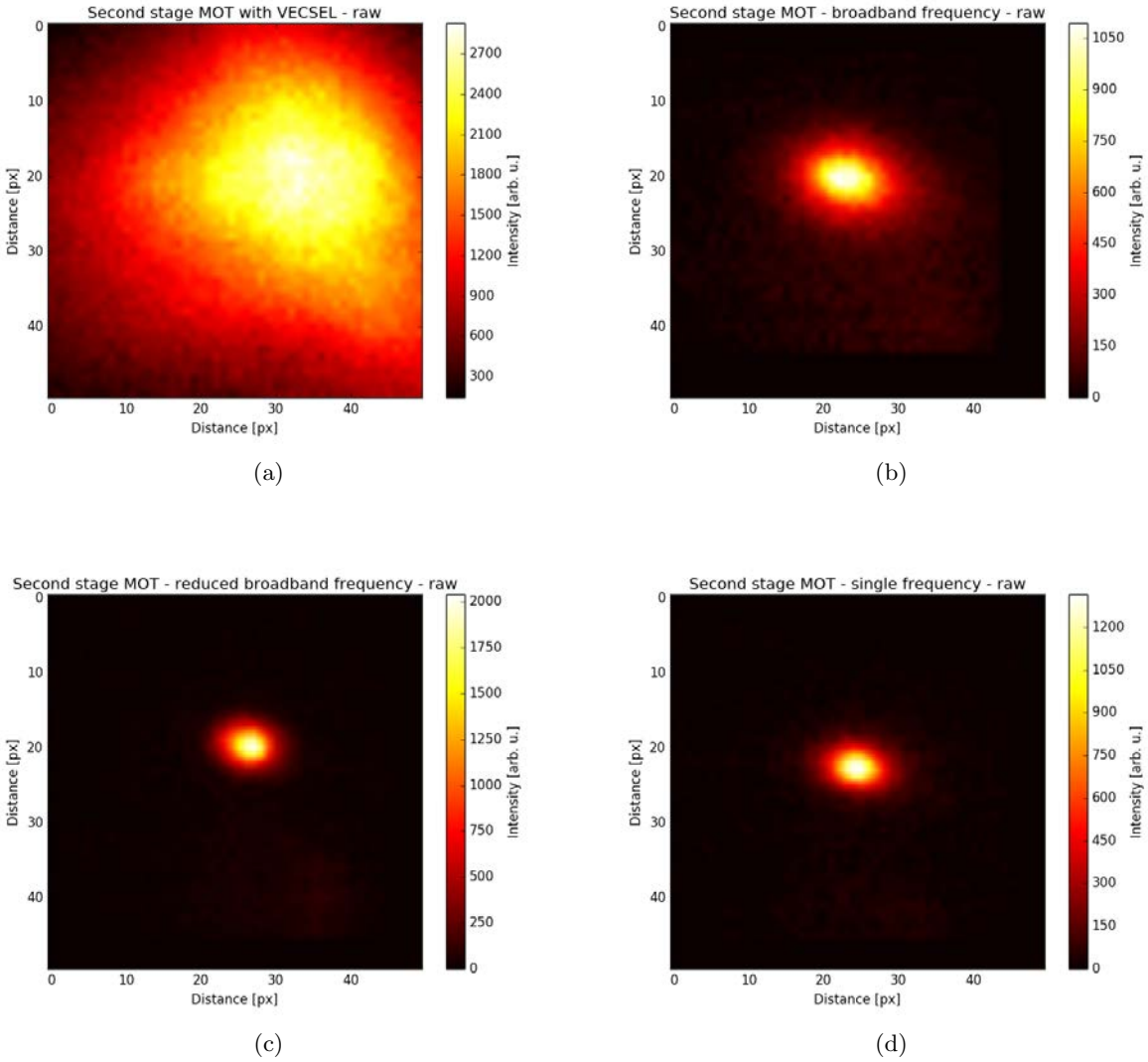

Figure 4.9: Fluorescence pictures of the second stage magneto-optical traps, obtained by probing the blue ${}^1S_0 - {}^1P_1$ transition after performing the cooling sequence. **(a)** Second stage MOT obtained with a VECSEL. The estimated number of atoms in the MOT is 1×10^6. **(b)** Second stage MOT obtained with a commercial ECDL laser. The optical frequency of the laser was artificially broadened to improve the transfer ratio from the first stage MOT. The estimated number of atoms in the MOT is 6×10^6. **(c)** Same as (b) but with decreased frequency broadening and power. **(d)** Same as (b) and (c) but without artificial broadening (single frequency). The estimated number of atoms in the MOT is 5×10^6.

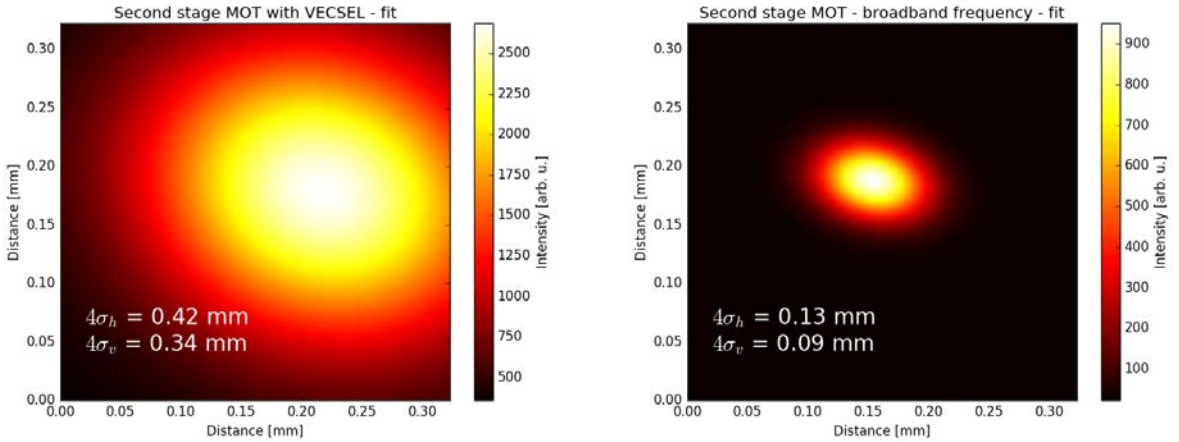

(a)

(b)

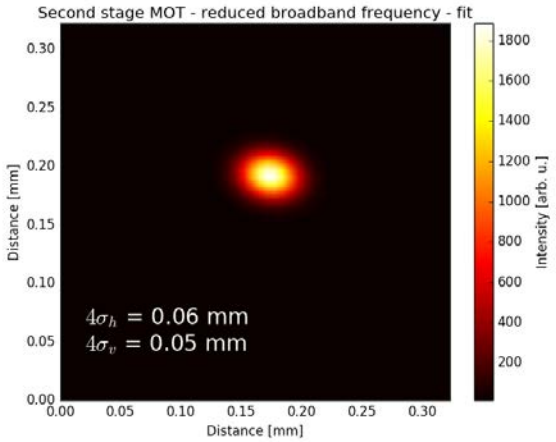

(c)

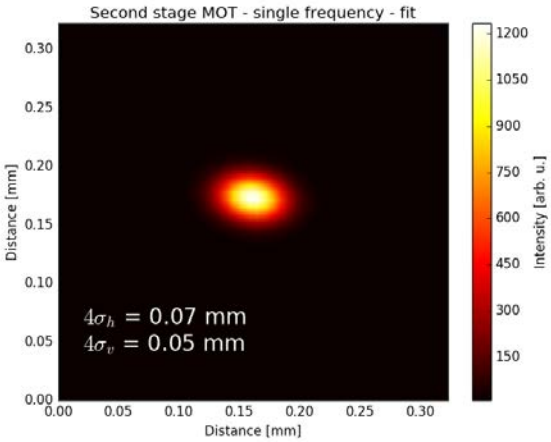

(d)

Figure 4.10: Fit to the fluorescence pictures of the second stage magneto-optical traps shown in figure 4.9. Each figure presents a 2-dimensional Gaussian function fitted to the raw data. **(a)** Second stage MOT obtained with a VECSEL. The horizontal and vertical diameters of the MOT, derived from the Gaussian fit, are equal to $4\sigma_h = 0.42$ mm and $4\sigma_v = 0.34$ mm, respectively. **(b)** Second stage MOT obtained with a commercial ECDL laser. The optical frequency of the laser was artificially broadened to improve the transfer ratio from the first stage MOT. **(c)** Same as (b) but with decreased frequency broadening and power. **(d)** Same as (b) and (c) but without artificial broadening (single frequency).

4.3 Frequency Stabilisation System

In pursuit of a transportable optical lattice clock, the construction of a mobile frequency stabilisation system (FSS) was necessary. This is used to stabilise multiple laser systems that are used in the strontium optical clock experiment. The main and most important part of the system is a reference cavity, which serves as a length standard and is used for referencing the wavelengths of the lasers. The FSS should be insensitive to any external factors like temperature or acceleration, while being relatively small, rigidly mounted and cost-effective at the same time.

4.3.1 Stability of a reference cavity

The standing wave inside a resonator of length L can only be formed by a wavelength, whose integer multiple is equal to double the length of the resonator $2L$. This condition can also be written as:

$$nL = N\frac{\lambda_{vac}}{2}, \tag{4.1}$$

where N is an integer called the longitudinal mode number, λ_{vac} is the wavelength in a vacuum, and n is the refractive index of the medium between the mirrors of the resonator, so that nL is the optical length of the resonator. Any variation in the optical length would change the value of the wavelength λ_{vac} that resonates, and therefore should be avoided. There are two main factors that can change the optical length: the temperature which changes the length of the spacer due to thermal expansion, and the refractive index, change in which can be caused, for example, by a change in air pressure.

Temperature

First, we consider the temperature fluctuations that would change the length of the spacer. Due to the thermal expansion, the length changes according to the following formula:

$$\frac{\mathrm{d}L}{\mathrm{d}T} = \alpha L, \tag{4.2}$$

where T stands for temperature and α is the coefficient of thermal expansion of the spacer. By differentiating equation 4.1 with respect to temperature, and by substituting in equation 4.2, we can derive a formula that

describes the change of the resonating wavelength, with a change in the temperature of the spacer:

$$\frac{\mathrm{d}\lambda_{vac}}{\mathrm{d}T} = 2\alpha\frac{nL}{N}. \tag{4.3}$$

Often, it is more convenient to use the optical frequency ν, instead of the wavelength. Knowing that $\lambda_{vac} = \frac{c_{vac}}{\nu}$, we can take its derivative with respect to temperature and substitute in equation 4.3. After a few transformations and simplifications, we obtain the following equation describing the deviation in the optical frequency, resulting from the deviation in the temperature of the spacer:

$$\frac{\mathrm{d}\nu}{\mathrm{d}T} = -\frac{1}{2}\alpha\frac{c_{vac}N}{nL}, \tag{4.4}$$

where c_{vac} is the speed of light in a vacuum. It is also useful to give a formula for the fractional wavelength temperature sensitivity:

$$\frac{\mathrm{d}\lambda}{\lambda} = \alpha\mathrm{d}T, \tag{4.5}$$

as well as the fractional frequency temperature sensitivity:

$$\frac{\mathrm{d}\nu}{\nu} = -\alpha\mathrm{d}T. \tag{4.6}$$

Interestingly, both fractional sensitivities, 4.5 and 4.6, are independent of the length of the resonator, the wavelength, and the refractive index. Moreover, we see that they closely follow the linear thermal expansion equation 4.2.

The best temperature controller, available in our laboratory, can stabilise the temperature to the 1 mK level in a 24 hour period. I will now analyse how three different materials would be affected by a temperature change of 1 mK. Let us consider a cavity, whose spacer is made of aluminium. The coefficient of thermal expansion of aluminium is 22.2×10^{-6} m/(m $\cdot$ K). Using equation 4.4, I can calculate that, for a 30 mm long spacer, it would result in a 9.65 MHz/mK sensitivity, if we consider the 38000^{th} longitudinal mode of the cavity, which corresponds roughly to a wavelength of 689 nm. Invar, with a CTE one order of magnitude lower than aluminium and equal to 1.5×10^{-6} m/(m$\cdot$K), gives us a sensitivity of 652 kHz/mK under the same conditions. The third material is ultra-low expansion (ULE) glass manufactured by Corning, with a mean coefficient of thermal expansion of $0 \pm 30 \times 10^{-9}$ m/(m $\cdot$ K) for temperatures between 5°C and 35°C. The calculated sensitivity for this material is 0 ± 13 kHz/mK. All of the above results are compared in table 4.1. It is clear that ULE is the best of all three, having the lowest value for the thermal sensitivity. If kept at the

Material	CTE [m/(m*K)]	T sensitivity (frac freq) [1/mK]	T sensitivity [kHz/mK]
Aluminium	22.2×10^{-6}	-2.2×10^{-8}	-9700 (@ 689 nm)
			-14000 (@ 461 nm)
Invar	1.5×10^{-6}	-1.5×10^{-9}	-650(@ 689 nm)
			-970 (@ 461 nm)
ULE	$0 \pm 30 \times 10^{-9}$	$0 \pm 30 \times 10^{-12}$	0 ± 13 (@ 689 nm)
			0 ± 19 (@ 461 nm)

Table 4.1: Comparison of different materials used for constructing an optical cavity. The temperature sensitivity is presented in fractional frequency units, as well as the temperature sensitivity for the red cooling transition wavelength (689 nm) and for the blue cooling transition wavelength (461 nm).

zero-crossing temperature, this material has a coefficient of thermal expansion close to zero, and therefore it is commonly used for the most demanding laser in the experiment, the clock laser. For the red cooling, we need a laser that would not drift away from the cooling transition. The linewidth of the cooling transition is approximately 7.5 kHz. From table 4.1, we see that the temperature sensitivity of the spacer made of ULE is the same order of magnitude as the transition's linewidth. If we stabilise the temperature of the cavity to the 1 mK level in a 24 hour period, in practice, it could mean that it would be necessary to correct the laser's frequency every day, which is acceptable. On the other hand, the linewidth of the transition used for the blue cooling has a linewidth of 32 MHz. This means that even the aluminium cavity would be good enough, if stabilised to the same 1 mK level. However, using the ULE material instead would lower the requirement of the temperature stabilisation down to the 0.1 K - 1 K level.

Air pressure

After analysing the temperature influence on the stability of the cavity and the stabilised lasers, we would like to see what the influence of the air pressure is, and whether it is necessary to keep the cavity under vacuum. Looking at equation 4.1

$$nL = N\frac{\lambda_{vac}}{2}, \tag{4.7}$$

we see that the resonance condition depends not only on the length of the resonator, but also on the refractive index of medium that fills the space between the mirrors, air in our case. The refractive index of air depends on many factors like humidity, air composition, temperature, but most significantly pressure, which is about a hundred times more influential, and relatively hard to control. The influence of atmospheric conditions on the refractive index of air was formulated by Edlén in [137] and updated by Birsch et al. in [138, 139].

The updated formula will be used to simulate how the optical frequency of the resonant mode changes with changing atmospheric pressure.

First, we would like to see how the air pressure changes in our laboratories. The pressure was recorded over a two month period in GGTop [140] laboratory (high-spec, without windows, with A/C), and for one month in iSense [141, 142] laboratory (low-spec, with windows, without A/C) by courtesy of Dr. Alexander Niggebaum. Both measurements were taken with a half hour acquisition rate. The data was compared with atmospheric pressure data, taken at the Birmingham international airport by the Met Office [143], and presented in figure 4.11. We see from the figure that the air pressure in the laboratories follows the pressure readings at the airport. Therefore, it is reasonable to use the data from the airport in our analysis due to it being a large dataset covering a few decades. Transforming equation 4.1, we obtain the optical frequency ν as a function of pressure P

$$\nu(P) = \frac{cN}{2L}\frac{1}{n(P)}. \tag{4.8}$$

Using this equation and the Edlén equations, we can calculate how the frequency of the cavity's resonant mode changes with atmospheric pressure. This is presented by the right axis in figure 4.11, as the refractive index in this pressure range can be approximated by a linear function. For the calculation, we have assumed a relative humidity of 50% and a temperature of 20°C.

We would like to consider two types of cavities: one with a vent hole, the other without the vent hole. The pressure inside the first cavity is well known, as it strictly follows the atmospheric pressure, while the pressure inside the second cavity is not as straightforward and we would like to analyse whether it stays constant. In my considerations, I assume that the cavities feature optically contacted mirrors, and the contacted mirrors were polished to reach a $\lambda/10$ flatness at $\lambda = 633$ nm. This means that the distance between the peak and valley of the flat surface is no greater than 63.3 nm, and therefore, the average distance between the two contacted surfaces is assumed to be around 60 nm. That space between the mirror and the spacer, although it is unnoticeable, may cause the air to leak from the inside to the outside, and vice versa. The flow of air caused by the difference in pressure inside and outside can be classified by using the Knudsen number [144]

$$\mathrm{Kn} = \lambda_{FMP}/d, \tag{4.9}$$

where λ_{FMP} is the mean free path of the particle, and d is the characteristic length of the physical system. The mean free path of an air particle in atmospheric pressure is around 68 nm. The Knudsen number calculated for the air flow between the mirror and the cavity is close to $\mathrm{Kn} = 1$. This value classifies

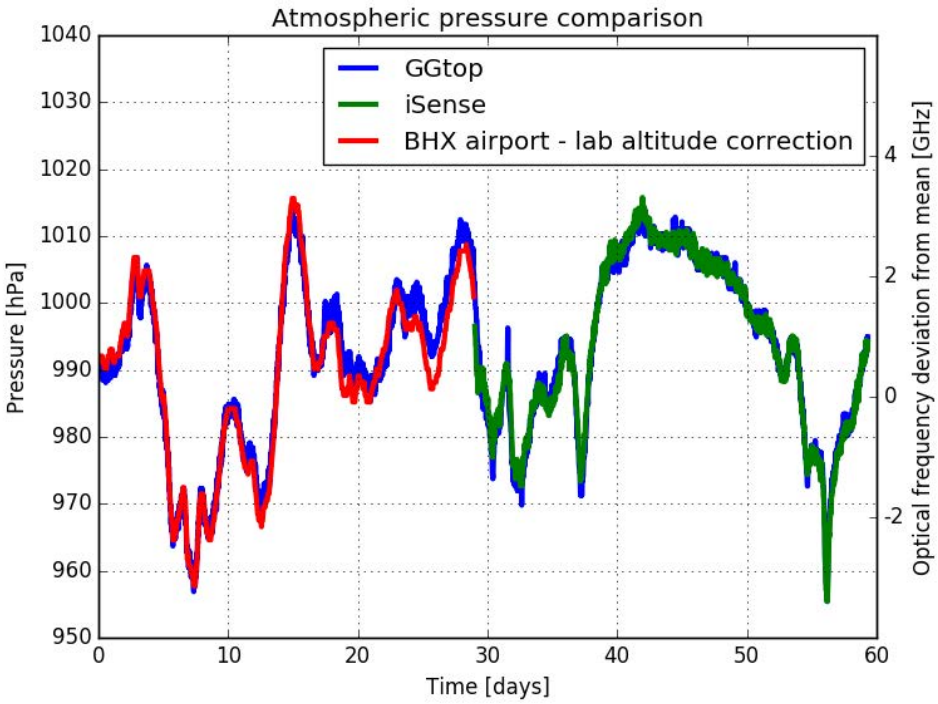

Figure 4.11: Atmospheric pressure measured at three different locations: the Birmingham International Airport (data taken by the Met Office [143]), GGtop laboratory, and iSense laboratory, both in the Quantum Hub, Metalurgy and Materials building of the University of Birmingham. The right vertical axis is the deviation of the simulated optical frequency from the mean value, caused by the pressure change inside a 30 mm long cavity operating at 689 nm.

the flow to be transitional according to Kandlikar [145], which means that the Navier-Stokes equations for the continuum flow are no longer valid and molecular flow should be considered, with the intermolecular collisions still playing a crucial role. Therefore, to simplify the problem, I will assume that the two surfaces are separated by an order of magnitude smaller distance, which lets us treat the flow as free molecular. I will show that even then, the distance is not small enough to keep the pressure inside the cavity invariable.

To simplify the problem, I will treat the space between the mirror and the spacer as a duct with a rectangular cross section, with the longer side equal to the circumference of the mirror. Following [144], the volumetric flow rate $\dot{Q}$ is proportional to the conductance of the duct C_m and the pressure difference

$$\dot{Q} = (P_{in} - P_{out})C_m, \tag{4.10}$$

where P_{in} and P_{out} is pressure on the inlet and outlet, respectively. Conductance of the duct can be expressed

as the entrance aperture conductance C_α multiplied by the transmission probability α.

$$C_m = C_\alpha \alpha. \tag{4.11}$$

The transmission probability can be calculated using an approximated formula from [144], for the transmission probability of a long duct of rectangular cross section

$$\alpha = \frac{16}{3\pi^{3/2}} \frac{a}{l} \ln\left(4\frac{b}{a} + \frac{3}{4}\frac{a}{b}\right), \tag{4.12}$$

where a, b, l are the height, width, and length of the duct, respectively. The calculated value of the probability in our example is 3.07×10^{-5}. The entrance aperture conductance C_α from equation 4.11 can be expressed by

$$C_\alpha = ab\sqrt{\frac{RT}{2\pi M_m}}, \tag{4.13}$$

where R is the universal gas constant, T is the absolute temperature, M_m is the molar mass or air. In our case it is equal to 2.8×10^{-8} $\frac{\mathrm{m}^3}{\mathrm{s}}$, making the duct conductance equal to 8.5×10^{-13} $\frac{\mathrm{m}^3}{\mathrm{s}}$.

By treating the air as an ideal gas, we can use the ideal gas equation $pV = nRT$, where p is the pressure, V is the volume, n is the number of moles of gas. Assuming the temperature stays constant, we can write

$$\dot{Q} = \frac{\mathrm{d}}{\mathrm{d}t}(pV) = RT\frac{\mathrm{d}n}{\mathrm{d}t}. \tag{4.14}$$

Using the ideal gas equation again, with the assumption that the volume and temperature inside the cavity does not change, we can write

$$\frac{P(t)}{n(t)} = \frac{P_0}{n_0}, \tag{4.15}$$

where P_0 and n_0 are pressure ($P_0 = P(t = 0)$) and number of moles ($n_0 = n(t = 0)$) at the beginning, respectively. By substituting $n(t)$ with the integrated formula 4.14, while assuming that the pressure at the inlet of the duct is equal to the atmospheric pressure $P_{in} = P_{atm}$, and the pressure at the outlet is equal to the cavity pressure $P(t) = P_{out}(t)$, we obtain

$$P(t) = \frac{P_0 - P_{atm}}{1 + RT/V_{cav}C_n t} + P_{atm}, \tag{4.16}$$

where V_{cav} is the volume of the cavity.

By analogy with electronic circuits, the small distance between the mirror and the spacer acts as a

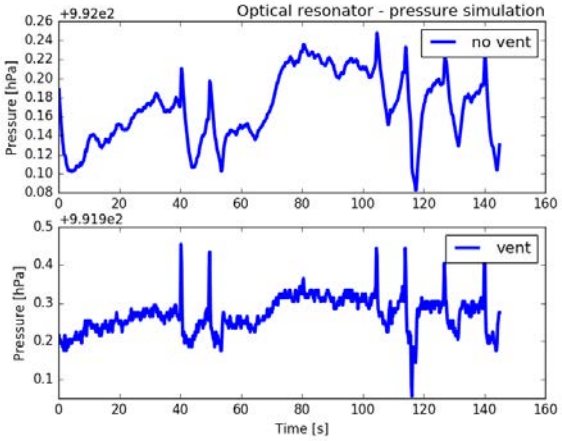

(a) Short-term measurement - spikes correspond to the opening and closing of the door

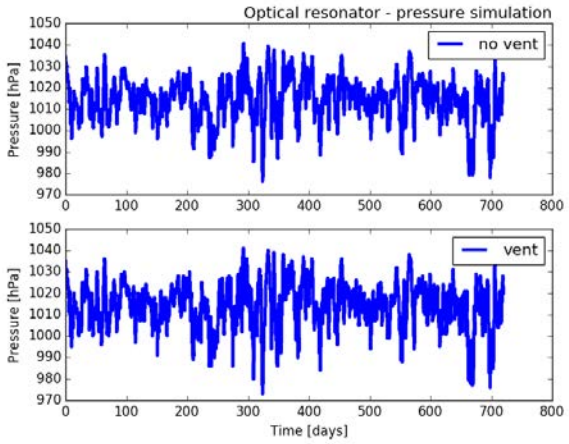

(b) Long-term pressure measurement

Figure 4.12: Simulation of the air pressure inside the cavity, with and without a venting hole. The vent hole plots (bottom) follow the ambient pressure. The pressure inside the cavity without the venting hole (upper) were simulated assuming a 30 mm long optical cavity with optically contacted mirrors, leaving a 6 nm spacing between the mirror and the spacer. The long-term data is based on the measurements taken by the Met Office [143].

resistor, while the volume of the cavity acts as a capacitor. Combining both elements results in a low-pass filter, where the cut-off frequency drops with a rise in resistance or volume. In the case of a 30 mm long cavity, 1 in outer diameter and 1/2 in inner diameter, the volume of the air inside is relatively small, and despite the high resistance of the mirrors, it will make the low-pass filter less effective in filtering the slowly changing atmospheric pressure fluctuations. In figure 4.12, a simulation of the air pressure inside the two types of cavities is presented, assuming an over-optimistic 6 nm space between the bonded mirror and the spacer. Figure 4.12a is based on a measurement inside the laboratory with a 4 Hz recording rate. Spikes in the figure, caused by the opening and closing of the door in the laboratory, are slightly damped, in the case of the cavity without the vent, but not completely. The long-term pressure behaviour is presented in figure 4.12b and it does not seem to differ for the two cavities. Based on the pressure data, we could simulate the resonant frequency change to calculate the fractional Allan deviation, which is presented in figure 4.13. In the same figure, the two vertical dashed lines represent the required instability levels for our blue and red cooling lasers. Levels were calculated by assuming that our lasers should not deviate from the atomic transition frequency by more than 1/10 of the natural linewidth of the transition. We see that both cavities have similar levels of instability, with the no-vent cavity being slightly better for lower interrogation times. Both cavities are on the edge of the required instability for the blue cooling laser, but only for short times.

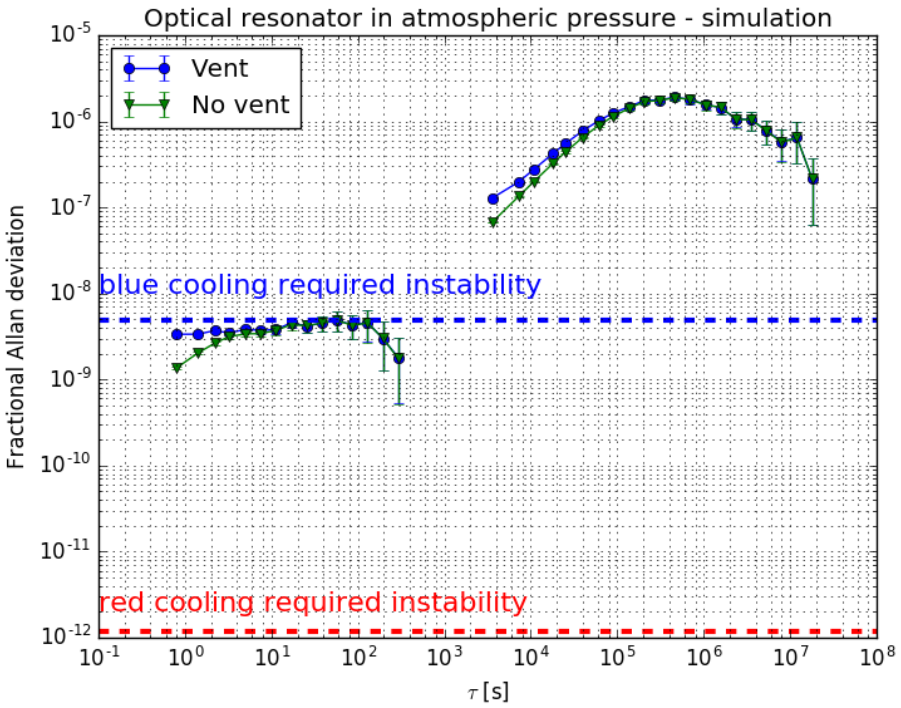

Figure 4.13: The fractional Allan deviation for the simulated frequency of the resonant mode of the cavity, based on the pressure data shown in figure 4.12. Vertical dashed lines represent the required instability levels for the blue and red cooling laser for strontium, assuming the laser should not deviate by more than 1/10 of the transition's natural linewidth.

In our experiment, we would like to stabilise both the blue cooling laser and the red cooling laser, using a small and portable reference cavity. One possibility is to use a cavity with a vent hole placed inside a vacuum chamber. This solution would ensure the independence of the refraction index from the air pressure, as long as the vacuum pressure level was kept at a relatively low and stable level (around 10^{-4} mbar). However, this solution also has the disadvantage of additional equipment like vacuum pumps being required, a rise in the power consumption by the experiment, and also the doubling of size in the case of small cavities. Another possibility is to further upgrade the no-vent cavity, by sealing the gap between the mirror and the spacer. The sealant should be carefully chosen, so as not to affect the thermal performance of the cavity. Therefore, it should either feature a small coefficient of thermal expansion, or be elastic. Here I propose using vacuum-grade grease (e.g. Apiezon L Grease); vacuum sealing wax (e.g. Apiezon Wax); silicone compound (e.g. Vacseal); or sodium silicate, which is also known as liquid glass, and commonly used for sealing and bonding. Using a sealant could not only provide a stable reference cavity, but would also make it easier to miniaturise, to make it a part of a compact mobile or space-compatible experiment. An alternative method

of obtaining a sealed optical bond might be using hydroxide-catalysis bonding method, described in more detail in [146].

4.3.2 Construction of a reference cavity

The reference cavity was designed to be relatively compact in comparison with some of the counter designs like the one presented by Nevsky et al. [59]. The spacer is of a cylindrical shape, 30 mm long and 1 inch diameter. It is made of ultra-low expansion (ULE) glass, which ensures low temperature fluctuations in the length of the cavity. Each end of the spacer is polished to provide a flat surface with a flatness below $\lambda/10$, and a parallelism of the two surfaces below 30 arc seconds.

The cavities' mirrors are made with 1/2 inch diameter fused silica substrates. One mirror is flat, while the other mirror is concave with a 0.5 m radius of curvature. The concave mirror features a flat ring on the edge of the concave side to make optical contact bonding possible. The reflective coating of the mirrors was custom designed, to support all the optical frequencies used in the strontium optical clock:

- 99.97% @ 689 nm;
- 99.7% @ 461 nm, 814 nm and 922 nm;
- $>$ 99.97% @ 698 nm;
- $>$ 99.95% @ 679 nm and 707 nm.

Each mirror also has anti-reflection coatings, on the opposite side, covering the same range of wavelengths.

The cavity was constructed by attaching the mirrors on each end of the spacer, by optical contact bonding. To do this, each surface of the spacer and the mirror was precisely cleaned with ultra-pure acetone and then joined together. Thanks to this technique, there is no need to use any glue, which would significantly affect the mean value of the coefficient of thermal expansion. The whole procedure was performed in a clean room, under a laminar flow hood, to avoid contaminating the surfaces. In figure 4.14, two identical optical cavities, with optically contact bonded mirrors are presented.

Cost-effectiveness of the cavity

The main goal of our new cavity was not only to reduce the size, but also to make it relatively cheap to produce. For a 30 mm long cavity, material price is not a problem, but precise machining and preparation may drive up the price. I have considered a spacer, which should be made of either ULE or Zerodur, to

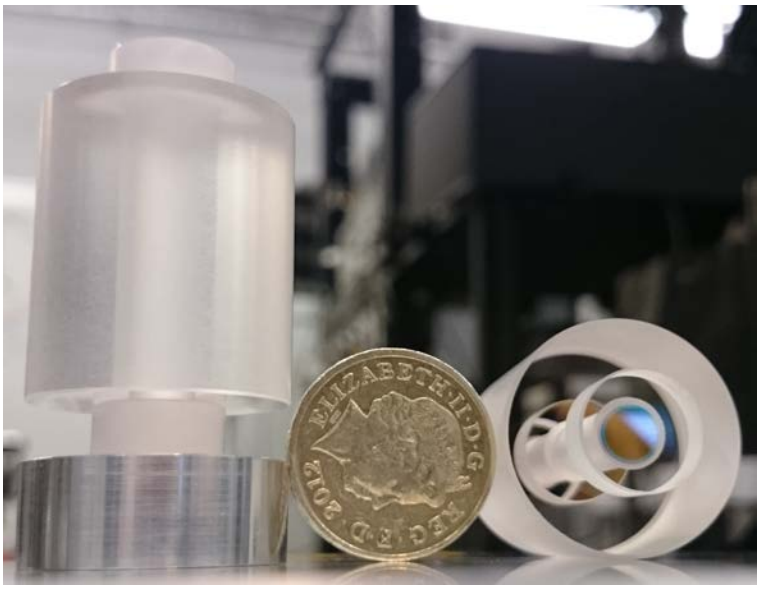

Figure 4.14: Reference cavities next to a pound coin.

have a low temperature sensitivity. I have asked three different companies for a quotation for ten pieces of 30 mm long spacer, with two parallel faces polished to obtain a $\lambda/10$ flatness. Through consultation with the companies, it was decided that the cavity should be of a cylindrical shape to minimise the costs. The three companies gave us quotations with huge price discrepancies:

- Company A: £872/pc,
- Company B: £3500/pc,
- Company C: £230/pc.

The difference in price comes from the different manufacturing processes and profiles of the company. The most expensive, company B, is a company producing components for the aerospace industry, which requires extreme precision and accuracy, meaning they would have to spend many work-hours on each spacer, driving the price high. Company A manufactures such a spacer by machining a long 1 in diameter rod, cutting it into 30 mm pieces, drilling each piece, and then polishing them together. This way, the material is not wasted and the amount of machining is minimised, but still it requires many work-hours. Company C has the most effective manufacturing process. It starts from a 30 mm thick plate of ULE material and does the polishing first. Then, the holes are drilled, and every piece is cut away with a milling machine. This approach requires greater care not to destroy the polished faces, but allows to obtain a very cost-effective way of producing the spacers.

The mirrors for the cavity are produced from fused silica, which has proven to be a good material for ultra-stable clock laser cavities, while being relatively cheap. The best dielectric coating method is ion-beam sputtering, which gives the lowest losses and should be used for ultra-high finesse mirrors. In our case, the largest finesse that we need to obtain is 10000, and therefore, it is enough to use a magnetron sputtering method, which is cheaper. In the case of ultra-stable clock cavities, it is also common to coat only the inner part of the mirror, leaving an uncoated edge for the optical contact bonding. Again, such a selective coating would increase the price of the cavity and is not necessary for our application, as the coated surface can also be optically contact bonded if flat enough.

By compromising and avoiding overkill in the components' quality, I was able to produce a portable reference cavity, with a material cost as low as £673/pc. The cavity may further lower the cost of the whole setup if it is proven that the vacuum is not necessary to obtain the required stability. For comparison, the price of an ultra-stable optical cavity, with a fancy geometry, can be up to £10000. If we had chosen company B to produce a spacer, and took the IBS coated mirrors, the price could reach £5000 per piece.

Free spectral range measurement

The spacer is specified to be 30.00 ± 0.02 mm long, which would correspond to a free spectral range of 4.996 ± 0.004 GHz. Since the mirrors are optical contact bonded to the spacer, we will assume that the distance between the flat mirror and the surface of the spacer is 0 ± 60 nm. One of the mirrors is concave with a 500 ± 2.5 mm radius of curvature, which makes the central point, on the concave surface of the mirror, to be 0.0068 ± 0.0005 mm away from the spacer. The distance between the central points of the mirrors should therefore be 30.01 ± 0.02 mm, making the free spectral range slightly smaller 4.993 ± 0.004 GHz.

Once the cavity is built, it is possible to measure the free spectral range to see whether it meets the expected value. For this, I used two lasers, one operating at around 689 nm, and the other around 698 nm. The cavity is temperature stabilised to around 20°C. First, I locked the 689 nm laser to the fundamental mode of the cavity using one of the laser outputs, while measuring the optical frequency of the laser on another output, using a Bristol Instruments wavelength meter model 671A, which was continuously calibrated with an internal HeNe laser, and can measure the optical frequency with 60 MHz absolute accuracy. The resonance of the cavity was read as $\nu_i = 434969.12 \pm 0.06$ GHz, which corresponds to the $N = i$ longitudinal mode of the cavity. By tuning the laser, I could find another mode at $\nu_{i-3} = 434954.19 \pm 0.06$ GHz, corresponding to the $N = (i-3)$ mode. Next, I modulated an output of the ultra-stable 698 nm laser, with an Electro-Optical Modulator, and coupled it into the cavity. The EOM generates a sideband in the frequency domain, which

can be simply tuned to reach the resonant frequency of the cavity. Again, I measured the optical frequency, with a wavelength meter, to be $\nu_j = 429229.97 \pm 0.06$ GHz, which corresponds to the $N = j$ longitudinal mode of the cavity. Knowing that $\frac{2nL}{c} = \frac{N}{\nu}$, I would like to find i and j, such that they satisfy the condition

$$\frac{\nu}{N} = \frac{\nu_i}{i} = \frac{\nu_{i-3}}{i-3} = \frac{\nu_j}{j}. \tag{4.17}$$

A script was written to find i and j, for which

$$\sqrt{(\frac{\nu_i}{i} - \frac{\nu_{i-3}}{i-3})^2 + (\frac{\nu_i}{i} - \frac{\nu_j}{j})^2 + (\frac{\nu_{i-3}}{i-3} - \frac{\nu_j}{j})^2} \tag{4.18}$$

is the smallest. Although many solutions have been found, only one of them lay within the estimated cavity length of 30.01 ± 0.02 mm. The obtained values are $i = 87158$ and $j = 86008$, giving the length of the cavity to be

$$L = 30.0274 \pm 0.0004 \text{ mm}. \tag{4.19}$$

The free spectral range of the cavity is therefore equal to

$$FSR = 4.99058 \pm 0.00006 \text{ GHz}. \tag{4.20}$$

The obtained value for the free spectral range will be used in the next subsection for calculating the finesse of the cavity.

Finesse measurement

To assess whether the target reflectivity of the mirrors was achieved, I performed a measurement of the finesse. Since the cavity's finesse is expected to be between 1000 and 10000 for different wavelengths, measuring the finesse by ring-down spectroscopy is relatively difficult, as it is a very short time effect and would require a very fast photodiode. An alternative is measuring the linewidth of the cavity. To do this, it is necessary to have a laser with a linedwidth either much smaller than the cavity's linewidth or comparable but accurate and well known.

Linewidth measurement at 698 nm

The spectroscopy of the cavity at 698 nm was relatively easy to perform, as this is the wavelength of the clock laser, which has a very narrow linewidth below 1 kHz, much smaller than the expected linewidth of

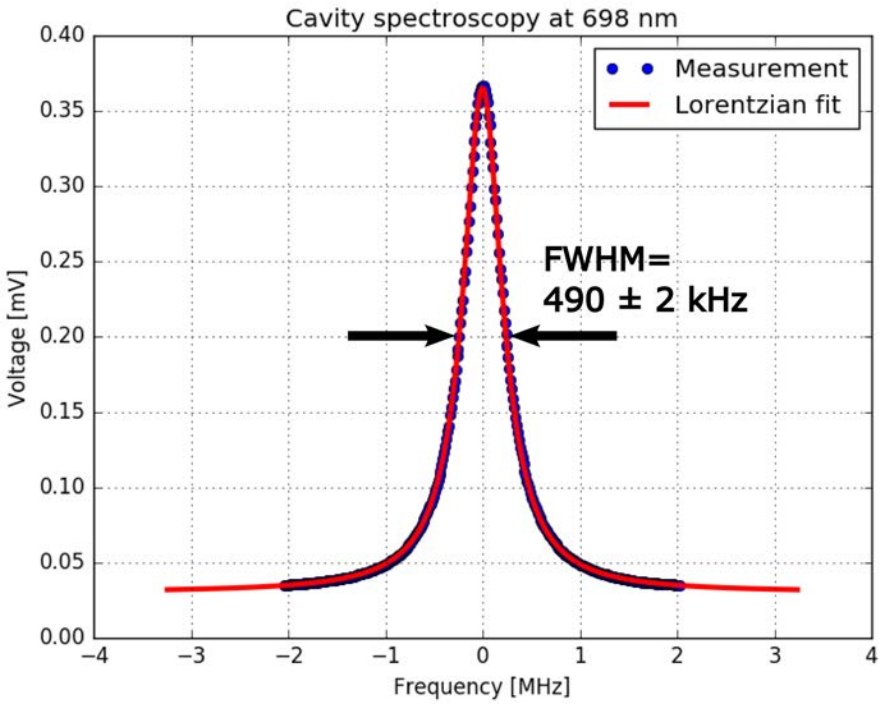

Figure 4.15: Linewidth of the reference cavity at 698 nm. The blue points are the measured data points. The red curve is a Lorentzian fit.

the cavity. For the measurement, the clock laser remained locked to the clock cavity. The fibre-coupled output of the laser was modulated with an electro-optical modulator (EOM) to generate sidebands. One of the sidebands was then used to scan through the resonance of the cavity, while the photodiode measured the intensity of the transmitted light. The transmission signal is presented in figure 4.15. The frequency sweep was performed with a function generator referenced to a GPS disciplined rubidium standard. The sweep took 500 steps across a 6 MHz span with a step time of 0.01 s. The signal from the photodiode was recorded with an oscilloscope, and each of the 500 steps was averaged over the step time to get a set of points, to which a Lorentzian curve was fitted. From the fitting parameters, it was possible to determine the full width at half maximum (FWHM) of the fitted Lorentzian to be 490 ± 2 kHz. The fit was performed with the least-squares method, where the standard deviation of each point from the averaging was used as a weight for the fitting.

To calculate the finesse $\mathcal{F}$ of the cavity, we use the following relation

$$\mathcal{F} = \frac{FSR}{\delta\nu}, \tag{4.21}$$

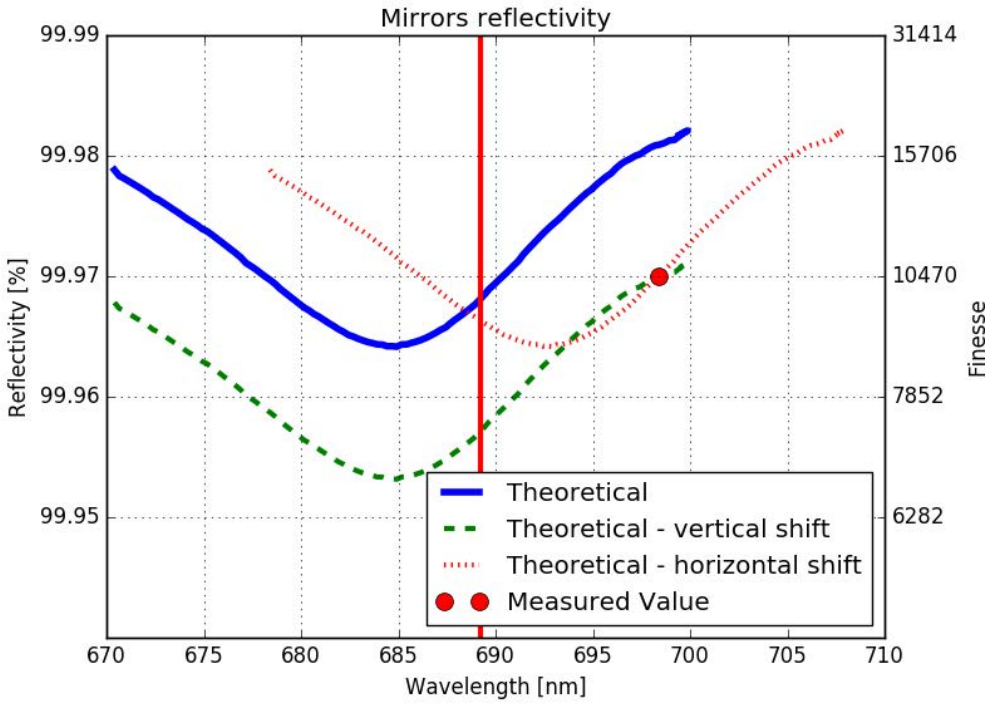

Figure 4.16: Reflectivity and corresponding finesse of the mirrors for the 'red' wavelengths. The blue solid line is the targeted reflectivity curve of the design (reflection calculated from a refined theoretical design by Layertec GmbH). The red point is the measured value of the reflectivity at the wavelength of the clock laser (698.4 nm). The dashed green line is the corrected reflectivity curve assuming additional constant losses, lowering the whole spectrum. The fine-dashed red curve is the corrected reflectivity curve assuming a spectral shift due to manufacturing tolerances. The solid red vertical line represents the wavelength of the red cooling laser (689 nm).

where $\mathcal{F}$ is the finesse and $\delta\nu$ is the cavity's resonance linewidth [92]. The finesse value at 698 nm is equal to

$$\mathcal{F}_{698nm} = 10190 \pm 50. \tag{4.22}$$

The reflectivity of the mirrors is calculated according to the transformed equation 2.12 in the following form

$$R = 1 + 2\sin^2\left(\frac{\pi}{2\mathcal{F}}\right) - \sqrt{(\sin^2\left(\frac{\pi}{2\mathcal{F}}\right) + 1)^2 - 1}, \tag{4.23}$$

to get a value of $R = 99.9692 \pm 0.0002\%$.

Finesse at 689 nm

The measurement of the finesse at 689 nm would be more difficult due to the large linewidth of the used laser compared with the linewidth of the cavity. To assess the finesse at this wavelength, I used the targeted reflectivity curve of the design, that was calculated by Layertec GmbH, who designed and manufactured the mirror coatings. The curve is presented in the figure 4.16 with a solid blue line. By performing the measurement of the linewidth at 698 nm, as described in subsection 4.3.2, we could derive the reflectivity of the mirrors at that wavelength, which is presented in the figure 4.16 with a red point. It is clearly seen that the measured reflectivity value at 698 nm is lower than the targeted reflectivity, and therefore the whole curve must have shifted as well. There are two possibilities for this. First, our mirrors might not be clean enough, and therefore have additional losses from scattering or absorption. This would affect the reflectivity by shifting the curve down, and lowering it by roughly 0.01% from its targeted values. For 689 nm, it would mean a shift from the target of 99.97% to 99.96%. The second possibility is that, due to the tolerances used in the manufacturing process, the curve has shifted spectrally in the horizontal direction. Then, the targeted value of the reflectivity for 690 nm corresponds to the measured reflectivity value at 698 nm. With the spectral shift equal to 8 nm, the reflectivity at 689 nm would still stay close to 99.97%. Although the finesse at 689 nm cannot be precisely determined, we can estimate its value to be between 7000 and 10000.

4.3.3 Cavity housing

Thermal shielding

The reference cavity was constructed to be relatively small, and to be part of a mobile experiment. This requires a rigid mounting that could withstand variable acceleration in all directions. On the other hand, it is important to keep the temperature as stable as possible, to reach a stability at the 1 mK level or better. To reach these two requirements, the cavity's rigid housing was designed to act as a thermal shield as well. For this reason, it features multilayer passive shielding that is well used in ultra-stable clock lasers.

The cross section of the full housing assembly is shown in figure 4.17. First, the cavity is mounted inside an inner cylindrical shell, made of aluminium, using four 4 mm diameter soda-lime glass beads symmetrically distributed on the bottom, and two viton balls on the top. Each ball is constrained by an approximately 3.5 mm diameter hole, inside the aluminium can. The viton balls are used to push on the cavity so that it cannot move, while the glass spheres provide thermally resistant single-point support, and are rigid enough to ensure that the optical axis of the cavity stays in place. The inner can is then mounted using the same

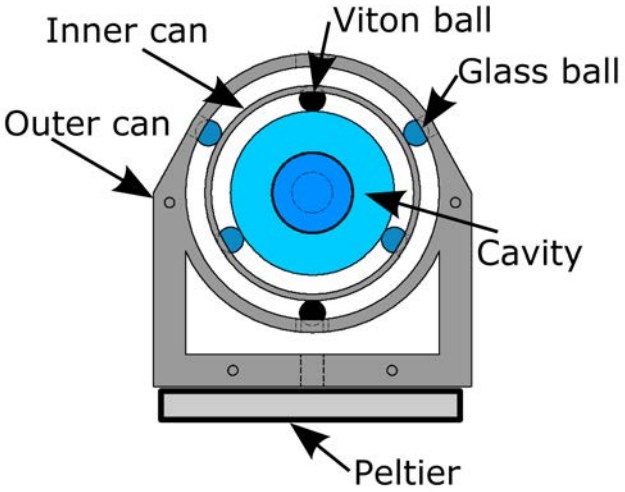

Figure 4.17: Design of the housing for the mobile cavity. The outer can is made of monolithic piece of aluminium, which is temperature stabilised with a Peltier element. The inner can is also made of aluminium and is mounted inside the outer can with symmetrically distributed beads, which provides low thermal contact between the layers. One of the bead is made of viton to provide elasticity and radial force holding the can inside. The same mounting method is used to hold the optical cavity inside the inner can.

method inside an outer thermal shield, except for the balls positions which are rotated 180° around the optical axis. Not only does this maximise the thermal distance between the outer shield and the cavity, but also makes it symmetrical, to distribute the heat evenly. The temperature of the outer can is stabilised with a thermo-electric cooler (TEC) element that is placed on the bottom of the can. The outer can's cross section shape is a combination of the O-shape profile and U-shape profile, and it is made of a monolithic piece of aluminium to provide a better thermal conductivity and homogeneity. The advantage of the O-shape profile is that it fits the cavity better, making the distance between the cavity and the shield the same at any point. The disadvantage of the O-shape profile is the lack of a flat surface that could be used for attaching a TEC module. Combining it with the U-shape profile solves this problem. Each can is closed with a lid at the front, while the rear side is a part of the monolithic body. The whole housing assembly is also constructed to be vacuum-compatible. This means that all the materials are suitable to be placed under vacuum with little outgassing, and was designed to avoid trapped air pockets that could cause virtual leaks.

Vacuum system

If necessary, the cavity might be put inside a vacuum chamber, to improve its thermal stability and avoid the fluctuations in the refractive index of air. Vacuum system is planned to be built in the very near future.

Figure 4.18: Ion pump with an attached compression valve. The ion pump controller is visible in the background, showing the pressure in units of mbar.

Low-cost disposable compression pinch valve

The biggest advantage of our cavity is its compactness. Adding a vacuum chamber to the design brings the necessity of using extra components like a vacuum valve, used for evacuating air from the chamber, which is very big in comparison with the rest of the setup. To keep the stabilisation system small, a low-cost compression valve was developed. It is made of a homogeneous piece of oxygen-free cooper, in the shape of a straight pipe, with two DN16CF flanges on each end. In contrast to the stainless steel flanges, the copper flanges cannot have a knife-edge for sealing, as the copper is too soft. Instead, the flange features an annulus shaped ridge, that acts like a copper gasket, which is used to seal two flanges together. Since the compression valve was designed to be disposable, the lack of the removable gasket does not bring any disadvantage to the system.

To close the valve, first a pliers wrench is used to flatten the copper tube until the thickness is small enough to use a bolt cutter. With a bolt cutter, it is possible to apply a very large pressure on the tube, causing the copper to seal itself. It is advised to perform a three-step compression on the flattened part. First, to seal one side of the tube (vacuum chamber), second, to seal another side of the tube (turbo pump), and then, to finish with a cut in-between to separate the two parts. A traditional valve is suggested to be mounted on the turbo pump side, which could be closed before the compression sealing process. This will

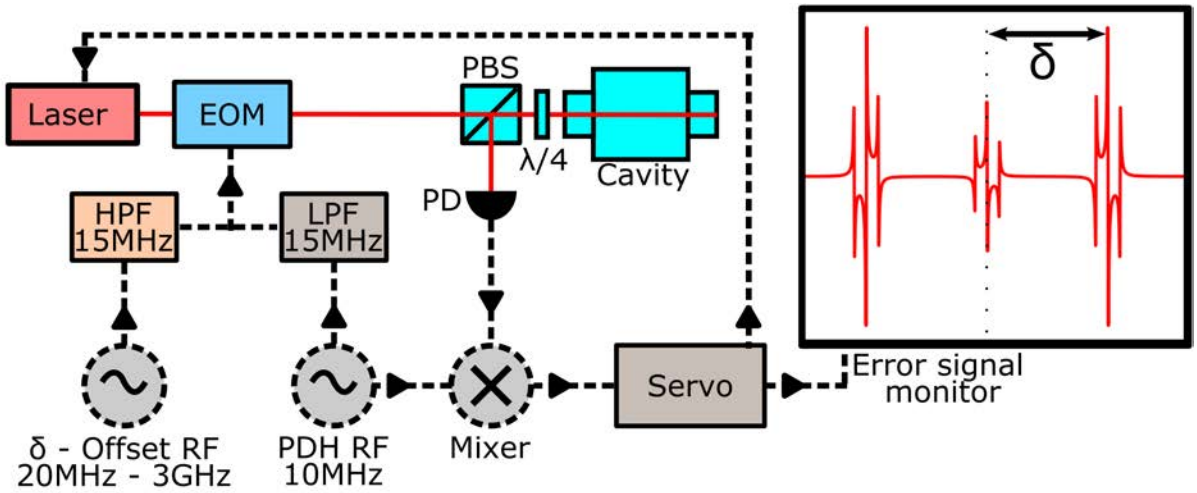

Figure 4.19: Diagram presenting realisation of a dual-sideband locking method. Offset radio frequency (RF) signal δ from the function generator is combined with the Pound-Drever-Hall (PDH) radio frequency signal with a tee and sent to an electro-optic modulator (EOM). To isolate the two frequency generators, a low-pass filter (LPF) and high-pass filter (HPF) are used before the tee. The EOM phase-modulates the laser light, which then passes through a polarising beam splitter (PBS), quarter-wave plate ($\lambda/4$) to be coupled into the optical cavity. The cavity reflected beam is diverged to hit a fast photo diode (PD). Signal from the photo diode is demodulated with PDH radio frequency signal using a mixer to obtain an error signal. The error signal is then amplified by a servo controller and used to stabilise the laser.

protect the turbo pump from any abrupt leaks that can occur during the pinching process. A successfully compressed valve is presented in figure 4.18. It was tested with a pressure level of 4×10^{-9} mbar, which is more than good enough for the reference cavities, and we believe that the valve can also be used for ultra-high vacuum (UHV) systems, if baked before the compression.

The valve is very easy to manufacture, and costs a few tens of pounds if done by our mechanical workshop. It can be done in any size, both DN16CF or DN32CF, with the pipe diameter being limited by the cutting capacity of the bolt cutter. The equipment used for compressing the valve costs less than £150 making it affordable for every laboratory.

4.3.4 Laser stabilisation method

Dual-sideband locking

Cavity miniaturisation brings the disadvantage of a rising free spectral range with a decrease in the cavity's length. It is common in various experiments for the lasers to be locked to a fundamental mode of the optical resonator, while the laser beam frequency is tuned with a double-pass acousto-optical modulator (AOM) to reach a desired frequency (e.g. atomic transition frequency). On one hand, using an AOM is an efficient

solution for low frequencies, below a few hundred MHz. On the other hand, the AOM usually has a small radio frequency bandwidth, which limits the tuning range of the AOM. For our 30 mm long cavity, the free spectral range is equal to 5 GHz. This means that in the most pessimistic scenario, we would have to have a 1.25 GHz AOM in a double-pass configuration which, if it exists, would be extremely inefficient.

An alternative to using a double-pass AOM is a dual-sideband locking method. It uses a high bandwidth electro-optical modulator (EOM) to generate offset sidebands in the frequency domain, and another EOM to generate locking sidebands on each offset sideband. This method utilises the high RF bandwidth of a fibre-based EOM reaching even a few GHz. In figure 4.19, a diagram of the locking scheme is presented. In practice, it is the same as Pound-Drever-Hall method described in [147] except for an extra function generator generating the offset radio frequency δ. This frequency is combined with the Pound-Drever-Hall RF using a tee. Low-pass and high-pass filters are additionally used to avoid interference between the two frequency generators. This lets us use only one EOM instead of two. An error signal is generated by mixing the PDH RF with the signal from the photo diode. The shape of the obtained error signal is also presented in figure 4.19. It is possible to stabilise our laser to either of the offset sidebands, and by changing the offset RF frequency, we can change the frequency of the laser over a wide range of a couple of GHz.

Instead of changing the frequency of the laser beam, it is possible to change the cavity length by changing the temperature, or mechanically applying a force on the spacer to cause its deformation of the spacer. However, those shifts all the resonance lines, so they can be used only when one laser is in use. Thanks to the dual-sideband method, we can lock many lasers at the same time, and easily tune them without any mechanical interference.

Multi-frequency locking

Another challenge is whether it is possible to use one cavity, with strontium-selective broadband mirrors, to stabilise all the lasers:

- 461 nm - blue cooling laser,
- 679 nm - repump I laser,
- 689 nm - red cooling laser,
- 707 nm - repump II laser,
- 813 nm - optical lattice laser.

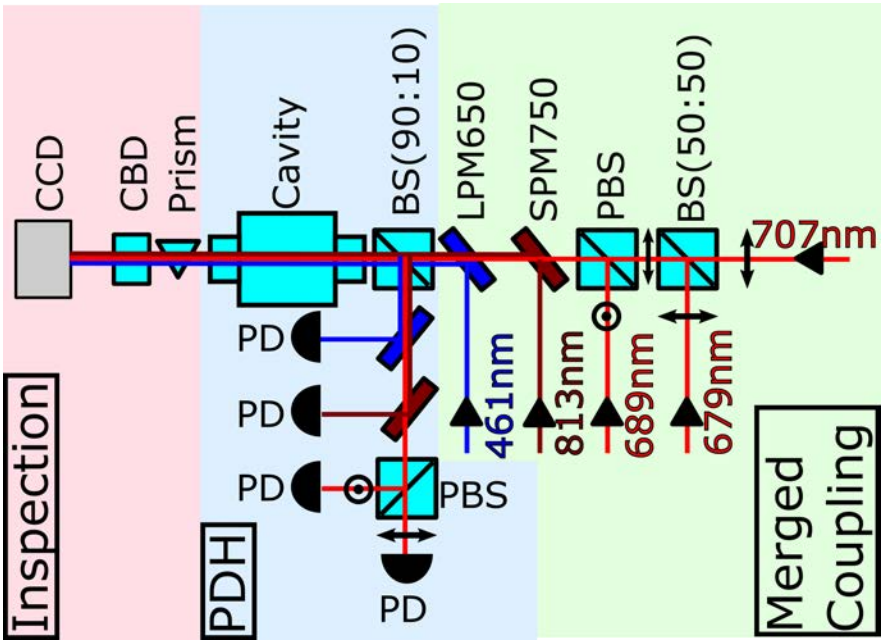

Figure 4.20: Scheme of frequency stabilisation system. Merged coupling is responsible for combining the beams and coupling them into the cavity. The blue 461 nm beam is merged using a long-pass mirror (LPM650). The lattice 813 nm laser is merged using a short-pass mirror (SPM750).The repump lasers are combined using the same polarisation with a non-polarising beam splitter (BS(50:50)), with a 50:50 reflection:transmission ratio. The red cooling laser 689 nm, having an orthogonal polarisation to the repump lasers, can be combined using a polarising beam splitter (PBS). The Pound-Drever-Hall (PDH) part is used to separate the beams reflected back from the cavity, to use them for the Pound-Drever-Hall locking of every individual laser. A non-polarising beam splitter with 90:10 reflection:transmission ratio (BS(90:10)) is used to diverge the cavity reflected beam to detect it with a photo diode (PD). The cavity transmission beams enter the inspection part, where a dispersive prism separates them, causing them to hit a different point on a CCD (charge-coupled device) camera. A calcite beam displacer (CBD) is used to separate the repump lasers from the red cooling laser using polarisation. A CCD camera is used to inspect the quality of the cavity's modes.

To use a single cavity, it is necessary to find a way of combining all of those wavelengths into one beam that would be coupled into the cavity. It is also important for the Pound-Drever-Hall (PDH) stabilisation method to distinguish between the reflected beams. In figure 4.20, the planned scheme for locking the lasers using one cavity is presented. The green-background region is responsible for merging the beams together and coupling them into the cavity. The blue cooling laser (461 nm) is relatively easy to merge with the other beams, for example, by using a long-pass dichroic mirror (LPM650) with a cut-off wavelength of 650 nm, which reflects blue 461 nm and transmits wavelengths above 650 nm. For merging the lattice laser (813 nm), we use the same method, but with a short-pass dichroic mirror (SPM750) with a cut-off wavelength of 750 nm instead. This reflects 813 nm beam while transmitting wavelengths below 750 nm. Combining the red lasers (679 nm, 689 nm, 707 nm) into one beam is more difficult because their wavelengths are very close

to each other. The red cooling laser (689 nm) can be combined with the repump lasers by using two linear orthogonal polarisations and a polarising beam splitter (PBS). The two repump lasers are less important and can be merged with a non-polarising beam splitter (BS(50:50)), having the same polarisation. In the Pound-Drever-Hall locking method, it is necessary to diverge the cavity reflected beam from the incident beam. Usually, an optical Faraday isolator or a quarter wave plate, with a polarising beam splitter, is used to separate the reflected beam, but then it would not be possible to use it with many wavelengths and polarisations. As shown in figure 4.20, in the blue background, we use a non-polarising beam splitter with 90:10 reflection:transmission ratio (BS(90:10)) instead, which allows to diverge the reflected light, to split it back with long-pass/short-pass mirrors and PBS, onto fast photo diodes (PD) for Pound-Drever-Hall locking. To distinguish between the two repump lasers sharing the same polarisation, it is possible to use a different PDH modulation frequency for each laser beam, and use radio-frequency (RF) high-pass and low-pass filters to separate the PDH photo diode signals before demodulation. In the red background in figure 4.20, the cavity transmitted beam is inspected with a CCD camera to see whether the lasers are locked to the right mode of the cavity. A dispersive prism is used to separate the overlapped laser beams, to hit different parts of the CCD camera. A calcite beam displacer (CBD) is used to additionally split the red lasers, using their polarisation.

Locking many lasers using one resonator brings the advantages of saving space, using less equipment, as well as having the same reference for all the lasers. The knowledge on any long-term drift detected in one of the lasers can be used to apply correction to all the lasers simultaneously. The system can be small, and it is possible to use integrated optics and fibre integrated components to miniaturise it even more. A disadvantage of the system is that we need to use a beam splitter with a 90:10 reflection:transmission ratio, which will transmit only 10% of the incoming light, to be coupled into the cavity. Still, the 90% output can be used for something else, like power level diagnostics, or can be coupled into a wavelength meter. Also, the powers necessary for the locking are relatively low (~ 10 μW level), so the loss is still small compared with the power level of the main output of the laser. In the presented configuration, it is also possible that the red cooling 689 nm laser has an orthogonal polarisation with respect to the other beams, which can increase stability and avoid cross-talking.

CHAPTER 5

ULTRA-STABLE INTERROGATION LASER

The interrogation laser is a vital element for every optical clock. Its role is to provide a stable optical frequency, which is used to interrogate the atomic clock transition. The interrogation data can then be used to correct the laser's frequency, so that it stays on resonance. Apart from its important role in the optical atomic clock, such an ultra-stable laser can also be used in a vast range of experiments covering fields like fundamental physics investigation [148], communication [70], and astrophysics [63].

In this chapter I present the development of the ultra-stable interrogation lasers for spectroscopy of the clock transition in strontium. At the beginning, I present the construction of a stationary system at the University of Birmingham that was built to serve as a reference to further the development of a mobile system. The laser is constructed in a modular package and the only element that stops the system from being mobile is the reference cavity that is not rigidly mounted. I present possible sources of instability and measures of how to isolate from them. Also in this chapter, I present the assembly of a mobile interrogation laser that was developed towards space applications within the Space Optical Clock (SOC2) project. Some characterisations of the laser are presented such as instability measurement, acceleration sensitivity, pressure sensitivity and laser power sensitivity. At the end of this chapter I compare the instability of the stationary system with the SOC2 mobile system, as well as, with the RF frequency standards used in the laboratory.

5.1 Stationary interrogation laser

The stationary system consists of a modular external cavity diode laser (ECDL) stabilised to an ultra-stable optical cavity. The entire optical part of the system, including the laser, stands on a vibration isolation platform. The entire system has dimensions $\sim 460 \times 510 \times 1000$ mm^3 and is subject to further miniaturisation.

5.1.1 ECDL design

An ECDL was built in a Littrow configuration, using a ruled grating with 1800 lines per millimetre. An anti-reflection coated laser diode is used to avoid interference with light reflected back from the grating. Both the laser diode and a $f = 3.1$ mm collimation lens are mounted inside a collimation package, which provides easy adjustment of the position and polarisation. The grating is mounted on a mirror mount with very fine adjustment screws, which provides coarse tuning of the laser. For the fine tuning, a piezoelectric transducer is mounted between the screw and platform of the mirror mount. All the elements are enclosed inside a case made of aluminium, which forms the external cavity of the ECDL, with approximately 10 cm distance between the laser diode and the grating. The aluminium case is temperature stabilised using two thermoelectric coolers (TEC) on the bottom, with a 10k thermistor mounted next to the laser diode to optimise for the temperature stability of the laser diode. The hot side of the TECs is attached to the thick aluminium base of the laser's box, which serves as a heat sink. The ECDL case, as a part of the entire laser system, is shown in figure 5.1a.

The laser beam exits the ECDL cavity through a wedged window, which protects the grating and diode against dirt and dust coming from the outside. With two mirrors on adjustable mounts, the beam is guided through a tandem Faraday optical isolator (FOI), which provides approximately 57 dB isolation. This protects the laser against the reflected light, which might cause instabilities in the laser's optical frequency, or even break the laser diode. After the isolator, another two mirrors on adjustable mounts are used to couple the laser light into a polarisation maintaining FC/APC fibre by a fibre coupler (FC). Just before the fibre coupler, the beam passes through a calcite polarisation beam displacer (PBD), which provides a high extinction ratio of 100 000:1. The beam displacer is used to clean the polarisation before injecting the beam into the polarisation maintaining fibre.

The laser also features screened wiring inside the box with SMA connectors for controlling the PZT. This helps to avoid cross-talking between the wires, and provides an appropriate cable type for the RF part of the signal for the PZT. A picture of the complete laser box is presented in figure 5.1b.

The laser diode is operated at room temperature and outputs powers up to 35 mW, measured at the output of the ECDL cavity. When tuned close to the desired frequency of the $^1\mathbf{S}_0 \rightarrow {}^3\mathbf{P}_0$ clock transition in strontium, which is approximately equal to 429.228 THz, the power measured after the isolator is equal to 24 mW for a 77.6 mA laser current (90 mA recommended maximum current). After the isolator, the laser beam is coupled into a fibre beam splitter, which splits one input into three outputs, labelled from 1 to 3, as presented in figure 5.2.

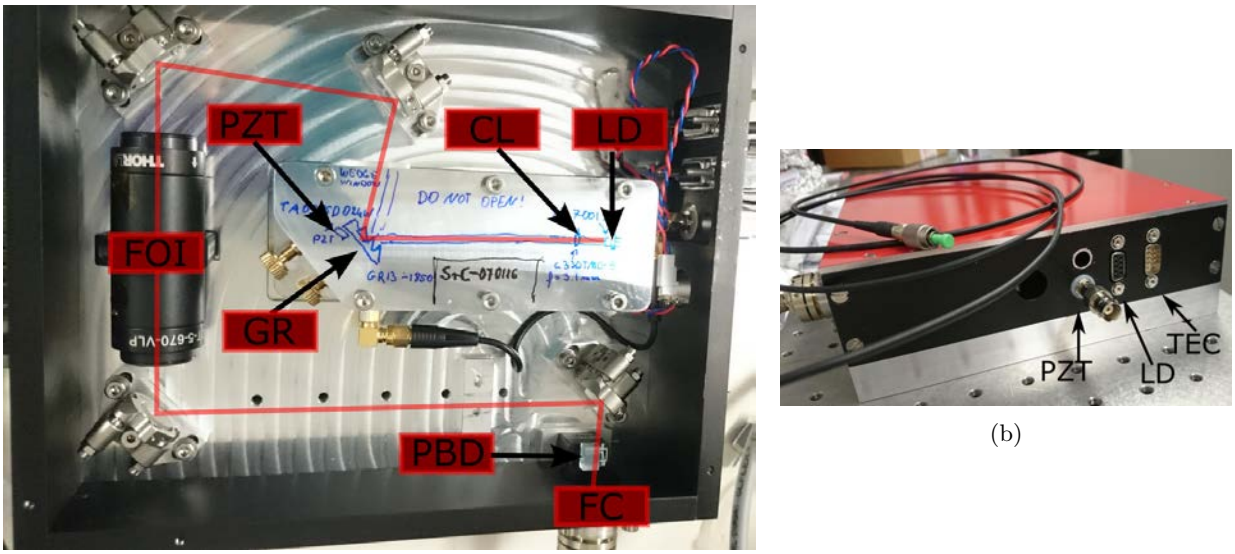

(a)

(b)

Figure 5.1: **(a)** External cavity diode laser design for the interrogation laser. LD – laser diode; CL – collimation lens; GRT – grating; PZT – piezoelectric transducer; FOI – Faraday optical isolator; PBD – polarisation beam displacer; FC – fibre coupler. **(b)** Laser box with labelled backplane connectors for the piezoelectric transducer (PZT) voltage, laser diode (LD) current and thermoelectric cooler (TEC) temperature stabilisation.

The power levels at the outputs are equal to 3.4 mW, 2.7 mW, and 3.2 mW for output number 1, 2, and 3, respectively. The first output is connected with a fibre-to-fibre connector to a fibre-coupled integrated optical phase modulator (EOM). The EOM is used to generate side-bands in the optical frequency spectrum, necessary for the Pound-Drever-Locking of the laser to a reference cavity. The second output is used for inspection with a wavelength meter and an optical comb. The third fibre output provides light that can be guided with a fibre to the atomic package, with which to interrogate the atoms.

5.1.2 Stabilisation of the laser

Although an ECDL may have an intrinsic narrow linewidth (30 – 100 kHz), it is much larger than the linewidth of a clock transition (1 mHz – 1 Hz). Also, its optical frequency deviates due to mechanical instabilities, temperature variations, and atmospheric pressure fluctuations. Therefore, it is necessary to stabilise the laser to a stable, narrow linewidth reference to both narrow down the linewidth of the laser and limit its drifts. A reference that is commonly used in laser stabilisation is the resonant mode of an ultra-stable optical resonator (Fabry-Pérot interferometer) with an ultra-high finesse.

The ECDL laser is stabilised with the Pound-Drever-Hall (PDH) method, described in detail in [147]. A

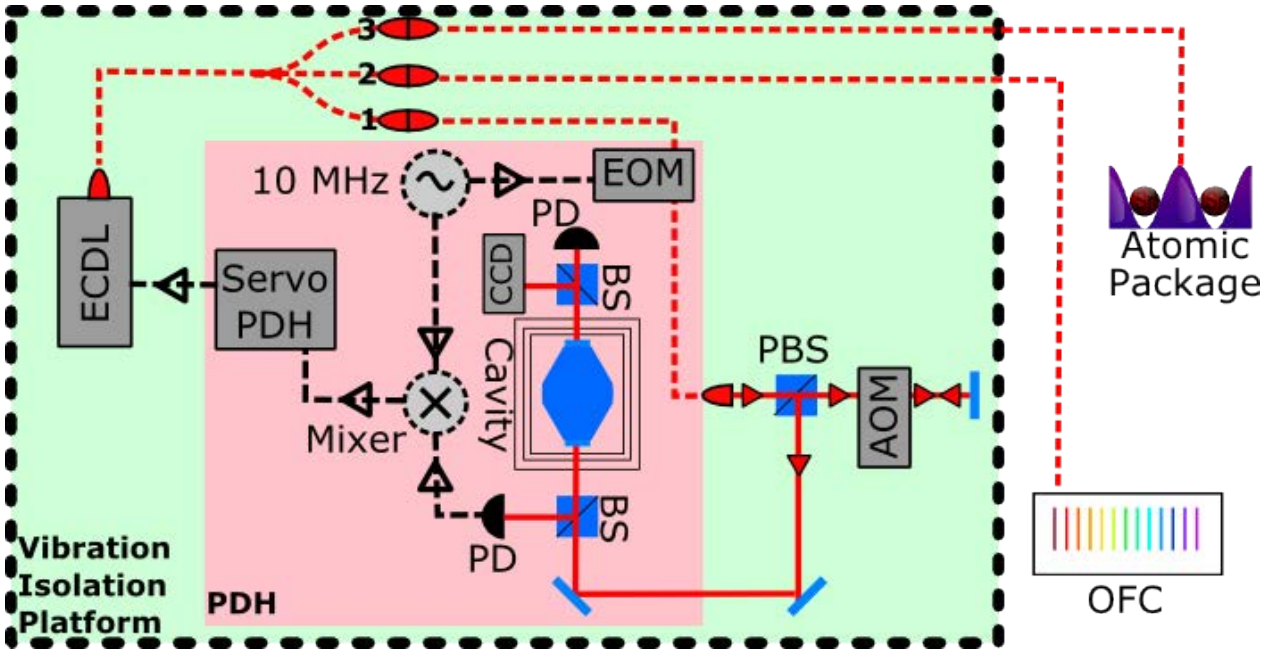

Figure 5.2: Locking and distribution of the interrogation laser. ECDL – external cavity diode laser; EOM – electro-optical modulator; AOM – acousto-optical modulator; BS – beam splitter; OFC – optical frequency comb; PD – photodiode; CCD - charge-coupled device camera; PDH – Pound-Drever-Hall.

schematics of the PDH locking setup is shown in red area in figure 5.2. The Laser beam is phase modulated with a fibre integrated electro-optical modulator to generate sidebands needed for the PDH locking. The collimated beam double-passes an AOM operated at 80 MHz, and passes through a mode-matching lens that optimises the overlap between the cavity and beam modes. The beam passes through the 90:10 (reflection:transmission) beam splitter and is coupled into the reference cavity. Most of the cavity reflected light is diverted by the 90:10 beam splitter into a fast photodiode. The RF part of the signal from the photodiode is demodulated with a 10 MHz signal, which is also used for driving the EOM. The 10 MHz signal comes from a 4-channel direct digital synthesiser (DDS) that is referenced by a GPS disciplined rubidium oscillator that will be described in subsection 5.3.3. The output of the mixer, where the signal is demodulated, gives an error signal that is amplified and filtered by PDH servo, and fed back to the laser for a fast lock with the laser diode current, and slow lock with the laser's PZT. At the transmission output there is a 50:50 beam splitter that splits the laser beam between a photodiode and CCD camera, both used for inspecting the lock quality.

5.1.3 Reference cavity

The reference cavity was manufactured by Advanced Thin Films. It is made of an ultra low expansion (ULE) glass spacer with optically contact bonded ULE mirrors. One of the mirrors is planar, whereas the other is concave with a 1 m radius of curvature (ROC), and both have a diameter of 25.4 mm. The length of the spacer is equal to 77.5 mm. The shape of the spacer is designed to optimise its performance for the cavity standing in an upright, vertical direction. It features a midplane ring, used to support the cavity at three points which are located at equal distances from both mirrors, providing a 3-fold symmetry of the system. In this configuration, vertical acceleration causes both mirrors to displace in phase, roughly by the same distance, effectively reducing the sensitivity of the cavity to seismic noise [149].

5.1.4 Thermal shield and vacuum system

The reference cavity needs to be under a stable environment with ultra-low temperature and pressure fluctuations. A special vacuum system was constructed to provide these conditions, and its cross section is presented in figure 5.3.

Vacuum chamber

The most outer can of the system is a vacuum chamber made from a stainless steel CF150 reducing cross. On the top of the cross, there is a stainless steel CF150 blank flange with an indium sealed 1 inch window in the centre, for optical access to the cavity. The flange is sealed with the cross using a copper gasket. The bottom flange is made of aluminium, which cannot be sealed with a copper gasket. Therefore, a viton gasket is used instead. The flange also has an indium sealed window, used for optical access to couple the beam into the optical cavity. The window is tilted to avoid the etalon effect and prevent the reflected beam from interfering with the rest of the setup. The flange is made of aluminium, rather than stainless steel, for better thermal properties. Additionally, the flange features fins on the bottom side to increase heat exchange with the air, since it also serves as a heatsink for the thermoelectric coolers (TEC) mounted on the inner side. The cross also has two CF32 connectors on the sides. A military 19 pin connector feedthrough is mounted on one of them, while the other one is used to connect the valve with the 20 l/s ion pump. The ion pump keeps the pressure level inside the vacuum chamber below 1×10^{-7} mbar.

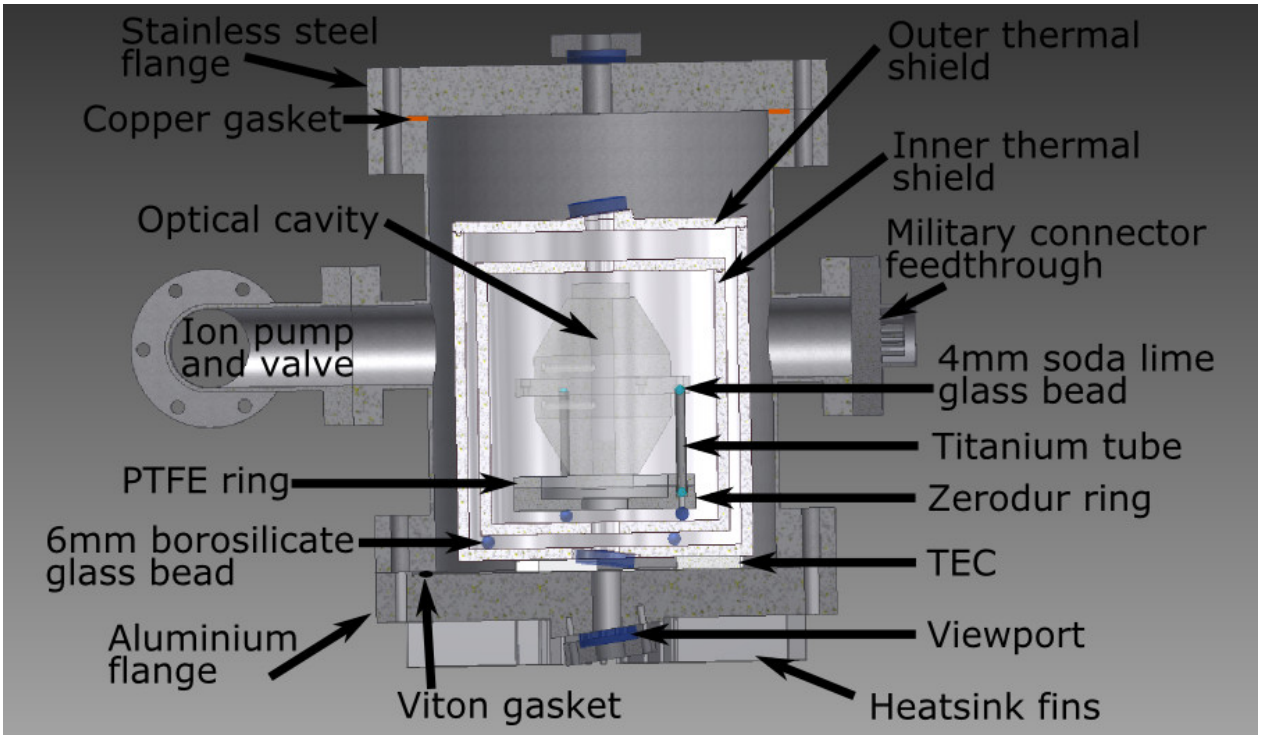

Figure 5.3: Cross section of the vertical cavity vacuum system. The vacuum chamber is made from a CF150 reducing cross, with two CF150 flanges on each end. The optical cavity is placed inside two thermal shields. The outer thermal shield is temperature stabilised with three thermoelectric coolers (TEC).

Thermal insulation

The temperature of the reference cavity has to be stabilised to below the μK level, to stabilise the interrogation laser down to a 1×10^{-15} fractional frequency instability level. Usually, the best temperature controllers are able to stabilise the temperature at a mK level, which is not good enough for the reference cavity. For that reason, a special passive thermal shielding has been developed, to filter fast temperature fluctuations. Slow temperature drifts would still be present, but slow enough that they could be easily compensated for by referencing the stabilised laser to the atomic clock transition.

The optical cavity is placed inside two thermal shields made of aluminium. The outer shield stands on three thermoelectric coolers (model PKE71A0020 from Peltron GmbH), which are used to stabilise its temperature. Home made thermal grease, consisting of ultra-high vacuum grease mixed with powdered silver, is applied on each side of the TEC to improve thermal contact between the surfaces. Grease was chosen over the glue, due to different coefficients of thermal expansion that would induce internal stress inside the TEC, and could lead to its breakage. Two 10k thermistors are attached to the outer shield, one at the top and one at the bottom. The bottom one is used as a probe for stabilising the temperature. The other 10K thermistor

is attached at the midpoint of the inner shield for monitoring the temperature. Three spherical glass beads are used to separate the two thermal shields to decrease thermal conductivity between the layers. A spherical shape, for the supports, is advantageous because of a single-point contact with a tangential surface. The aluminium thermal shields and the inner side of the bottom vacuum flange are highly polished, to further reduce the conductivity between the layers due to radiation, by lowering the emissivity coefficient.

The reference cavity is placed inside the inner shield, on three titanium tubes with a 4.25 mm outer diameter and 0.25 mm wall thickness. Such legs provide both rigid support, and relatively low thermal conductance, compared with other shapes and materials. On each end of the tube, a 4 mm diameter spherical glass bead is glued to provide uniform support for the cavity, with a low thermal contact between the surfaces. Titanium legs stand on a low thermal expansion Zerodur ring, which also stands on three glass beads. A PTFE ring is placed on top of the Zerodur ring to give additional support to the titanium legs, to avoid twisting of the cavity body. Additionally, a layer of aluminium foil is placed between the inner thermal shield and the cavity, to maximise the thermal time constant between the cavity and the outer thermal shield.

The thermal time constant between the outer and inner shield was measured to assess the thermal insulation abilities of the system. First, the temperature of the outer shield was set to 20°C, and left over a couple of months to allow the inner shield and the cavity to approach this temperature. Next, the set temperature of the outer shield was changed to approximately 25°C. It took approximately 10 minutes for the outer shield to stabilise to the new temperature setting. During this process, readings of the inner shield thermistor resistance were taken with an Agilent 34410A multimeter, for a period of 100 hours at 10 s intervals. The measured data points are presented in figure 5.4a with blue circles (not distinguishable due to high resolution of the measurement). The function fitted to the data is shown as a red curve, comprising two exponential functions, one of which is amplitude modulated with a sine, creating a damped oscillator curve. From the fitted function, a time constant for the first exponent is calculated to be $\tau_1 = 25$ hours. This time constant is assigned to the radiative heat exchange between the layers. The second exponent gives us a short-term time constant equal to $\tau_2 = 5$ hours, which might be assigned to temperature stabilisation across the outer shield, or heat conduction through the glass supports. The sine component might originate from the temperature controller, which after changing the temperature set point, slightly overshoots by approximately 0.1 K and oscillates before it finally stabilises. For comparison, figures 5.4c and 5.4e show fits with exponential function only and double-exponential function, respectively. Corresponding fit residuals plots are shown in figures 5.4d and 5.4f, respectively. It can be clearly seen when comparing the three fit residuals figures, that 5.4b, with the lowest amplitude and no obvious pattern being visible corresponds to the best fitting function.

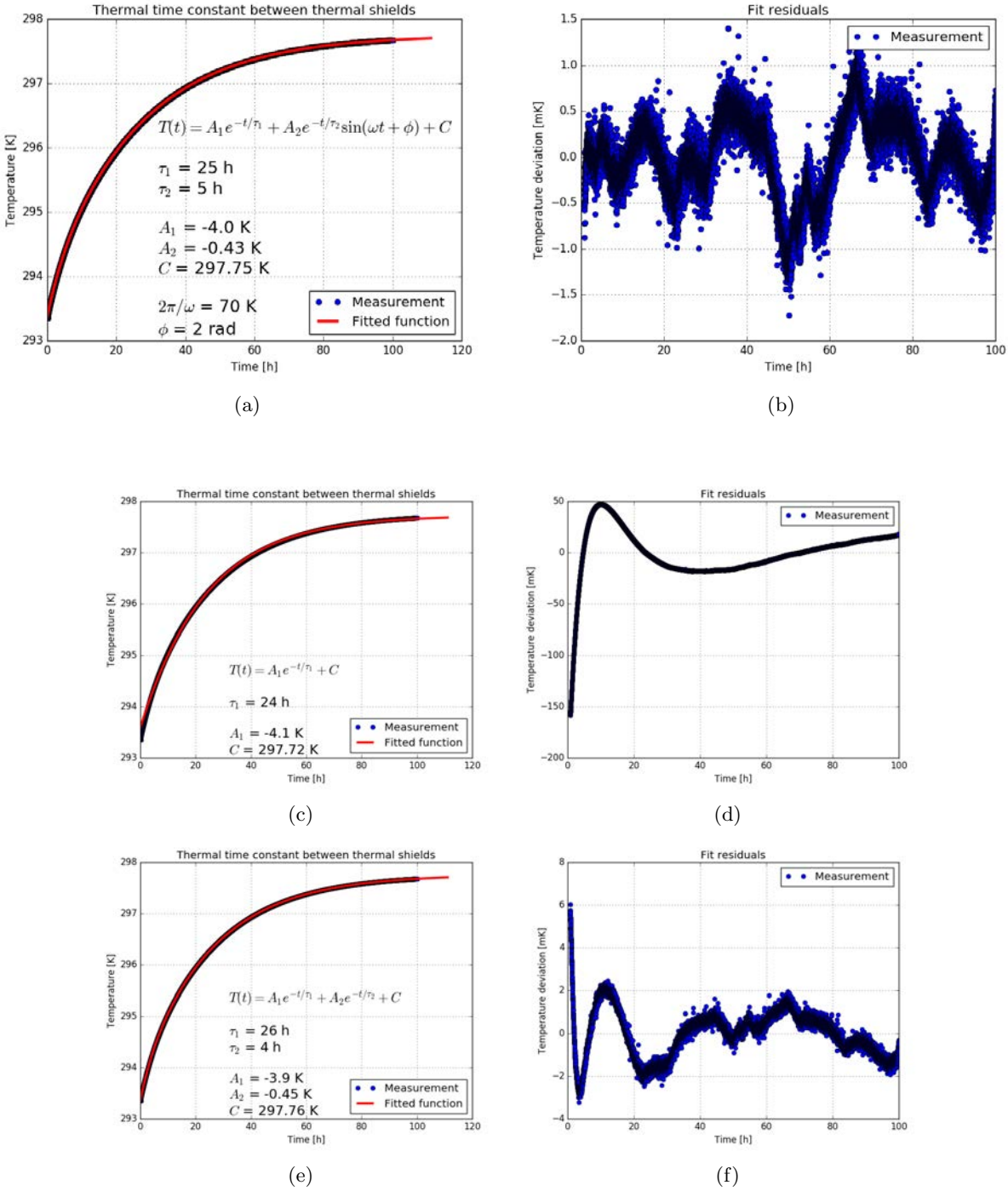

Figure 5.4: **(a)** Measurement of thermal time constant between the outer thermal shield and the inner thermal shield. The temperature of the outer shield was changed and blue points represent temperature values on the inner shield. The red curve shows a fitted exponential function with sinusoidal, exponentially decaying oscillations as per equation on the plot. **(b)** Fit residuals for 5.4a **(c)** Single-exponential fit. **(d)** Fit residuals of single-exponential fit. **(e)** Double-exponential fit. **(f)** Fit residuals of double-exponential fit.

By analogy with electronic circuits, highly polished layers of aluminium, separated by a vacuum, act as a thermal resistor with resistance R, which when combined with the heat capacitance C of the thermal shield, form a thermal low-pass filter. With a thermal time constant $\tau = RC = 25$ h, we can calculate the cut-off frequency of the low-pass filter according to the formula $f_c = \frac{1}{2\pi\tau}$, giving the result of $f_c = 1.8$ μHz. By knowing the mass of the inner shield, it is possible to calculate its capacitance $C_{in} = 0.678$ kJ/K. The thermal resistance between the shields can be calculated from the relation $\tau = RC$, giving the result $R = 135$ K/W. The average emissivity factor ϵ of the shields' surfaces can be estimated, by transforming the formula for radiation heat transfer between two bodies into the following form:

$$\epsilon = \frac{A_1/A_2 + 1}{A_1 R\sigma(T_2 + T_1)(T_2^2 + T_1^2) + A_1/A_2}. \tag{5.1}$$

In this equation, A_1 and A_2 are the areas of the outer and inner shield, respectively, R is the thermal resistance between the layers, σ is the Stefan-Boltzmann constant, and T_1 and T_2 are the temperatures of the outer and inner shield, respectively. To obtain this formula, the view factor was assumed to be equal to 1. The estimated value of emissivity $\epsilon = 0.038$ is in accordance with the value range $\epsilon = 0.02 - 0.05$ taken from the literature [150, 151], for highly polished aluminium.

5.1.5 Finesse

During the cavity vacuum system rebuild, the reference cavity was stored in a cupboard for more than a month, in atmospheric pressure. Although it was boxed in a protective case, it could have been exposed to dust and humidity that could affect the cavity's finesse. When the cavity was placed back into the refurbished vacuum chamber, cavity ring-down spectroscopy was performed to see if the cavity finesse had degraded.

The cavity was first locked to the cavity, both with a fast current and slow PZT. When the unlimited integrator on the PDH servo controlling the slow PZT was switched to reset mode, causing the laser to immediately fall out of the lock, the signal from the transmission photodiode was recorded with an oscilloscope. The recorded signal is presented in figure 5.5 with an exponential decay curve fitted as a red line. The measured decay time from the fitted function is equal to $\tau = 27.234 \pm 0.015$ μs, which corresponds to a finesse of 331000 ± 500.

The finesse of the same cavity, measured three years earlier by Johnson in [152], was equal to 341000 ± 2000, which indicates the finesse is on a similar level. Therefore, no significant degradation of the finesse was observed.

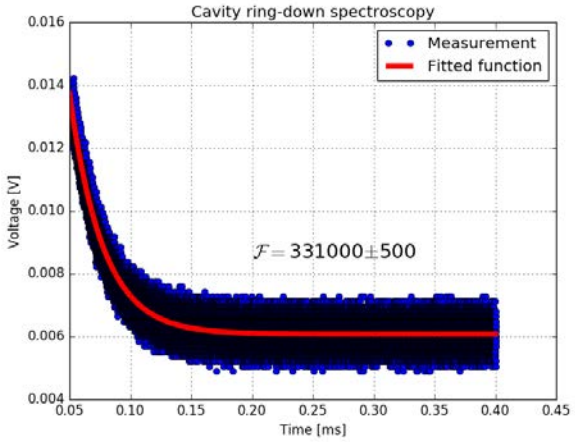

Figure 5.5: Finesse measurement with cavity ring-down spectroscopy. The red curve shows an exponential fit to the data (blue circles).

5.1.6 Stability measurement

The stability of the laser was assessed by comparing its frequency against another stationary clock laser system, featuring a 10 cm long horizontal cavity with a finesse of 285000 ± 2000, described in [152]. To do this, both lasers were stabilised to a resonant mode close to the clock transition frequency (~ 429.228 THz), and their outputs were superimposed on a fast photodiode, mounted on a bias-T for a faster response. The beat note frequency was taken from the AC-coupled output of the bias-T. The amplified and filtered signal was recorded using a computer connected to a dead-time-free frequency counter. A linear function was fitted to the frequency data, to get the value of cavity linear drift which was equal to 3 Hz/s. Since the linear drift can be compensated for with an AOM, by programming its DDS, it was removed from the frequency readings. Fractional Allan deviation was calculated using a script written in python, and is drawn with a blue line in figure 5.6, showing an instability level of 5×10^{-15} at 1 s. This result shows a significant improvement compared to the earlier implementation of the laser, presented by Johnson in [152], which reached a 2×10^{-14} instability level at 1 s. Although the instability is already low, there is still capacity for improvement, so that it reaches the estimated thermal noise limit of 1×10^{-15}, presented in the figure with a dashed red line.

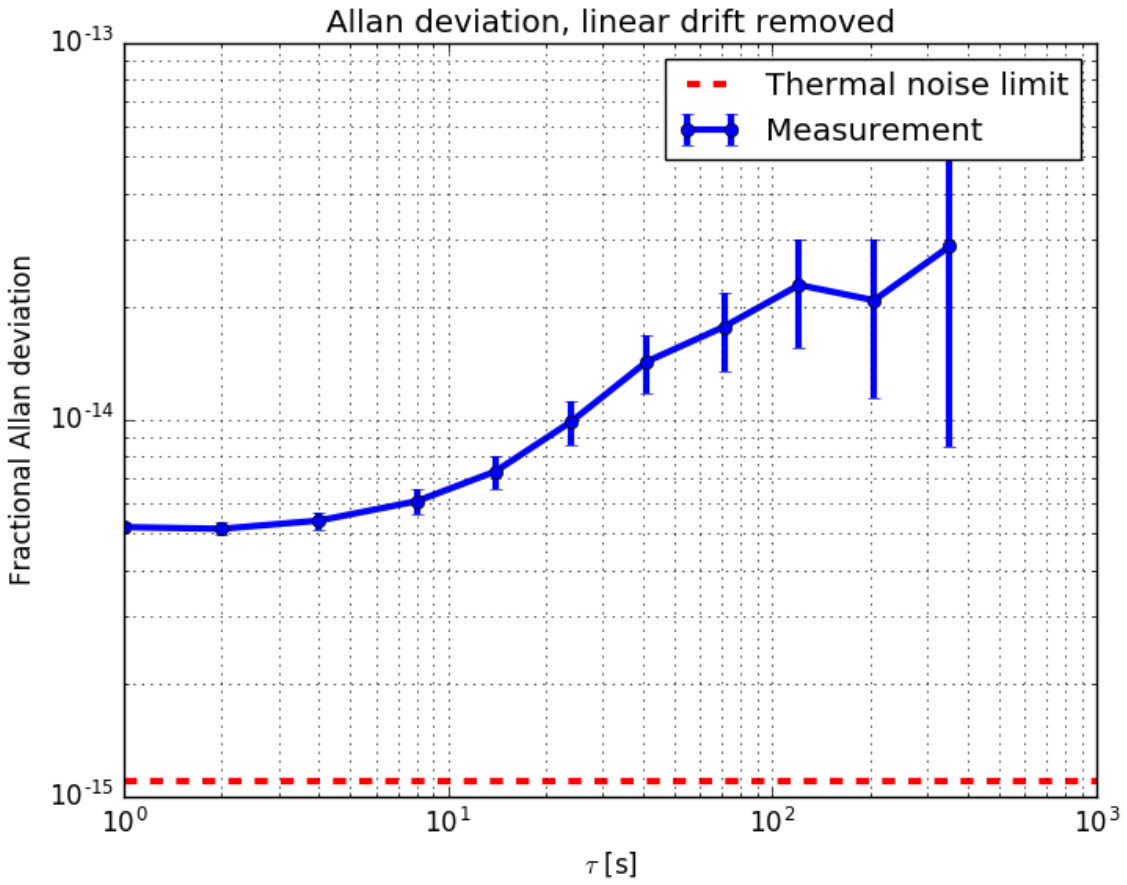

Figure 5.6: Fractional Allan deviation of the beat note frequency, with the linear drift removed, showing the relative instability between the vertical-cavity and horizontal-cavity clock lasers. There is a visible improvement at 1 s, from 2×10^{-14} to 5×10^{-15}, when compared with result obtained by Johnson in [152].

5.2 Acoustic insulation

To reach the thermal noise limit of the cavity, it is important to isolate the laser system from other sources of noise. One significant source is acoustical noise that is transferred both through the air and table, and causes the reference cavity to vibrate. Vibrations, as with any other kind of acceleration, will change the distance between the mirrors, degrading the stability performance of the optical reference.

The acceleration sensitivity for a similar vertical cavity design was measured by Ludlow et al. [149] to be 7×10^{-10}/g. It is required to isolate the system from external vibrations, with acceleration values at the 1×10^{-6}/g level, to be able to reach an instability level of 1×10^{-15}.

5.2.1 Sound reflection

The power of a sound wave can be reduced in three different ways: by reflection, absorption, or diffraction. To build a high performance acoustic insulation box, it is crucial to reflect sound waves coming from the outside, and absorb, as much as possible, the sound residues that were transmitted through the wall. It is clear that the right choice of materials is crucial in designing the acoustic insulation box. The outer surface of the box wall should be made of a rigid material that reflects most of the sound, whereas the inner part of the box should be lined with sound absorptive material.

Every material has an acoustic impedance, which describes the material's ability to transfer sound waves [153]. The characteristic impedance Z of a material is expressed in Rayl units, and its value depends on the density of the material ρ, and the speed of sound inside the material c. It can be calculated by multiplying those two values, as presented by the following equation

$$Z_0 = \rho_0 c_0. \tag{5.2}$$

The index 0 means that those values are derived for static air pressure $p_0 = 1$ atm and constant density. Comparison of the characteristic impedance values, for different materials, is presented in table 5.1.

Sound waves are reflected at the boundary of two materials. Reflection R and transmission T coefficients of the boundary are described by the following formulas [153]

$$R = \frac{Z_2 - Z_1}{Z_2 + Z_1}, \tag{5.3}$$

$$T = \frac{2Z_2}{Z_2 + Z_1}, \tag{5.4}$$

Material	Characteristic impedance (MRayls)	Material	Characteristic impedance (MRayls)
Aluminum	17.0	Lucite	3.2
Brass	40.0	Concrete	8.0
Copper	44.5	Ice	2.95
Iron(cast)	33.5	Cork	0.12
Lead	23.2	Oak	2.9
Nickel	51.5	Pine	1.57
Silver	39.0	MDF*	1.7
Steel	47.0	Rubber (hard)	2.64
Glass (Pyrex)	12.9	Rubber (soft)	1.0
Quartz (X-cut)	15.3	Air at 20° C	0.000415

Table 5.1: Characteristic impedance values for different solids and air. Data taken from [154]. *Value for the medium density fibreboard (MDF) spans greatly for various manufacturing methods, here calculated for Young's modulus number $E = 4$ GPa and density $\rho = 750$ kg/m^3.

where Z_1 and Z_2 are the acoustic impedances of the first medium where the original wave propagates and the second medium that reflects the wave, respectively. Using 5.3 and 5.4 we can derive a simple relation between R and T

$$T = R + 1 \tag{5.5}$$

Since it is common to use the sound power level to describe acoustic properties, it is useful to use the sound power reflection r and transmission τ coefficients instead, which have the following forms

$$r = R^2, \tag{5.6}$$

$$\tau = T^2 \frac{Z_1}{Z_2}. \tag{5.7}$$

Note that contrary to the reflection R and transmission T coefficients, the power reflection r and transmission r coefficients add up to one

$$r + \tau = 1 \tag{5.8}$$

The formula for the power reflection coefficient 5.6 can be used to choose the materials that will reflect the sound the best. Maximising the reflection means maximising the difference in the materials' impedance $|Z_2 - Z_1|$. Comparing the values in the table 5.1, we find that a cork is outstanding when it comes to a

solid with a low acoustic impedance, and it is the most effective when combined with a material having high acoustic impedance. Creating a boundary made from cork and steel, gives us a power reflection coefficient of $1 - r_{cs} = 1 \times 10^{-2}$. A boundary of air and steel would give us a very good value of $1 - r_{sa} = 4 \times 10^{-5}$, compared to $1 - r_{oa} = 6 \times 10^{-4}$ for oak and air.

5.2.2 Reflection versus medium thickness

To learn how the thickness of the medium improves the sound reflectivity, it is necessary to consider a three-medium problem. As presented in [153], the following formula describes the reflection coefficient

$$R = \frac{(1 - Z_1/Z_3)\cos(kl) + i(Z_2/Z_3 - Z_1/Z_2)\sin(kl)}{(1 + Z_1/Z_3)\cos(kl) + i(Z_2/Z_3 + Z_1/Z_2)\sin(kl)}, \tag{5.9}$$

where Z_1, Z_2, and Z_3 are the impedances of each medium, $k = 2\pi/\lambda$ is the wave number, l is the thickness of the second medium, and i is the imaginary unit. Note that for small angles, where $kl << 1$, sine can be approximated by its argument, and cosine by 1, simplifying the formula to

$$R = \frac{Z_3 - Z1}{Z_3 + Z_1}, \tag{5.10}$$

which is the same as equation 5.3 for the two medium problem. The transmission coefficient can be calculated using the formula 5.5. It is now clear that for small values of kl, the middle medium is invisible for the passing wave. For example, assuming a sound velocity in the air of 343 m/s, a 2 cm thick oak wall sandwiched by air, and that the small angle approximation can be used for angles smaller than 30°, we obtain a value for the critical frequency equal to $f_{cr} = 142$ Hz. The oak wall can be treated as being invisible, for waves with a frequency lower than the critical frequency value.

5.2.3 Soundproof enclosure

The number of equipment, together with the air conditioning unit inside the laboratory, makes the laboratory a noisy environment which we need to isolate our ultra-stable clock lasers from. Ultra-stable clock laser systems used to have two acoustic boxes, one for each cavity. After moving the system to a new stone table, table surface was limited and it was necessary to build a bigger box that could fit two clock lasers inside.

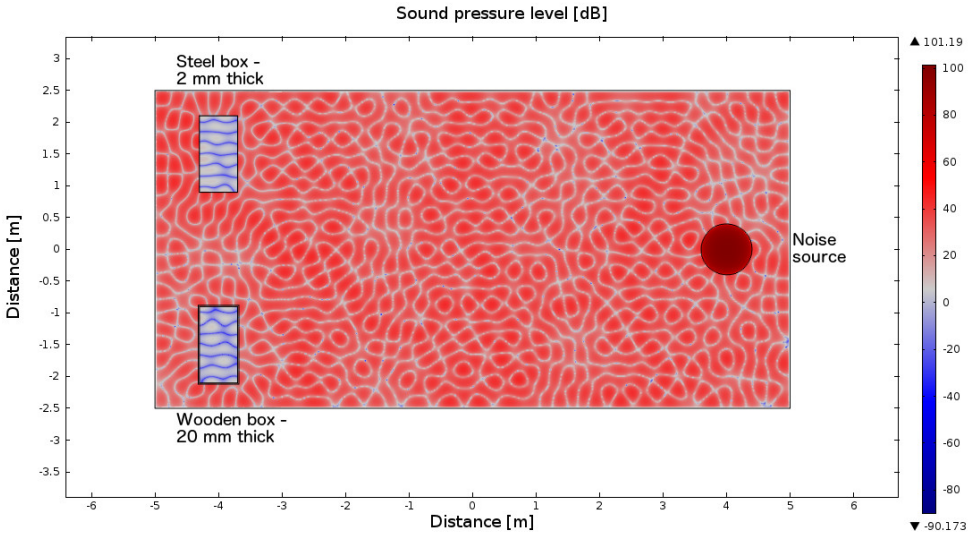

(a) Simulation of the sound pressure level inside soundproof enclosures for a frequency equal to $f = 1000$Hz. The red circle is a monopole sound source, rectangles on the left are acoustic enclosures made of 2 mm thick steel (upper rectangle) and 20 mm thick oak wood (lower rectangle). The blue colour inside the boxes indicates reduced sound pressure level

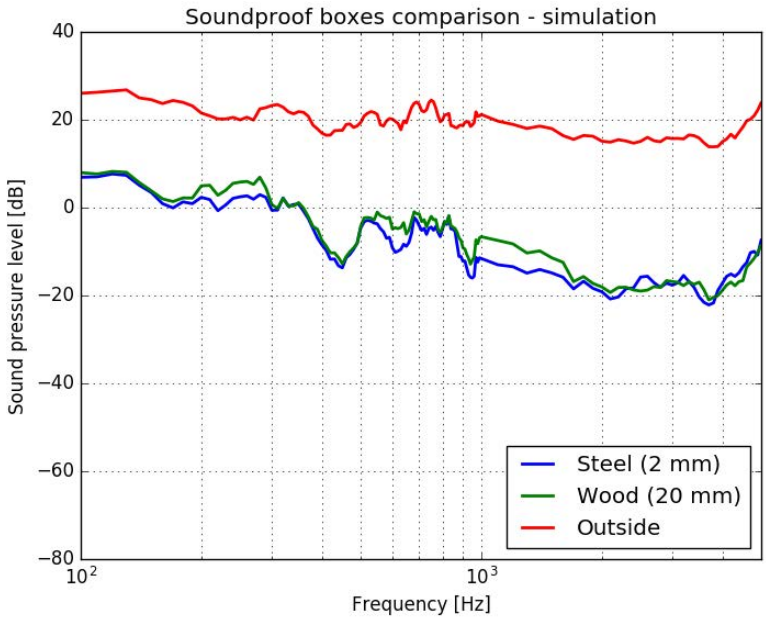

(b) Mean sound pressure levels inside the oak box (blue curve), inside the steel box (green curve), and outside the boxes (red curve). For better visibility, the curves have been smoothed using a moving average over ten samples. It is clear that the steel box with cork inside, should isolate from sound, better than the wooden box.

Figure 5.7: Acoustic enclosure sound pressure level simulation

Acoustic enclosure simulation

Sound propagation inside the laboratory was modelled as a 2D model, with a monopole sound source, using COMSOL Multiphysics modelling software. Two acoustic boxes were placed symmetrically in the room, at the same distance from the noise source as presented in figure 5.7a. One of the boxes (top) is made of a 2 mm thick steel, whereas the other one (bottom) is made of 20 mm thick wood. The sound pressure level is presented in the figure using colours, where red denotes a high pressure level, and blue a low pressure level. It is clear from the figure, that both boxes significantly reduce noise inside. In figure 5.7b, the mean sound pressure levels, inside and outside the boxes, are presented as a function of the frequency of the noise source. The performance of the boxes are at a similar level. Each of them gives approximately 20 dB attenuation for sound at low frequencies (around 100 Hz), and it increases with the frequency, reaching 30 dB above 1000 Hz.

An important point to mention is that the simulation does not account for the sound absorption abilities of the material, and therefore, wood might be a better choice for the material. A similar material to wood, with even higher absorption abilities, is medium density fibreboard (MDF). The characteristic impedance of the MDF depends strongly on the manufacturing process as the physical properties such as Young's modulus E and material density ρ may vary. Using the basic formulas for the impedance 5.2 and speed of sound in the material $c = \sqrt{E/\rho}$, it is possible to estimate characteristic impedance of the MDF to be 1.7 MRayls. For this calculation Young's modulus and density was chosen to be equal to $E = 4$ GPa and $\rho = 750$ kg/m^3, respectively. The estimated value is slightly higher than pine and lower than oak, which was shown in table 5.1. Having similar properties to wood, the MDF has also other advantages such as high homogeneity, cost effectiveness and ease of processing. Thus, it was chosen to build the soundproof enclosure with.

Clock lasers enclosure

The soundproof enclosure is made of a 20 mm thick medium density fibreboard (MDF). The box was originally supplied with a 1 inch thick blue acoustic foam, with 1 inch long spikes. Due to high dusting, the foam had to be removed because it was not appropriate for use around optical components. It was replaced with a 2 inch thick acoustic foam, mounted on a 6 mm thick MDF. The foam has a density of 90 kg/m^3, and a hardness of 180 N. According to the manufacturer specifications, the noise reduction coefficient (NRC) of the foam is equal to 0.78, where an NRC equal to 1 indicates perfect absorption. Between the foam acoustic tile and the box, a thin layer of the Green Glue was applied. The Green Glue is an elastomeric particulate compound, which according to specifications, damps the low frequency noise. The acoustic foam tile was mounted using screws, as advised by the Green Glue manufacturer. The patent describing the elastomeric

particulate compounds can be found in reference [155].

Noise measurements were carried out to test the acoustical performance of the new box. Sound power levels were compared between the new box, old box, and outside the box. Additional measurements were taken in an empty office, as a reference for how noisy the laboratory environment is. The microphone used for taking measurements with, can be treated as a flat-response microphone, between 100 Hz and 10 kHz. The results are presented in figure 5.8. As shown in the plot, the enclosures are not very effective in the low frequency region, where they are 'invisible' to the sound waves. However, an improvement can be seen for the 'new box' at the 100 Hz region, which could be achieved by applying the elastomeric particulate compound between the box layers. At higher frequencies, it is clear that the both boxes are very effective, with the inside of the box comparable to an empty and quiet office. The curves were obtained by computing the power spectral density using Welch's method, with a segment length of 1024.

5.2.4 Table-transferred noise

In our laboratory, a very problematic source of vibrational noise is the air conditioning unit that stands directly on the floor. Thus, more effort than usual is required to isolate from this floor-transferred noise. While it is important to isolate the airborne sound from the laser system, it is important not to forget that an even larger amount of sound can be transferred through the floor to the table, and then to the entire system.

Simulation

Following the same reasoning as for the soundproof enclosure, it is necessary to have two materials with extreme values for the characteristic impedance, so that the reflection coefficient was as high as possible. This task is more difficult when it comes to isolating the table legs, as the material has to support a high load. Looking at the table 5.1, it is clear that a combination of steel and air is one of the most effective solutions, giving a power transmission coefficient as low as $\tau_{air-steel} = 3.5 \times 10^{-5}$. For this reason, most of the optical tables are floated on air cushions, reducing the noise being transferred through its legs. Unfortunately, the heavy stone table that supports clock lasers cannot be floated on air cushions and another solution has to be found.

Cork is another material with a low characteristic impedance, which in addition, is a solid. A boundary of steel and cork results in a power transmission coefficient of $\tau_{cork-steel} = 1 \times 10^{-2}$. Although it is over two orders of magnitude higher than the boundary of steel and air, it can be part of a multilayer cork-steel

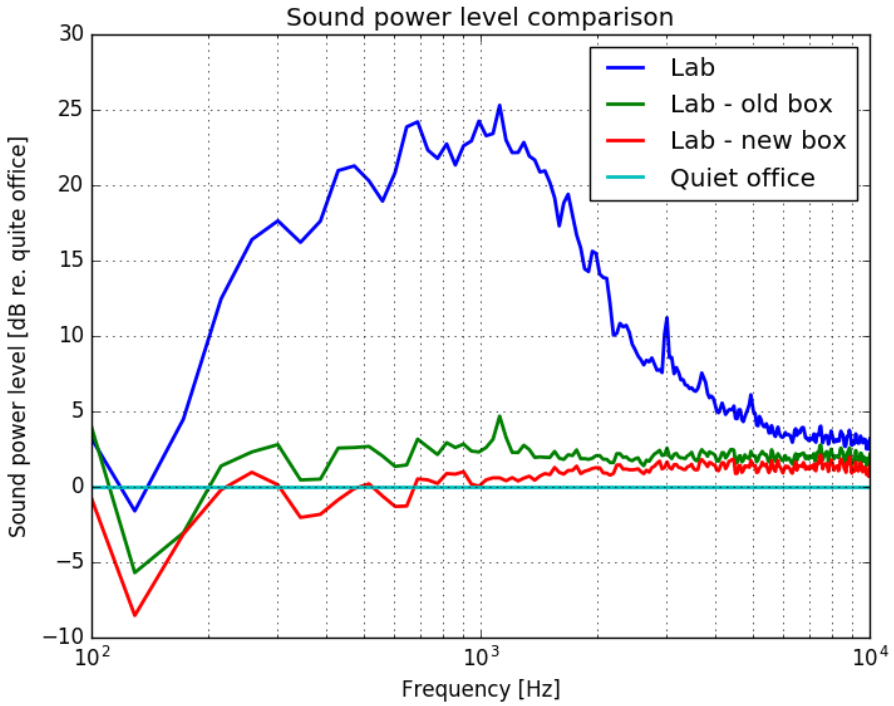

Figure 5.8: Sound power levels relative to an empty, quiet office (turquoise). The red curve corresponds to the inside of the new box, the green curve to the old box, and the navy blue curve to the laboratory background noise without any box.

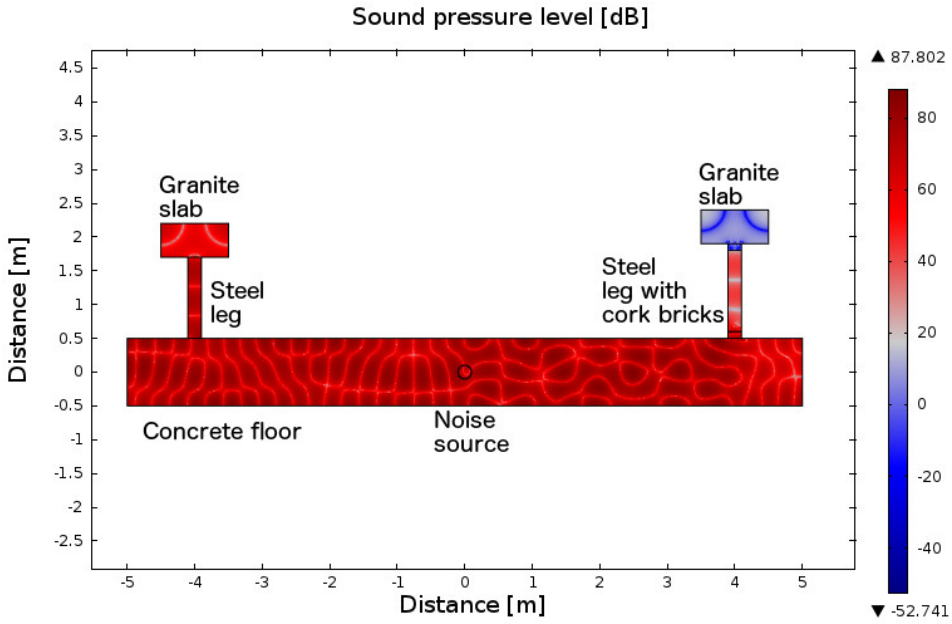

(a) Simulation of the sound pressure level in the laboratory for a frequency of $f = 511$Hz. Values on the axes are coordinates in meters, the red circle is a monopole sound source, rectangles on the left are acoustic enclosures made of 4 mm steel, and 3 mm cork (upper rectangle), and 20 mm oak board (lower rectangle). It was assumed that the walls of the laboratory act as soft boundaries (they absorb the incident waves).

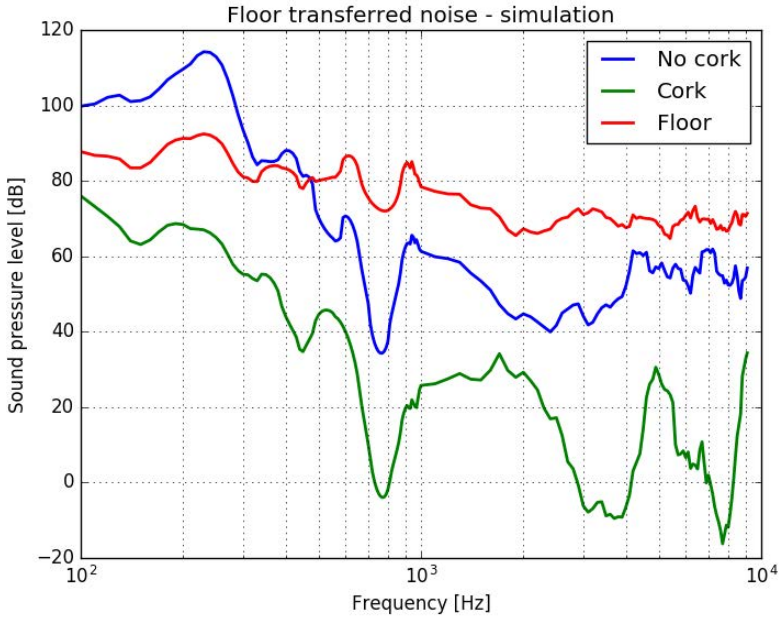

(b) Mean sound pressure levels on the granite table with a steel leg (blue curve), on the granite table with additional cork bricks (green curve), and directly on the floor (red curve). For better visibility, the curves have been smoothed using a moving average over ten samples. It is clear that the cork bricks help in reflecting the sound waves, which leads to better noise isolation.

Figure 5.9: Table-transferred acoustic noise simulation

system, that can even outperform the air floated tables. For reference, the value of the power transmission coefficient, for a boundary of concrete and steel, is equal to $\tau_{concrete-steel} = 0.5$

A simulation, using COMSOL Multiphysics modelling software, was carried out to confirm the choice of materials. In the model, a concrete floor was considered, with a monopole noise source placed centrally in the middle, as presented in figure 5.9a. Two tables, each represented by a granite slab supported by a steel leg, are standing on the floor, each at the same distance from the noise source and from the floor edge. The table on the right side of the figure, additionally has two cork bricks. One is placed between the concrete floor and the steel leg, while another is placed between the steel leg and the granite slab. The colours in the figure show sound pressure levels due to sound propagation in the setup, with red showing high pressure levels, and blue showing low pressure levels. Clearly, the table featuring the cork bricks (on the right of the figure) is better isolated from the floor, showing reduced sound pressure levels.

In figure 5.9b, the mean value of the sound pressure level as a function of source frequency is plotted for the granite slab without cork (blue line), with the cork (green line), and for the concrete floor (red line). The table with the cork bricks shows significant improvement over the table without the cork bricks, with insulation between 20 dB and 40 dB for most frequency values.

Measurement

The ultra-stable laser systems had to be moved from the floated optical bench, standing in the middle of the laboratory, to a heavy $\sim$ 1 ton granite table in the laboratory corner. The granite slab rests on a steel frame with five legs, each leg having adjustable bottom and top supports. The fifth leg is located between two other legs, and allows the choice between a three-point support or a traditional four-point support table. A 10 cm thick brick was placed under each leg of the table, to maximise the reflection of the sound waves propagating in the floor. Similarly, a cork brick was put between the steel frame and the granite slab of the table.

Measurements were performed to assess the effectiveness of the cork bricks. To do this, a sledgehammer was used to excite vibrations in the floor, while a PCB 393B31 acceleration sensor was used to measure the Z-component of the acceleration on the table surface, and an additional sensor was placed on top of a vibration isolation platform, which stood on the table surface. The sledgehammer features a built-in dynamometer, which triggers the measurement acquisition and gives the value of the excitation force. First, six measurements were performed, with the table standing on three legs, and the cork bricks in place. Next, six measurements were performed for the table standing on three legs, with one cork brick replaced by a

steel brick instead. The averaged power spectral density is presented in the top of figure 5.10. Clearly, the blue line representing the vibration on the granite slab with the cork under the table's legs, is lower than the green line representing the same table without the cork brick. Data for the vibration isolation platform is also presented, but do not show any difference due to the low resolution of the used sensor (1×10^{-12} g^2/Hz).

Note that the experiment was carried out with only one leg without the cork brick, and the vibrations in the table for the 'Granite, no cork' measurement (green line) would be even higher, if all legs had their cork brick removed.

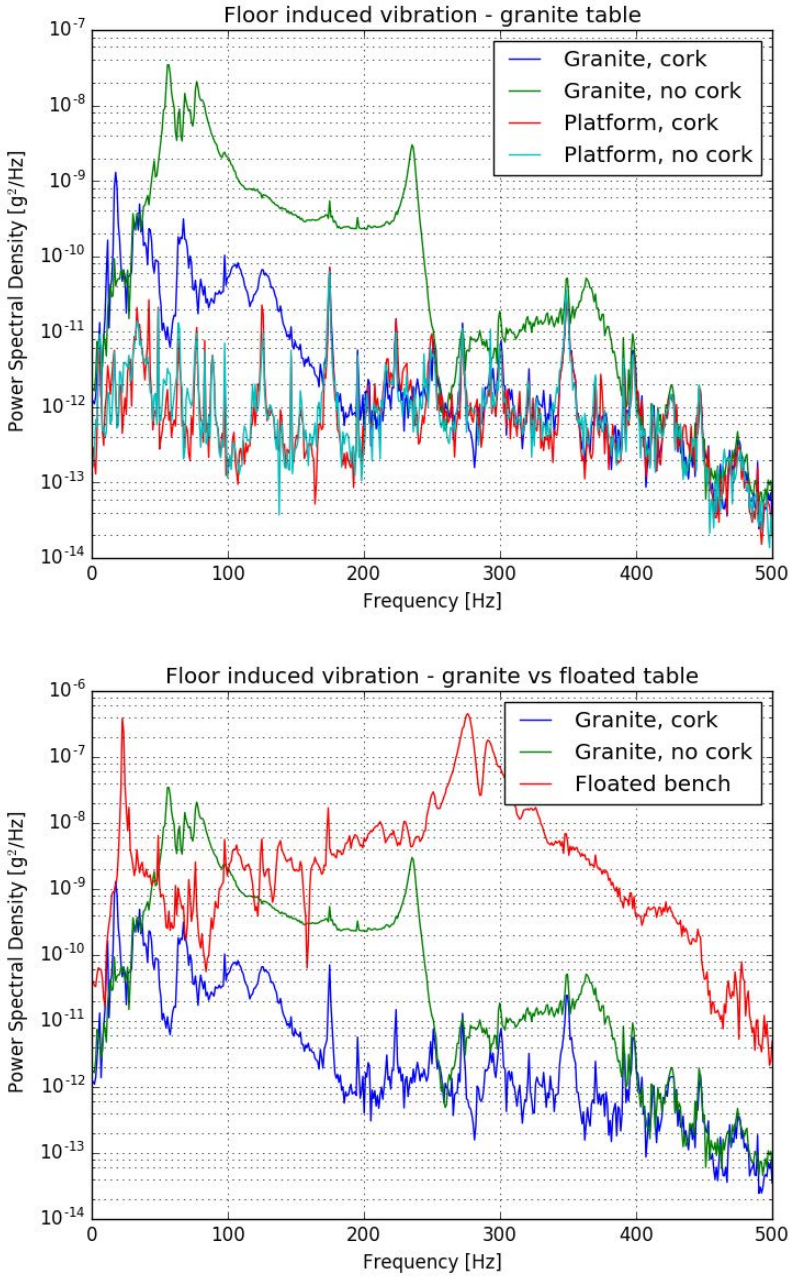

Figure 5.10: Measurement of the vibration transferred from the floor to the optical table. In the top figure, the ~ 1 ton granite table is considered with and without a cork brick under its leg. The acceleration was also measured on the vibration isolation platform, which stood on top of the table. An improvement is clearly visible for the table with the cork bricks. The acceleration level on the platform remains unchanged, probably due to an insufficient sensitivity of the acceleration sensor. In the bottom figure, a comparison between the granite table and floated optical bench (both in the same laboratory) is presented. A sledgehammer with a built-in dynamometer was used to excite the vibrations in the floor.

The red curve in the bottom part of figure 5.10 shows the acceleration level for the air floated table in the laboratory. Although it should outperform the granite table, the level of the vibrations is very high, comparable to the vibration level measured directly on the floor. Possible reasons for this are that the vibrations might have transferred through the cables, or the table was not well adjusted to the load it was holding. The latter may mean that the air pressure is too high, causing the table to push against the mechanical limiter. These issue will be reviewed and fixed in the near future.

5.3 Stability of the lasers and frequency shifters

When constructing a stable optical clock, it is necessary to provide a stable frequency standard, which could be used as a reference for frequency generators, driving equipment such as acousto-optical modulators (AOM), or electro-optical modulators (EOM). The frequency standard can also be useful in stabilising the optical frequency comb, or as a reference for measuring devices such as spectrum analysers and frequency counters.

Every laser used in the strontium clock experiment needs to be stable enough to stay on the absolute optical frequency of the atomic transition that it is meant to address. It means that the required stability depends on the natural linewidth of the transition it is used for, as well as on the linewidth of the laser. In order to meet the requirements, it is often necessary to stabilise the laser to an additional external reference; for example atomic spectroscopy, a stable optical Fabry-Pérot resonator, another laser, or a RF frequency standard through the optical frequency comb. On top of that, the ability to finely tune the laser's frequency is crucial, and this is done by using either an AOM, or EOM (please refer to the dual-sideband locking method in subsection 4.3.4). The stability of the frequency driving the AOMs and EOMs needs to stable enough so that it does not affect the stability of the optical frequency of the beam passing through those modulators.

5.3.1 Stability requirements for the lasers

Let ν_{atom} be the optical frequency and γ the natural linewidth of the atomic transition. Then, γ/ν_{atom} will be the linewidth of the transition in fractional frequency units. By making the assumption that the laser at the optical frequency of the transition should not deviate by more than $1/10^{\text{th}}$ of the linewidth, it is possible to obtain a condition for the required instability $\sigma_{\nu_{laser}}$ of the laser's frequency ν_{laser} as follows

$$\sigma_{\nu_{laser}} < \frac{\gamma}{10 \cdot \nu_{atom}} < \sigma_{\nu_{atom}} = \frac{\gamma}{\nu_{atom}}, \tag{5.11}$$

Name	Transition	Wavelength	Optical frequency	Natural linewidth	Required instability
Blue cooling	$^1\mathbf{S}_0 \rightarrow {}^1\mathbf{P}_1$	461 nm	651 THz	32 MHz	4.9×10^{-9}
Red cooling	$^1\mathbf{S}_0 \rightarrow {}^3\mathbf{P}_1$	689 nm	435 THz	7.5 kHz	1.7×10^{-12}
Repump 1	$^3\mathbf{P}_0 \rightarrow {}^3\mathbf{S}_1$	679 nm	441 THz	1.4 MHz	3.2×10^{-10}
Repump 2	$^3\mathbf{P}_2 \rightarrow {}^3\mathbf{S}_1$	707 nm	424 THz	7 MHz	1.7×10^{-9}
Clock ^{88}Sr	$^1\mathbf{S}_0 \rightarrow {}^3\mathbf{P}_0$	698 nm	429 THz	1 Hz	2.3×10^{-16}
Clock ^{87}Sr	$^1\mathbf{S}_0 \rightarrow {}^3\mathbf{P}_0$	698 nm	429 THz	1.2 mHz	2.8×10^{-19}

Table 5.2: Required fractional frequency instability of the lasers used to address the transitions in ultra-cold strontium. To obtain the result, the criterion that the laser cannot drift by more than $\gamma/10$ was assumed, where γ is the natural linewidth of the atomic transition. For simplicity, it was also assumed that the linewidth of the laser is much smaller than the natural linewidth of the transition.

where $\sigma_{\nu_{atom}}$ can be linked to the quality factor Q of the atomic transition in a simple relation $\sigma_{\nu_{atom}} = 1/Q$. The required laser instabilities for the strontium transitions are presented in table 5.2.

The ultimate stability of the lasers can be obtained by stabilising them to the most stable laser in the experiment, the clock laser, the stability of which is presented in section 5.1.6, figure 5.6. This could be done in a few different ways. One solution would be locking the optical frequency comb to the ultra-stable clock laser. The teeth of the laser would then share the same level of stability and could be used to lock all the different lasers. Another solution would be having a Fabry-Pérot transfer cavity, with one mirror mounted on a piezo-electric actuator. By injecting an ultra-stable clock laser to the cavity, it would be possible to lock the cavity to the laser. The same cavity could then be used to stabilise other lasers, provided that the cavity features highly reflective mirrors, for the wavelengths of interest.

5.3.2 Stability requirements for the frequency shifters

Now let us consider using a frequency shifter to tune the laser's optical frequency ν_{laser}, by the frequency of the shifter f_{RF}, to match the frequency of the atomic resonance

$$\nu_{atom} = \nu_{laser} + f_{RF}. \tag{5.12}$$

The instability of f_{RF} is equal to $\sigma_{f_{RF}}$ in fractional frequency units of the frequency shifter. The combined instability of the laser's frequency, and the frequency shifter's frequency, should therefore be smaller than

Name	Transition	Wavelength	Natural linewidth	Instability $\sigma_{f_{RF}}$ for AOM shift $f_{RF} = 80$ MHz	Instability $\sigma_{f_{RF}}$ for EOM shift $f_{RF} = 2.5$ GHz
Blue cooling	$^1\mathbf{S}_0 \rightarrow {}^1\mathbf{P}_1$	461 nm	32 MHz	4.0×10^{-2}	1.3×10^{-3}
Red cooling	$^1\mathbf{S}_0 \rightarrow {}^3\mathbf{P}_1$	689 nm	7.5 kHz	9.4×10^{-6}	3.0×10^{-7}
Repump 1	$^3\mathbf{P}_0 \rightarrow {}^3\mathbf{S}_1$	679 nm	1.4 MHz	1.8×10^{-3}	5.6×10^{-5}
Repump 2	$^3\mathbf{P}_2 \rightarrow {}^3\mathbf{S}_1$	707 nm	7 MHz	8.8×10^{-3}	2.8×10^{-4}
Clock ^{88}Sr	$^1\mathbf{S}_0 \rightarrow {}^3\mathbf{P}_0$	698 nm	1 Hz	1.3×10^{-9}	4.0×10^{-11}
Clock ^{87}Sr	$^1\mathbf{S}_0 \rightarrow {}^3\mathbf{P}_0$	698 nm	1.2 mHz	1.5×10^{-12}	4.8×10^{-14}

Table 5.3: Required fractional frequency instability of the frequency shifters used for the fine-tuning of lasers used in the ultra-cold strontium experiment. Frequency shifting in the experiment may be done either by using an AOM, which most commonly provides a 80 MHz shift; or an EOM, which can be used to tune the frequency by up to 2.5 GHz. To obtain the results, a criterion was assumed whereby the optical frequency of the laser beam cannot drift by more than $\gamma/10$, where γ is the natural linewidth of the atomic transition. For simplicity, it was also assumed that the linewidth of the laser is much smaller than the natural linewidth of the transition.

$1/10^{\text{th}}$ linewidth of the atomic transition

$$\sqrt{(\nu_{laser} \cdot \sigma_{\nu_{laser}})^2 + (f_{RF} \cdot \sigma_{f_{RF}})^2} < \nu_{atom} \cdot \frac{\gamma}{10 \cdot \nu_{atom}} < \nu_{atom} \cdot \sigma_{\nu_{atom}}. \tag{5.13}$$

Making the assumption that the laser is already stable enough ($\nu_{atom} \cdot \sigma_{\nu_{atom}} >> \nu_{laser} \cdot \sigma_{\nu_{laser}}$), we obtain

$$\frac{f_{RF}}{\nu_{atom}} \cdot \sigma_{f_{RF}} < \frac{\gamma}{10 \cdot \nu_{atom}} < \sigma_{\nu_{atom}}. \tag{5.14}$$

This simply leads to the following condition for the fractional frequency instability of the RF signal

$$\sigma_{f_{RF}} < \frac{\gamma}{10 \cdot f_{RF}}. \tag{5.15}$$

In table 5.3 the required instabilities of optical frequency shifters are presented. As always, the most crucial is the clock laser, and the frequency shifters need to be driven with a very stable frequency source.

5.3.3 Rubidium frequency standard

As the frequency stability is very important in the clock experiment, it is necessary to use a very good frequency standard, as a reference to other oscillators. The best solution would be to use the ultra-stable

strontium optical clock as a reference. However, this is in the development stage and not yet available. For this reason, a rubidium frequency standard, the model FS725 from Stanford Research Systems is used, as this provides a very stable and accurate frequency, compared with alternative crystal-based oscillators. Despite its high stability, the standard is still liable to long-term drifting in the frequency. It is possible to compensate for the drift, by providing a reference 1 PPS (pulse per second) signal. Such a signal could be obtained from GPS satellites, which are referenced to the UTC time standards.

Green circles in figure 5.11 present the instability of the rubidium frequency standard. The data points were obtained by measuring the frequency of one frequency standard with a frequency counter referenced by another identical frequency standard and then calculating the fractional Alan deviation. Blue circles show the same SRS FS725 rubidium frequency standards, but GPS disciplined. The GPS disciplined data features a bump around 5×10^3 s, which is caused by the standards' frequency being corrected by the GPS signal. In this case, the rubidium standard outputs a 1 PPS signal, which is compared with the 1 PPS signal coming from the GPS receiver [156]. To obtain the accurate referencing, the GPS signal is integrated with a long time constant of $\tau_1 = 65,536$ s, and used to calibrate the rubidium standard. This results in the 1 PPS signal of the standard exponentially approaching the 1 PPS signal coming from the GPS, with a time constant of $\tau_n = 8,095$ s. The time constant τ_n is in accordance with the position of the bump (~ 5000 s) in the Allan deviation plot. To predict the stability of the 1 PPS GPS signal, a function $f(\tau) = B/\sqrt{\tau}$ was fitted to the tail of the GPS disciplined standard, and is drawn with a blue dashed line, with the fitting parameter equal to $B = 1.2 \times 10^{-10}$. For comparison, the instability of a GPS receiver presented by Michael A. Lombardi in [157] reaches 4×10^{-12} at 10^3 s, and 1×10^{-13} at 10^5 s, which is close to the instability of the GPS, represented by the fitted function. The difference in instability may be attributed to the low-cost GPS receivers used to discipline the rubidium standard, which occasionally dropped the 1 PPS signal.

The rubidium standard can be used to stabilise the optical frequency comb, which would transfer its frequency into the optical frequency region. Comparing the instability plot of the standard, with the required stability data in table 5.2, we see that its performance would be good enough to stabilise the low-demanding blue cooling laser, and repump lasers. However, the short term stability of the standard would not be enough for the more demanding red cooling laser. This implies that the additional optical frequency standard is necessary for the red cooling laser.

The rubidium standard is most useful when it comes to referencing the frequency shifters. As shown in table 5.3, its stability is good enough to reference the frequency shifters of all the lasers in the ^{88}Sr optical clock experiment. Using a high-frequency shifter, referenced by the rubidium standard, might limit the

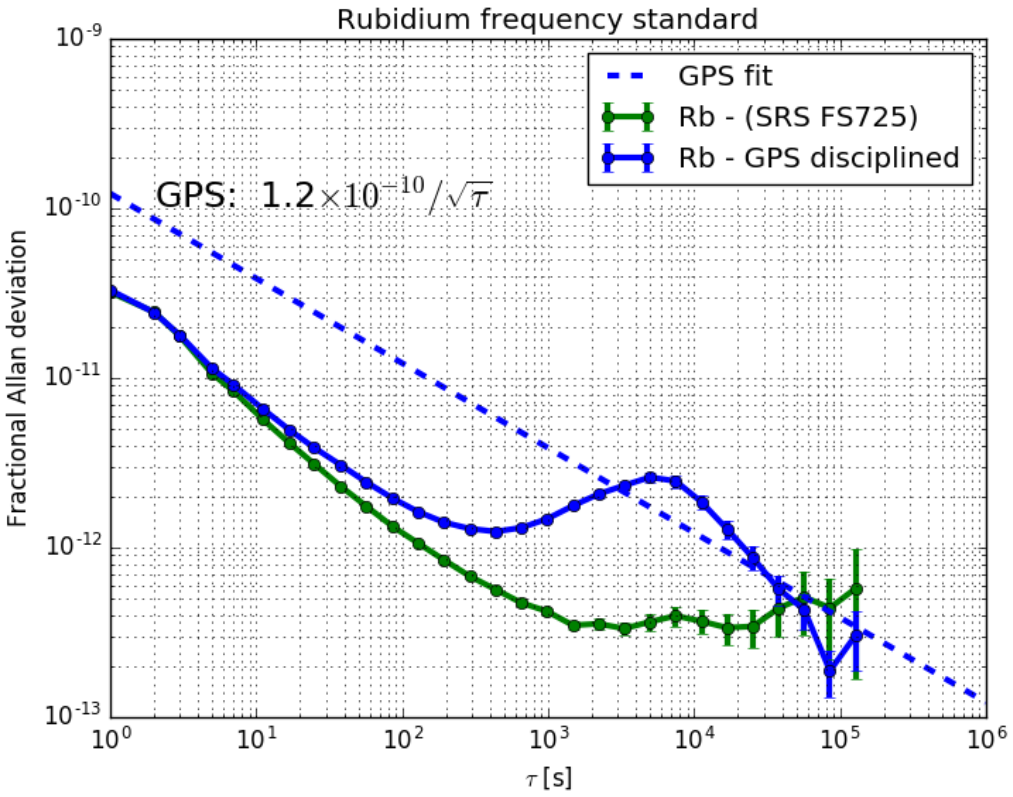

Figure 5.11: Rubidium standard instability (green points) compared with the same rubidium standard disciplined with the GPS signal (blue points). The dashed blue line shows the fit to the tail of the GPS disciplined standard instability, and it predicts the stability of the GPS 1 PPS signal. See text for more detail.

performance of the ^{87}Sr clock, due to the narrow linewidth of the probed transition.

5.4 Mobile interrogation laser

In this section I will present the construction and characterisation of the mobile interrogation laser, which was developed within the Space Optical Clock 2 (SOC2) project. A part of this work was also published in [158].

The SOC2 project [159, 160] is part of the European Space Agency's (ESA) ELIPS-3 programme. It is run by an international consortium of universities and companies across Europe, and funded by the European Union's Seventh Framework Programme. The main goal of the project is to construct a transportable optical atomic clock, that will outperform existing microwave clocks, and serves to prepare optical clocks for future use at the International Space Station (ISS). Such a clock could be used in the future, to test the theory of general relativity, map the gravitational potential of the Earth, or perform interferometry in space [159].

5.4.1 Reference cavity

The cavity vacuum assembly is presented in figure 5.12. The vertical position of the cavity was chosen to reduce the influence of seismic noise [76]. The cavity is mounted on three thin titanium legs with screws, using bush washers and Belleville washers, to ensure the cavity would not loosen over time. The titanium legs are attached to a gold-plated aluminium outer thermal shield, which is similarly suspended on three titanium legs inside a gold-plated aluminium vacuum chamber. Additionally, there is an extra gold-plated aluminium inner thermal shield attached to the cavity, to provide better thermal stability for the cavity. The many shielding layers around the cavity acts as a thermal low-pass filter, filtering fast changes in the temperature. Gold plating is used to decrease the emissivity of the material's surface, and therefore decrease heat transfer between the layers due to radiation. The temperature of the outer thermal shield is stabilised with a copper finger, which is used as a thermal feed-through, with a thermoelectric cooler (TEC) attached outside the vacuum chamber. The vacuum chamber around the cavity is necessary to eliminate the heat transfer between the layers due to convection, as well as reduce the atmospheric pressure fluctuations, which would change the refractive index between the mirrors of the cavity. The vacuum chamber is designed to maintain a low pressure level of around 10^{-7} mbar, by use of a 2 l/s ion pump and a getter. Along the axis of the vacuum chamber, there are two tilted viewports, one for coupling the light into the cavity, and one for inspecting the transmission through the optical resonator. The light is delivered to the system with a

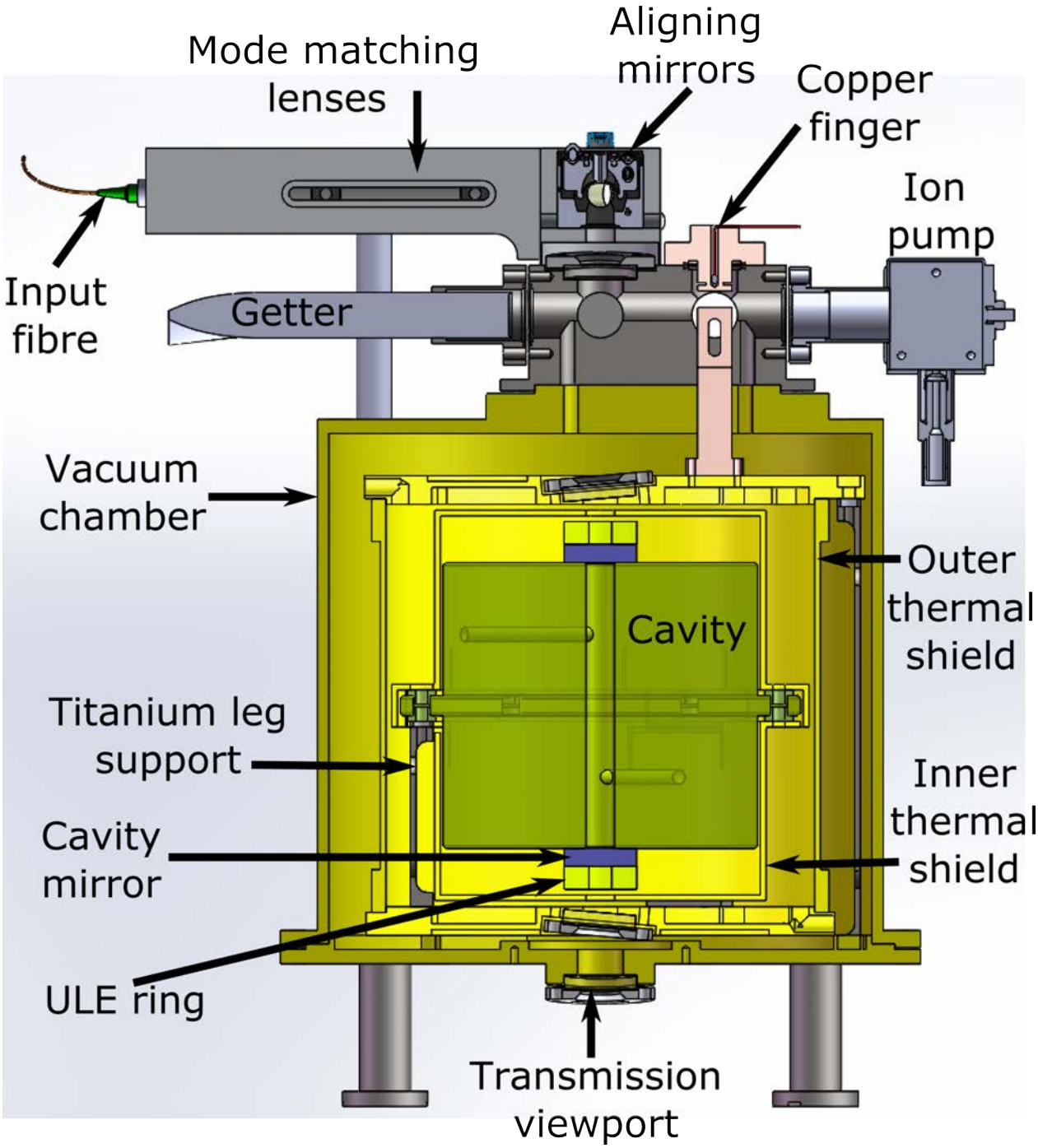

Figure 5.12: Tranportable optical cavity assembly. Courtesy of Dr Rodolphe Le Targat.

polarisation maintaining fibre, collimated and shaped with mode matching lenses, to get the best overlap of the Gaussian beam with the mode of the cavity.

The cavity's spacer is a cylindrical shape, 100 mm long with a 110 mm diameter, and is made of ultra-low expansion (ULE) glass. The spacer features a 7 mm thick collar, located at the equator, that is used to support the cavity close to its midpoint. A high-reflection coated dielectric mirror is optically contacted to each side of the cavity. The mirrors are made of a fused silica substrate, which has a coefficient of thermal expansion (CTE) much higher than ULE. To compensate for the mismatch of CTE, an ULE annulus ring is optically contacted to each mirror. This method allows us to obtain a lower thermal noise limit of 5×10^{-16} compared with the standalone ULE mirrors with a thermal noise value of over 8×10^{-16}. The optical cavity is made from a 1 m radius of curvature concave mirror and a flat mirror. This gives us a 272 μm and 258 μm $1/e^2$ Gaussian beam radii on the concave and the flat mirror, respectively at 698 nm.

Transportation of the reference cavity

The in-vacuum reference optical cavity package, for the interrogation laser of the space optical clock project, was developed at LNE-SYRTE, Paris Observatory in Paris, France, and then transported by car by Dr R. Le Targat and Dr J. Lodewyck to Physikalisch-Technische Bundesanstalt (PTB) in Braunschweig, Germany. The route is presented in figure 5.13. The ion pump maintaining the vacuum in the system, was powered by a car socket throughout the 820 km long journey, successfully keeping the vacuum at a low level without any interruptions. The cavity mounting has been proven to keep the cavity in place throughout the journey, without any problems or misalignment.

5.4.2 Laser head

The laser head was developed at Leibniz Universität Hannover in Germany, and the design is presented in figure 5.14. It is a fibre-coupled single diode laser, which is relatively compact. The diode can be kept at a temperature close to room temperature, which is advantageous to the system. The laser diode (LD), on a special mount, is temperature stabilised with a thermo-electric cooler (TEC), and collimated with a collimating lens (CL). The collimated beam passes through a 1 nm full width at half maximum (FWHM) interference filter (IF), which is used for the coarse tuning of the wavelength, and then a cat's eye lens (L1) focuses the beam onto an out-coupling mirror, with 30% reflectivity and mounted on a piezo-electric transducer (PZT). The PZT lets us tune the wavelength of the laser, by changing the length of the external cavity, between the laser diode and the mirror. The re-collimating lens (L2) collimates the beam, after the

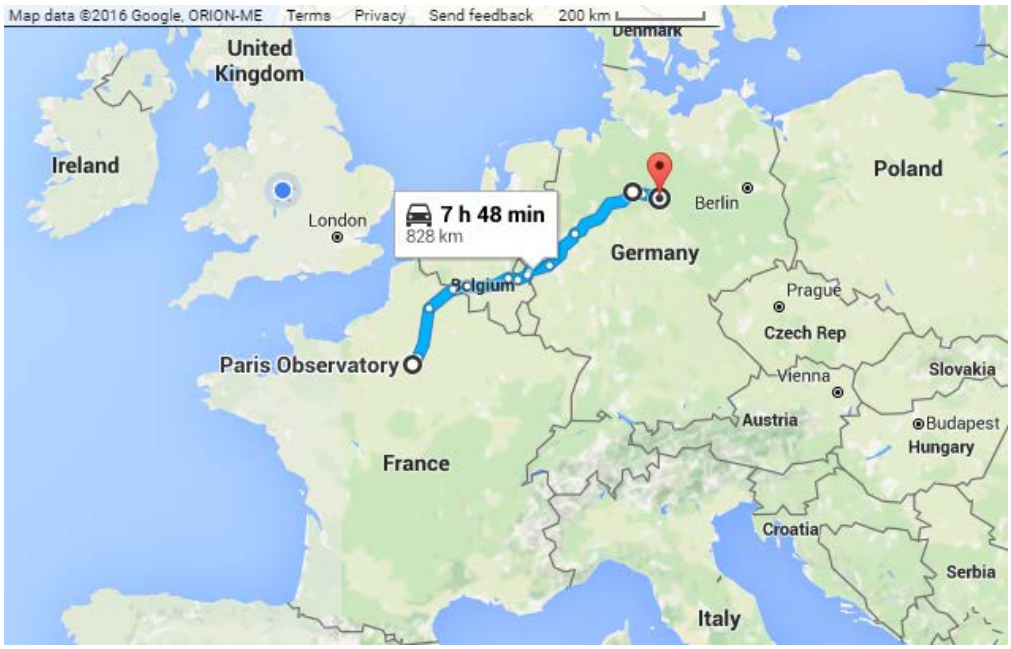

Figure 5.13: The optical resonator in a vacuum chamber was transported from Paris, France, to Braunschweig, Germany, approximately 830 km by car. Courtesy of Google Maps.

cat's eye retro-reflector, back to its original shape. The two mirrors (M1 and M2) are used to inject the light into the polarisation-maintaining fibre with a fibre coupler (FC). Before reaching the fibre-coupler, the beam passes through two optical Faraday isolators (OFI1 and OFI2), to avoid any interference by back-reflected light shining onto the laser diode.

This laser head design brings many advantages to our system. Its greatest one is its high power of 15 mW, after the fibre ($\tilde{3}$0 mW before the fibre), while using a single diode only. It gives us enough power for the whole experiment, and it replaced a previously used laser in a master-slave configuration. Another major advantage of the laser is that it can be easily tuned by rotating an interference filter, which does not divert the laser beam and it stays well injected into the fibre. Also, the interference filter is attached to a rotatable mount which can be accessed without opening the lid. The previously used laser head had to be kept at a relatively high temperature of around 50°C to reach the desired wavelength. In our laser head, the diode is stabilised at the room temperature, which is easier to do and consumes less power. It is important for a laser intended to be used in space.

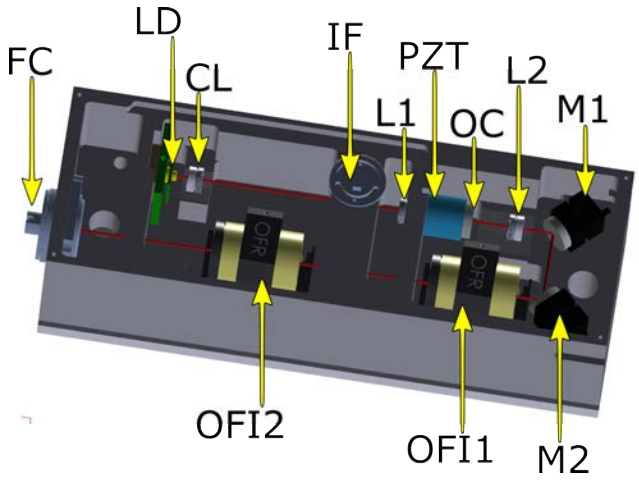

Figure 5.14: Laser head of the ultra-stable 698 nm laser. LD - laser diode; CL - collimating lens; IF - interference filter; L1 - cat's eye lens; PZT - piezo-electric transducer; OC - out-coupling mirror; L2 - re-collimating lens; M1, M2 - fibre-coupling mirrors; OFI1, OFI2 - optical Faraday isolators; FC - Fibre coupler. Figure also used in [158].

5.4.3 Distribution module

As presented in figure 5.15 and 5.16, the laser head is placed inside a distribution module, where the beam is first mode-filtered with a single mode, polarisation maintaining fibre. Then the laser light is split between three branches using a polarising beam splitter and a non-polarising beam splitter. The first branch is used for Pound-Drever-Hall stabilisation to the high finesse reference cavity, presented in subsection 5.4.1. To do this, the beam first passes through a double-pass 200 MHz AOM1, and is coupled into a fibre-coupled EOM. After the fibre, the beam is shaped with mode-matching lenses, and coupled into the cavity using two mirrors. One of the mirrors is also a non-polarising beam splitter, with a 10:90 reflection:transmission splitting ratio. The beam that is reflected back, from the cavity, transmits through the beam splitter and hits the photodiode. The radio frequency (RF) part of the signal from the photodiode is filtered, amplified, and demodulated, using the EOM's frequency to generate the PDH error signal. The error signal is then amplified using servo electronics. The fast output from the servo electronics is fed back to the DC-coupled fast modulation input of the laser head for fast locking. The slow output is fed back to the laser's PZT for slow locking. On the cavity's output, there is an additional photodiode monitoring the power level of the light that is transmitted through. The voltage on the photodiode is compared with a reference voltage, to correct the power level, before the cavity, with the AOM1, so that the transmitted power is stable. The AOM1 is also used for frequency shifting the frequency of the laser, so that it is kept at the resonance frequency of the clock transition in strontium.

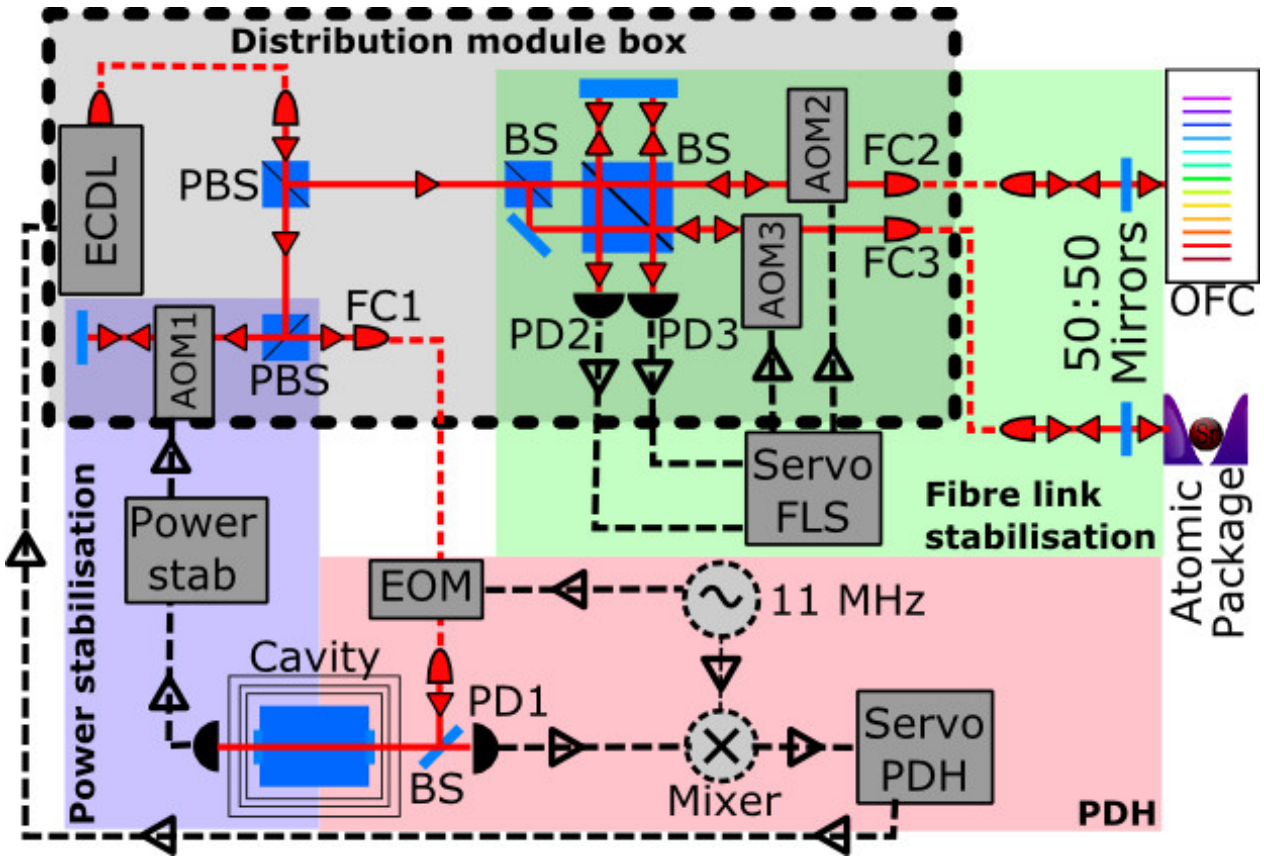

Figure 5.15: Distribution module. ECDL - external cavity diode laser; PBS - polarising beam splitter; BS - non-polarising beam splitter; AOM - acousto-optical modulator; EOM - electro-optical modulator; FC - fibre coupler; PD - photodiode; PDH - Pound-Drever-Hall; FLS - fibre link stabilisation; OFC - optical frequency comb.

The second and third branches are sent to the optical frequency comb (OFC) and the atomic package, respectively. The light is frequency shifted with an 80 MHz AOM, which also acts as an optical switch, and coupled into the fibre. After the fibre output, there is a half-reflecting mirror which reflects part of the light back into the fibre. The reflected light passes through the AOM again and is superimposed with original beam before it hits the photodiode. At the photodiode, the beat note frequency is read to be of double the modulation frequency of the AOM (160 MHz). This frequency is phase-locked, by a fibre link stabilisation servo, to a reference frequency by modifying the AOM's frequency. This way, any phase-shifts that have accumulated inside the fibre, due to thermal effects and mechanical instability, are cancelled out. The advantage of this system is that one beam splitter and one reference beam mirror are used for both beams, which effectively lets us stabilise the fibre link between the atomic package and the optical frequency comb.

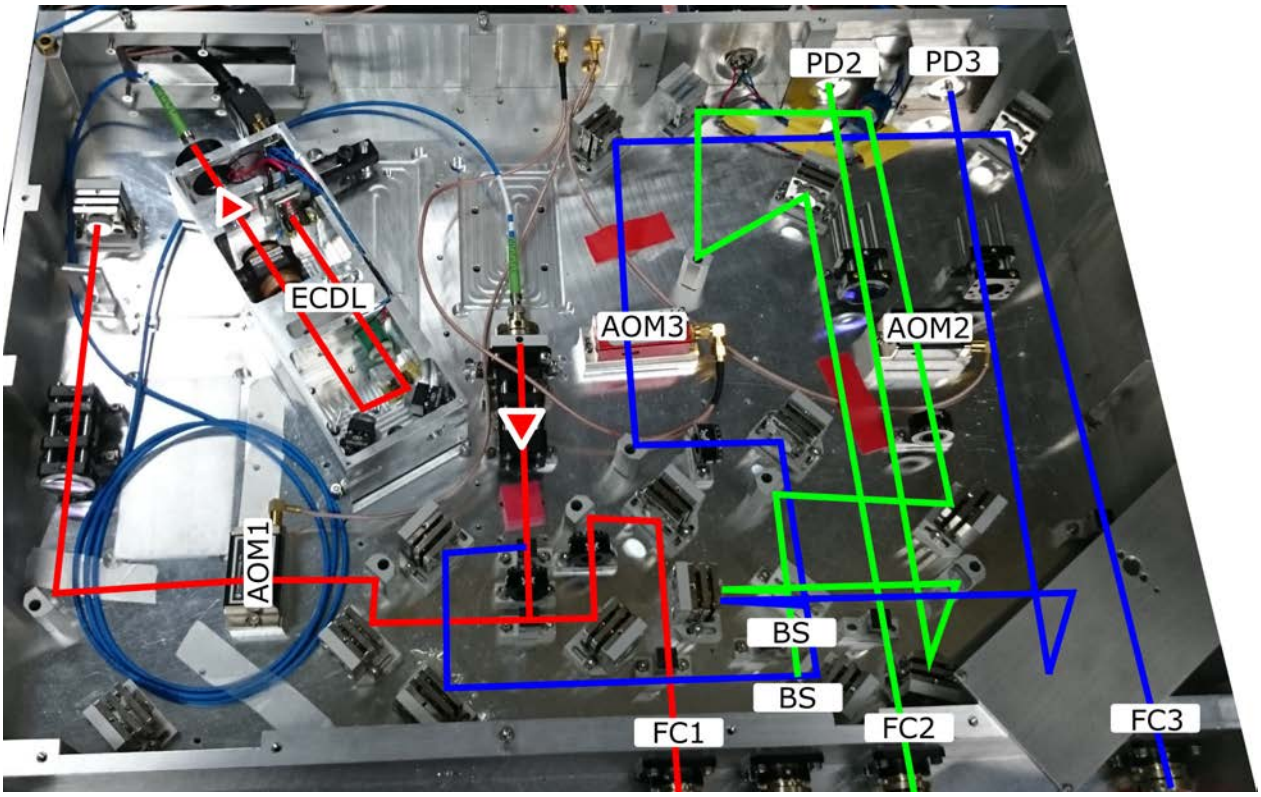

Figure 5.16: Picture of the distribution module. Labels as in the schematic figure 5.15. Red colour represents the initial beam, also used for PDH locking. Blue colour line and green colour line present beam path used for the atomic package and the the optical frequency comb respectively.

By and large, the system features all necessary components for operating the optical atomic clock, including the fibre link stabilisation, power stabilisation, AOMs for switching on and off the beams and for fine-tuning the frequency to reach the atomic resonance. Despite many outputs and the fibre link stabilisation, the laser head gives enough power to operate them all without amplification. It is also easy to change the laser's frequency on the atomic output, to switch between the ^{88}Sr and ^{87}Sr isotopes, which is presented in figure 5.17. The optical frequencies of the SOC2 laser were established by measuring a beat note frequency between the laser's OFC output and the stationary ultra-stable laser called 'Beast', which is stabilised to the ^{87}Sr clock transition. The Beast laser is described in detail by Häfner in [71, 80]. Our beat note is read to be 57 MHz, which places our laser output frequency between the ^{87}Sr and ^{88}Sr clock transitions, about 23 MHz away from ^{87}Sr, and roughly 39 MHz away from ^{88}Sr. This frequency difference can be tuned with AOM1 or by changing the AOM2/AOM3 frequency.

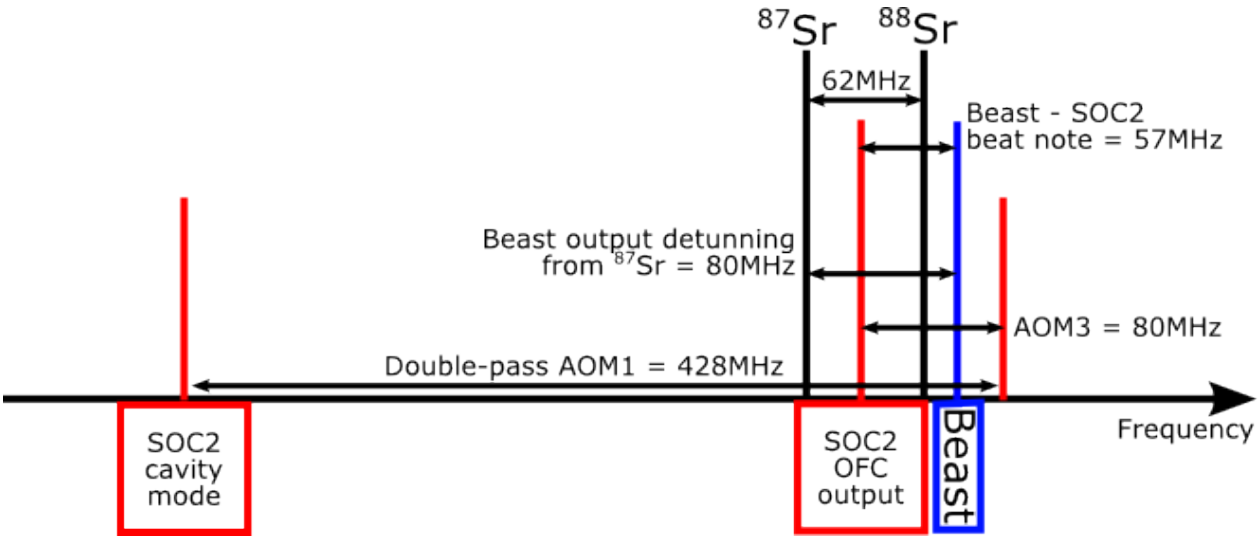

Figure 5.17: Frequencies chart of the mobile interrogation clock laser beams in relation to the strontium clock transitions and the Beast stationary laser.

5.4.4 Mode matching and coupling efficiency

It is necessary to match the Gaussian mode of the laser beam with the fundamental Gaussian mode of the cavity, in order to obtain an efficient injection. This process is commonly know as the mode matching of the laser beam. In our setup, we have built a telescope, after the collimated output of the fibre-coupled EOM, to overlap the modes as much as possible. The telescope is formed by f = 60 mm and f = 25 mm lenses that reduce the waist of the beam by a factor of 2.4, giving a theoretical value, for the mode overlap, of above 99% if placed at the optimal distance. To measure the coupling efficiency, we measured the the power level of the cavity reflected part of the beam, using the DC-coupled output of the Pound-Drever-Hall (PDH) photodiode. We measured the reflected power levels in three situations; when the laser is unlocked ($P_{unlocked}$), when the laser is locked to the carrier ($P_{c-locked}$), and when the laser is locked to the PDH sideband ($P_{s-locked}$). In the first case, we measured the combined power of the two sidebands $2P_s$, and the carrier P_c. During the second measurement, we obtained a value for the power level corresponding to the two sidebands $2P_s$, plus the power of the carrier, partially reflected back due to the inefficient coupling, $(1-\epsilon)P_c$, where ϵ is the coupling efficiency coefficient. The third step of the measurement gave us a power level equal to the sum of the power of the carrier P_c, the power of the first sideband P_s, and the partially reflected power of the second

sideband $(1-\epsilon)P_s$. Thus, we obtain the simultaneous equations

$$\left\{ \begin{array}{l} P_{unlocked} = P_c + 2P_s \\ \\ P_{c-locked} = (1-\epsilon)P_c + 2P_s \\ \\ P_{s-locked} = P_c + P_s + (1-\epsilon)P_s \end{array} \right\} \tag{5.16}$$

which we can use to calculate the relative power in the sideband $P_s/P_c = 21\%$, as well as the coupling efficiency $\epsilon = 0.69$. The efficiency value is smaller than expected from the calculations, which we assign to mechanical tolerances. Thanks to the efficiency value being known, we will be able to evaluate the power absorbed/scattered by the cavity.

To lock the laser to one of the sidebands, we have simply changed the phase of the demodulation signal on the DDS by 180°, which inverts the error function, allowing us to lock to the sideband using exactly the same settings and cabling.

5.4.5 Stability performance of the laser

The stability of the SOC2 clock laser was assessed by comparing its frequency to the Beast laser's frequency. It was performed by measuring the beat note frequency with a dead-time-free frequency counter; the FXE from K+K GmbH. To do this, two beams were overlapped and shone over a fast photodiode. The signal from the photodiode was filtered, amplified, and sent to the frequency counter. To analyse the instability of the SOC2 laser, we computed the fractional frequency Allan deviation, which is plotted in figure 5.18. When calculating the Allan deviation, the linear frequency drift was removed. The plot shows a 24-hour long measurement, with the blue dotted line. The green squared line shows the best 1-hour slot within the full measurement, which was found using a script that analysed each 1-hour long window to find the best stability. The best instability the laser achieved in under 1 s is 7.9×10^{-16}. Thanks to the Beast laser being one order of magnitude more stable than our mobile laser (8×10^{-17} in two seconds [71]), we can assume that the plotted Allan deviation represents our SOC2 interrogation laser only. The estimated thermal noise limit of our cavity is approximately 5×10^{-16}. The minimum value of the measured instability is therefore very close to the estimated thermal noise limit. The full measurement being less stable than the best 1-hour window is probably caused by the pressure fluctuations, inside the cavity vacuum chamber, that were observed at the ion pump controller. We will analyse the influence of the vacuum level fluctuations, in more detail, in the

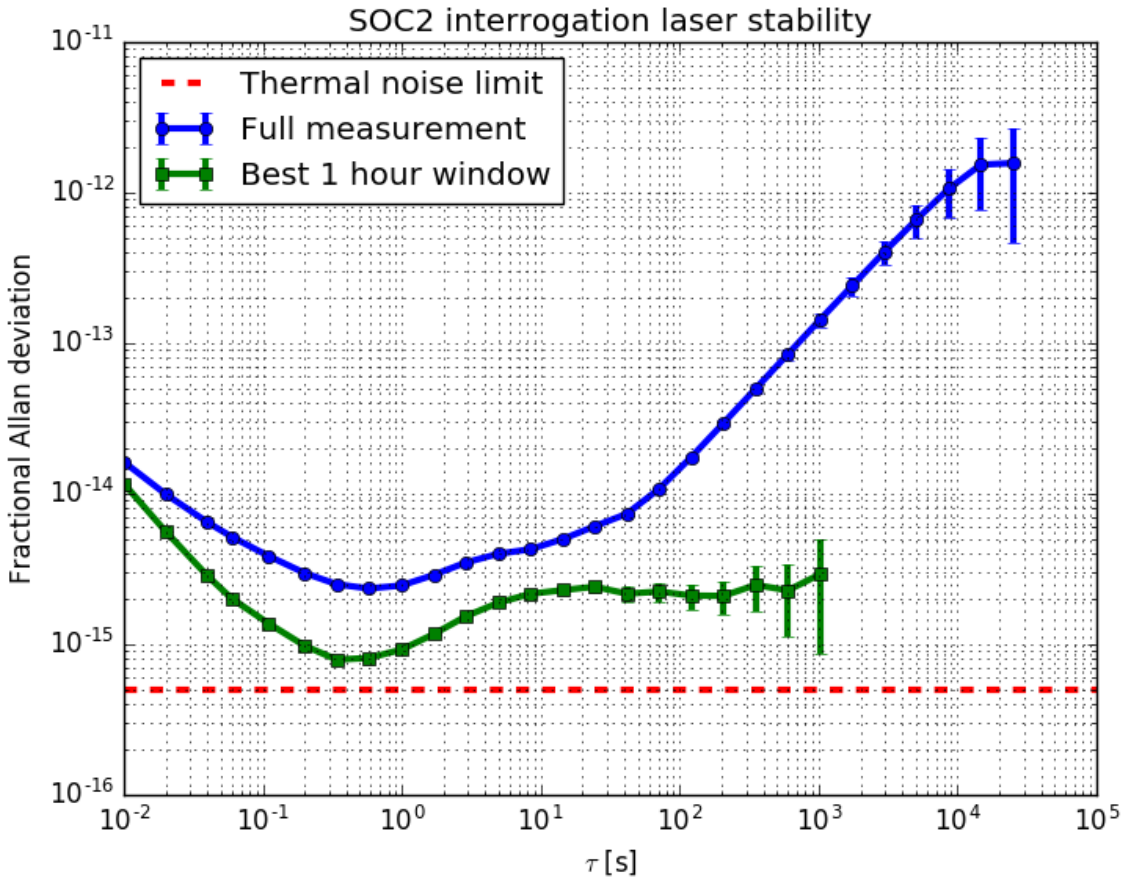

Figure 5.18: Fractional Allan deviation of the SOC2 interrogation laser with linear drift removed. The blue dotted line shows a 24-hour long measurement. The green squared line shows the best 1-hour slot within the full measurement, and is seen to be approaching the minimum of 7.9×10^{-16}. The thermal noise limit of the cavity is presented by the red dashed line. Figure also used in [158].

next subsection.

5.4.6 Influence of the vacuum pressure level on stability

The resonant mode frequency of the cavity depends on the optical length of the optical resonator, as shown by the formula 4.1 in section 4.3.1

$$nL = N\frac{\lambda_{vac}}{2}, \tag{5.17}$$

where n is the refractive index of air, L is the distance between the mirrors, N is the mode's number (integer), and λ_{vac} is the laser's wavelength in vacuum. The optical length is proportional to the refractive index of the medium n, in which the light propagates. Although the refractive index in vacuum is equal to 1 by definition,

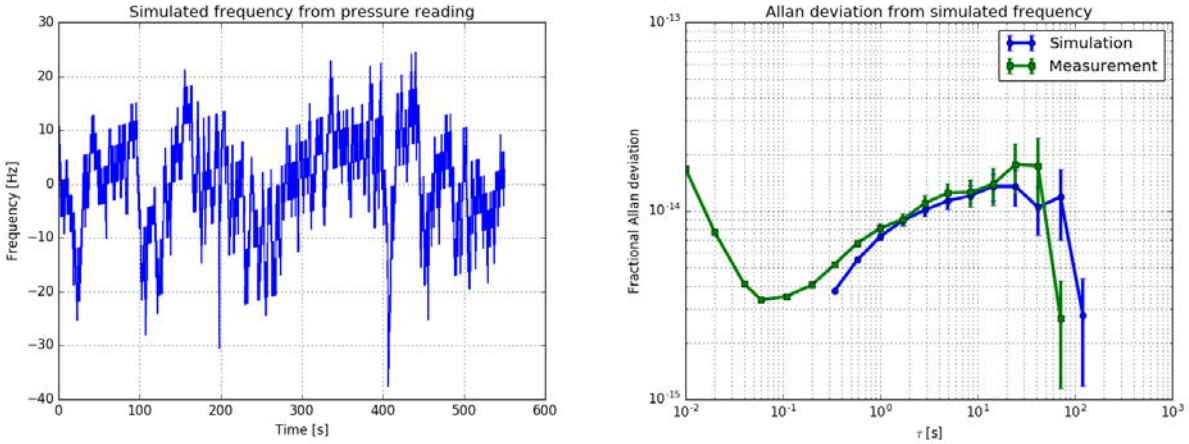

(a) Frequency simulation.

(b) Fractional Allan deviation.

Figure 5.19: **(a)** Simulated frequency of the resonant mode of the cavity. The simulation was based on the ion pump current readings, using the modified Edlén equations to estimate the refractive index of air inside the cavity. **(b)** The blue circled line represents the fractional Allan deviation of the simulated frequency. The green squared line represents the fractional Allan deviation of the measured frequency of the laser, which was taken on the same day as the pressure measurement. Both frequencies have the linear drift removed. Figures also used in [158].

the perfect vacuum does not exist, and the residual pressure level keeps the refractive index slightly higher.

We have noticed the presence of pressure fluctuations, in the vacuum chamber of the clock laser, that could influence the stability of the laser. The vacuum chamber was designed to maintain the pressure level at 1×10^{-7} mbar, however, due to leaks in the base flange, the pressure level fluctuates and was 2.5×10^{-6} mbar during the measurements. To see what influence it would have on the cavity's mode frequency, we have recorded the current through the ion pump, to simulate the change in the refractive index inside the vacuum chamber. The recorded current level was used to calculate the pressure inside the vacuum chamber, which was used to calculate the refractive index of air using the modified Edlén equations [137, 138, 139]. The calculated refractive index is $n - 1 = 4.21 \times 10^{-7}$, and the pressure sensitivity of the pressure level is estimated to be -120 Hz/(10^{-6} mbar) or -3×10^{-13}/(10^{-6} mbar) in fractional frequency units. The simulated frequency is presented in figure 5.19a. The fractional Allan deviation of the simulated frequency was calculated and is presented in figure 5.19b as blue circles, together with the fractional Allan deviation calculated for the measured frequency of the laser (green squares). Both measurements were performed roughly at the same time and linear drifts were removed for both of them. As shown in the figure, the simulation curve and the measurement curve are very close to each other, which suggests that the residual pressure fluctuations might be the main reason for the instability of the clock laser. The vacuum chamber leak is planned to be fixed in

the near future.

5.4.7 Power sensitivity

When the laser is locked to the cavity, the laser's beam travels between the mirrors of the cavity, causing the power to accumulate inside the cavity. Part of the power leaks outside, and the other part is scattered or absorbed by the mirror coating. The absorbed part of the light leads to local heating of the mirror coating and the mirror substrate, causing deformation. We would like to investigate how the distance between the mirrors changes due to this effect. More information about the photo-thermal effect in mirrors can be found in the article by Farsi et al. [161].

The laser remained stabilised to the fundamental mode of the cavity, with approximately 20 μW of light being sent into the cavity. This power can easily be changed with the double-pass AOM1 shown in figure 5.15. To examine the power sensitivity, we have modulated the power, before the cavity, with a square signal with the modulation period equal to 20 s. By using a photodiode on the output of the cavity, we could measure the transmitted power amplitude which was found to be 0.5 μW, and corresponds to about 20% modulation depth. Simultaneously, the frequency of the laser was measured with a frequency counter, to observe a double exponential curve, also presented in figure 5.20. The black points show an averaged frequency measurement, with the linear drift removed. The red curve is a double exponential fit $f(x) = \mathrm{A}\exp(-\mathrm{B}x)+\mathrm{C}\exp(-\mathrm{D}x)+\mathrm{E}$. The two time constants from the fitted function are equal to $1/B = 3.05$ s and $1/D = 0.24$ s. The amplitudes for the long-term and the short-term effects are equal to $A = -37$ Hz and $C = -53$ Hz, respectively. From the amplitude values, it is possible to calculate the overall power sensitivity, which is equal to 180 Hz/μW or $4.2 \times 10^{-13}/\mu$W in fractional frequency units.

During standard operation of the clock, we measured approximately 1.5 μW of power transmitted through the cavity. To obtain a 10^{-15} instability level, this power has to be stable at a level of 3.5 nW or 2.3×10^{-3} in relative power. The power before the EOM is at the 1 mW level, and it is required that it would not fluctuate by more than 2.3 μW. However, due to spatial mode filtering with the polarisation maintaining fibre, and the fluctuating laser amplitude, the power fluctuations were observed to exceed this limit.

To ensure that the power fluctuations in the beam would not affect the instability level of the clock laser, we have introduced a power stabilisation system into our setup. As presented in figure 5.15, the photodiode is used to measure the cavity's transmitted power. The voltage from the photodiode is then compared with a reference voltage by a servo, which modifies the RF power sent to the AOM, to keep the transmitted optical power on a stable level. The AOM needs to be operated below the maximum efficiency RF power value,

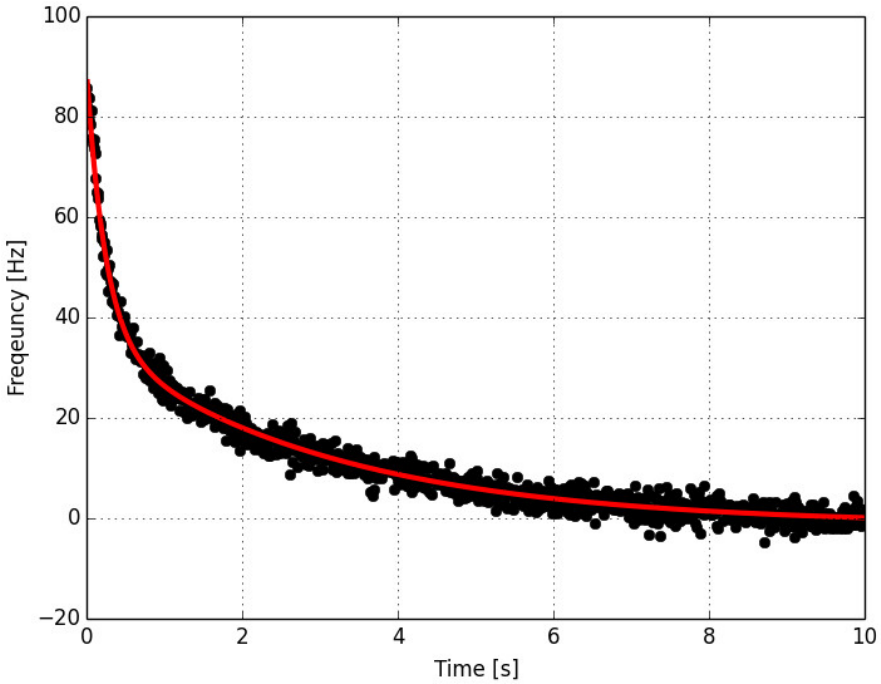

Figure 5.20: Power sensitivity measurement. Power of the laser beam injected to the optical resonator is reduced, which leads to deformation of the resonator's mirrors due to the photo-thermal effect. Black points show the relative optical frequency change of the interrogation laser, after the power level is changed. Red curve shows a double-exponential fit to the data points.

to ensure a roughly linear response to the RF power change. To assess whether the power stabilisation is working, we analyse the fractional Allan deviation of the laser's frequency when the power stabilisation is turned on and when it is turned off. In figure 5.21, the fractional Allan deviation when the power stabilisation is turned on and off is represented by blue points and green squares, respectively. We see that with the power stabilisation turned on, the laser's instability reaches lower values for averaging times τ larger than 100 ms. The reduction, although noticeable, is smaller than expected. As described in subsection 5.4.6, the pressure level in the chamber might cause additional frequency fluctuations of the laser. It is therefore believed, that the power stabilisation performance measurement was limited from the relatively high pressure level in the vacuum chamber.

5.4.8 Acceleration sensitivity

As the ultra-stable laser is a part of a mobile system, it is also important to know how it behaves when it accelerates in various directions. The most crucial element of the laser is the reference cavity, as the laser is

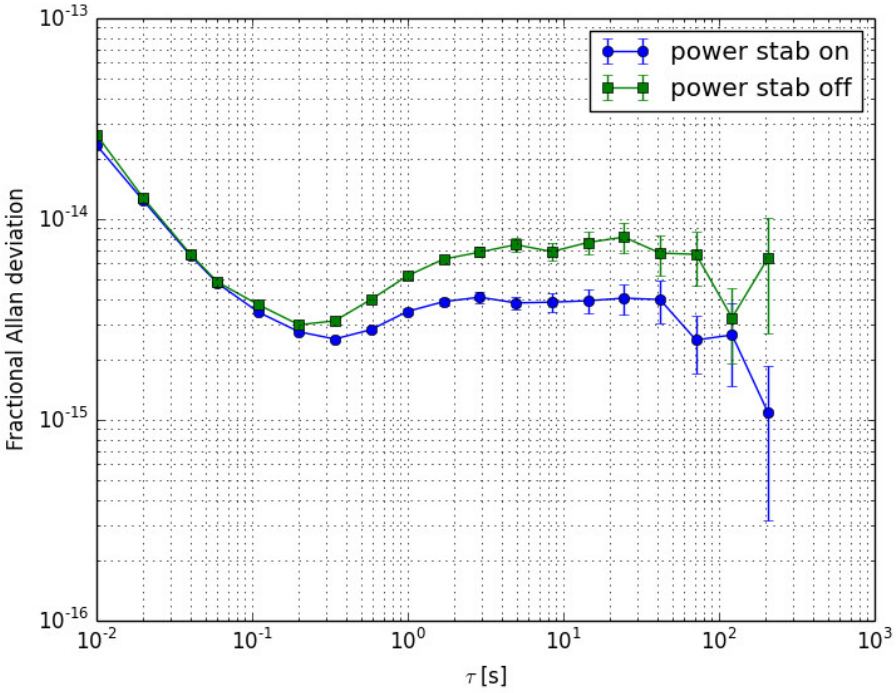

Figure 5.21: Fractional Allan deviation of the laser's frequency with power stabilisation turned on (blue points) and turned off (green squares). Figure also used in [158].

stabilised to it and its frequency closely follows the resonance frequency of the cavity. In this section we will analyse how sensitive the frequency of the laser is to acceleration change on the reference cavity. This can be done in two different ways. An active way would be when the cavity is shaken in different directions, while accelerometers measure the acceleration values along the three axes. A static way allows us to average the results over a longer period, as we only use the gravitational acceleration, but, by rotating the cavity, can change the direction in which it is applied. Thanks to this, we can use an acceleration value which is very well known. To measure the acceleration sensitivity we will use the static approach.

Measurements were performed in five directions: Z, X, Y, X' and Y', which are also shown in figure 5.22a. First, the acceleration sensitivity was measured in the Z direction, by flipping the cavity upside down. The revolution of the cavity is shown in figure 5.22b, with a beat note frequency visible on a spectrum analyser at the top of the figure. In this way, the acceleration along the Z axis was changed from $-g$ to $+g$, where $g \approx 9.81$ m/s^2 is the value of the Earth's gravitational acceleration. To see how the frequency changes, while the flipping was performed, the laser remained locked to the cavity and its frequency was recorded using a frequency counter. The recorded frequency is presented in figure 5.23a. The red line and the blue

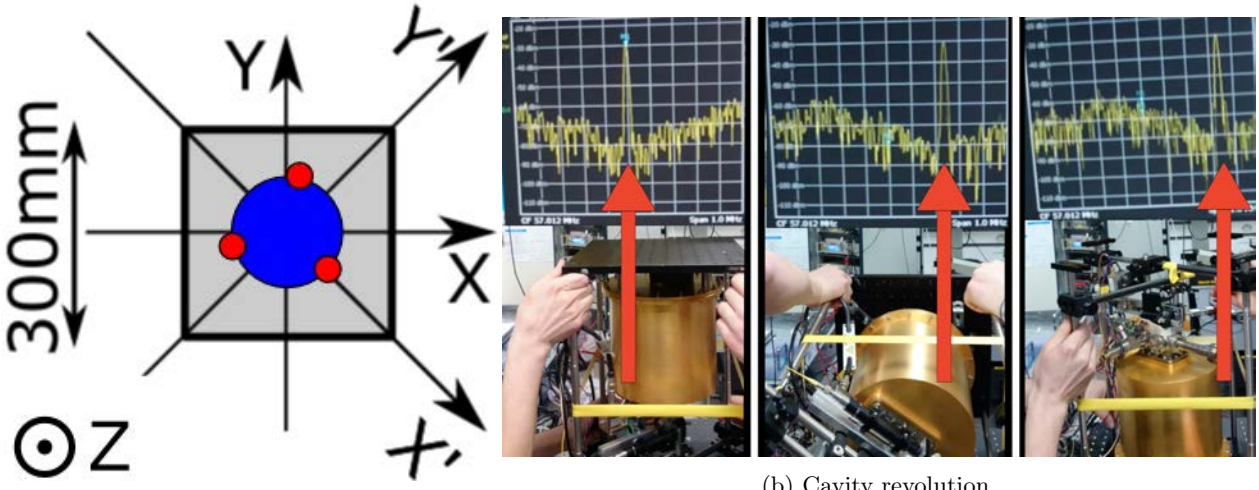

(a) Coordinates.

(b) Cavity revolution.

Figure 5.22: **(a)** Coordinates assigned to the cavity (top view). The blue circle represents the cavity, whereas the red circles show the position of the supports. **(b)** The procedure for measuring acceleration sensitivity in the Z direction. At the top of the figure, a spectrum analyser screen is visible, with a red arrow pointing at the beat note frequency. The span of the spectrum analyser is 1 MHz. Figure also used in [158].

line represent linear functions fitted to the frequency, when the cavity rests upside down and in its upright position, respectively. To obtain a value for the sensitivity, the frequency shift was divided by the change in acceleration, in that direction, to get a result of $S_Z = -3.6 \times 10^{-10}$/g.

The measurement of the acceleration sensitivity in the X and Y directions were performed in a similar way. The frequency change from the cavity's upright position to when the cavity was lying on its side was measured. Since the acceleration sensitivity value along Z direction was already known from the previous measurement, it was only necessary to rotate the cavity by 90°. This way, the gravitational acceleration vector overlapped with the X and Y axis, for the acceleration sensitivity measurement in the X and Y direction, respectively. The observed frequency shift is presented in figure 5.23b for the X axis, and in figure 5.23c for the Y axis. The shift results from zeroing the acceleration along the Z axis, and from applying an acceleration g along the X and Y direction. Since we already know the value of the acceleration sensitivity in the Z direction, we can use it to extract the X and Y sensitivities from the measurement. The sensitivities in X and Y direction are equal to $S_X = -5.8 \times 10^{-10}$/g and $S_Y = -3.1 \times 10^{-10}$/g, respectively.

In figure 5.23, the equations of the fitted linear functions are also presented. From the equations we can see that not only the frequency shifts, but also the drift of the cavity changes for different positions. This can be caused by the relaxation of the material, and internal stresses caused by the mounting.

The acceleration sensitivity measurement along X' direction was performed by tilting the cavity, by small

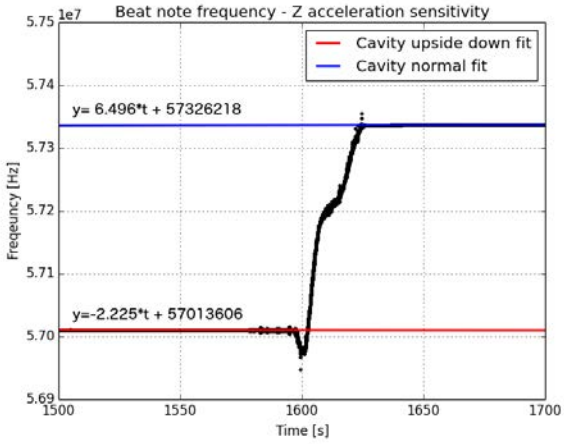

(a) Frequency change during 180° revolution.

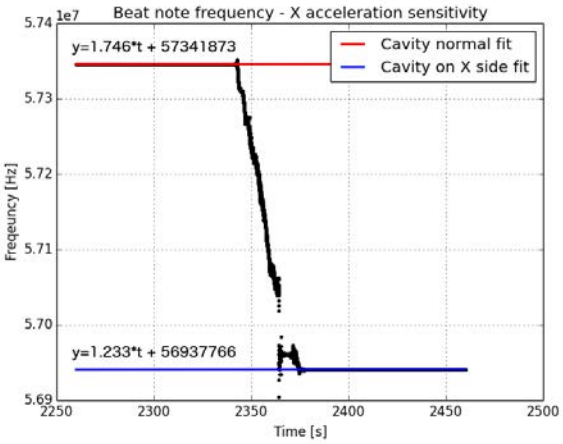

(b) Frequency change during 90° revolution.

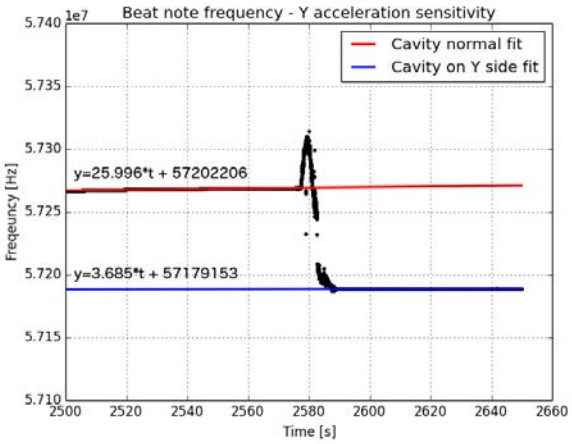

(c) Frequency change during 90° revolution.

Figure 5.23: Acceleration sensitivity measurements in **(a)** Z direction, **(b)** X direction and **(a)** Y direction.

angles α and $-\alpha$ in the X' direction, as presented in figure 5.24. By tilting the cavity by both positive and negative angle α, we change the acceleration along the Z axis to the same value, from $g\cos(\alpha)$ to $g\cos(-\alpha) = g\cos(\alpha)$. Therefore, if we subtract the frequencies at those two different positions, we will obtain a frequency shift, resulting from the change in acceleration along the X' axis from $g\sin(\alpha)$ to $g\sin(-\alpha)$.

The measurement was carried out in the following sequence. First, the cavity was levelled in its upright position. Second, the cavity was tilted towards the positive values of the x' axis by $\alpha = 2.7°$, so that the X' axis was pointing slightly downwards (exactly as presented in figure 5.24). Third, the cavity was tilted towards the negative values of the X' axis by the same angle ($-\alpha = -2.7°$). Last, the cavity was again levelled in its upright position. During the whole sequence, the frequency of the laser was measured with a frequency counter, and it is plotted in figure 5.25a. The red line in the figure shows a linear fit to the

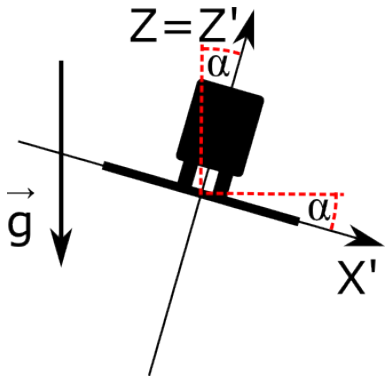

Figure 5.24: Procedure for the acceleration sensitivity measurement along the X' and Y' axes.

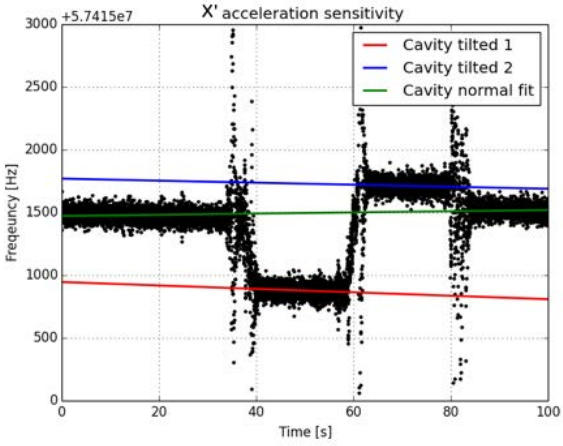

(a) Frequency change during a 90° revolution.

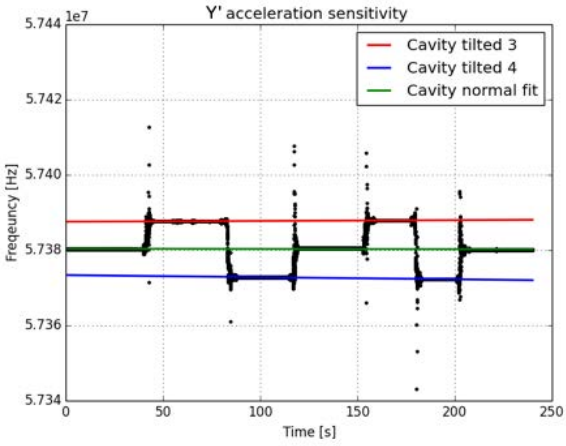

(b) Frequency change during a 90° revolution.

Figure 5.25: Acceleration sensitivity measurements in **(a)** X' direction and **(b)** Y' direction

frequency, when the cavity is tilted by a positive angle α. The blue line shows a linear fit to the frequency, when the cavity is tilted by a negative angle $-\alpha$. The green line shows a linear fit to the frequency, when the cavity is levelled in its upright position. From the fitting parameters, we can see that the frequency changed by $\Delta f(\alpha) = -527$ Hz and $\Delta f(-\alpha) = 297$ Hz for the positive angle and negative angle tilt, respectively. This change is partly caused by the decreasing acceleration value along the Z axis, which shifts the frequency by $\Delta f_Z(\alpha) = S_Z \Delta a_Z(\alpha)$, where S_Z is the acceleration sensitivity along the Z axis, and $\Delta a_Z(\alpha)$ is the value of the acceleration change along the Z axis. In our case, the acceleration changes from a_Z = -g to a_Z = -g cos (α), giving $\Delta a_Z(\alpha)$ = g(cos $(\alpha) - 1$). Similarly, part of the frequency change results from the increasing acceleration along the X' axis, from $a_{X'} = 0$ to $a_{X'} = \sin(\alpha)$, giving $\Delta a_{X'}(\alpha) = g \sin(\alpha)$. We can

now write the following equation

$$\Delta f(\alpha) = \Delta f_Z(\alpha) + \Delta f_{X'}(\alpha) = S_Z \Delta a_Z(\alpha) + S_{X'} \Delta a_{X'}(\alpha) = S_Z \mathrm{g}(1 - \cos(\alpha)) + S_{X'} \mathrm{g} \sin(\alpha). \tag{5.18}$$

For positive angle tilt and negative angle tilt we can write the following simultaneous equations:

$$\left\{ \begin{array}{l} \Delta f(\alpha) = S_Z \mathrm{g}(1 - \cos(\alpha)) + S_{X'} \mathrm{g} \sin\alpha \\ \\ \Delta f(-\alpha) = S_Z \mathrm{g}(1 - \cos(\alpha)) - S_{X'} \mathrm{g} \sin\alpha \end{array} \right\} \tag{5.19}$$

The only unknown in these simultaneous equations are the sensitivity values S_Z and $S_{X'}$. Solving these equations using the fitting parameters, we obtain the sensitivity in the X' direction $S_{X'} = -2.0 \times 10^{-11}/\mathrm{g}$ and Z direction $S_Z = -2.4 \times 10^{-10}/\mathrm{g}$, which is in good agreement with the result obtained by flipping the cavity upside down.

The sensitivity in the Y' direction was obtained in a similar way to the X' direction, with a slightly different sequence. First, the cavity was levelled. Second, the cavity was tilted by a negative angle $-\alpha = -2.7°$, so that the Y' axis pointed slightly upwards. Third, the cavity was tilted to the other side by a positive angle $\alpha = 2.7°$, so that the Y' axis pointed slightly downwards. Then, the cavity was levelled and the sequence was repeated. The measured frequency is presented in figure 5.25b. The green line shows a linear fit to the frequency, when the cavity is positioned in its upright position. The red line is a linear fit to the frequency, when the cavity is tilted by a negative angle $-\alpha$. The blue line is a linear fit to the frequency, when the cavity is tilted by a positive angle α. Again, from the fitting parameters, we obtain $\Delta f(\alpha) = -7027$ Hz and $\Delta f(-\alpha) = 7160$ Hz for the positive angle and negative angle tilt, respectively. Solving the set of simultaneous equations

$$\left\{ \begin{array}{l} \Delta f(\alpha) = S_Z \mathrm{g}(1 - \cos(\alpha)) + S_{Y'} \mathrm{g} \sin\alpha \\ \\ \Delta f(-\alpha) = S_Z \mathrm{g}(1 - \cos(\alpha)) - S_{Y'} \mathrm{g} \sin\alpha \end{array} \right\} \tag{5.20}$$

we obtain a value, for the sensitivity in the Y' direction, equal to $S_{Y'} = -3.5 \times 10^{-10}/\mathrm{g}$. The sensitivity value for Z, calculated from the measurement, is equal to $S_Z = 1.4 \times 10^{-10}/\mathrm{g}$; however, due to the relatively large sensitivity in the Y' direction, the value cannot be determined accurately.

Ideally, thanks to the axial symmetry of the system, we should only need to distinguish between two types of acceleration sensitivity: axial and radial. Due to mechanical constraints, manufacturing tolerances,

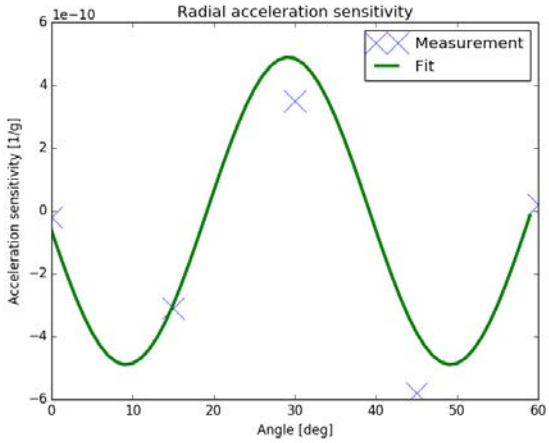

Figure 5.26: Radial acceleration sensitivity as a function of the azimuthal angle. Blue crosses show the measured values of the acceleration sensitivity. The green curve shows a sinusoidal fit to the points.

and the type of mounting, we observe different values for the acceleration sensitivity, for different azimuth angles. I define the azimuthal angle φ as an angle measured from the X' axis (fig. 5.22a). This way, for the X' axis $\varphi_{X'} = 0°$, for the X axis $\varphi_X = 45°$, for the Y' axis $\varphi_{Y'} = 90°$, and for the Y axis $\varphi_Y = 135°$. Using the 3-fold symmetry of the system, we assume that the sensitivity $S(\varphi)$ has the condition:

$$S(\varphi) = S(\varphi + 120°). \tag{5.21}$$

From the performed measurements, we have also observed that the additional antisymmetric condition applies:

$$S(\varphi) = -S(\varphi + 180°). \tag{5.22}$$

Both conditions 5.21 and 5.22 lets us narrow the range of arguments from the full angle 360° to just 60°, giving:

- $S_{X'} = S(\mathbf{0}°) = -S(\mathbf{60}°)$,
- $S_X = S(45°) = S(\mathbf{45}°)$,
- $S_{Y'} = S(90°) = -S(\mathbf{30}°)$,
- $S_Y = S(135°) = S(\mathbf{15}°)$.

The sensitivity values, for the azimuthal angles in bold, are plotted in figure 5.26 with blue crosses. The radial acceleration sensitivity function is expected to be a periodic function, to not break the symmetry

conditions 5.21 and 5.22. The green curve in the figure shows a sinusoidal fit to the points, with amplitude 4.9×10^{-10}/g and period 40°. The root mean square (RMS) radial acceleration sensitivity is therefore equal to $S_{r-RMS} = 3.5 \times 10^{-10}$/g

Compared with counter designs, the cavity does not have a smaller acceleration sensitivity, which is probably the result of a rigid mounting, which can withstand very large values, of several g, for the acceleration in any direction.

5.5 SOC2 atomic package

One of the University of Birmingham roles, within the SOC2 project, was to construct a neutral strontium atomic package, and integrate it with the laser systems. The atomic package provides a cooled and trapped strontium atomic cloud, which serves as a reference for the complete clock. It consists of a permanent-magnet Zeeman slower, developed at the National Physical Laboratory (NPL) [162], as well as an atom oven and science chamber, both developed at the University of Birmingham. The details on the construction of the package can be found, in detail, in a thesis written by L. L. Smith from the University of Birmingham [83].

The development of the package can be described by obtaining three milestones: trapping the atoms into the first-stage magneto-optical trap (MOT), the second-stage magneto-optical trap, and then transferring them into the optical lattice. After obtaining those milestones and optimising the package, the system was transported to the German national metrology institute Physikalisch-Technische Bundensanstalt (PTB), to be integrated with the clock laser and characterised.

During the development and optimisation, the system was also used to test, for the first time, a newly emerging type of laser, for the laser cooling of strontium. The semiconductor disk laser (SDL) was successfully used to obtain a demanding second-stage red MOT, which is described in subsection 4.2.4.

5.5.1 Package transportation

The atomic package needed to be transported from the University of Birmingham to the Physikalisch-Technische Bundesanstalt (PTB) in Braunschweig, Germany. PTB is a German national metrology institute, where the atomic package was integrated with the mobile interrogation laser described in the section 5.4. As a metrology institute, PTB not only has primary frequency standards, but also another strontium lattice optical clock that can be used to characterise the performance of the space optical clock.

The atomic package was transported overnight, by approximately 1100 km, using a van. Pictures of the

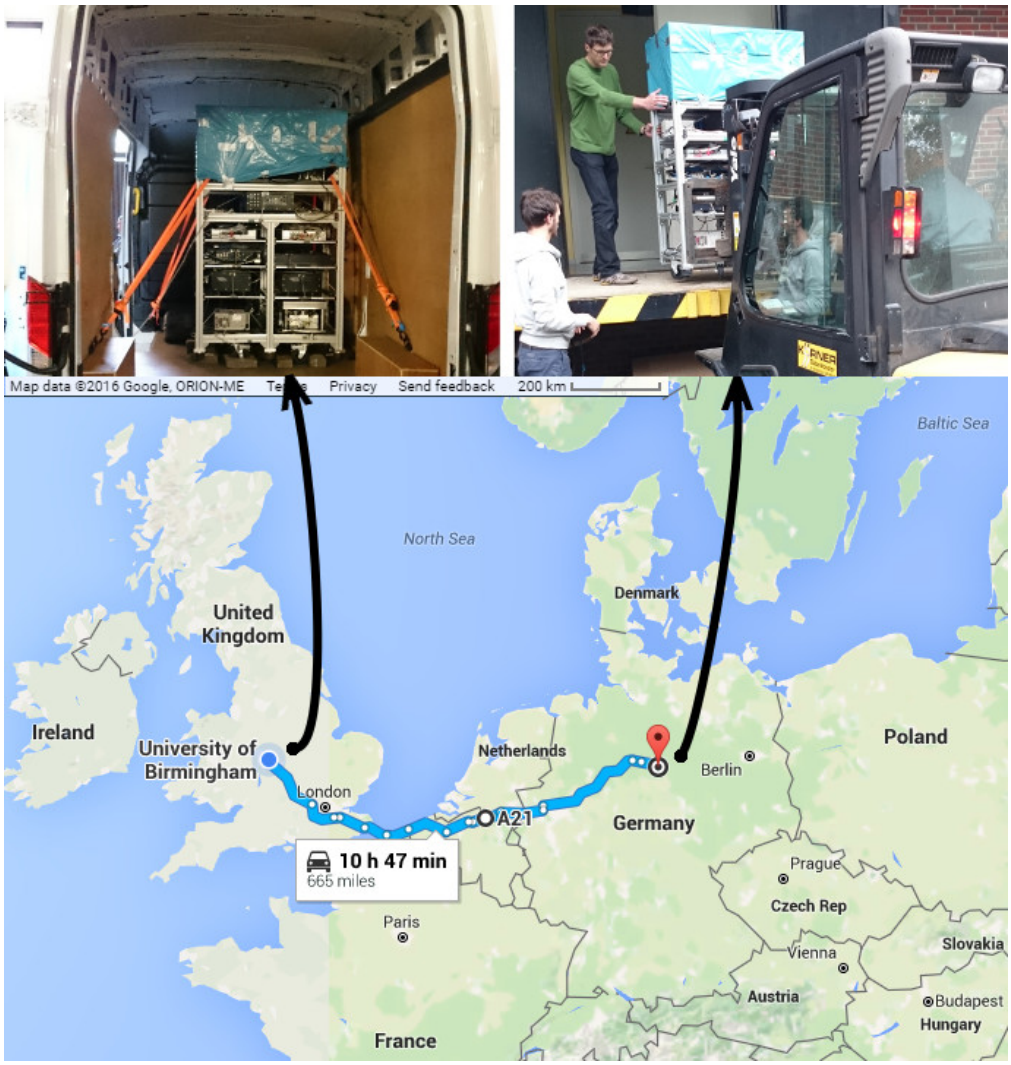

Figure 5.27: Atomic package transportation from the University of Birmingham to PTB in Braunschweig, Germany, approximately 1100 km by car. Courtesy of Google Maps.

system being loaded and unloaded from the van are presented on the top of figure 5.27. The transportation route is presented on a map in the same figure, and is marked with a blue curve. The system was not powered throughout the journey, including the ion pumps maintaining the ultra-high vacuum inside the science chamber. Despite this, the pressure level inside the science chamber stayed at a low level, and the ultra-high vacuum was restored at the destination by turning the ion pumps back on. This proves the high robustness of the system, as the system remained sealed and leak-free, in spite of high vibration levels and changing acceleration. For more information about the atomic package, please refer to [83].

5.6 Interrogation of the clock transition

After the SOC2 atomic package was transported to PTB, it was integrated with the clock laser described in section 5.4. In this section I will show the results obtained by using the mobile interrogation laser to probe the strontium clock transition in the transportable atomic package.

5.6.1 Clock transition spectroscopy

Ultimately, the clock laser is necessary for interrogating the atoms that provide the long-term reference, to keep the laser stable and accurate. Before the laser is used to stabilise to the $^1\mathbf{S}_0 \rightarrow {}^3\mathbf{P}_0$ clock transition, it needs to be frequency tuned to be close to the transition. To do this, we have utilised the beat note between our laser and the stationary optical clock system that is operating using the ^{87}Sr isotope. Next, by having the ^{88}Sr atoms trapped in the lattice, we could scan the frequency of the clock laser output in search for the resonance line. A helpful tool in tuning the laser closer to the resonance was the frequency chart in figure 5.17 presented in section 5.4.

In figure 5.28a, the first interrogation of the atoms is presented. The blue points represent the measured data, while the red curve shows a fitted Gaussian function. The full width at half maximum (FWHM) is equal to 880±20 Hz. During this measurement, the pressure in the vacuum chamber was relatively high, causing the laser's spectral line to broaden over the measurement period. The measured linewidth is therefore dominated by the linewidth of the laser, which is a Gaussian shape due to the nature of the pressure fluctuations inside the vacuum chamber.

The pressure level inside the clock laser vacuum chamber was temporarily improved from 10^{-6} mbar to 10^{-7} mbar, by increasing the ion pump voltage for a short time, to lower the current leakage. Lowering the pressure level helped with reducing the linewidth of the laser, which in result lead to a narrower spectroscopy results, as shown in figure 5.28b. This time, the fitted function has a Lorentzian shape, as expected, with the FWHM equal to 32 ± 2 Hz.

Despite a short-term pressure level improvement, the clock laser has still shown poor instability, on the 10^{-14} level, after a couple of hours when the pressure level degraded again. To provide stable laser light for the atoms, the SOC2 clock laser was phase-locked to the stationary 'Beast' laser [71]. To do this, we utilised the beat note detection setup, which was previously used to study the stability of the laser. The beat note frequency was sent to a phase comparator, where it was compared with a stable frequency taken from a referenced DDS (direct digital synthesiser). The phase difference was then used to compensate for any beat note frequency drifts, by using a double-pass AOM (AOM1 in figure 5.15), to transfer the stability of the

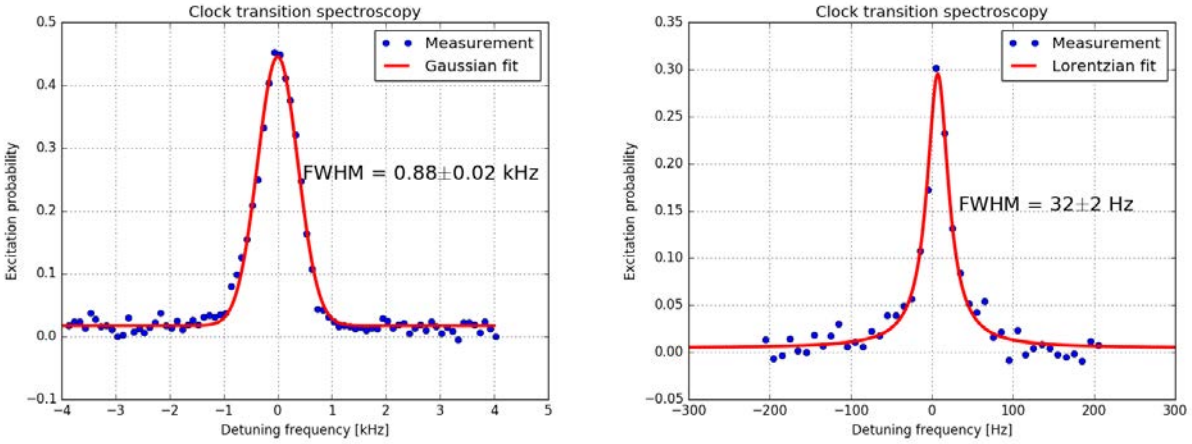

(a) First interrogation

(b) The best interrogation

Figure 5.28: Spectroscopy of the clock transition in ^{88}Sr with the mobile interrogation laser. **(a)** The first interrogation is presented with blue points and red curve is a Gaussian fit to the points. The broad linewidth and Gaussian shape is caused by the instability of the pressure level in the reference cavity vacuum chamber. **(b)** Plot showing the best interrogation results when the pressure level in the clock laser vacuum chamber was temporarily lowered. Blue points show the measured spectroscopic data, while red curve is a Lorentzian fit to the data. A tenfold reduction of the measured linewidth can be observed.

stationary clock laser system onto the SOC2 clock laser. The interrogation of the clock transition, with the clock laser phase-locked to the Beast clock laser, was performed and the result is presented in figure 5.29. The linewidth of the fitted Lorentzian function equals 9.3 ± 0.9 Hz. The linewidth of the transition is mostly limited by the bosonic nature of the ^{88}Sr isotope, introduced by collisions between the atoms in the cloud. In the future, the laser will be used with the fermionic ^{87}Sr isotope, which is less abundant and therefore harder to work with, but the linewidth can be significantly reduced by 3 orders of magnitude down to 1.2 mHz [101].

5.6.2 ^{88}Sr clock preliminary results

By repeatedly interrogating the clock transition, it is possible to get information on the absolute frequency drift of the clock laser. It is also possible to apply correction to the clock laser's frequency after every interrogation sequence, so that it stays around the absolute frequency of the strontium clock transition.

As previously shown, the ^{88}Sr clock transition was interrogated with the clock laser, in order to obtain the spectral line shape of the transition. The same transition was then used to correct the clock laser's frequency. The stability of the ^{88}Sr referenced clock laser, against the stationary Beast ultra-stable system, is represented by the black triangles in figure 5.30. As expected, the longer the clock transition is being interrogated for, the more accurate the result, and the lower the frequency instability, as the systematic

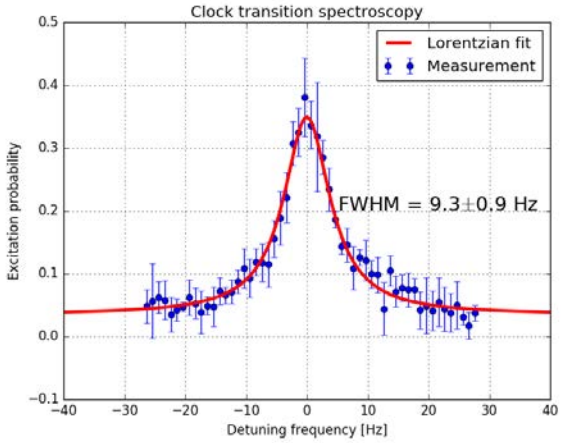

Figure 5.29: Spectroscopy of the clock transition in ^{88}Sr with a phase-locked SOC2 clock laser to a more stable reference laser. The obtained transition linewidth is narrower than without the phase-lock, which shows a room for improvement of the interrogation laser stability. The instability is most likely caused by too high pressure level in the reference cavity vacuum chamber. Data also presented in [114].

errors average out. The black dashed line shows a fit to the data $f(\tau) = A/\sqrt{\tau}$, where $A = 3.9 \times 10^{-16}$, and represents the potential performance of the ^{88}Sr clock, assuming white frequency noise dominates. This is the best instability measurement obtained with the bosonic atoms, and more thorough results are expected in the near future [163]. For the most recent update on the results, please refer to a thesis by S. Origlia [164].

5.7 Frequency references' instability comparison

Up to this point, different oscillators have been presented. Depending on the application and the requirements, some might be a better choice than others. For example, a laser referenced to an ultra-stable cavity has a very good frequency stability in the short term, but due to temperature drifts in the optical resonator, the long-term stability might be worse than some of the crystal oscillators.

Different frequency oscillators are compared in figure 5.31. Red triangles represent the stand-alone SOC2 mobile interrogation laser (data also presented in figure 5.18). Magenta upside-down triangles represent the stability of the University of Birmingham stationary interrogation laser (data also presented in figure 5.6). Black triangles show the preliminary ^{88}Sr clock transition stability (data also presented in figure 5.30). Data points drawn with green circles represent Stanford Research Systems (SRS) FS725 rubidium frequency standard. Blue circles show the same SRS FS725 rubidium frequency standard but GPS disciplined (data also presented in figure 5.11). Cyan coloured diamonds show the instability of a DDS (model 409B from Novatech), which is limited by its internal reference. Yellow square points represent the instability of a VCO

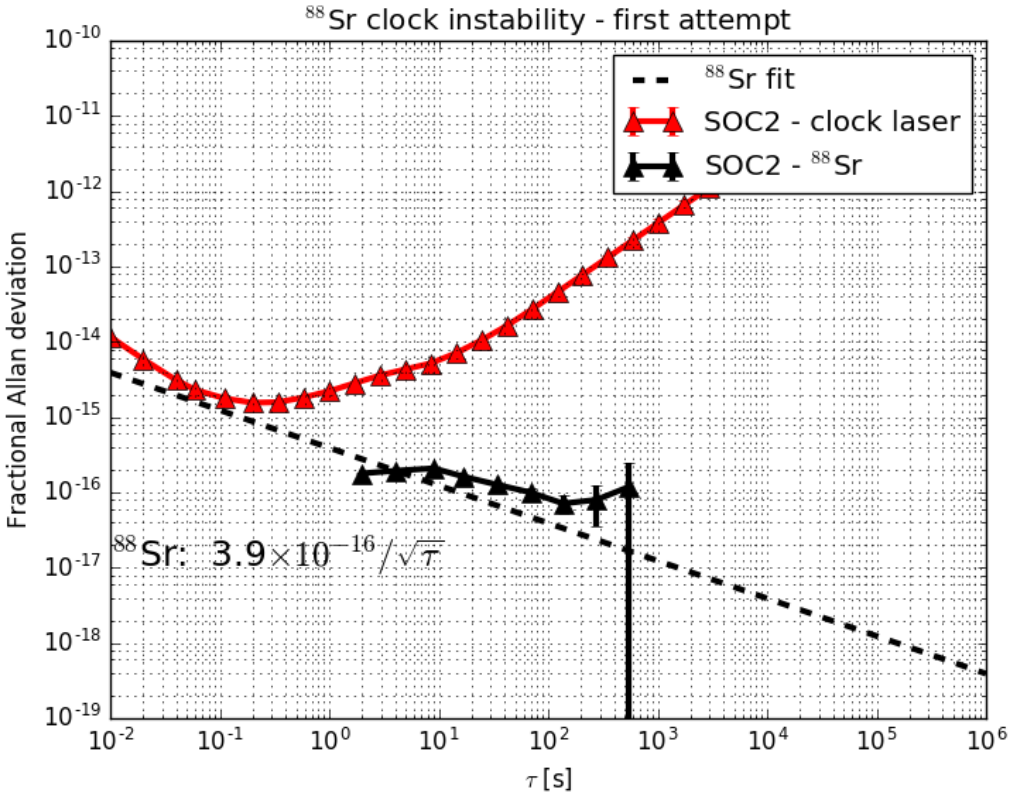

Figure 5.30: The instability of the ultra-stable clock laser at its best performance (red triangles) and the same clock laser referenced to the clock transition in ^{8}8Sr atoms. The dashed black line shows a fit to the data and represents the potential performance of the strontium optical clock. The black interrogation data points courtesy of S. Origlia.

(ZX95-100-S+ from Minicircuits), the stability of which is most probably limited by the stability of the reference voltage.

As expected, the best stability is obtained with the interrogation laser locked to strontium atoms, which averages down with 3.9×10^{-16} $\sqrt{\mathrm{s}/\tau}$ rate. Next are the ultra-stable lasers, featuring very good instability level $< 10^{-14}$ but only for a couple of seconds because of the slow drift of the reference cavity. It is beneficial to use an ultra-stable laser as a stable frequency reference, but only to obtain good stability in short time scales up to 100 – 1000 s. After that time other RF frequency references, such as the rubidium frequency standard SRS FS725, can obtain a better performance. The rubidium frequency standard can be additionally disciplined with the GPS signal, that averages down with 1.2×10^{-10} $\sqrt{\mathrm{s}/\tau}$ rate. Such a GPS disciplined frequency reference is not only a stable frequency source but also accurate, as the GPS signal used for disciplining comes from calibrated GPS satellites' atomic clocks. Frequency from the direct digital

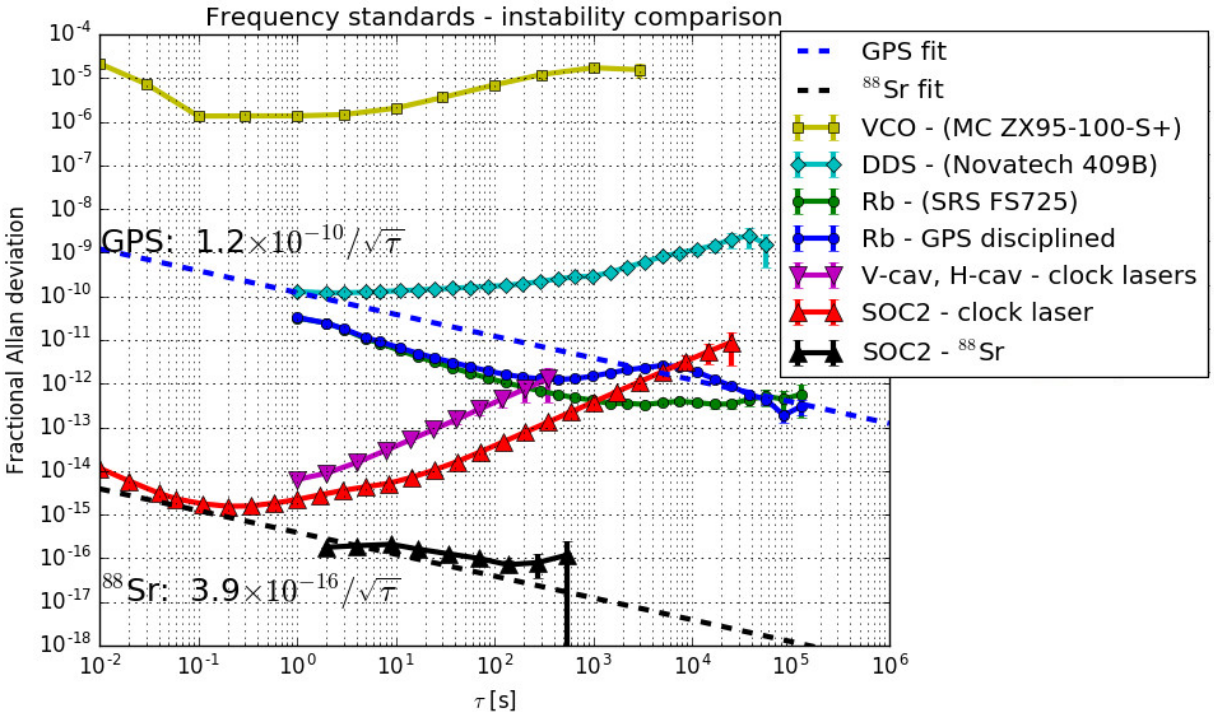

Figure 5.31: Instability comparison of various frequency standards.

synthesiser (DDS) starts on a good stability level of 10^{-10}, and then it slowly drifts away. The drift could be removed for example by disciplining it to the GPS signal, as it was done with the rubidium frequency standard. The worst measured frequency source was the VCO. It needs a stable voltage source that is used as a reference standard and it is possible that the frequency stability was limited by the stability performance of the voltage reference.

In section 5.3 we have discussed frequency stability requirements for lasers and frequency shifters, used in the strontium lattice clock. Having an access to the optical frequency comb, it is possible to transfer stability of any radio or optical frequency source into the lasers' optical frequency. Referring to the table 5.2, which shows the frequency stability requirements for the lasers, it is possible to learn that the GPS disciplined rubidium frequency standard is good enough to stabilise blue cooling laser and repumping lasers. It also should be good enough to stabilise the red broadband second-stage cooling laser, however, the stability might be not good enough for the single-frequency second-stage cooling laser. Best results would be obtained by stabilising all the lasers, used in the cooling, to the interrogation laser that is referenced to the clock transition.

The analysis of what frequency source would be a suitable reference for the frequency shifters can be done

by referring to table 5.3 in section 5.3. The VCO is good enough to drive an 80 MHZ frequency shifter for blue cooling and both repump lasers. It is also good enough to drive a 2.5 GHz frequency shifter for the same lasers, however, the optical frequency of the 679 nm repump laser might drift away after $\sim$ 100 s. For the second-stage red cooling laser, it is better to use a more stable frequency source, such as the DDS. The DDS might also be good enough for an 80 MHz frequency shifter in the clock laser system, used for interrogating ^{88}Sr atoms for up to $\sim 10^4$ s. For a 2.5 GHz frequency shifter, it is recommended to use more stable frequency source, for example the rubidium frequency standard. Finally, the rubidium frequency standard can have insufficient stability for the frequency shifters used in a clock laser setup that interrogates the narrower ^{87}Sr transition. Instead, the interrogation laser's frequency should be used.

5.8 State-of-the-art clock lasers

At the beginning of this chapter I described the stationary ultra-stable interrogation laser. The instability of the laser was measured to reach 5×10^{-15} at 1 s. This is better than the first iteration of the laser (2×10^{-14}) presented by S. Johnson [152]. Although the interrogation laser is not as stable as state-of-the-art ultra-stable lasers with temperature compensated fused silica mirrors [71, 76], its instability is only 5 times higher than the laser using similar cavity design with ULE mirrors ($\sim 1 \times 10^{-15}$), presented by Ludlow et al. [149]. To perform the absolute characterisation of an oscillator's stability, it is necessary to have an even more stable reference. Alternatively, it is possible to closely estimate the performance by having two reference oscillators operating with a similar performance, and using the three-corner hat method [165]. Unfortunately, at this stage neither did we have a more stable nor two similar references to compare with. It is believed that the instability measurement was limited by the reference ultra-stable laser, based on a horizontal-cavity and described in detail by S. Johnson [152]. Better characterisation of the lasers might be possible in the future, as the next generations of the stationary ultra-stable clock laser will be constructed.

In this chapter, I have also described the mobile ultra-stable laser for space applications, which I have assembled, characterised and prepared for integration with the atomic package. The laser obtained instability value of 7.9×10^{-16}, close to the estimated thermal noise limit of $\sim 5 \times 10^{-16}$. The stability performance of the laser is on a similar level as state-of-the-art transportable ultra-stable lasers. For example the laser presented by Argence et al. [76] reached instability 5×10^{-16} and the laser presented by Koller et al. [52] reached 4×10^{-16}. It is believed that the stability performance is limited by relatively high pressure level in the optical resonator vacuum housing ($\sim 10^{-6}$ mbar), which will be improved in the very near future.

The acceleration sensitivity of the mobile laser's optical resonator is between 2.0×10^{-11}/g and $5.8 \times$

10^{-10}/g as measured for different axes. This values are not as good as in its archetype presented by Argence et al. [76], with acceleration sensitivity values between 1×10^{-11}/g and 4×10^{-11}/g. Nevertheless, the obtained values are similar as in other cavity designs presented by Leibrandt et al. [75] (4×10^{-11}/g – 1×10^{-10}/g), Nazarova et al. [77] (3.2×10^{-11}/g – 3.0×10^{-10}/g) and Chen et al. (1.7×10^{-11}/g – 3.9×10^{-10}/g). The acceleration sensitivity should be good enough for the laser to be used on the international space station when placed in the vibration isolation platform. The cavity design presented by Webster et al. [79] (1×10^{-13}/g – 2.5×10^{-11}/g) can be considered in the future to improve the acceleration sensitivity for more demanding mobile applications. This cavity, however, is rather expensive to produce and very difficult to construct in a bigger size that would increase the stability performance. Apart from increasing the passive insensitivity, the further upgrades may also include an active feedback stabilisation system, such as the one presented by Leibrandt et al. [75].

Future developments of the ultra-stable lasers can utilise crystalline coatings, which feature very high reflectivity values and have smaller thermal noise limit [73, 74]. By using those coatings in the force insensitive cube cavity (Webster et al. [79]) it will be possible to outperform current transportable ultra-stable lasers, reaching instability level of 10^{-17} in the room temperature. Also in the future, the ultra-stable lasers can use another approach in order to improve their performance and, for example, replace the Fabry-Pérot resonators with other kinds of reference.

Spectral hole burning (SHB) is a promising alternative to the ultra-stable optical cavities. With this method, it is possible to bleach a spectral hole in a broad absorption spectrum of the material [166]. The frequency of a spectral hole can be tailored to match the requirements for a desired application, and it can feature a very narrow linewidth [167]. It can serve as a secondary frequency standard, and it can be used to stabilise a laser, for example by using the well known PDH locking method [168]. The downside of the SHB is that the material requires to be under a very low temperature in order to keep the spectral hole. This means that an extra high-end cryogenic system might be required. The latest achievements in the field include stabilisation of the laser to obtain instabilities of 6×10^{-16} [169]. Although this result is not as good as for the cryogenic silicon optical cavity, it might lead to the further advancements in the near future.

CHAPTER 6

CONCLUSIONS AND OUTLOOK

Precision timekeeping plays an important role in the modern world. It impacts many aspects of everyone's life by being used, both directly and indirectly, in navigation, telecommunication, economy, metrology, manufacturing and more. It is also necessary and commonly used in many fields of scientific research, where it allows for obtaining more accurate results, effectively pushing the boundaries of the modern science.

There always is a demand for the improvement of the clocks and frequency oscillators. A list of possible improvements includes not only increased performance, for example stability, accuracy or precision, but also a mobile design that is insensitive to external factors, and a more compact size. The miniaturisation process is very difficult and it brings many challenges. Usually, it is very difficult or even impossible to keep the full performance of a lab-based experiment, while significantly reducing its size. In many cases a compromise has to be found between the size of a device and its performance. On the other hand, it is important to remember that it is not only the size that makes the experiment mobile. For it to be mobile, it also needs to be designed in a certain way that makes it insensitive to external factors like changing value and direction of the acceleration vector.

The main focus of my thesis was to develop mobile subsystems necessary for the construction of the optical clock. The clock that is being developed will be based on neutral strontium atoms, and we want it to be flexible so it could be used with both ^{87}Sr and ^{88}Sr isotopes. The lattice strontium clock usually requires 6 tunable lasers for the first-stage cooling, second-stage cooling, repumping-I, repumping-II, interrogating the clock transition and the optical lattice, corresponding to wavelengths of 461 nm, 689 nm, 679 nm, 707 nm, 698 nm and 813 nm, respectively. Each of this lasers needs to be stabilised in order to stay at the exactly right wavelength. Other experiments usually use separate stabilisation system for each of the lasers and either stabilise them to the atomic spectroscopy, wavelength meter or optical cavity. This work gave a ground to

believe that all of those lasers can be locked to a single optical cavity, which effectively saves space and money. In section 4.3 I have presented a prototype of such a cavity, which has a custom-tailored mirror coating to meet different requirements for each of the lasers. This work also suggests a method of injecting all the six lasers into a single cavity, suitable for using the PDH locking method with, and still letting to do the mode inspection on the transmitted light. Furthermore, when using the traditional PDH locking method, it is only possible to lock at the frequency of the longitudinal mode of the cavity, which might be different from the resonant frequency of the atomic transition. This is another challenge that makes it difficult to stabilise multiple lasers to a single cavity. In this work I suggest that a fibre-coupled EOM can be used to implement a simple dual-sideband locking method to obtain a smoothly tunable locking point between the FSR of the optical cavity. In the near future, the frequency stabilisation system and its cavity will be upgraded and characterised in more detail. It will be tested with other lasers and the frequency optical comb will be used to measure the drift of the cavity. It will also be upgraded with the vacuum chamber in order to obtain a more stable environment.

On the laser side, my thesis focused mainly on two laser systems with the most extreme requirements: the 698 nm interrogation laser and 689 nm second-stage cooling laser. Those two lasers need to have very narrow linewidths and be ultra-stable in order to successfully use them in the experiment. In sections 4.1 and 4.2 I presented two different laser technologies that could serve as the 689 nm second stage cooling laser. The first is a tunable MOPA system based on the semiconductor laser diode and semiconductor tapered amplifier. The semiconductor laser has an advantage of a low cost, but it is still difficult to obtain good power levels in that wavelength range. However, we show that good power levels can be reached with a modular home-built MOPA system with very small driving electronics and without any water cooling. The laser is stabilised to the multiple-laser stabilisation system, and is part of the mobile MiniClock project.

The second laser described in section 4.2 is based on a semiconductor disk laser. We used a newly developed prototype of the laser at 689 nm and were the first group to obtain a demanding second-stage strontium MOT with that laser. It brings advantage of high power levels, good beam profile, narrow linewidth and a very broad tunability. The laser required water cooling, which also caused vibration leading to frequency instability. Characterisation of the laser provided a very important feedback that will contribute to the further development of the laser to enhance its stability and ease of use in the near future.

A laser that is discussed the most in this thesis is the interrogation 698 nm laser as it is the heart of the optical clock, hence it requires the highest attention. This dissertation talked about two interrogation laser systems. The stationary system based at the University of Birmingham described in 5.1 and a mobile system

developed within the SOC2 project, currently placed at PTB in Germany, and presented in section 5.4. The stationary system was constructed to be a base for the further experiments and a tool that could be used for the stabilisation of the optical frequency comb and characterisation of the other lasers. We obtained good stability results making it the most stable laser with the narrowest linewidth in Birmingham. It also became one of the few state-of-the-art ultra-stable lasers in the UK. In the near future, the stationary laser will be used to investigate the entanglement between the strontium atoms in the optical lattice.

The mobile interrogation laser described in this thesis is part of the SOC2 project. It was developed as an early-stage study, preparing the strontium optical clock to be used at the international space station (ISS). As described in 5.4, it is one of the most stable mobile lasers, built in a special way to withstand high values of acceleration. The measured vibrational sensitivity makes it suitable to be used in the ISS. It was integrated with the SOC2 atomic package to form a mobile strontium lattice clock, where we managed to measure a record-low instability value for the bosonic clock of $< 4 \times 10^{-16}/\sqrt{\tau}$. Furthermore, the SOC2 atomic package was recently used to observe a very narrow linewidth of the ^{88}Sr clock transition, equal to 220 mHz [163]. Currently, the mobile interrogation laser is being upgraded to further increase its stability and address the problems with the leaking vacuum chamber. A major plan of the SOC2 project for the near future is to further optimise the system to obtain a record-low inaccuracy at 10^{-17} level for ^{88}Sr. Next, the system will be used with the fermionic ^{87}Sr isotope to obtain similar levels of instability and inaccuracy. When that is operational and well tested, the mobile clock will be transported to various locations around the world, to be tested in the field, and compared with other laboratory-based state-of-the-art optical clocks. Most recently the package became part of a new project called I-SOC (Space Optical Clock on the ISS), funded by the European Space Agency (ESA). Within the project there is a plan of using an ESA antenna to compare the mobile clock with the atomic clock ensemble in space (ACES) on the ISS. Further plans also include using the mobile clock for the measurement of the gravitational red shift and search of the dark matter topological defects crossing the Earth [66].

Overall, this thesis contributed to development of state-of-the-art lattice strontium clocks. Making those clocks mobile will open a new possibility for comparison between different labs around the world. Apart from the fundamental science research, this can also contribute to redefinition of second in the future.

LIST OF REFERENCES

[1] E. A. Abbott, *Flatland: A romance of many dimensions*. OUP Oxford (2006).

[2] T. Nicholson et al., *Systematic evaluation of an atomic clock at* 2×10^{-18} *total uncertainty*, Nature Communications **6** (2015).

[3] A. Picard, P. Barat, M. Borys, M. Firlus and S. Mizushima, *State-of-the-art mass determination of 28 Si spheres for the Avogadro project*, Metrologia **48** (2), S112–S119 (2011).

[4] Y. Azuma et al., *Improved measurement results for the Avogadro constant using a 28 Si-enriched crystal*, Metrologia **52** (2), 360–375 (2015).

[5] B. W. Mangum and D. D. Thornton, *Determination of the triple-point temperature of gallium*, Metrologia **15** (4), 201–215 (2005).

[6] G. Benedetto, R. M. Gavioso, R. Spagnolo, P. Marcarino and A. Merlone, *Acoustic measurements of the thermodynamic temperature between the triple point of mercury and 380 K*, Metrologia **41** (1), 74–98 (2004).

[7] M. Moldover and J. P. M. Trusler, *Accurate acoustic thermometry I : The triple point of gallium*, Metrologia **25** 165–187 (1988).

[8] I. B. of Weights and M. (BIPM), *The international system of units (SI) - 8th edition*. STEDI MEDIA, 1, Boulevard Ney, 75018 Paris, France (2006).

[9] M.-C. Amann, T. Bosch, M. Lescure, R. Myllyla and M. Rioux, *Laser ranging: a critical review of usual techniques for distance measurement*, Optical engineering **40** (1), 10–19 (2001).

[10] A. Longstaff, *Calendars from around the World*, Greenwich: National Maritime Museum (2005).

[11] A. Waugh, *Sundials: their theory and construction*. Courier Corporation (2012).

[12] A. A. Mills, S. Day and S. Parkes, *Mechanics of the sandglass*, European Journal of Physics **17** (3), 97 (1996).

[13] G. Dohrn-van Rossum, *History of the hour: Clocks and modern temporal orders*. University of Chicago Press (1996).

[14] M. Bennett, M. F. Schatz, H. Rockwood and K. Wiesenfeld, *Huygens's clocks*, Proceedings: Mathematics, Physical and Engineering Sciences 563–579 (2002).

[15] F. Riehle, *Frequency standards: basics and applications*. John Wiley & Sons (2006).

[16] J. Maxwell, *A treatise on electricity and magnetism*. Oxford: Clarendon Press (1873).

[17] O. S. W. Gerlach, *Der experimentelle Nachweis der Richtungsquantelung im Magnetfeld*, Zeitschrift für Physik **9** (1), 349–352 (1922).

[18] I. I. Rabi, *Space quantization in a gyrating magnetic field*, Physical Review **51** 652–654 (1937).

[19] I. I. Rabi, J. R. Zacharias, S. Millman and P. Kusch, *A new method of measuring nuclear magnetic moment*, Physical Review **53** (4), 318 (1938).

[20] N. F. Ramsey, *History of early atomic clocks*, Metrologia **42** (5), S1–S3 (2005).

[21] N. F. Ramsey, *A new molecular beam resonance method*, Physical Review **76** 996–996 (1949).

[22] J. Terrien, *News from the international bureau of weights and measures*, Metrologia **4** (1), 41–45 (1968).

[23] P. Forman, *Atomichron®: The atomic clock from concept to commercial product*, Proceedings of the IEEE **73** (7), 1181–1204 (1985).

[24] R. Wynands and S. Weyers, *Atomic fountain clocks*, Metrologia **42** (3), S64–S79 (2005).

[25] S. Chu and C. Wieman, *Laser cooling and trapping of atoms: Introduction*, Journal of the Optical Society of America B **6** (11), 2020–2022 (1989).

[26] J. L. Hall, M. Zhu and P. Buch, *Prospects for using laser-prepared atomic fountains for optical frequency standards applications*, Journal of the Optical Society of America B **6** (11), 2194–2205 (1989).

[27] M. A. Kasevich, E. Riis, S. Chu and R. G. DeVoe, *RF spectroscopy in an atomic fountain*, Physical Review Letters **63** 612–615 (1989).

[28] A. Clairon, C. Salomon, S. Guellati and W. D. Phillips, *Ramsey resonance in a Zacharias fountain*, Europhysics Letters **16** (2), 165–170 (1991).

[29] P. Dickson, *Sputnik: The shock of the century*. Bloomsbury Publishing USA (2001).

[30] H. D. Black, *Early development of Transit, the Navy navigation satellite system*, Journal of Guidance, Control, and Dynamics **13** (4), 577–585 (1990).

[31] B. Hofmann-Wellenhof, H. Lichtenegger and J. Collins, *Global positioning system: theory and practice*. Springer Science & Business Media (2012).

[32] N. D. Bhaskar, J. White, L. A. Mallette, T. A. McClelland and J. Hardy, *A historical review of atomic frequency standards used in space systems*, in *Proceedings of 1996 IEEE International Frequency Control Symposium*, 24–32 (1996).

[33] C. Bartholomew, *Satellite frequency standards*, Navigation **25** (2), 113–120 (1978).

[34] J. White, F. Danzy, S. Falvey, A. Frank and J. Marshall, *NTS-2 cesium beam frequency standard for GPS*, in *Proceedings of the Eighth Annual Precise Time and Material Interval (PTTI) Applications and Planning Meeting. Held at Naval Research Laboratory, November 30-December 2, 1976. Prepared by Goddard Space Flight Center, Greenbelt, MD 20771, pp. 637-664*, 637–664 (1977).

[35] W. M. Itano, J. C. Bergquist, J. J. Bollinger, J. M. Gilligan, D. J. Heinzen, F. L. Moore, M. G. Raizen and D. J. Wineland, *Quantum projection noise: Population fluctuations in two-level systems*, Physical Review A **47** 3554–3570 (1993).

[36] L. Hollberg, C. W. Oates, G. Wilpers, C. W. Hoyt, Z. W. Barber, S. Diddams, W. Oskay and J. Bergquist, *Optical frequency/wavelength references*, Journal of Physics B **38** (9), S469–S495 (2005).

[37] T. Udem, R. Holzwarth and T. W. Hänsch, *Optical frequency metrology.*, Nature **416** (6877), 233–237 (2002).

[38] R. Kliese et al., *Difference-frequency combs in cold atom physics*, `arXiv:1308.6766`, (2016).

[39] C. W. Chou, D. B. Hume, T. Rosenband and D. J. Wineland, *Optical clocks and relativity*, Science **329** (5999), 1630–1633 (2010).

[40] J. L. Pacôme Delva, *Atomic clocks: new prospects in metrology and geodesy*, `arXiv:1308.6766`, (2013).

[41] A. Einstein, *Relativity: The special and the general theory*. Princeton University Press (2015).

[42] S. Blatt et al., *New limits on coupling of fundamental constants to gravity using* ^{87}Sr *optical lattice clocks*, Physical Review Letters **100** 140801 (2008).

[43] T. Rosenband et al., *Frequency ratio of Al+ and Hg+ single-ion optical clocks; metrology at the 17th decimal place*, Science **319** (5871), 1808–1812 (2008).

[44] B. Altschul et al., *Quantum tests of the Einstein equivalence principle with the STE-QUEST space mission*, Advances in Space Research **55** 501–524 (2015).

[45] J. Aron, *Atomic time lord to battle sneaky high-speed trades*. Retrieved on 15/01/2017. `https://www.newscientist.com/article/dn25423-atomic-time-lord-to-battle-sneaky-high-speed-trades/`.

[46] R. Bajaj, S. L. Ranaweera and D. P. Agrawal, *GPS: location-tracking technology*, Computer **35** (4), 92–94 (2002).

[47] X. Li, G. Dick, M. Ge, S. Heise, J. Wickert and M. Bender, *Real-time GPS sensing of atmospheric water vapor: Precise point positioning with orbit, clock, and phase delay corrections*, Geophysical Research Letters **41** (10), 3615–3621 (2014).

[48] X. Li, G. Dick, C. Lu, M. Ge, T. Nilsson, T. Ning, J. Wickert and H. Schuh, *Multi-GNSS meteorology: Real-time retrieving of atmospheric water vapor from BeiDou, Galileo, GLONASS, and GPS observations*, IEEE Transactions on Geoscience and Remote Sensing **53** (12), 6385–6393 (2015).

[49] I. Ushijima, M. Takamoto, M. Das, T. Ohkubo and H. Katori, *Cryogenic optical lattice clocks*, Nature Photonics **9** (3), 185–189 (2015).

[50] B. J. Bloom, T. L. Nicholson, J. R. Williams, S. L. Campbell, M. Bishof, X. Zhang, W. Zhang, S. L. Bromley and J. Ye, *An optical lattice clock with accuracy and stability at the* 10^{-18} *level.*, Nature **506** (7486), 71–75 (2014).

[51] S. L. Campbell et al., *A Fermi-degenerate three-dimensional optical lattice clock*, Science **358** (6359), 90–94 (2017).

[52] S. Koller, J. Grotti, A. Al-Masoudi, S. Dörscher, S. Häfner, U. Sterr, C. Lisdat et al., *Transportable optical lattice clock with* 7×10^{-17} *uncertainty*, Physical Review Letters **118** (7), 073601 (2017).

[53] T. Nicholson, M. Martin, J. Williams, B. Bloom, M. Bishof, M. Swallows, S. Campbell and J. Ye, *Comparison of two independent Sr optical clocks with* 1×10^{-17} *stability at* 10^3 *s*, Physical Review Letters **109** (23), 230801 (2012).

[54] Y. Jiang, A. Ludlow, N. Lemke, R. Fox, J. Sherman, L.-S. Ma and C. Oates, *Making optical atomic clocks more stable with* 10^{-16}*-level laser stabilization*, Nature Photonics **5** (3), 158–161 (2011).

[55] A. D. Ludlow, M. M. Boyd, J. Ye, E. Peik and P. O. Schmidt, *Optical atomic clocks*, Reviews of Modern Physics **87** 637–701 (2015).

[56] J. Millo, D. V. Magalhães, C. Mandache, Y. Le Coq, E. M. L. English, P. G. Westergaard, J. Lodewyck, S. Bize, P. Lemonde and G. Santarelli, *Ultrastable lasers based on vibration insensitive cavities*, Physical Review A **79** 1–7 (2009).

[57] S. Bize et al., *Cold atom clocks and applications*, Journal of Physics B **38** (9), S449–S468 (2005).

[58] Q. Chen, E. Magoulakis and S. Schiller, *High-sensitivity crossed-resonator laser apparatus for improved tests of Lorentz invariance and of space-time fluctuations*, Physical Review D **93** (2), 022003 (2016).

[59] A. Nevsky, S. Alighanbari, Q.-F. Chen, I. Ernsting, S. Vasilyev, S. Schiller, G. Barwood, P. Gill, N. Poli and G. M. Tino, *Robust frequency stabilization of multiple spectroscopy lasers with large and tunable offset frequencies*, Optics Letters **38** (22), 4903 (2013).

[60] S. Herrmann, A. Senger, K. Möhle, M. Nagel, E. Kovalchuk and A. Peters, *Rotating optical cavity experiment testing Lorentz invariance at the* 10^{-17} *level*, Physical Review D **80** (10), 105011 (2009).

[61] P. Antonini, M. Okhapkin, E. Göklü and S. Schiller, *Test of constancy of speed of light with rotating cryogenic optical resonators*, Physical Review A **71** (5), 050101 (2005).

[62] A. Cygan, D. Lisak, P. Morzyski, M. Bober, M. Zawada, E. Pazderski and R. Ciuryo, *Cavity mode-width spectroscopy with widely tunable ultra narrow laser*, Optics Express **21** (24), 29744 (2013).

[63] B. P. Abbott et al., *LIGO: the laser interferometer gravitational-wave observatory*, Reports on Progress in Physics **72** (7), 076901 (2009).

[64] J. M. Hogan and M. A. Kasevich, *Atom-interferometric gravitational-wave detection using heterodyne laser links*, Physical Review A **94** (3), 033632 (2016).

[65] P. Wcisło, P. Morzyński, M. Bober, A. Cygan, D. Lisak, R. Ciuryło and M. Zawada, *Experimental constraint on dark matter detection with optical atomic clocks*, Nature Astronomy **1** 0009 (2016).

[66] A. Derevianko and M. Pospelov, *Hunting for topological dark matter with atomic clocks*, Nature Physics **10** (12), 933–936 (2014).

[67] M. Nagel, K. Möhle, K. Döringshoff, S. Schikora, E. Kovalchuk and A. Peters, *Ultra-stable cryogenic optical resonators for tests of fundamental physics*, `arXiv:1308.5582`, (2013).

[68] P. Ghelfi et al., *A fully photonics-based coherent radar system*, Nature **507** (7492), 341–345 (2014).

[69] T. Fortier et al., *Generation of ultrastable microwaves via optical frequency division*, Nature Photonics **5** (7), 425–429 (2011).

[70] H. Al-Taiy, N. Wenzel, S. Preußler, J. Klinger and T. Schneider, *Ultra-narrow linewidth, stable and tunable laser source for optical communication systems and spectroscopy.*, Optics Letters **39** (20), 5826–9 (2014).

[71] S. Häfner, S. Falke, C. Grebing, S. Vogt, T. Legero, M. Merimaa, C. Lisdat and U. Sterr, 8×10^{-17} *fractional laser frequency instability with a long room-temperature cavity*, Optics Letters **40** (9), 2112–2115 (2015).

[72] D. G. Matei et al., 1.5 μm *lasers with sub-10 mHz linewidth*, Physical Review Letters **118** 263202 (2017).

[73] G. D. Cole, W. Zhang, M. J. Martin, J. Ye and M. Aspelmeyer, *Tenfold reduction of Brownian noise in high-reflectivity optical coatings*, Nature Photonics **7** (8), 644–650 (2013).

[74] G. D. Cole, D. Follman, P. Heu, C. Deutsch, C. Pawlu and M. Aspelmeyer, *Low-noise substrate-transferred crystalline coatings for precision interferometry*, in *Optical Interference Coatings*, MB–5, Optical Society of America (2016).

[75] D. R. Leibrandt, M. J. Thorpe, M. Notcutt, R. E. Drullinger, T. Rosenband and J. C. Bergquist, *Spherical reference cavities for frequency stabilization of lasers in non-laboratory environments*, Optics Express **19** (4), 3471–3482 (2011).

[76] B. Argence, E. Prevost, T. Lévèque, R. Le Goff, S. Bize, P. Lemonde and G. Santarelli, *Prototype of an ultra-stable optical cavity for space applications.*, Optics Express **20** (23), 25409–20 (2012).

[77] T. Nazarova, F. Riehle and U. Sterr, *Vibration-insensitive reference cavity for an ultra-narrow-linewidth laser*, Applied Physics B: Lasers and Optics **83** 531–536 (2006).

[78] Q.-F. Chen, A. Nevsky, M. Cardace, S. Schiller, T. Legero, S. Häfner, A. Uhde and U. Sterr, *A compact, robust, and transportable ultra-stable laser with a fractional frequency instability of* 1×10^{-15}*.*, The Review of Scientific Instruments **85** (11), 113107 (2014).

[79] S. Webster and P. Gill, *Force-insensitive optical cavity.*, Optics Letters **36** (18), 3572–3574 (2011).

[80] S. Häfner, *Ultra-stabile Lasersysteme für Weltraum- und Bodenanwendungen*. Ph.D. thesis, Leibniz Universität Hannover (2015).

[81] B. O. Kock, *Magneto-optical trapping of strontium for use as a mobile frequency reference*. Ph.D. thesis, University of Birmingham (2013).

[82] W. He, *Towards a miniaturized strontium optical lattice clock*. Ph.D. thesis, University of Birmingham (2017).

[83] L. L. Smith, *A transportable strontium optical lattice clock towards space*. Ph.D. thesis, University of Birmingham (2016).

[84] G. Whitrow, *Time in history: Views of time from prehistory to the present day*. Oxford paperbacks. Oxford University Press (1989).

[85] S. Mereghetti, *The strongest cosmic magnets: soft gamma-ray repeaters and anomalous X-ray pulsars*, The Astronomy and Astrophysics Review **15** (4), 225–287 (2008).

[86] D. J. Thompson, *Gamma ray pulsars*, Cosmic Gamma-Ray Sources 149–168 (2004).

[87] F. Michel, *Origin of millisecond pulsars*, Nature **329** (6137), 310–312 (1987).

[88] J. G. Hartnett and A. N. Luiten, *Colloquium: Comparison of astrophysical and terrestrial frequency standards*, Reviews of Modern Physics **83** (1), 1 (2011).

[89] A. Wolszczan, *Applications of pulsar timing*, Acta Cosmologica **23** 127–130 (1997).

[90] E. S. Ferre-Pikal and F. L. Walls, *Frequency standards, characterization*. Wiley Online Library (2005).

[91] C. Audoin and B. Guinot, *The measurement of time: time, frequency and the atomic clock*. Cambridge University Press (2001).

[92] B. E. Saleh and M. C. Teich, *Fundamentals of photonics*, vol. 22. Wiley New York (1991).

[93] L. Brovelli and U. Keller, *Simple analytical expressions for the reflectivity and the penetration depth of a Bragg mirror between arbitrary media*, Optics Communications **116** (4-6), 343–350 (1995).

[94] M. L. Gorodetsky, *Thermal noises and noise compensation in high-reflection multilayer coating*, Physics Letters A **372** (46), 6813–6822 (2008).

[95] T. Kessler, T. Legero and U. Sterr, *Thermal noise in optical cavities revisited*, Journal of the Optical Society of America B **29** (1), 178–184 (2012).

[96] S. J. Orfanidis, *Electromagnetic waves and antennas*, (2002). `http://www.ece.rutgers.edu/~orfanidi/ewa/`.

[97] E. Bava, A. Godone and G. Rietto, *Rabi and Ramsey interrogations of metastable beams*, Applied Physics B **41** (3), 187–196 (1986).

[98] D. Halliday and R. Resnick, *Fundamentals of physics*. John Wiley & Sons (1981).

[99] Z. Leś, *Podstawy fizyki atomu*. Warszawa: Wydawnictwo Naukowe PWN SA (2015).

[100] B. Zietek, *Optoelektronika*. Wydawnictwo Uniwersytetu Mikolaja Kopernika (2011).

[101] S. G. Porsev, A. D. Ludlow, M. M. Boyd and J. Ye, *Determination of Sr properties for a high-accuracy optical clock*, Physical Review A **78** 032508 (2008).

[102] S. Jennings, *The mean free path in air*, Journal of Aerosol Science **19** (2), 159–166 (1988).

[103] M. S. Safronova, S. G. Porsev, U. I. Safronova, M. G. Kozlov and C. W. Clark, *Blackbody-radiation shift in the Sr optical atomic clock*, Physical Review A **87** 012509 (2013).

[104] C. Grebing, A. Al-Masoudi, S. Dörscher, S. Häfner, V. Gerginov, S. Weyers, B. Lipphardt, F. Riehle, U. Sterr and C. Lisdat, *Realization of a timescale with an accurate optical lattice clock*, Optica **3** (6), 563–569 (2016).

[105] F. Riehle, *Towards a redefinition of the second based on optical atomic clocks*, Comptes Rendus Physique **16** (5), 506–515 (2015).

[106] P. Gill, *When should we change the definition of the second?*, Philosophical Transactions of the Royal Society of London A: Mathematical, Physical and Engineering Sciences **369** (1953), 4109–4130 (2011).

[107] F. Riehle, *Optical clock networks*, Nature Photonics **11** (1), 25–31 (2017).

[108] H. Margolis et al., *International timescales with optical clocks (ITOC)*, in *European Frequency and Time Forum & International Frequency Control Symposium (EFTF/IFC), 2013 Joint*, 908–911, IEEE (2013).

[109] H. Hachisu et al., *Direct comparison of optical lattice clocks with an intercontinental baseline of 9000 km*, Optics Letters **39** (14), 4072–4075 (2014).

[110] C. Lisdat et al., *A clock network for geodesy and fundamental science*, Nature Communications **7** (2016).

[111] T. Akatsuka, H. Ono, K. Hayashida, K. Araki, M. Takamoto, T. Takano and H. Katori, *30-km-long optical fiber link at 1397 nm for frequency comparison between distant strontium optical lattice clocks*, Japanese Journal of Applied Physics **53** (3), 032801 (2014).

[112] P. Gill, *Is the time right for a redefinition of the second by optical atomic clocks?*, in *Journal of Physics: Conference Series*, vol. 723, 012053, IOP Publishing (2016).

[113] J. Sansonetti and G. Nave, *Wavelengths, transition probabilities, and energy levels for the spectrum of neutral strontium (Sr I)*, Journal of Physical and Chemical Reference Data **39** (3), 033103 (2010).

[114] S. Origlia et al., *Development of a strontium optical lattice clock for the SOC mission on the ISS*, in *SPIE Photonics Europe*, 990003–990003, International Society for Optics and Photonics (2016).

[115] M. M. Boyd, *High precision spectroscopy of strontium in an optical lattice: Towards a new standard for frequency and time*. Ph.D. thesis, University of Colorado (2007).

[116] H. Katori, T. Ido, Y. Isoya and M. Kuwata-Gonokami, *Magneto-optical trapping and cooling of strontium atoms down to the photon recoil temperature*, Physical Review Letters **82** 1116–1119 (1999).

[117] M. Schioppo, N. Poli, M. Prevedelli, S. Falke, C. Lisdat, U. Sterr and G. M. Tino, *A compact and efficient strontium oven for laser-cooling experiments*, Review of Scientific Instruments **83** (10), (2012).

[118] O. Kock, W. He, D. Świerad, L. Smith, J. Hughes, K. Bongs and Y. Singh, *Laser controlled atom source for optical clocks*, Scientific Reports **6** 37321 (2016).

[119] H. J. Metcalf and P. Van der Straten, *Laser cooling and trapping*. Springer, New York (1999).

[120] *Laser cooling and trapping of atoms*, Journal of Optical Society of America **20** (5), 887–908 (2003).

[121] K. Dieckmann, R. Spreeuw, M. Weidemüller and J. Walraven, *Two-dimensional magneto-optical trap as a source of slow atoms*, Physical Review A **58** (5), 3891 (1998).

[122] M. Yasuda and H. Katori, *Lifetime measurement of the $^3P_2$ metastable state of strontium atoms*, Physical Review Letters **92** (15), 153004–1 (2004).

[123] R. Santra, K. V. Christ and C. H. Greene, *Properties of metastable alkaline-earth-metal atoms calculated using an accurate effective core potential*, Physical Review A **69** 042510 (2004).

[124] W. Qiang, L. Bai-Ke, Z. Yang, L. Ye, W. Shao-Kai, W. Min-Ming, Z. Er-Jun, L. Tian-Chu and F. Zhan-Jun, *Magneto-optical trapping of ^{88}Sr atoms with 689 nm laser*, Chinese Physics Letters **28** (3), 033201 (2011).

[125] N. Poli, M. Schioppo, S. Vogt, S. Falke, U. Sterr, C. Lisdat and G. M. Tino, *A transportable strontium optical lattice clock*, Applied Physics B: Lasers and Optics **117** (4), 1107–1116 (2014).

[126] S. B. Nagel, *Ultracold collisions in atomic strontium*. Ph.D. thesis, Rice University (2008).

[127] T. Legero, J. S. R. V. Winfred, F. Riehle and U. Sterr, *Ultracold ^{88}Sr atoms for an optical lattice clock*, in *Frequency Control Symposium, 2007 Joint with the 21st European Frequency and Time Forum. IEEE International*, 119–122, IEEE (2007).

[128] M. Takamoto, F.-L. Hong, R. Higashi and H. Katori, *An optical lattice clock*, Nature **435** (7040), 321–324 (2005).

[129] T. Legero, D. Matei, R. Weyrich, F. Riehle, U. Sterr, W. Zhang, L. Sonderhouse, J. Robinson and J. Ye, *Optical cryogenic silicon resonators*, in *Precision Electromagnetic Measurements (CPEM 2016), 2016 Conference on*, 1–2, IEEE (2016).

[130] M. Fleming and A. Mooradian, *Spectral characteristics of external-cavity controlled semiconductor lasers*, IEEE Journal of Quantum Electronics **17** (1), 44–59 (1981).

[131] M. G. Littman and H. J. Metcalf, *Spectrally narrow pulsed dye laser without beam expander*, Applied Optics **17** (14), 2224–2227 (1978).

[132] F. J. Duarte, *Tunable lasers handbook*. Academic Press (1996).

[133] M. G. Tarallo, *Development of a strontium optical lattice clock*. Ph.D. thesis, University of Pisa (2009).

[134] Y. Cunyun, *Tunable external cavity diode lasers*. World Scientific (2004).

[135] L. J. Curtis, *Atomic structure and lifetimes: a conceptual approach*. Cambridge University Press (2003).

[136] D. Pabœuf and J. E. Hastie, *Tunable narrow linewidth AlGaInP semiconductor disk laser for Sr atom cooling applications*, Applied Optics **55** (19), 4980–4984 (2016).

[137] B. Edlén, *The refractive index of air*, Metrologia **2** (2), 71 (1966).

[138] K. P. Birch and M. J. Downs, *An updated Edlén equation for the refractive index of air*, Metrologia **30** (3), 155–162 (1993).

[139] K. P. Birch and M. J. Downs, *Correction to the updated Edlén equation for the refractive index of air*, Metrologia **31** 315–316 (2005).

[140] A. Niggebaum, *Towards mobile quantum sensors for gravity surveys*. Ph.D. thesis, University of Birmingham (2016).

[141] C. V. Rammeloo, *Optimisation of a cold-atoms interferometer for gravimetry*. Ph.D. thesis, University of Birmingham (2017).

[142] J. I. Malcolm, *Construction of a portable platform for cold atom interferometry*. Ph.D. thesis, University of Birmingham (2016).

[143] Met Office (2006): UK Hourly Weather Observation Data, Part of the Met Office Integrated Data Archive System (MIDAS). NCAS British Atmospheric Data Centre, 2016. `http://catalogue.ceda.ac.uk/uuid/916ac4bbc46f7685ae9a5e10451bae7c`.

[144] J. M. Lafferty, *Heat transfer and fluid flow in minichannels and microchannels*. Wiley-Interscience (1998).

[145] S. Kandlikar, S. Garimella, D. Li, S. Colin and M. R. King, *Heat transfer and fluid flow in minichannels and microchannels*. Elsevier (2005).

[146] A. Preston, B. Balaban and G. Mueller, *Hydroxide-bonding strength measurements for space-based optical missions*, International Journal of Applied Ceramic Technology **5** (4), 365–372 (2008).

[147] E. D. Black, *An introduction to Pound–Drever–Hall laser frequency stabilization*, American Journal of Physics **69** (1), 79–87 (2001).

[148] C. Eisele, a. Y. Nevsky and S. Schiller, *Laboratory test of the isotropy of light propagation at the* 10^{-17} *level*, Physical Review Letters **103** (9), 1–4 (2009).

[149] a. D. Ludlow, X. Huang, M. Notcutt, T. Zanon-Willette, S. M. Foreman, M. M. Boyd, S. Blatt and J. Ye, *Compact, thermal-noise-limited optical cavity for diode laser stabilization at 110ˆ15*, Optics Letters **32** (6), 641 (2007).

[150] J. Bartl and M. Baranek, *Emissivity of aluminium and its importance for radiometric measurement*, Measurement Science Review **4** (3), 31–36 (2004).

[151] J. Singham, *Tables of emissivity of surfaces*, International Journal of Heat and Mass Transfer **5** (1-2), 67–76 (1962).

[152] S. Johnson, *Narrow linewidth lasers for use with neutral strontium as a frequency standard*. Ph.D. thesis, University of Birmingham (2013).

[153] D. T. Blackstock, *Fundamentals of physical acoustics*. John Wiley & Sons (2000).

[154] L. Kinsler and A. Frey, *Fundamentals of acoustics*. Wiley (1962).

[155] B. Ravnaas, *Acoustic damping compositions having elastomeric particulate*, (2010). `https://www.google.com/patents/US20100261023`. US Patent App. 12/757,743.

[156] Stanford Research Systems (2015): FS725 rubidium frequency standard operation and service manual. URL date 10/08/2015:. `http://www.thinksrs.com/downloads/PDFs/Manuals/FS725m.pdf`.

[157] R. Bishop, *The mechatronics handbook, second edition - 2 volume set*. Mechatronics Handbook 2e. CRC Press (2002).

[158] D. Świerad et al., *Ultra-stable clock laser system development towards space applications*, Scientific Reports **6** 33973 (2016).

[159] S. Schiller et al., *The space optical clocks project: Development of high-performance transportable and breadboard optical clocks and advanced subsystems*, in *EFTF 2012 - 2012 European Frequency and Time Forum, Proceedings*, 412–418 (2012).

[160] K. Bongs et al., *Development of a strontium optical lattice clock for the SOC mission on the ISS*, Comptes Rendus Physique **16** (5), 553–564 (2015).

[161] A. Farsi, M. Siciliani De Cumis, F. Marino and F. Marin, *Photothermal and thermo-refractive effects in high reflectivity mirrors at room and cryogenic temperature*, Journal of Applied Physics **111** (4), 043101 (2012).

[162] I. R. Hill, Y. B. Ovchinnikov, E. M. Bridge, E. A. Curtis and P. Gill, *Zeeman slowers for strontium based on permanent magnets*, Journal of Physics B **47** (7), 075006 (2014).

[163] S. Origlia. Personal communication (2017).

[164] S. Origlia, *TBD*. Ph.D. thesis, Heinrich Heine University Düsseldorf (Expected 2018).

[165] T. Kessler, C. Hagemann, C. Grebing, T. Legero, U. Sterr, F. Riehle, M. J. Martin, L. Chen and J. Ye, *A sub-40-mHz-linewidth laser based on a silicon single-crystal optical cavity*, Nature Photonics **6** (10), 687–692 (2012).

[166] G. C. Bjorklund et al., *Persistent spectral hole-burning: science and applications*, vol. 44. Springer Science & Business Media (2012).

[167] P. Sellin, N. Strickland, J. Carlsten and R. Cone, *Programmable frequency reference for subkilohertz laser stabilization by use of persistent spectral hole burning*, Optics letters **24** (15), 1038–1040 (1999).

[168] N. Strickland, P. Sellin, Y. Sun, J. Carlsten and R. Cone, *Laser frequency stabilization using regenerative spectral hole burning*, Physical Review B **62** (3), 1473 (2000).

[169] M. J. Thorpe, L. Rippe, T. M. Fortier, M. S. Kirchner and T. Rosenband, *Frequency stabilization to* 6×10^{-16} *via spectral-hole burning*, Nature Photonics **5** (11), 688–693 (2011).